LOW IONIZATION NUCLEAR EMISSION LINE REGIONS: THE "MISSING LINK" IN THE ACTIVE GALACTIC NUCLEUS POPULATION

by

Rachel Dudik

A Dissertation
Submitted to the
Graduate Faculty
of
George Mason University
in Partial Fulfillment of
The Requirements for the Degree
of
Doctor of Philosophy
Physical Sciences

Committee:

Dr. Shobita Satyapal, Dissertation Director

Dr. Joseph Weingartner, Committee Member

Dr. Rita M. Sambruna, Committee Member

Dr. Rebecca Goldin, Committee Member

Dr. Maria Dworzecka, Committee Member

Dr. Robert Ehrlich, Department Chairperson

Dr. Peter Becker, Associate Dean for Graduate Studies, College of Science

Dr. Vikas Chandhoke, Dean, College of Science

Date: 11/06/07

Fall Semester 2007
George Mason University
Fairfax, VA

Low Ionization Nuclear Emission Line Regions:
The "Missing Link" in the Active Galactic Nucleus Population

A dissertation submitted in partial fulfillment of the requirements for the degree of Doctor of Philosophy at George Mason University

By

Rachel Dudik
Master of Science
George Mason University, 2005
Bachelor of Arts
St. John's College, 2002

Director: Dr. Shobita Satyapal, Professor
Department of Physics and Astronomy

Fall Semester
2007 George Mason University
Fairfax, VA

Epigram

If you start something, finish it,
and do it right, or don't do it at all.
FBM

Acknowledgments

This milestone in my life has only been made possible by numerous selfless people, who have taken the time, energy, and care to cultivate, educate, and foster my many years of development.

I must first thank my family. My mother, Margaret Dudik, has called nearly every night for 10 years to offer support and words of confidence that have guided me through some of my most difficult academic struggles. My father, Roger Dudik, has never failed to provide advice and encouragement when I needed them most. He and my step-mother, Sherry Dudik, have believed in me even when I did not. My grandmother, Betty Dudik, generously accompanied me on numerous college visits and, with my father, made certain I was able to attend any institution I chose. She, like my father, has always provided the most uplifting guidance and support. My parents and my grandmother have always known I would find success even when I was uncertain. For their confidence, encouragement, and loyalty I am deeply indebted.

My siblings have inspired me with their own pursuits. My brother, Eliot Dudik, has taught me that success will come to those who follow their passions. My sister, Allison Dudik, has taught me to be firm in my convictions and to have confidence in my opinions. Finally my brother, Blair Dudik, has taught me that determination, will, and a good sense of humor can tackle even the toughest adversaries. I thank them for all their support over the last five years

In addition to my immediate family, numerous others, who, throughout my college career, have made my academic goals achievable. Mrs. Marilyn Higuera was my undergraduate thesis adviser. I will never forget the day she had me recite Maxwell's equations in an oral examination; I was so nervous I swore I would never study physics again. Mrs. Higuera spent countless hours reviewing/revising numerous drafts of my undergraduate thesis. Although philosophical in nature, this paper was perhaps my first true scientific exercise, since the underlying hypothesis was disproven in the same fifty pages in which it was defined.

I am deeply indebted to Dr. James Beall, without whom I would have no dissertation for which to write acknowledgements. Jim was my laboratory tutor at St. John's College, and he introduced me to Shobita Satyapal, my doctoral adviser. Jim has always had a plan for me, and has mentored my future since I met him at SJC. I can only hope, one day, to be his clone.

Dr. Shobita Satyapal, my "academic mother," is by far the most selfless adviser who ever existed. She has painstakingly directed my academic progress. She was essential to the success of my first presentation, my first published paper, and to the completion of this dissertation. She has spent endless hours correcting and editing in an effort to teach me how write and speak clearly, properly, and with confidence. She has always kept my best interests in mind and has never ceased to make my goals her own. She has an obvious devotion to knowledge and a true desire to share it. I am deeply grateful for everything she has done for me throughout these five years.

Besides Shobita, three people became very important to my graduate school accomplishments, spending countless hours tutoring me in numerous astrophysical subjects. Dr. Joseph Weingartner has been continuously available to help me solve any physics problem. His insight and overall willingness to discuss my work has led to stronger publications and a more complete understanding of the physics behind our results. Like Shobita, Joe maintains a devotion to knowledge that is contagious. Dr. Rita Sambruna and Dr. Mario Gliozzi have taught me everything I know about X-ray astronomy. Rita was an academic adviser when I first entered the George Mason University physics program and has continued as my mentor during assignments at NASA/Goddard. She attended all of my presentations and supported me through all five years of graduate study. Dr. Mario Gliozzi shared an office with me at George Mason, and was a steadfast source of answers. Mario is responsible for teaching X-ray analysis procedures which are foundational to my research and dissertation. In addition, he unselfishly spent hours coaching my defense preparations and drilling me with questions relevant for defense of my dissertation. In the past five years he has shown unflagging dedication to my growth and success as an astronomer. Without his commitment and perseverance I would not be able to do what I can today. I would like to thank Joe, Rita, and Mario for their efforts, friendship, support and confidence.

In addition to these people numerous collaborators have spent many hours reviewing and commenting on our work. I am very grateful to Dan Watson, Jackie Fischer, Eli Dwek, Paul Martini, Kartik Sheth, Eckhard Sturm, Peter Van Hoof, Davide Donato, and Frederic Galliano for their enlightening and thoughtful comments and expertise that have significantly improved the research presented in this dissertation. I am also thankful for the invaluable data analysis assistance from Dan Watson, Joel Green, Brian O'Halloran, Devin Vega, and Diana Marcu. In addition I very grateful for the NASA Graduate Student Researchers Program through which I received nearly two years of financial support. Additional funding from numerous NASA grants include (but are not limited to) NAG5-11432 and NAG03-4134X.

Others have made my graduate school experience one of the most fabulous experiences of my life, and therefore, deserve mention. In some ways these people are the most important because, as my peers, I have always judged myself based partially on their actions and accomplishments. Their amazing senses of humor and devoted friendships have influenced my attitude and my way of thinking. Therefore, thank you:

- to Maria Dworzecka who accepted me into the Physical Sciences program and who advised me for five years.

- to Frederic Galliano for his numerous late-night tutorials and especially for his commas.
- to Monica Anatalio for her friendship and for teaching me how to write a sentence.
- to George Nelson for his confidence and for letting me borrow his car.
- to Davide Donato, who will some day rule the world, since he already rules his own.

Finally, but perhaps foremost, I am forever grateful to Christopher Tourigny, who has supported me through everything and without whom I would only be one.

Table of Contents

List of Tables

List of Figures

List of Symbols

ACIS	AXAF Charged coupled Imaging Spectrometer
AGN	Active Galactic Nucleus
BH	Black Hole
BHM	Black Hole Mass
BLR	Broad-Line Region
CCD	Charge Coupled Device
FIR	Far Infrared
FWHM	Full Width at Half Maximum
HDL	High Density Limit
HRC	High Resolution Camera
HETG	High Energy Transmission Grating
HST	Hubble Space Telescope
IR	Infrared
IRAC	Infrared Array Camera
IRAS	Infrared Astronomical Satellite
IRS	Infrared Spectrometer
ISM	Interstellar Medium
L_{FIR}	Far-infrared Luminosity
L_{FIR}/L_B	Infrared Brightness Ratio
L_X	X-ray Luminosity
L_{Edd}	Eddington luminosity
L_{BOL}	Bolometric luminosity

LDL	Low Density Limit
LETG	Low Energy Transmission Grating
LL	Low Luminosity
LLAGN	Low Luminosity Active Galactic Nucleus
LINER	Low Ionization Nuclear Emission-line Region
LWS	Long Wavelength Spectrometer
MIPS	Multiband Imaging Photometer for Spitzer
MIR	Mid-infrared
N_H	Galactic H I column density
NLR	Narrow-Line Region
NLS1	Narrow-Line Seyfert 1 Galaxy
RG	Radio Galaxy
RL	Radio Loud object
RQ	Radio Quiet object
RQQ	Radio Quiet Quasar
SED	Spectral Energy Distribution
SSC	Spitzer Science Center
UV	Ultra-Violet
VLBI	Very Long Baseline Interferometer
XSPEC	X-ray spectral fitting package

Abstract

LOW IONIZATION NUCLEAR EMISSION LINE REGIONS:
THE “MISSING LINK” IN THE ACTIVE GALACTIC NUCLEUS POPULATION

Rachel Dudik, PhD

George Mason University, 2007

Dissertation Director: Dr. Shobita Satyapal

The horizon of the universe, once thought to extend only to the disk of the Milky Way, is now known to embrace a host of diverse galaxies, from active galaxies such as quasars and Seyfert galaxies to normal galaxies such as our own. The recent discovery that virtually all local galaxies harbor massive nuclear black holes, has provided convincing evidence that active galactic nuclei (AGNs) and normal galaxies are indeed connected. The nature of this connection and the evolutionary history connecting them, however, continues to be elusive.

Low Ionization Nuclear Emission-line Regions (LINERs) are the dominant population of ’active’ galaxies in our local universe and may indeed be the missing piece to the evolutionary puzzle. LINERs are defined by optical line ratios uncharacteristic of photoionization by normal main sequence stars. While classical AGNs represent at most a few percent of the galaxy population, LINERs constitute as much as 50% of the total local extragalactic population. However, despite several decades of intense research, the ionization mechanism responsible for the unusual LINER spectrum remains a mystery. What is the ionization mechanism responsible

for the empirical line ratios characteristic of LINER galaxies? How do LINERs fit into the overall evolution of galaxies as we know it? Are LINERs a subclass of AGN? What is the evolutionary connection, if any, between galaxies with heavy starburst activity and AGNs?

The majority of LINERs are dust enshrouded and therefore very luminous in the far-infrared. The far-infrared (far-IR) luminosity to the luminosity in the optical B-band ($\lambda_{center} = 4400\AA$), the so-called IR-brightness ratio, can be used as a gauge of the amount of dust in host galaxy. LINERs span a wide range of LFIR/LB ratios, tending predominantly toward the IR-bright end. However, the majority of research to-date has been based on optically selected samples which are partial toward IR-faint LINERs. This bias toward IR-faint galaxies could have important consequences on statistical analyses which examine the fraction of LINERs hosting AGNs. In order for an accurate picture of LINERs to emerge, IR-bright as well as IR-faint galaxies must be studied. What fraction of IR-bright LINERs are AGNs?

In light of the open questions regarding these remarkable objects, the central goal of this dissertation is to carry out a systematic multi-wavelength X-ray imaging and Infrared spectroscopic survey of nearby LINERs spanning a wide range of IR-brightness ratios in order to 1) characterize the dominant energy source responsible for their optical line ratios, 2) compare the AGN detection rate in our infrared selected sample with the optically selected samples, 3) determine the luminosities, spectral characteristics and accretion properties of the AGN-LINERs and compare them with the standard active galaxies, and finally, 4) relate the host galaxies properties to the properties of the central source in an attempt to constrain the role of LINERs in galaxy evolution and formation models.

Chapter 1: INTRODUCTION AND MOTIVATIONS

1.1 Background on AGN

Immanuel Kant posited the presence of what he called "island universes" in his Universal Natural History and the Theory of Heavens published in 1755. Though no direct scientific evidence of this phenomenon existed at the time, this "fantasy" would become a reality many years later through the work of Hubble and many others like him. The universe is now known to embrace a host of diverse galaxies, with different shapes, sizes, and spectral features. My research specifically focuses on active galaxies–galaxies thought to contain a central, accreting black hole. Active galaxies, unlike dormant "normal" galaxies, emit across the entire electro-magnetic spectrum, from radio to gamma-rays. Low Ionization Nuclear Emission Line Regions are one such class of active galaxy and are the subject of this dissertation.

An Active Galactic Nucleus (AGN) is now known to be an actively accreting black hole. In the standard model for an AGN, an active galaxy is comprised of a narrow line region, a broad line region, an accretion disk of very hot plasma, a dusty torus and, in some AGN, kpc-Mpc sized radio jets emanating from the nucleus. A sketch of this paradigm is given in Figure 1.1. The observational characteristics of all classes of AGN are consistent with this so called unified model. The unified model also explains differences in the observational properties of AGN subclasses, including the ionization state (determined from line ratios) or the presence or absence of broad emission features thought to depend on the inclination angle of the torus with respect to our line of sight. In the following brief outline I examine some of the physical processes and observational characteristics that constitute the spectral energy distributions (SEDs) of most AGN.

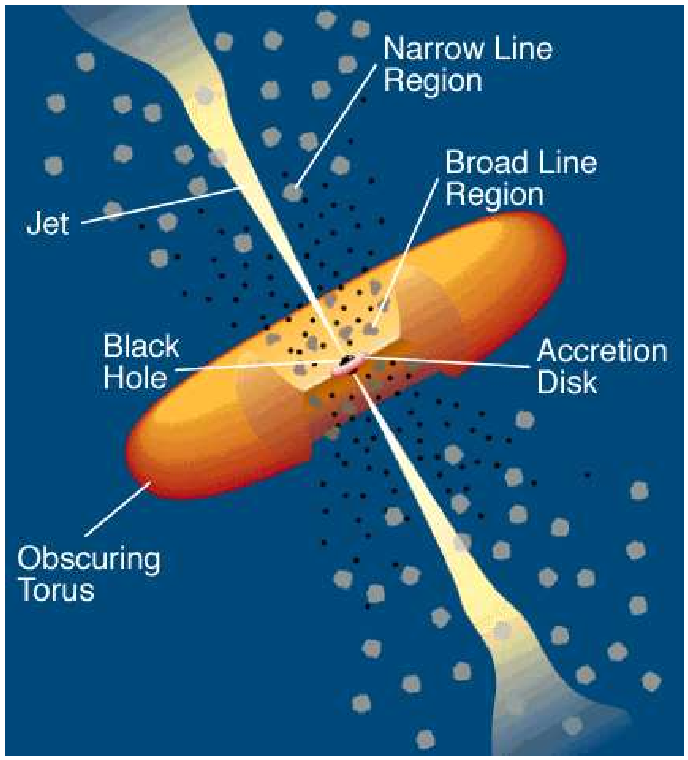

Figure 1.1: Artist's view of an actively accreting black hole

Schematic representation of an AGN that shows the dusty torus, the accretion disk, the narrow line region and bi-polar jets. Image taken from http://www.mssl.ucl.ac.uk/www_astro/agn_model.gif.

In a survey of 109 bright quasars from the Palomar-Green survey, Sanders et al. (1989) found that the SEDs of most quasars are remarkably similar. Despite the continuity in the full spectra, various components of the overall SED make these objects extraordinarily complex. More complex than, for instance, the SEDs of normal galaxies, such as the Milky Way. The SEDs of normal galaxies stem from the superposition of numerous black-bodies created by the inhabiting stars. Figures

1.2a and 1.2b show a comparison of an AGN SED and the Milky Way's SED. The components of an AGN SED are:

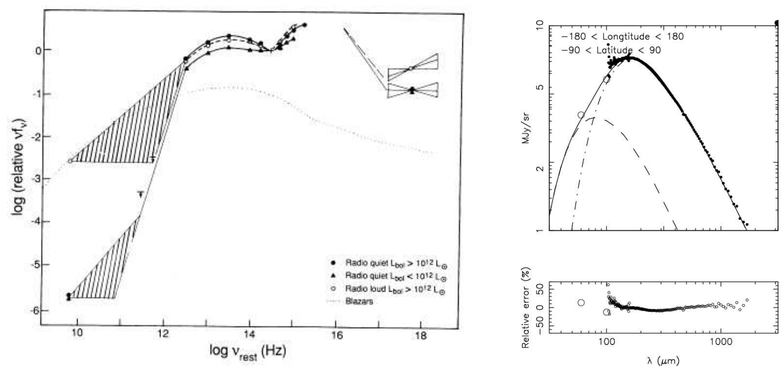

Figure 1.2: The SED of an AGN vs.the SED of the Milky Way

Spectral energy distribution of an AGN is apposed to a normal galaxy such as the Milky Way shown here. Radio Loud (RL) and Radio Quiet (RQ) AGNs are distinguished by empty and full symbols respectively. Normal galaxies have SEDs consistent with the superposition of numerous black bodies from the inhabiting stars; whereas, AGNs have SEDs that emit across the entire electromagnetic spectrum. (AGN SED taken from Sanders, 1989. SED of the Milky Way taken from Misiriotis et al., 2006).

Radio Emission

AGNs can be either RL or RQ depending on the ratio of radio to optical emissions. RL objects are objects that emit heavily at the radio frequencies. Specifically galaxies are defined as RL when their 5 GHz flux to optical B-band flux is greater than 10 ($F_{5GHz}/F_B \geq 10$), all others are RQ. The radio emission in RL AGNs is known to be synchrotron radiation predominantly from bipolar jets extending from the nucleus. RQ AGNs are thought to have little or no jet component.

Infrared Emission

Emission between 2μm and 1mm, the so-called "infrared bump" is thought to result from absorption and re-radiation of accretion disk photons by dust grains in the torus (Sanders et al., 1989). In addition, the infrared (IR) spectra of many

AGNs display multiple, prominent, narrow (several hundred km s^{-1}), fine-structure emission lines thought to originate in the so-called narrow line region (NLR, Capetti, et al., 1995, 1997; Schmitt & Kinney 1996; Falcke et al., 1998; Ferruit et al., 1999; Schmitt et al., 2003). These emission lines can be used to distinguish AGN-like nuclei from starburst-like nuclei. Whereas AGNs are capable of producing lines from ions with extraordinarily high ionization potentials, starburst and normal galaxies are characterized by lower excitation spectra which are characteristic of HII regions ionized by young stars (e.g. Genzel et al., 1998; Sturm et al., 2002; Satyapal et al. 2004). Finally ratios of these lines have been used to probe and characterize the ionizing continuum, to distinguish low ionization sources from higher ionization AGNs (Genzel et al., 1998; Sturm et al., 2002; Satyapal, 2004; Sturm et al., 2006).

Optical/Ultra-Violet Emission

The broad component in the 10nm to 0.3μm spectral range, known as the "big blue bump" is thought to result from quasi-thermal emission (10,000 to 100,000 K) from an accretion disk around the black hole (Sanders et al., 1989). Like the IR, the optical/UV spectra also contains multiple narrow fine structural lines, the ratios of which have been used to categorize various AGN subclasses such as Seyfert, LINERs and Transition nuclei (Heckman, 1980; Stauffer, 1982; Keel, 1983; Veilleux & Osterbrock, 1987; Ho, 1996; Ho, Filippenko, & Sargent, 1997a) . In addition, some AGNs show broad permitted lines with widths exceeding 10^3 km s^{-1} in their optical spectra. These so called "Type 1" AGNs are thought to be viewed "face-on" without any obscuration by the torus. This vantage point provides a view of both the NLR and the Broad Lined Region (BLR) which results in both broad and narrow lines in the optical spectrum. On the other hand, "Type 2" AGNs are thought to be seen "edge-on," with a dusty torus obscuring a view of the BLR. The resultant optical spectrum lacks broad lines (See Figure 1.3 for details).

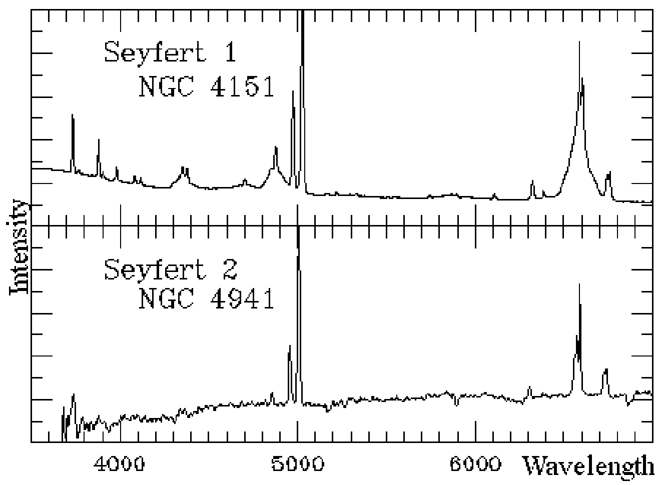

Figure 1.3: Optical spectrum of a Type 1 and a Type 2 AGN

The optical spectrum of a Type 1 AGN shows broad permitted lines. Type 1 AGNs are thought to be viewed "face-on without any obscuration by the torus. This vantage point provides a view of both the NLR and the BLR which results in both broad and narrow lines in the optical spectrum. On the other hand, Type 2 AGNs are seen edge-on, with a dusty torus obscuring a view of the BLR (Taken from http://vega.bac.pku.edu.cn/∼wuxb/agn/spectra.gif).

X-ray Emission

The hard (2-10keV) X-rays observed in AGNs are thought to be produced by inverse compton scattering of optical/UV accretion disk photons by electrons in a hot corona surrounding the accretion disk. Some of the photons are absorbed by the accretion disk and others are reflected toward the observer. Some of those that are absorbed produce a broad Fekα feature at 6.4 keV–a signature of the rapidly rotating disk. The width of the line often corresponds to velocities around tens of thousands of km s^{-1} (Mushotzky et al., 1995). The profile of the FeKα feature depends strictly on the gravitational, potential well, around the black hole and the size of the emitting region (e.g. Guilbert & Rees, 1988, Fabian et al., 1989). The line centroid provides information on the ionization state of the matter close to the black hole.

1.2 The Discovery of LINERs

Low Ionization Nuclear Emission Line Regions (LINERs) were first discovered in a joint optical and radio survey of the nuclei of bright galaxies conducted by Heckman et al. (1980). The optically complete (Crane, 1977) magnitude-limited sample of 93 nearby galaxies included a broad range of galaxy types with $B_T \geq 12.0$ mag. In his investigation, Heckman (1980, hereafter Heckman) discovered a sub-class of galaxy with prominent emission lines from ions with low ionization potentials. Dubbed "active" by Heckman, these objects are different from normal HII galaxies because their optical emission-lines are not typical of those associated with or excited by normal stars. Heckman used the low ionization, forbidden lines of oxygen to distinguish these low ionization emission-line regions from standard Seyferts and HII regions. As shown in Figure 1.4, when compared to typical AGNs, LINERs have very prominent [OII] and [OI] line emissions, relative to their [OIII] emissions. Specifically LINERs were classified by Heckman from this diagram to have $[\mathrm{OI}]_{6300\mathring{A}}/[\mathrm{OIII}]_{5007\mathring{A}} > 1/3$ and $[\mathrm{OII}]_{3727\mathring{A}}/[\mathrm{OIII}]_{5007\mathring{A}} > 1$.

While the unusual line ratios typical of LINERs can not be the result of normal stellar processes, the true nature of the ionizing mechanism in this study is ambiguous. For example, the Hα luminosities of the LINERs were found to be comparable to typical giant HII regions with luminosities ranging from 10^{38} to 10^{40} erg s^{-1} (Heckman, Kennicutt 1978); whereas, typical Seyfert nuclei show Hα around 10^{41} to 10^{43} erg s^{-1} (Adams & Weedman 1975). In addition, many LINERs seemed to lack the featureless, nonstellar, blue continuum component (the big blue bump) standard for many AGNs. Finally, although not a necessary condition, Heckman's radio analysis

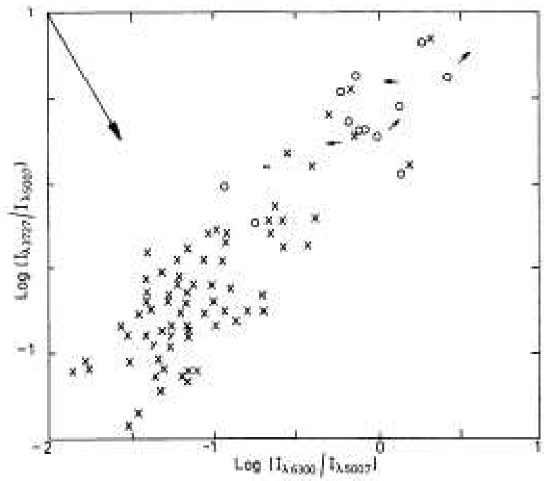

Figure 1.4: Heckman diagnostic diagrams

The Heckman diagnostic diagram for LINERs (open circles) as compared with Seyferts and radio galaxies (crosses). Taken from Heckman, 1980.

showed that a nuclear compact radio source was common in many LINERs. Indeed, after investigating multiple interpretations and models for the optical and radio spectra in these objects, Heckman concluded that the process responsible for the observed line ratios must be primarily shock heating.

In an optical spectroscopic investigation similar to that of Heckman, Veilleux & Osterbrock (1987, hereafter VO1987) explored the emission-line properties of LINERs further. Concerned with isolating the most appropriate line ratios for a two-dimensional classification of emission line nuclei, VO1987 developed a set of more sensitive line ratio diagnostics. The VO1987 classification scheme was based on criteria designed to eliminate observational effects, e.g. reddening and data analysis effects, e.g. uncertainty in line deblending. Their criteria for the new line ratios were: 1) The lines are strong and easily measurable. 2) The lines are close in wavelength to avoid the effects of reddening. 3) The lines are not blended together to avoid any ambiguity in the deblending procedure. And finally, 4) the ratios are of forbidden lines to permitted HI lines to avoid abundance-sensitivities. The diagnostic diagrams of VO1987 appear Figure 1.5 and the resulting spectral classification for LINERs is:

1. Seyfert Nuclei: $[\mathrm{OI}]_{6300\mathring{A}} \geq 0.08\mathrm{H}\alpha_{6583\mathring{A}}$
   $[\mathrm{NII}]_{6583\mathring{A}} \geq 0.6\ \mathrm{H}\alpha_{6583\mathring{A}}$
   $[\mathrm{SII}]_{6716,6731\mathring{A}} \geq 0.4\ \mathrm{H}\alpha_{6583\mathring{A}}$
   $[\mathrm{OIII}]_{5007\mathring{A}} \geq 3\ \mathrm{H}\beta_{4861\mathring{A}}$

2. LINER Nuclei: $[\mathrm{OI}]_{6300\mathring{A}} \geq 0.17\mathrm{H}\alpha_{6583\mathring{A}}$
   $[\mathrm{NII}]_{6583\mathring{A}} \geq 0.6\ \mathrm{H}\alpha_{6583\mathring{A}}$
   $[\mathrm{SII}]_{6716,6731\mathring{A}} \geq 0.4\ \mathrm{H}\alpha_{6583\mathring{A}}$
   $[\mathrm{OIII}]_{5007\mathring{A}} < 3\ \mathrm{H}\beta_{4861\mathring{A}}$

3. HII regions: $[\mathrm{OI}]_{6300\mathring{A}} < 0.08\mathrm{H}\alpha_{6583\mathring{A}}$
   $[\mathrm{NII}]_{6583\mathring{A}} < 0.6\ \mathrm{H}\alpha_{6583\mathring{A}}$
   $[\mathrm{SII}]_{6716,6731\mathring{A}} < 0.4\ \mathrm{H}\alpha_{6583\mathring{A}}$

VO1987 developed a very different interpretation of LINER SEDs from that of Heckman. VO1987 and Heckman agree that photoionization by a black body spectrum (e.g. hot, young stars) is likely not the ionization mechanism responsible for LINER spectra. However, VO1987 found that models photoionized by a power-law spectrum provide a better fit to the observed line intensities of LINERs than do shock-heating models. V01987 further argued that the presence of weak, broad components in the narrow emission lines of many LINERs strongly favors an intimate relationship between LINERs and Seyferts, further supporting the photoionization interpretation. Thus, the elusive origin of these optical line ratios, once again, was debatable.

While identifying the ionization mechanism in LINERs has been the goal of a number of investigations, at this point in the LINER timeline (Heckman, Stauffer, 1982; Ferland & Netzer, 1983; Halpern & Steiner, 1983; Keel, 1983; Stasinska,

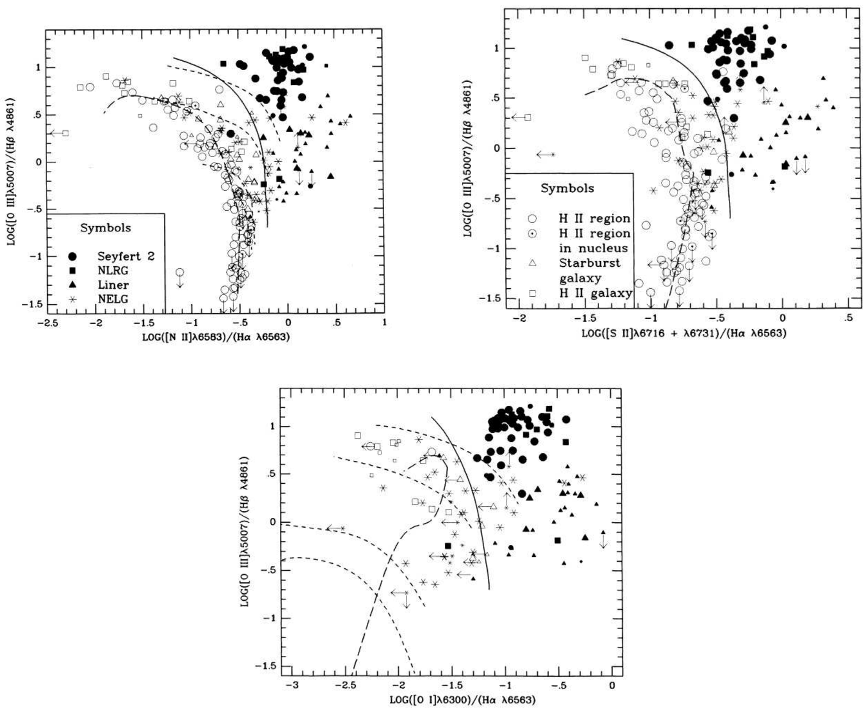

Figure 1.5: Veilleux and Osterbrock 1987 diagnostic diagrams

Diagnostic diagrams taken from Veilleux & Osterbrock, 1987) The VO1987 classification scheme was based on criteria designed to eliminate observational effects such as reddening and data analysis effects such as uncertainty in line deblending.

1984; VO1987), very little was known about the ionization mechanism responsible for characteristic LINER spectra. The survey that most impacted this conundrum was the Palomar survey of emission line galaxies.

The majority of research on LINERs stems from an optical Palomar survey led by Ho, Filippenko and Sargent (1995, hereafter HFS1995) of 486 emission-line galaxies. The only selection criteria for this survey was that the galaxies have optical magnitude $B_T \geq 12.5$ mag and declination, $\delta > 0°$. The study included both LINERs, dwarf Low Luminosity (LL) Seyferts, and HII regions. In this work HFS1995 (and Ho, 1996) adopted the classification scheme of VO1987, but included an additional class of objects which they call transition objects. These galaxies show [OI] strengths that are intermediate between HII nuclei and LINERs. While stellar models can account for their [OI] fluxes, they also may represent composite objects, containing both HII and LINER nuclei. Transition objects in this instance are the same as LINERs except that 0.08 H$\alpha \geq$ [OI] $\geq$ 0.17 Hα.

In the first part of the study, Filippenko and Sargent (1985) and Ho, Filippenko and Sargent (1997) used detection of the broad Hα ($\lambda\lambda$ 6200-6880) as a signature of the BLR in AGNs. Ho, Filippenko and Sargent (1997) found that 22 of 94 LINERs (23%) show definite Hα broadening. These findings are consistent with the previous studies of LINERs by Heckman. Notably, Broad Hα detections will readily detect AGNs in Type 1 nuclei, but this measurement has the potential to miss many Type 2 AGNs, as well as those heavily buried AGNs of which the optical band is attenuated or absorbed.

In a second part of his study, Ho (1999) used a multi-wavelength analysis to investigate the SEDs of seven low luminosity AGNs. Four of these are definite LINERs, the other three are border-line LINER/LL Seyferts. Hos study used data from the *Very Large Base Interferometer* (*VLBI*) for the radio, the *Infrared Astronomical Satellite* (*IRAS*) for the Far-infrared (FIR), ground based measurements for the near and mid-IR, the *Hubble Space Telescope* for the optical and UV, and *Rosat* and *Einstein* for the X-rays. Ho (1999) found that the SEDs of LINERs show a significant deficiency in the optical/UV portion of the spectrum when compared with the SEDs of standard AGNs (see Figure 1.6). Ho (1999) suggested that this deficit may result from a different kind of LLAGNs accretion flow, one that is radiatively inefficient. However, little is known about the optical/UV deficiency in LINERs– whether it is intrinsic (i.e. that AGN-LINERs are a "different" type of AGN) or whether LINERs are typical AGNs that suffer from severe dust obscuration.

In a third portion of this survey a subset of the Palomar sample was observed in the X-rays which used the Chandra Space Telescope. This study included 8 LINERs and 16 LL-Seyferts and HII regions (Ho et al. 2001). Ho et al. (2001) show that : 1) Because the hard X-rays effectively penetrate dust, they are a powerful tool for diagnosing the central source in LINERs, and 2) LINERs show three types of nuclei, those consistent with AGNs, those consistent with starbursts, and those with no X-ray source at all.

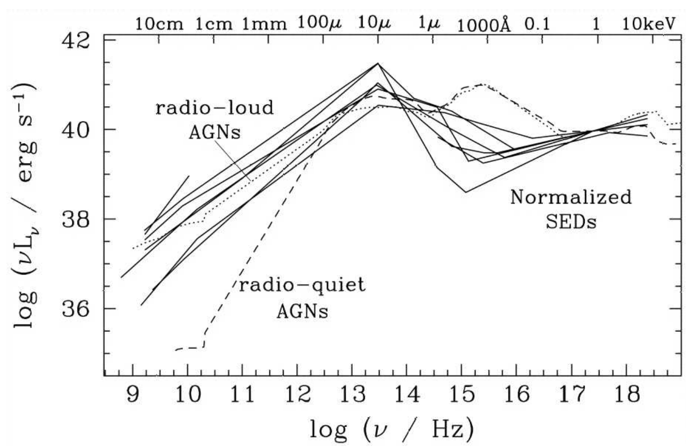

Figure 1.6: SEDs of LINERs

SED of LINERs compared with standard quasars. Ho found that the SEDs of LINERs show a significant deficiency in the optical/UV portion of the spectrum when they are compared with the SEDs of standard AGNs (Figure taken from Ho, 1999).

The final part of the study, conducted by Nagar et al. (2000), was a 15GHz radio survey of the most nearby (D $\leq$ 19Mpc) LINERs, LL Seyferts and transition nuclei. Here Nagar et al. (2000) found compact radio emission in 57% (17 of 30) LINER and LL Seyfert galaxies. Nagar et al. (2000) (See also Falcke et al., 1999, 2000; Nagar 2005) concluded that at least 50% of LL Seyfert galaxies and LINERs in the sample are accretion powered with the radio emission presumably coming from jets or advection dominated accretion flow (ADAFs). However they found compact radio emission in only 1 of 18 transition nuclei. In addition they uncovered the presence of a compact radio core strongly correlated with the presence of a broad Hα line. This implies that Type1 AGNs are more likely to have jet- or ADAF-like radio spectra. In a follow-up study, Nagar et al. (2001) examined the 5, 8.4, and 15 GHz spectra of the 16 brightest radio nuclei. In this analysis, jets are inferred based on: 1) the detection of pc-scale radio extensions, 2) the domination of pc-scale jet emission over unresolved core emission in 3/16 of the brightest nuclei, and 3) the lack of any clear correlation between the radio spectral shape and black hole mass as expected from the dependence of the radio turnover frequency on black hole mass in ADAF and convection dominated accretion flow (CDAF) models. In a final study, using extremely high, spatial resolution, 5 and 15 GHz, observations, Nagar et al. (2002) again found that at least half of all LINERs and LL Seyferts contain AGN-like radio nuclei. In addition they find that transition nuclei with compact radio cores tend to have optical line ratios very close to LINERs and LL Seyferts. Lastly, Nagar et al. (2002) find compact radio cores, preferentially, in massive ellipticals and Type 1 galaxies.

1.3 Possible Problems and Unanswered Questions

Perhaps the most important finding in 20 years of research is that LINERs constitute a significant fraction of the nearby galaxy population. Indeed, one third to as many as one half of all galaxies in the local universe are LINERs (Heckman, 1980; Ho, 1996; Stauffer, 1982). Despite the fact that they are the dominant population among local galaxies, they are surprisingly the least understood galaxy population. *What is the excitation mechanism responsible for the unusual LINER optical line ratios?* In his seminal paper on LINERs, Heckman suggested that LINERs may connect "active" to "normal" nuclei; however, astonishingly little has been found to confirm this. *Could LINERs be the missing evolutionary link between normal and active galaxies?* Indeed, the total number of LINERs actually containing AGNs is still unknown.

The known population, as indicated by the most comprehensive catalogue to date (Carrillo, 1999), includes 450 galaxies which span a wide range of distances, morphological classifications, and over all properties of the host galaxy. In particular these galaxies span a wide range of far-infrared (FIR) luminosities. FIR is predominantly associated with emission by dust. Most of the dust particles in galaxies have sizes comparable to the wavelengths of optical and UV light. For this reason, most of the radiation emitted at optical and UV wavelengths is absorbed by the dust and re-emitted in the FIR spectrum. Therefore, a ratio of the FIR luminosity to the luminosity in the optical B-band ($\lambda_{center} = 4400\mathring{A}$), the so-called IR-brightness ratio, can be used as a gauge of the amount of dust in a host galaxy.

As depicted in Figure 1.7, the total LINER population spans a wide range of IR-brightness ratios, with the majority of galaxies at the dusty, IR-bright end. As can also be seen in this figure, the Palomar survey of LINERs constitutes a very small portion of the total LINER population that predominantly describes the IR-faint population. At the same time, it overlooks the IR-bright population of LINERs. This bias toward IR-faint galaxies could have important consequences for statistical analyses which examine the fraction of LINERs hosting AGNs. In order for an accurate picture of LINERs to emerge, IR-bright as well as IR-faint galaxies must be studied. *What fraction of IR-bright LINERs are AGNs?*

In summary, LINERs are the dominant population of galaxies in the earths local universe and, surprisingly, the least understood. LINERs are defined by an optical spectrum displaying narrow emission lines of low ionization, uncharacteristic

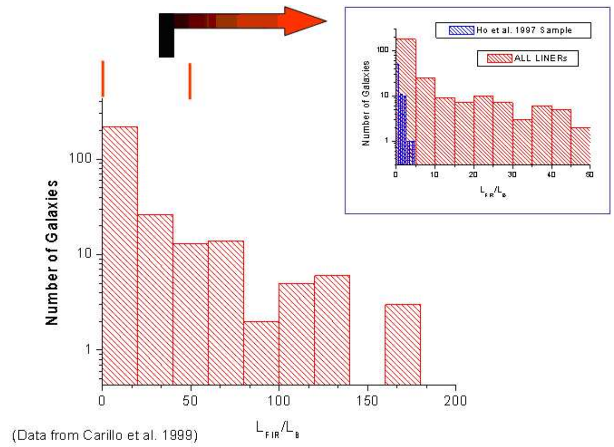

Figure 1.7: Range in IR-brightness for LINERs

.Histogram of the total number of known LINERs (Carrillo, 1999) as a function of IR-brightness. The blue bars in the histogram in the right corner represent the sample covered by Ho et al. (1997). As shown here, this optically selected sample covers the IR-faint population of LINERs only.

of photoionization from normal stars. Multiple sources (including unusual stars such as Wolf Rayet stars, super novae winds, shock heating from cloud collisions, and AGNs) have been proposed as the excitation mechanism responsible for producing the observed line ratios. However, to date, the nuclear source powering LINERs is still under debate. Because these galaxies are so numerous, an accurate picture of the central source for LINERs is critical to further galaxy formation and evolution studies. Thus, in light of the unanswered questions cited above, the central goals of this study are:

- Uncover and understand the mechanisms responsible for the optical line ratios in LINERs.
- Determine the luminosities, spectral characteristics and accretion properties of these galaxies and compare them with the standard active galaxies.

- Relate the host galaxies properties to the properties of the central source in an attempt to constrain the role of LINERs in galaxy evolution and formation models.

The following chapters introduce new ways to investigate the central properties using a joint mid-infrared and X-ray multi-wavelength approach.

Chapter 2: MULTI-WAVELENGTH OBSERVATIONS AND ANALYSIS

2.1 Introduction

In general the Earth's atmosphere is opaque to X-rays, meaning the atmosphere absorbs or scatters most X-ray and the photons never actually reach the Earth. In addition to absorbing most of the infrared radiation, the Earth's atmosphere also radiates in the infrared which contaminates and pollutes most ground-based extragalactic observations. For this reason any significant X-ray, mid- and far-IR observations of extragalactic objects must occur above the Earth's atmosphere via balloons (in the early years of X-ray astronomy), airplanes (e.g. SOFIA) or satellites (e.g. *Chandra*, *Infrared Space Observatory, ISO*, *Spitzer*). Consequently, state-of-the-art space-based observatories such as *Chandra*, *ISO*, and *Spitzer* are critical to the success of any multi-wavelength endeavor. The following sections review the satellites and analysis tools used for the data reduction and analysis in this study.

2.2 *Chandra* Observations and Data Analysis

The *Chandra* X-ray Observatory (CXO), successfully launched on July 23, 1999, is currently operating. This observatory, best known for its superior spatial resolution, is unmatched by any other X-ray observatory. It therefore provides an ideal platform from which to study the most obscured sources, such as the IR-bright LINERs mentioned in Chapter 1.

Two primary observational instruments are on-board *Chandra*. The first, the High Resolution Camera (the HRC), produces high resolution imaging and fast timing measurements. The second instrument is the Advanced CCD Imaging Spectrometer (ACIS), a two dimensional array of small detectors which provide imaging (ACIS-I) and spectroscopy (ACIS-S) of X-ray sources. The ACIS-I, designed for high-resolution spectrometric imaging, is a 2×2 array of Charged Coupled Devices (CCDs). Each CCD has 1024×1024 pixels of $\sim$ 0.5" size (See Figure 2.1). The ACIS-S is a 1×6 array which includes two back-illuminated CCDs, one of which is at the focal position (See Figure 2.1). The back illuminated CCDs cover a broad bandwidth compared to front illuminated chips. The back illuminated CCDs are best for high-resolution, spectrometric imaging of soft (0.2-2keV) X-ray sources (See Weisskopf 1999). Both ACIS-I and ACIS-S have spatial resolution of 0.5". The ACIS instruments can be used in combination with the High Energy Transmission Grating (HETG) or Low Energy Transmission Grating (LETG) to obtain higher resolution spectra. This research primarily utilizes the ACIS-S.

2.2.1 *Chandra* Imaging Analysis Overview

The Advanced CCD Imaging Spectrometer (ACIS-S) provided Archival *Chandra* observations of all LINER targets presented in this study. In general, the source was placed at the nominal aim point of the S3 CCD because this front and back illuminated chip is more sensitive to the soft X-rays than the front illuminated chips alone.

Most observations were completed using the standard 3.2s frame time, although a few bright objects the PI requested shorter frame times (0.44 s). As a result, for most observations the nuclear counts were insufficient for photon pileup to be significant.

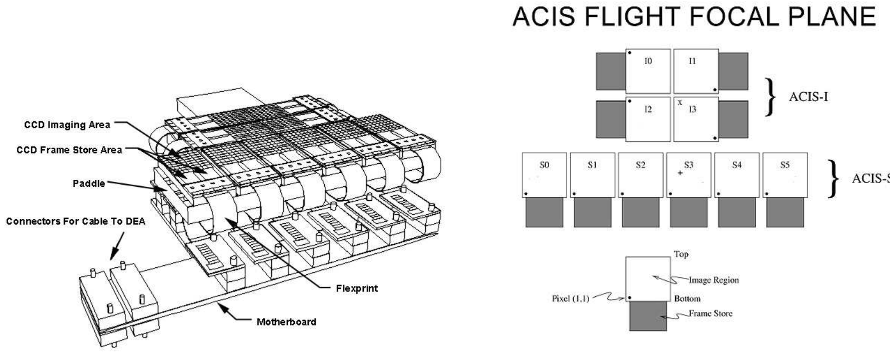

Figure 2.1: CCD Imaging Spectrometer (ACIS)

The Charged Coupled Device (CCD) Imaging Spectrometer (ACIS) and the two focal plane instruments, ACIS-I and ACIS-S on board *Chandra*. (Taken from http://chandra.harvard.edu/about/science_instruments2.html)

Pileup occurs when many lower-energy photons encounter the detector at the same time, so that the detector registers two or more lower-energy photons as a single high energy photon resulting in a distortion of the spectrum and an underestimate of the photon count-rate. In some cases, where the pileup is relatively low, the spectrum can be corrected using a pileup model based on the algorithm proposed by Davis (2001, See also Section 2.2.2) in XSPEC. The exposure times vary for each object. In some cases, detected background flares, subtracted from the original observation, resulted in shorter exposure times for these objects.

The *Chandra* data were processed using the latest version of the data analysis software CIAO which incorporates the most up-to-date calibration files provided by the *Chandra* X-Ray Center. Nuclear counts were generally taken from a 2" annulus around the nucleus, where the position was determined by either radio observations, if available, or Two Micron All Sky Survey (*2MASS*) observations. A nearby circular region with a radius 30" and free of spurious X-ray sources defined the background for all observations. This study classifies detections when the X-ray counts corresponding to a background subtracted, 2" extraction radius centered on the radio or infrared nucleus are at least 3σ. For most sources, the detected counts were insufficient to employ detailed spectral fits. Therefore, the nuclear count rate was converted to 2-10 keV X-ray luminosities assuming an intrinsic power law spectrum with photon index Γ=1.8 and using Galactic interstellar absorption. This study adopted the sample power-law slope (Ho et al., 2001) which is typical for low luminosity AGN (Γ ranges from 1.6-2.0; see also Terashima & Wilson, 2003). The published intrinsic X-ray luminosities for relevant galaxies are always reported.

This study adopts the X-ray morphological designations of Ho et al. 1999. In this scheme, Class (I) objects exhibit a dominant nuclear point source, Class (II) objects exhibit multiple off-nuclear point sources of comparable brightness to the nuclear source, Class (III) objects reveal a nuclear point source embedded in diffuse emission, and Class (IV) objects display no nuclear source. In addition, this study classifies AGN-LINERs as those galaxies with hard nuclear point sources coincident with the *VLA* or *2MASS* nucleus and a 2-10keV luminosity $\geq 2\times10^{38}$ ergs s^{-1}.

2.2.2 X-spec Spectral Fitting

Photon counts were sufficient for detailed spectral fits in a few cases. XSPEC, a command-driven interactive X-ray spectral fitting package, is the software package used to perform the spectral analyses on these objects (Arnaud, Dorman & Gordan, 2007). XSPEC allows the construction of composite models starting from more than 120 simpler components. The χ^2 statistic tests the "goodness of the fit", where:

$$\chi^2 = \sum \frac{(C(I) - C_p(I))^2}{(\sigma(I))^2}. \tag{2.1}$$

Here C_p(I) is the predicted count spectrum; C(I) is the observed data, and σ(I)

Table 2.1: $\Delta\chi^2$

Confidence	Num of Parameters		
	1	2	3
0.68	1.00	2.30	3.50
0.90	2.71	4.61	6.25
0.99	6.63	9.21	11.30

The delta statistic, $\delta\chi^2$ as a function of confidence level and the number of varied parameters (taken from Avni 1976, see also Arnaud, Dorman & Gordan 2007)

is the error for the specific instrument channel. After establishing the χ^2 value, tabulation of the "goodness of fit" and the "confidence interval" follows. The goodness of fit is simply the ratio of the χ^2 statistic to the degrees of freedom (d.o.f.) resulting from the model parameters. If χ^2/d.o.f.$\sim$ 1, then the model is acceptable. If χ^2/d.o.f is much greater or much less than 1.0, then the fit is either rejected or the fit is not unique. Varying that parameter and tabulating the change in χ^2 accordingly ($\delta\chi^2$) yields the confidence of a given parameter. This resulting delta statistic corresponds to a specific confidence level as shown in Table 1.

The following is a list of the most common spectral model components used in the X-ray spectral analyses presented in this research (see also Arnaud, Dorman & Gordan, 2007).

- ZWABS and WABS: This model describes photo-electric absorption using Wisconsin cross-sections (Morrison and McCammon 1983). The absorptions description is: M(E) = $e^{[-n_H\sigma(E[1+z])]}$, where n_H is the column density, and σ(E) in the cross section is a function of energy and redshift. If z = 0, then the absorption is Galactic and the model is WABS with only column density as the varying parameter. If z is the redshift of the source, then the absorption is intrinsic to the source, and the model is ZWABS with both column density and redshift as parameters.

- POWERLAW: This is a simple power law model described as A(E) = K*$E^{-\gamma}$, where γ is the photon index and K is the normalization (at 1eV).

- BROKEN POWERLAW: The is a broken power law component where at energy, E, less than some break energy, E_{break} the model is as described as a POWERLAW. At energies greater than E_{break} the models description is: A(E) = K*${E_{break}}^{\gamma_2-\gamma_1}$*$E^{\gamma_2}$, where γ_1 and γ_2 are the photon indices above and below the break.

- GAUSSIAN: A simple Gaussian profile, in this case, is the method used to fit possible FeKα components. The line profile is: $A(E) = \frac{(1+z)K}{\sigma\sqrt{2\pi}}e^{E(1+z)-E_L/2\sigma}$, where E_L is the line energy; σ is the line width, and K is the normalization.

- APEC: APEC code v.1.3.1 calculates an emission spectrum from collisionally-ionized diffuse gas (see http://hea-www.harvard.edu/APEC/ for details).

- PILEUP: Pileup, a new tool instituted in XSPEC, has its basis in the algorithm proposed by Davis (2001) (See http://space.mit.edu/davis/papers/pileup2001.pdf Arnaud, Dorman & Gordan, 2007).

In all cases, the initial procedure is to fit the sources to a single power-law model with the absorption column density fixed at the Galactic value. Subsequently, modification of this base model occurs, using additional components, until attainment of the minimum χ^2. The final step is calculation of the errors of the best-fit parameters.

2.3 Infrared Analysis

2.3.1 The Satellites

The Infrared Space Observatory(*ISO*)

ISO, launched on November 17, 1995 and operational until May 1998, had unprecedented sensitivity at mid-IR wavelengths. Rivaled in its day only by the *Infrared Astronomical Satellite* (*IRAS*), *ISO* discovered a multitude of previously unknown mid-IR features, such as polycyclic aromatic hydrocarbon (PAH) features and large, broad silicate features in the mid-IR spectra of star forming galaxies and AGN.

ISO comprised four main instruments: short and long wavelength spectrometers (SWS and LWS), infrared camera (ISOCAM), and photo-polarimeter (ISOPHOT). ISOCAM is a photometric and spectral imaging camera that operated in the 2.5-17 micron band. ISOPHOT consisted of three subsystems for multi-filter photometry from 3 to 240 microns and spectrophotometry at wavelengths 2.5-5 microns and 6-12 microns. LWS covered the 43-197 micron wavelength interval and provided spectral resolving power, λ / $\Delta\lambda$ of approximately 200. Finally SWS was operated in the 2.4 to 45 micron wavelength interval and had spectral resolving power of $\sim$ 1500. Although it includes some ISOPHOT observations, the current research primarily utilizes SWS observations.

SWS had four main modes: SWS01, SWS02, SWS06, and SWS07. SWS01 provided low resolution full grating scans. The design of SWS02 permitted grating scans of individual spectral lines. SWS06 offered spectral readings at random wavelength intervals–ideal for isolating the wavelength intervals pertinent to a specific project. Finally the design of SWS07 provided for extraordinarily sensitive observations. The majority of the research in this study utilizes SWS02 and SWS06.

The Spitzer Space Telescope

Spitzer, launched on August 23, 2003 remains operational. The instruments on board *Spitzer* must be cryogenically cooled, thus the lifetime of the mission is dependent on the lifetime of this coolant. *Spitzer* is the last observatory to be launched in NASA's Great Observatories Program - a family of four orbiting observatories (which includes *Chandra*) operating in spectra from gamma-rays to the infrared and designed to study the formation and evolution of galaxies, stars and planets.

Spitzer comprises three main instruments: Infrared Array Camera (IRAC), Infrared Spectrometer (IRS), and the Multi-band Imaging Photometer for *Spitzer* (MIPS, See http://ssc.spitzer.caltech.edu/ documents/SOM/ for details). IRAC provides photometric images at 3.6, 4.5, 5.8, and 8.0μm. All four detector arrays are 256$\times$256 pixels^2 with one pixel measuring 1.2". MIPS is a long wavelength photometer capable of making high resolution images at 24, 70, and 160 μm. Finally, IRS is capable of both high and low resolution spectroscopy. Low resolution spectra is available from 5 to 38 μm with spectral resolving power, λ / $\Delta\lambda$ = 64 - 128. High resolution spectra (λ / $\Delta\lambda \sim$ 600) is also available from the interval of 9.9 to 37 microns.

The mid-IR research in this study is predominantly spectroscopic, and therefore, utilizes primarily the IRS detectors. The majority of spectral data comes from the short-wavelength, low-resolution module (SL2, 3.6"$\times$57", λ = 5.2-7.7μm) and both the short-wavelength, high-resolution (SH, 4.7"$\times$11.3", λ = 9.9-19.6μm) and long-wavelength, high-resolution (LH, 11.1"$\times$22.3", λ = 18.7-37.2μm) modules of IRS (See Figure 2.2 for a schematic of the IRS modules). IRS can operate in two modes: staring and mapping.

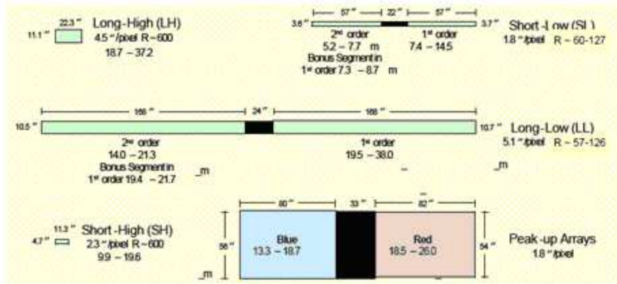

Figure 2.2: *Spitzer* IRS modules

Cartoon of the IRS modules and their properties. (Taken from http://ssc.spitzer.caltech.edu/irs/documents/pocketguide.pdf)

2.3.2 *Spitzer* and *ISO* Spectroscopic Observations

ISO Data Analysis

The *ISO*-SWS02 and/or SWS06 (de Graauw et al. 1996) observed one to nine different spectral lines over the 2.4-45 μm wavelength interval in the galaxies presented here.

Data reduction used the *ISO* Spectral Analysis Package ISAP (Sturm et al., 1998), and the most recent set of calibration parameters of the SWS Interactive Analysis package (Lahius et al., 1998, Wieprecht et al., 1998). Prior to line profile extraction, and flux and uncertainty measurements, data manipulation included subtraction of dark current, removal of cosmic ray glitches and noisy detectors, flat-fielding, and a separate co-addition of data in each scan direction. This work defines detections when the flux is at least 3σ.

In addition to the SWS observations, Chapter 4 utilizes a subsample of ISOPHOT observations from *ISO*. The PHT-S consists of a dual grating spectrometer with a resolving power of 90 (Laureijs et al. 2003). Band SS covers the range 2.5 to 4.8 μm, while band SL covers the range 5.8 to 11.6 μm. PHT-S aperture operates in both rectangular chopping triangular chopping modes. For the rectangular chopping mode, the satellite pointed to a position between the source and an off-source, and the chopper moved alternatively between these two positions. The triangular chopping mode, on the other hand, pointed, alternatively towards the $24'' \times 24''$ aperture of PHT-S at the peak of the emission and then towards two background positions off the source. The source was always in the positive beam in the spacecrafts Y-direction. A spectral response function, derived from several calibration stars of different brightnesses, observed in chopper mode provided the basis for calibration of the spectra (Acosta-Pulido et al., 2000). The relative spectrometric uncertainty of the PHT-S spectrum is 10% when comparing different parts of the spectrum that are more than a few μm apart. The absolute photometric uncertainty is 10% for bright calibration sources.

All PHT data processing used the ISOPHOT Interactive Analysis (PIA) system, version 10.0 (Gabriel 2002). Data reduction consisted primarily of the removal of instrumental effects such as radiation events. The disturbance is usually very short and the slope of the ramp after the glitch is similar to the slope before it. 6.2 μm line fluxes are corrected for instrumental effects and background emission and are fit by integrating the flux above the best fit linear continuum in the 5.86-6.54μm (rest-frame) wavelength interval.

Spitzer Data Analysis

The SSC processed the *Spitzer* data using latest IRS pipeline prior to download. Preprocessing includes ramp fitting, dark-sky subtraction, droop correction, linearity correction, flat-fielding, and flux calibration (See *Spitzer* Observers Manual, Chapter 7, http://ssc.spitzer.caltech.edu/ documents/som/ som8.0.irs.pdf). Further processing of the *Spitzer* data used the SMART v. 5.5.7 analysis package (Higdon et al., 2004). A full manual describing *Spitzer* high-resolution data analysis with SMART appears in Appendix A.

The slits for the SH and LH modules are too small for background subtraction to take place and separate SH or LH background observations do not exist for most of the galaxies in this study. Background-subtraction removed off-source emission from the nuclear spectrum in those few cases where dedicated, off-source, background files were available. For the SL2 module, background subtraction took place using either a designated background file when available or the interactive source extraction option. In the case of the latter, an initial verification of the exact position of the slit on the host galaxy occurred via *Leopard*, the data archive access tool available from the SSC. Careful definition of the source is in accordance with the boundary of the slit and the edge of the host galaxy. With no other obvious source present, the edge of the slit defined the background. In some cases, the host galaxy enveloped the slit and background subtraction could not take place. Both high and low resolution spectra had the ends of each order manually removed from the rest of the spectrum.

The *Spitzer* observations presented in this work are archived from various programs, including the *SINGS* Legacy Program, and therefore, contain both mapping and staring observations. All of the staring observations centered on the nucleus of the galaxy. The SH, LH, SL2 staring observations include data from two slit positions overlapping by one third of a slit. In general, in order to isolate the nuclear region in the mapping observations to allow comparing them to the staring observations, extraction included only those 3 overlapping slit positions coinciding with either radio or *2MASS* nuclear coordinates. Because the slits in both the mapping and staring observations occupy distinctly different regions of the sky, averaging the slits is not possible unless the emission originates from a compact source that each slit contains entirely. Therefore, the procedure for flux extraction was the following: 1) If the fluxes measured from the two slits differed by no more than the calibration error of the instrument, then the fluxes were averaged; otherwise, the slit with the highest measured line flux was chosen. 2) If an emission line was detected in one slit, but not in the other, then the detection was selected. This is true for all of the high and low resolution staring and mapping observations.

A simple Gaussian profile on a linear baseline was the basis for modeling and fitting all of the fine structure emission lines in this study. The Gaussian profile is:

$$P(\lambda) = \frac{1}{\sigma\sqrt{2\pi}} e^{(\lambda-\lambda_0)^2/-2\sigma^2} \tag{2.2}$$

where σ is the Full Width at Half Max (FWHM), and λ_0 is the line center. In all cases detections were defined when the line flux was at least 3σ.

For the absolute photometric flux uncertainty this research conservatively adopts a 15% calibration error, based on the assessed values given by the *Spitzer* Science Center (SSC) over the lifetime of the mission (See *Spitzer* Observers Manual, Chapter 7, http://ssc.spitzer. caltech.edu/documents/ som/som8.0.irs.pdf and IRS Data Handbook http://ssc.spitzer. caltech.edu/irs/dh/dh31_v1.pdf, Chapter 7.2). This error is a calculation from multiple SSC observations of various standard stars throughout the *Spitzer* mission. The dominant component of the total error arises from the uncertainty at mid-IR wavelengths in the stellar models used in calibration. This error is systematic rather than Gaussian in nature. For all galaxies with previously published fluxes, this study reports those published flux values. In all cases, the extracted fluxes agree with the published values to within the adopted calibration error of 15%.

Chapter 3: A *CHANDRA* SNAPSHOT SURVEY OF IR-BRIGHT LINERS: A POSSIBLE LINK BETWEEN STAR FORMATION, AGN-FUELING AND MASS ACCRETION

This Chapter was published by R. P. Dudik, S. Satyapal, M. Gliozzi, & R. M. Sambruna 2005, ApJ, 620, 113

3.1 Introduction

In Section 1.3 we showed that the majority of LINERs are IR-bright and are expected to contain obscured nuclei. In such galaxies, mid-IR spectroscopic and high spatial resolution X-ray observations are ideal probes of possible buried AGN cores. Mid-IR lines not only penetrate dust-enshrouded regions, but they also provide powerful tools to discriminate between gas photoionized by a central AGN or young stars, or shock-excited gas. Likewise, sensitive hard X-ray observations at high spatial resolution can provide a definite probe of obscured AGNs, out to column densities of a few times 10^{24} cm^{-2}. Those galaxies that reveal a compact hard X-ray nuclear source should also display high excitation fine structure lines in the mid-infrared, where dust obscuration is minimal. By expanding the sample of LINERs studied to include a larger range of IR-brightness ratios, an understanding of possible evolutionary sequences as well as the physical significance of IR-brightness in the LINER class can for the first time be explored.

To investigate the properties of the IR-bright population, we undertook a *Chandra* "snapshot" survey of a sample of nearby IR-bright LINERs. In this paper, we build on our previous archival *Chandra* study of LINERs (Satyapal, Sambruna, & Dudik 2004; henceforth SSD04) as well as previous studies of LINERs dicussed in Section 1.2 in order to increase the sample of IR-bright LINERs and obtain a more comprehensive understanding of this important class of objects.

The outline of this paper as follows. In Section 3.2, we summarize the sample selection criteria for the new observations presented in this work and describe the basic properties of the LINER sample used in our analysis. In Section 3.3, we discuss the analysis and assumptions adopted in deriving black hole masses, bolometric luminosities, and Eddington ratios. In Section 3.4 we present our results, including a discussion of our derived AGN detection rates, a comparison with other AGN indicators, X-ray morphological findings, luminosities, and correlations between various quantities. In Section 3.5 we discuss the implications of our correlations and summarize our conclusions in Section 3.6.

3.2 The Sample

The survey sample was selected from the multi-frequency LINER catalog from Carillo et al. (1999), which consists of an extensive database of 476 LINERs compiled from the literature. We selected all nearby IR-bright sources that satisfy the following criteria: 1) $L_{FIR}/L_B > 3$ and 2) $D < 30$ Mpc ($H_0 = 75$ km s^{-1} Mpc^{-1}, $q_0 = 0.5$), excluding the few objects that meet these criteria that were already observed by *Chandra*. Our targets range in distance from approximately 8 to 26 Mpc, with a median distance of 14 Mpc. The sample, consisting of a total of 16 objects, is summarized in Table 3.1a. We note that one IR-faint galaxy, NGC 4350, was accidently included in our program. Fourteen of our targets have been optically classified as LINERs according to the Veilleux & Osterbrock (1987) diagnostic diagrams. NGC 3125 and IC 1218 are classified as LINERs according to the Heckman (1980) criteria.

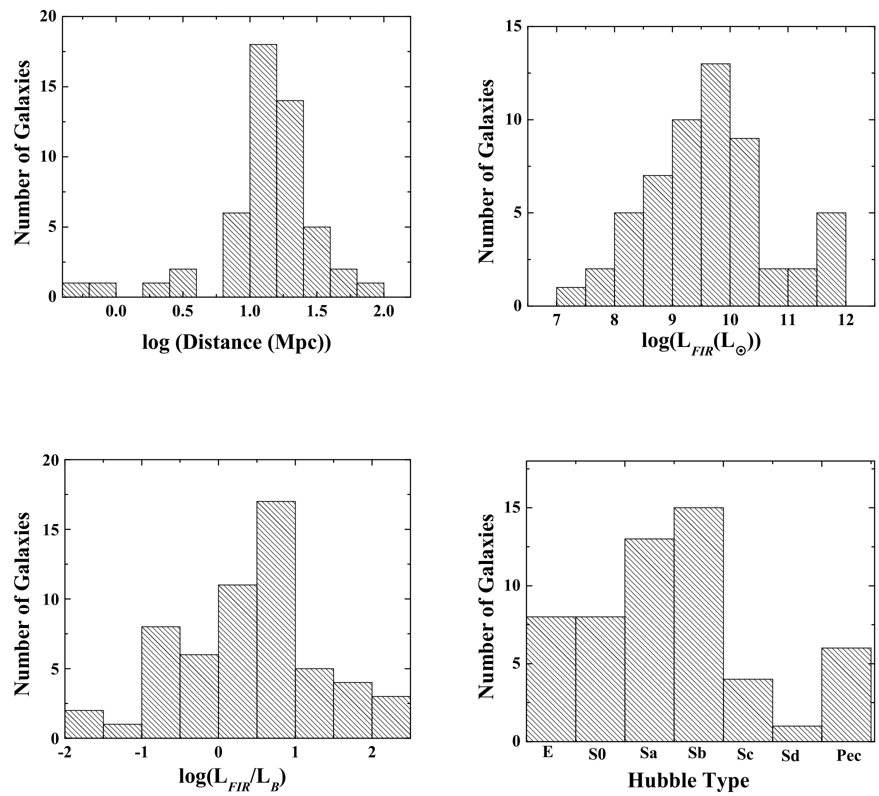

Figure 3.1: Statistics of the sample

Characteristics of the expanded *Chandra* sample of LINERs from this paper, SSD04, & H01. Most galaxies are nearby and span a wide range of luminosities, IR-brightness ratios, and Hubble types.

In order to enlarge the statistics of our present analysis, and explore the physical significance of IR-brightness in the LINER class, we combined our sample with the LINER/transition objects from SSD04 and H01. The entire *Chandra* dataset contains

58 LINERs. In this paper, we refer to this dataset as the "expanded sample." We emphasize that this expanded sample is heterogenous and not complete and therefore subject to selection biases. Also, our definition of an IR-bright LINER as one with $L_{FIR}/L_B > 3$ is largely arbitrary; the LINERs in the expanded sample form a continuous distribution in L_{FIR}/L_B that ranges from 0.1 to 162.9. The basic properties of the expanded sample are summarized in Figure 3.1 and Tables 3.1a, 3.1b, & 3.1c. We conducted a literature search to determine which objects were observed at optical and radio wavelengths, listing in Table 3.1 all LINERs displaying broad Hα emission lines or flat spectrum radio cores suggestive of an AGN.

Data analysis and reduction techniques for the *Chandra* observations presented here is outlined in Section 2.2. In Table 3.2 we list the details of the *Chandra* observations and in Table 3.3 we list the observed X-ray fluxes and upper-limits for the sample.

3.3 Analysis

In order to gain a better physical understanding of nuclear activity in LINERs and its relation to IR-brightness, we explored the relationship between IR-brightness and the fundamental quantities of black hole mass, bolometric luminosity and mass accretion rate for all confirmed AGN-LINERs in our expanded sample. The assumptions adopted and associated uncertainties are described below.

3.3.1 Black Hole Masses

Published black hole masses exist and were adopted in this work for 19 of the 58 LINERs listed in Table 3.1. These estimates were obtained for the most part through direct modeling of stellar and gas kinematics. For those galaxies with measured central velocity dispersions, we estimated the black hole masses using the tight

Table 3.1: Properties of the Expanded Sample

Galaxy Name (1)	Distance (Mpc) (2)	Hubble Type (3)	Optical Class (4)	log (L_{FIR}) (5)	L_{FIR}/ L_B (6)	Broad H_α? (7)	FRS (8)	N_H cm^{-2} (9)	$\log(M_{BH})$ ($M_\odot$) (10)
4.1a: New Chandra Observations: Sample Properties									
NGC 0660	11.3	SB(s)a;p.	T	10.1	34.4	no[a]	no[d]	4.9	7.35
NGC 1055	13.3	SBb;sp	T	9.9	7.7	no[a]	···	3.4	6.53
NGC 3125	11.5	S	L*	9.0	9.0	···	···	5.7	5.77
NGC 4013	11.1	Sb	T	9.2	5.2	no[a]	···	1.4	···
NGC 4102	11.2	SAB(s)b?	T	10.0	23.5	no[a]	···	1.8	···
NGC 4350[†]	16.6	SA0	L	8.3	0.2	no[a]	no[d]	2.6	7.99
NGC 4419	16.8	SB(s)a	T	9.6	5.0	no[a]	no[d]	2.7	6.94
NGC 4527	23.2	SAB(s)bc	T	10.4	8.7	no[a]	no[d]	1.9	8.25
NGC 4666	20.3	SABc	T	10.4	11.7	no[b]	no[e]	1.7	···
NGC 4713	8.7	SAB(rs)d	T	8.8	3.2	no[a]	no[d]	2.0	···
NGC 4750	21.6	(R)SA(rs)ab	L	9.7	3.4	yes[3]	···	1.7	···
NGC 5005	12.6	SAB(rs)bc	L	9.8	3.6	yes[3]	no[d]	1.1	···
NGC 5678	25.6	SAB(rs)b	T	10.1	6.5	no[a]	···	1.3	···
NGC 5954	26.2	SAa:;p.	T	10.1	18.5	···	···	3.3	6.81
IC 1218	14.8	S?	L*	8.5	4.8	···	···	4.1	···
NGC 7465[⋆]	26.3	(R')SB(s)0:	T	9.7	7.2	···	···	6.0	7.59[+]
4.1b: SSDO4: Sample Properties									
0248+4302	205.2	Gpair	L	11.5	138.3	no[a]	···	1.0	···
1346+2650	253.0	cD;S0?	L	10.6	3.5	no[a]	···	1.2	9.07[+]
2312-5919	178.4	Merger	···	11.7	89.6	no[b]	···	2.8	···
2055-4250	171.3	Merger	···	11.7	66.6	no[b]	···	3.9	···
IC1459	22.6	E3	L	8.6	0.1	···	···	1.2	9.00[g]
MRK266NE	112.2	Compact;p.	L	11.2	25.8	no[a]	···	1.7	···
MRK273	151.1	Ring gal.	L	11.8	162.9	no[b]	···	1.1	7.74
NGC0224	0.8	SA(s)b	···	9.0	0.5	···	···	0.1	7.57
NGC0253	2.6	SAB(s)c	···	9.9	9.8	···	···	1.4	7.07
NGC0404	2.4	SA(s)0	L	7.3	0.6	no[a]	no[f]	5.3	5.88
NGC0835	54.3	SAB(r)ab;p.	L	10.6	9.0	···	···	2.2	8.97
NGC1052	29.6	E4	L	9.1	0.3	yes[c]	···	3.1	8.29[g]
NGC3031	3.6	SA(s)ab	L	8.4	0.1	yes[c]	yes[d]	4.2	7.79[g]
NGC3079	15.0	SB(s)c	L*	10.3	16.6	no[a]	···	7.9	7.65[g]
NGC3368	12.0	SAB(rs)ab	L	9.4	1.0	no[a]	no[d]	2.8	7.16
NGC3623	10.8	SAB(rs)a	L*	9.0	0.5	no[a]	no[d]	2.5	8.16
NGC4125	18.1	E6;pec	T	8.6	0.1	no[a]	···	1.8	8.50
NGC4278	16.1	E1-2	L	8.5	0.2	yes[c]	yes[d]	1.8	9.20[g]
NGC4314	12.8	SB(rs)a	L	9.0	1.2	no[a]	no[d]	1.8	7.22
NGC4374	18.4	E1	L	8.5	0.3	no[a]	yes[d]	2.6	9.20[g]
NGC4486	16.0	E+0-1;p.	L	8.3	0.0	no[a]	yes[d]	2.5	9.48[g]
NGC4569	16.8	SAB(rs)ab	T	9.7	1.1	no[a]	no[f]	2.5	7.58
NGC4579	16.8	SAB(rs)b	L	9.5	0.9	yes[c]	yes[f]	2.5	7.85[g]
NGC4696	39.5	E+1;p.	L	···	···	···	no[d]	8.1	8.60
NGC5194	8.4	SA(s)bc;p.	L	9.8	1.7	no[a]	no[d]	1.6	6.90[g]
NGC5195	7.7	SB01;p.	L*	9.4	3.0	no[a]	no[d]	1.6	7.90
NGC6240	97.9	I0:;p.	L	11.3	38.2	···	···	5.8	9.15
NGC6500	40.1	SAab	L	9.4	1.4	no[a]	yes[f]	7.4	8.82[g]
NGC6503	0.6	SA(s)cd	T	6.8	2.1	no[a]	no[d]	4.1	5.53
NGC7331	11.0	SA(s)b	T	9.8	3.8	no[a]	no[d]	8.6	7.91
UGC05101	157.6	S?	L	11.7	118.5	no[a]	···	4.2	···

Columns Explanation: See Properties of Expanded Sample continued, Table 4.1c below **References:** [a] Ho, Filipenko, & Sargent 1997a; [b] Veilleux et al 1995; [c] Ho et al. 1997b; [d] Nagar et al. 2002; [e] Dahlem et al. 1997; [f] Nagar et al. 2000; [g] Merloni, Heinz, & Di Matteo 2003 and references therein.

Table 3.2: Properties of the Expanded Sample continued

Galaxy Name (1)	Distance (Mpc) (2)	Hubble Type (3)	Optical Class (4)	log (L_{FIR}) (5)	L_{FIR}/ L_B (6)	Broad H_α? (7)	FRS (8)	N_H cm^{-2} (9)	log(M_{BH}) (M$\odot$) (10)
1c: H01 Sample Properties									
NGC 2787	7.5	SB0	L	7.8	0.3	yes[c]	yes[d]	4.26	7.59[g]
NGC 2841	12.0	Sb:	L	9.2	0.5	no[a]	yes[d]	1.48	8.42[g]
NGC 3489	12.1	SAB0	T	9.2	1.1	no[a]	no[d]	1.96	7.58
NGC 3627	10.3	SABb	T	10.1	4.1	no[a]	yes[d]	2.29	7.26[g]
NGC 3628	10.3	Sb p.	T	10.0	6.1	no[a]	no[d]	2.25	7.91[g]
NGC 3675	12.8	Sb	T	9.6	3.1	no[a]	no[d]	2.13	7.11[g]
NGC 4203	15.0	SAB0:	L	8.5	0.4	yes[c]	yes[d]	1.18	7.90[g]
NGC 4321	16.1	SABbc	T	10.1	2.8	no[a]	no[d]	2.32	6.81[g]
NGC 4494	17.1	E1	L	7.7	0.0	no[a]	no[d]	1.54	7.65[g]
NGC 4594	9.8	Sa	L	9.0	0.2	no[a]	...	2.80	9.04[g]
NGC 4826	7.5	Sab	T	9.6	1.8	no[a]	no[d]	2.63	7.74

Columns Explanation: Col(1):Common Source Names; ⋆ NGC 7465 experienced severe pileup and has been excluded from our results and discussion; † This galaxy is IR-faint and was accidently observed in our program. Col(2): Distance (for H_0= 75 km $s^{-1}Mpc^{-1}$; the distance of NGC 4419 was taken from Ho et al. 1997b); Col(3): Morphological Class; Col(4): Optical classification scheme: All galaxies in this sample were classified using the Veilleux et al. 1995 / Ho et al. 1997 optical classification scheme, with the exception of NGC 3125 and IC 1218 which were classified using the Heckman 1980 scheme. Col(5): Far-infrared luminosities (in L$\odot$) correspond to the 40-500μm wavelength interval calculated using the prescription of Sanders & Mirabel 1996; Col(6): L_B: B magnitude see Carrillo et al (1999); Col(7): LINERs with broad Hα emission; Col(8): LINERs with a flat radio spectrum (NGC 4419 shows a steep radio spectrum.) Col(9): Galactic N_H(in units of$\times$ 10^{20} cm^{-2}); Col(10): Mass of central black hole calculated using the stellar velocity despersion in the formula: $M_{BH} = 1.2(\pm0.2)\times10^8$ $M_\odot(\sigma_e/200$ km $s^{-1})^{3.75(\pm0.3)}$) (from Ferrarese & Merritt 2000; Gebhardt et al. 2000; Tremaine et al. 2002), $^+$Calculated using the prescription of Kormendy & Richstone 1995; Ferrarese & Merritt 2000; & Gebhardt et al. 2003, log(M_{BH}) = -1.58($\pm$2.09) - 0.488($\pm$0.102)M_B. **References:** [a] Ho, Filipenko, & Sargent 1997a; [b] Veilleux et al 1995; [c] Ho et al. 1997b; [d] Nagar et al. 2002; [e] Dahlem et al. 1997; [f] Nagar et al. 2000; [g] Merloni, Heinz, & Di Matteo 2003 and references therein.

correlation between black hole mass and stellar velocity dispersion (Ferrarese & Merritt 2000; Gebhardt et al. 2000; Tremaine et al. 2002), demonstrated to hold for nearby AGNs (Ferrarese et al. 2001; McLure & Dunlop 2002):

$$M_{\rm BH} = 1.2(\pm 0.2) \times 10^8 M_\odot (\sigma_e/200{\rm kms}^{-1})^{3.75(\pm 0.3).} \tag{3.1}$$

Here, σ_e is the luminosity-weighted line-of-sight velocity dispersion within the half-light radius and is within 10% of the central velocity dispersion. Central velocity dispersion measurements were found for 24 additional objects. All measurements were obtained from the catalog of central velocity dispersions listed in the Hypercat database (Velocity dispersions taken from the Hypercat database available online at http://www-obs.univ-lyon1.fr/hypercat, (Paturel et al. 1997)). For all LINERs without central velocity dispersion measurements in elliptical hosts, we used the correlation between the bulge magnitude and the black hole mass (Kormendy & Richstone 1995; Ferrarese & Merritt 2000; Gebhardt et al. 2003):

$$log(M_{\rm BH}) = -1.58(\pm 2.09) - 0.488(\pm 0.102) M_{\rm B}, \tag{3.2}$$

where M_{BH} is in solar masses and $M_{\rm B}$ is the total B-band magnitude of the host elliptical galaxy. Since the bulge magnitude is highly uncertain in spirals, we only employed equation 2 for the 2 ellipticals in our sample without central velocity dispersion measurements (NGC 7465 & MRK273, SSD04).

3.3.2 Bolometric Luminosities

In order to estimate the bolometric luminosities of our targets from our X-ray observations, knowledge of the bolometric correction factor appropriate for the LINER AGN class is required. While the broad-band Spectral Energy Distribution (SED) of traditional higher luminosity AGNs are relatively well-studied and follow a fairly universal shape (Elvis et al. 1994), the SEDs of the nuclear source in AGN-LINERs is not as well-known. In the few cases where broad spectral coverage of the nuclear source is available, the SEDs of LINERs are found to differ markedly from those of conventional AGNs (Ho 1999), resembling instead the SEDs predicted for radiatively inefficient accretion flows (e.g. Quataert & Narayan 1999; Narayan et al. 2002). From the SED measurements of seven low luminosity AGNs from Ho (1999), the 2-10 keV luminosity ranges from 2 to 9 % of the integrated bolometric luminosity. Using the mean value of $L_{\rm bol}$=34 × $L_{\rm X}$(2-10keV), we estimated the bolometric luminosities of all of our AGN targets using the nuclear 2-10 keV luminosities listed in Table 3.3. We note that these estimates are somewhat uncertain and a determination of the true error in this factor requires more extensive studies of the SEDs of the LINER class.

Once the black hole mass has been estimated, the Eddington luminosity can be calculated using $\mathrm{L_{Edd}} = 1.26 \times 10^{38} \mathrm{M_{BH}/M_{\odot}}$ ergs s^{-1} (e.g., Rees 1984; Peterson 1997). The bolometric luminosity of the AGN is directly proportional to the accretion rate, $\mathrm{L_{bol}} = \epsilon \dot{M}_{\mathrm{acc}} \mathrm{c}^2$, and therefore the ratio, $\mathrm{L/L_{Edd}} \propto \dot{M}_{\mathrm{acc}}/\dot{M}_{\mathrm{Edd}}$, is an indirect measure of the accretion rate relative to the critical Eddington value.

3.4 Results

3.4.1 AGN Detection Rate

Twenty-eight LINERs from the expanded LINER sample display a hard compact nuclear X-ray point source coincident with the *VLA* or *2MASS* nucleus. The minimum 2-10 keV luminosity of those objects displaying hard nuclear cores in the entire sample is 2×10^{38} ergs s^{-1} (NGC 2787; H01). Young supernova remnants, X-ray-binaries (XRBs), and/or hot diffuse gas from starburst-driven winds are known to emit X-rays, however these sources are weak and/or are usually spatially extended at the distances of our objects. For example, while intergalactic XRBs are known to reach luminosities of $\sim 10^{38}$ ergs s^{-1} (McClintock & Remillard 2003), typical XRBs have luminosities up to 10^{37} ergs s^{-1} (White, Nagase, & Parmar 1995). Several tens to over ten thousand XRBs, concentrated in a spatial extent of only a few tens of parsecs, would be required to produce the luminosities of the hard nuclear point sources, which is highly implausible. Moreover, the detection of a single hard nuclear point source coincident with the *VLA* or *2MASS* nucleus is highly suggestive of an AGN. Therefore, in this paper, we define AGN-LINERs as all LINERs displaying hard nuclear cores with luminosites $\mathrm{L_X}$ (2-10keV) $\geq 2 \times 10^{38}$ ergs s^{-1}.

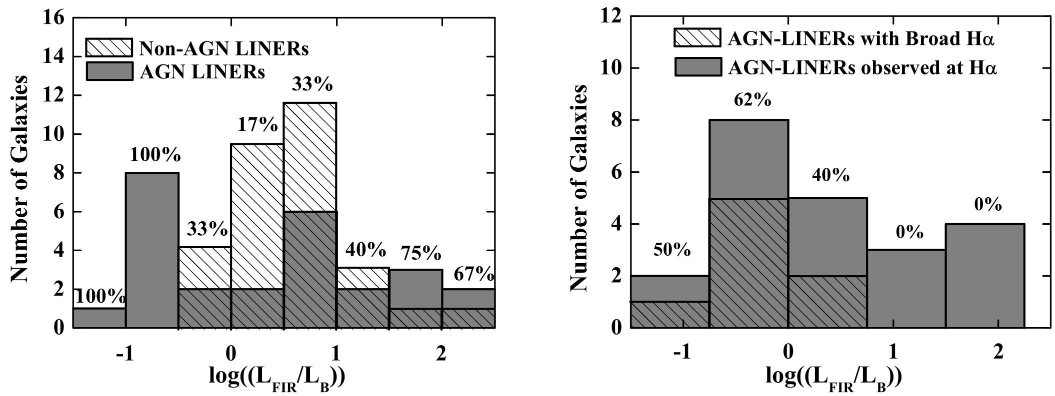

Figure 3.2: X-ray detection rates

3.2a: X-ray derived detection rate as a function of IR-brightness. Above each column we mark the percentage of observed galaxies displaying AGNs with respect to the total number of galaxies in a given luminosity ratio bin. 3.2b: Fraction of LINERs displaying Hα as a function of IR-brightness. Again above each column we mark the percentage of observed galaxies displaying a broad Hα line with respect to the total number of galaxies in a given luminosity ratio bin.

Our IR-bright LINER survey complements the SSD04 and H01 surveys with respect to L_{FIR}/L_B values and allows us to examine the X-ray-derived "AGN detection rate" as a function of IR-brightness. In Figure 3.2a we show the X-ray "AGN detection rate" as a function of IR-brightness. Our results indicate, with limited statistics, that the most extreme IR-faint LINERs are exclusively AGNs. The fraction of LINERs containing AGNs appears to decrease with IR-brightness and increase again at the most extreme L_{FIR}/L_B values. This result may simply indicate that most IR-faint galaxies, being generally deficient in dust and gas, are bulge-dominated systems, where there are not many sources of excitation other than an AGN that can produce a LINER-like spectrum. IR-bright galaxies, however, are generally dusty disk-dominated systems, where the presence of hot stars and starburst-driven shocks can easily give rise to a LINER spectrum (e.g., Isobe & Feigelson, 1992). LINERs with the most extreme L_{FIR}/L_B values are generally ultraluminous galaxies (e.g., Sanders & Mirabel 1996), where the large concentration of dust and gas in these often advanced merging systems conceivably increases the likelihood that an AGN is responsible for the LINER spectrum.

3.4.2 Comparison with Other AGN Indicators

Detection of broad Hα emission can be a powerful AGN diagnostic at optical wavelengths. However, broad optical lines can be ambiguous AGN indicators since they are dependent on viewing angle and dust obscuration, which is particularly a problem in IR-bright and low luminosity sources (Nagar et al. 2000). Indeed, broad lines have also been produced in starburst models (Terlevich et al. 1995). We searched the literature for optical observations at Hα wavelengths and list those galaxies which show broad Hα emission in Table 3.1. We compare the Hα and X-ray AGN diagnostics in Figure 3.2b. There are 24 X-ray classified AGN-LINERs observed at the Hα wavelength. Only 33% (8/24) show the broad lines, most of which are IR-faint. The objects with higher L_{FIR}/L_B values show no evidence of AGN activity at optical wavelengths, emphasizing the importance of high spatial resolution X-ray observations in the study of IR-bright LINERs.

Compact flat spectrum radio cores can also be a signature for accretion onto a black hole. We searched the literature for radio observations of the objects in our expanded sample. As can be seen from Table 3.1, 33 LINERs have corresponding radio observations. Ten of these sources show flat spectrum radio cores. Interestingly, two of these objects, NGC 2841 and NGC 3627, show no sign of AGN activity in the X-ray. In these cases, thermal emission from optically thin ionized gas in compact nuclear starbursts (Condon et al. 1991) can give rise to the observed radio properties from these sources. Detection of a flat spectrum radio core does not necessarily discriminate between nuclear starbursts and accretion onto black holes unless the brightness temperature exceeds 10^5 K (Condon et al. 1991). In the case of NGC 2841 and NGC 3627, the brightness temperature limit of $T_b > 10^3$-10^4K and $T_b > 10^{2.5}$-10^3K, respectively, is consistent with either a starburst nucleus or an AGN (Nagar et al. 2000).

Of the 28 LINERs with AGN signatures in the X-ray, only 14 have corresponding radio observations. Roughly half of these (8/14) show a flat spectrum radio core. A nuclear flat radio spectrum is not always a clear indicator of an AGN. For instance, flat spectrum compact radio cores are found in only ~10% of "classical" Seyfert galaxies (de Bruyn & Wilson 1978; Ulvestad & Wilson 1989; Sadler et al. 1995). In addition, while flat spectrum radio cores are known to be present in many elliptical galaxies (Heckman 1980), they are uncommon in spirals (Villa et al. 1990; Sadler et al. 1995). This limits the diagnostic capability of radio observations in our heterogenous LINER sample, again emphasizing the importance of high spatial resolution X-ray observations.

3.4.3 X-ray Morphologies

The X-ray images of all of the LINERs in this study have been classified into four morphological types according to the scheme adopted by H01. These classes are defined as follows: class (I) objects exhibit a dominant hard nuclear point source, class (II) objects exhibit multiple hard off-nuclear point sources of comparable brightness to the nuclear source, class (III) objects reveal a hard nuclear point source embedded in soft diffuse emission, and class (IV) objects display no nuclear source. Morphological class designations for all galaxies in our expanded sample are listed in Tables 3.3a, 3.3b, & 3.3c. We note that we adopt these morphological class designations for comparative purposes. These designations are somewhat subjective and furthermore depend on the detection limits for the three samples included in the analysis in this paper. We identify class (I) and class (III) objects as AGN-LINERs. Class (II) objects have off-nuclear sources of comparable brightness to the nuclear source. Therefore, these objects are more likely to be morphologically consistent with starburst galaxies, expected to contain a large population of young stars and scattered XRBs.

Seven of our objects (class IV) show no nuclear X-ray source. The flux limit for our exposures is 1×10^{-15} ergs s^{-1} cm^{-2}. This limit corresponds to a luminosity of L_X (2-10keV) $\approx 1 \times 10^{37}$ ergs s^{-1} assuming an intrinsic power law spectrum of photon index 1.8 and a median Galactic absorption of 2×10^{20} cm^{-2} for the median sample distance of $\sim$ 14 Mpc. This luminosity limit is at least an order of magnitude fainter than the weakest hard nuclear sources detected by H01 or SSD04.

Our non-detections imply either: 1) the lack of an energetically significant AGN, or 2) a highly obscured AGN. Assuming these objects harbor an AGN at least as luminous as our lowest luminosity AGN-LINER (2×10^{38} ergs s^{-1}), we can calculate the column density necessary to obscure an AGN in our non-detections (class IV objects.) Using our adopted power law of $\Gamma = 1.8$, the required column densities were calculated and are listed in Table 3.3. These column densities range from $\sim 3 \times 10^{22}$ to 1×10^{24} cm^{-2}. We note that the majority of AGN-LINERs are more luminous than 2×10^{38} ergs s^{-1}. The average luminosity of an AGN-LINER in the expanded sample is $\approx 9 \times 10^{42}$ ergs s^{-1}. The column density required to obscure an AGN of this luminosity is also listed in Table 3.3. As can be seen the column densities are extremely high - in all cases in excess of 10^{24} cm^{-2}. All but two of the upper limits in the expanded sample are below our lowest luminosity AGN-LINER. The upper limits on these two class (IV) objects (NGC3623, SSD04 & NGC4321 H01), do not allow us to classify them as either AGN- or non-AGN LINERs. These galaxies are therefore excluded from our calculations of the AGN detection rate and from Figures 3.2 and 3.3. In Figure 3.3 we compare our X-ray morphological designations with the

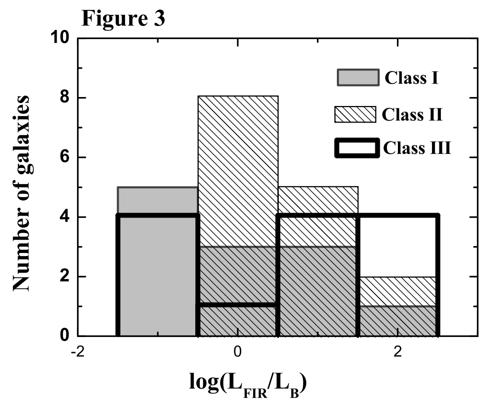

Figure 3.3: X-ray vs. IR-brightness

Morphological class as a function of IR-brightness.

IR-brightness of the objects. Plotted in this histogram, are the AGN-LINERs (class (I) and class (III) objects) and the detected non-AGN-LINERs (Class (II) objects). We find:

1. Those objects with the lowest IR-brightness ratio are always AGN-LINERs (class (I) and (III)).

2. Class (I) AGN-LINERs become less abundant as the IR-brightness ratio increases.

3. The most extreme IR-bright objects are mostly class (III) objects. We note that this point is a *suggestive trend*. At present, few galaxies occupy the extreme

IR-brightness bins. More data at either extreme of IR-brightness is therefore necessary to confirm the trend. This may indicate that class (III) objects, in addition to an AGN, contain circumnuclear starbursts, which would be expected for exceedingly IR-bright objects.

4. Class (II) objects, which have nuclei typical of starburst galaxies (non-AGN-LINERs) occupy and dominate the intermediate L_{FIR}/L_B regime. If these galaxies are starbursts they would not be expected to be extremely IR-faint.

3.4.4 X-ray Luminosities

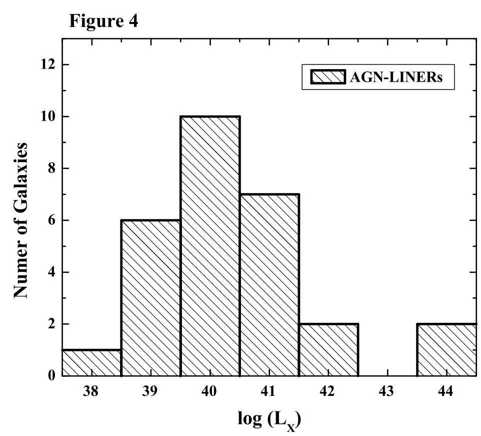

Figure 3.4: X-ray luminosities

Range of X-ray luminosities for the expanded sample.

From Tables 3.3a, 3.3b, & 3.3c, the X-ray luminosities (2–10keV) of the AGN-LINERs in our expanded sample range from $\sim 2 \times 10^{38}$ to $\sim 2 \times 10^{44}$ ergs s^{-1}. The full range of the X-ray luminosities in the combined samples is plotted in Figure 3.4. We note that the majority of objects occupy the 10^{39} to 10^{41} ergs s^{-1} luminosity range, higher than our luminosity threshold of L_X (2-10keV) = 2×10^{38}, and well above all of the upper limits in all three samples.

The majority of the 2-10 keV X-ray luminosities listed in Tables 3.3a, 3.3b, & 3.3c, were calculated assuming a power law with photon index $\Gamma = 1.8$ using the Galactic absorption listed in Table 4.1. Three of the fifteen LINERs (NGC 3125, NGC 4102, & NGC 5005) had counts sufficient to allow spectral fits, allowing us to assess the accuracy of the generic power-law model. In these models, the photon index ranged from 1.5 to 2.0 with an average of 1.8. We note that our average value and the value for Γ used in our generic power law model coincides with the value adopted by H01 and the average value found in low luminosity AGNs (Terashima et al. 2002). This range (1.5-2.0) in photon index has a marginal impact on the derived 2-10 keV flux, corresponding to a factor of less than 1.5 difference in our calculated luminosities. The models for the three galaxies are given in detail below.

NGC 3125: This galaxy's spectrum was fit using a single power law model with $\Gamma = 2.0^{+0.4}{}_{-0.3}$. The absorption column density was fixed at the Galactic value and an additional intrinsic absorption component was included in the model . The resulting intrinsic absorption for the best fit model was $N_{\rm H} = (5 \pm 2.5) \times 10^{21}$ cm^{-2}, which is significant at greater than 99% confidence level. The additional intrinsic absorption component corresponds to a factor of less than 2 difference in the luminosity calculated using our generic model ($\Gamma = 1.8$, Galactic absorption). The reduced χ^2 in our best fit model is 1.0 (13 Degrees of Freedom, d.o.f.).

NGC 5005: This galaxy was initially fit with a single power-law model ($\Gamma = 1.9^{+0.4}{}_{-0.2}$) with absorption column density fixed at the Galactic value. The resulting poor fit ($\chi^2{}_{\rm reduced} = 2.44$ with 7 d.o.f.) and the presence of a clear excess at soft energies, indicated the need for an additional component. A thermal component was applied (kT $= 0.90^{+0.2}{}_{-0.3}$ keV, $Z/Z_{\odot} = 1.0$ fixed), which yielded an acceptable fit for this galaxy ($\chi^2{}_{\rm reduced} = 0.94$ with 9 d.o.f.). The thermal component for NGC 5005 affects the flux by less than 3%.

NGC 4102: This galaxy too was initially fit with a single power-law model ($\Gamma = 1.5^{+0.6}{}_{-0.4}$) with absorption column density fixed at the Galactic value. The resulting poor fit ($\chi^2{}_{\rm reduced} = 3.9$ with 9 d.o.f.), and again the presence of a clear excess at soft energies, indicated the need for an additional component. A thermal component was applied (kT $= 0.54 \pm 0.4$ keV, $Z/Z_{\odot} = 0.20$). This fit was not adequate, however for NGC 4102. It was further improved ($\Delta\chi^2$ of 12.5 for 2 additional degrees of freedom) by adding a Gaussian component at a fixed energy of 6.4 keV in the source rest frame. The line is significant at a 90% confidence level, according to an F-test (but please see Protassov et al. 2002 for a discussion of using this method to assess line significance.) However, the energy range for the data set is not sufficient to determine the line parameters accurately. The residuals above 5-6keV show a clear excess, which cannot be ascribed to the background. This excess can be fit adequately with a Gaussian component, which does not necessarily imply the presence of a physical iron line at 6.4keV. Deeper *Chandra* observations or observations using the spectral capabilites of *XMM* would be needed to accurately assess the physical significance of this component. The thermal component for NGC 4102 affects the flux by less than 1%. The reduced χ^2 for this galaxy is 1.5 (5 d.o.f.). NGC 4102 is difficult to compare with the other objects in our sample because of the presence of the Gaussian component.

Assuming a zeroth order approximation that all AGN-LINERs have roughly the same intrinsic spectrum, the results obtained from the spectral analysis of NGC 3125 can be used to infer additional spectral information for the objects with lower countrates for which only a hardness ratio analysis could be performed (The hardness ratios are defined here as (H-S)/(H+S), where H represents the hard counts and S represents the soft counts in the nucleus). Since NGC4350, NGC 4419, and NGC 4527 have hardness ratios similar to NGC 3125, which showed the presence of a local absorption component, we hypothesize that those sources also have an absorption component in excess of the Galactic value. Similarly, NGC 660 and NGC 4750 have hardness ratios comparable to NGC 5005, which showed a clear excess at soft energies and required a thermal component in addition to the generic model. NGC 660 and NGC 4750 are likely to contain a similar thermal component in addition to Galactic absorption in their model. Thus our generic power-law model is likely to be a reasonably accurate model for all of the galaxies in our sample.

In Figures 3.5a and 3.5b we plot the X-ray flux versus the far-IR flux and the IR-brightness ratio. Plotting fluxes has the advantage of avoiding spurious correlations introduced by distance effects. As can be seen, we find no correlation in either plot. We applied a Spearman rank test to each of these plots (Kendall & Stuart 1976). A Spearman rank coefficient of 1 or -1 indicates a strong correlation and a value of zero indicates no correlation. For Figure 3.5a, the Spearman rank coefficient is r_S=-7 $\times$ 10^{-3}. For Figure 3.5b, we find a Spearman rank coefficient of r_S=-0.24.

3.4.5 Eddington Ratios and Trends with IR Brightness

Using the X-ray luminosities for our sample of AGN-LINERs, we calculated the corresponding Eddington ratios as outlined in Section 3.3. These values are listed in Table 3.3. In Figure 3.6, we show the distribution of $L/L_{\rm Edd}$ for the expanded sample. Consistent with previous studies (e.g. Ho 1999, Terashima et al. 2000), we find that LINERs generally have low Eddington ratios, with a median value of ~ 7

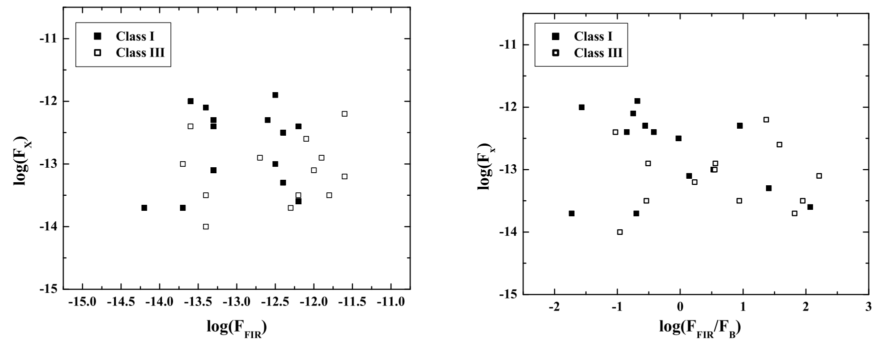

Figure 3.5: X-ray vs. IR fluxes

3.5a: X-ray flux vs. flux in the far-IR for the expanded sample of LINERs. 3.5b: X-ray flux vs. IR-brightness for the expanded sample of LINERs. As can be seen, no correlation is found in either plot.

$\times$ 10^{-6} for the expanded sample. At such low accretion rates ($\leq$ a few percent of the Eddington rate; see Narayan, Mahadevan, & Quataert 1998) the inner accretion flow is most likely radiatively inefficient (Terashima et al. 2004; Narayan et al. 1998, 2002).

In Figures 3.7a and 3.7b, we plot the Eddington ratio as a function of the far-IR luminosity and the IR-brightness ratio, respectively. Interestingly, we find a surprising trend in L/L_{Edd} vs. both L_{FIR} and L_{FIR}/L_B that extends over seven orders of magnitude in L/L_{Edd}. A Spearman rank test gives a correlation coefficient of r_S=0.64 between L/L_{Edd} and L_{FIR} with a probability of chance correlation of 2×10^{-3}, indicating a significant correlation between the two values. In the case of L/L_{Edd} vs. L_{FIR}/L_B, the Spearman rank test gives a correlation coefficient of r_S=0.57 with a probability of chance occurrence of 9×10^{-3}, also indicating a significant correlation.

We investigated whether this correlation is primary or whether it was induced by either distance effects or correlations between individually observed quantities

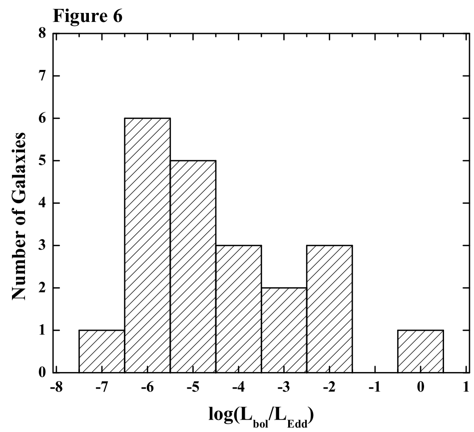

Figure 3.6: Eddington ratios

Histogram showing the full range of Eddington Ratios for the expanded sample.

used to calculate the Eddington ratio. From Section 3.4.4, we see that both F_X vs. $F_{\rm FIR}$ and $F_{\rm X}$ vs. $F_{\rm FIR}/F_{\rm B}$ show no correlation, suggesting that Figures 3.7a and 3.7b represent a fundamental correlation. Furthermore, the partial Spearman rank correlation coefficient goes up when the distance is fixed ($P_S = 0.66$ for $L/L_{\rm Edd}$ vs. $L_{\rm FIR}$ and $P_S = 0.67$ for $L/L_{\rm Edd}$ vs. $L_{\rm FIR}/L_{\rm B}$), suggesting that the Eddington ratio and the IR luminosity and IR-brightness in LINER galaxies are indeed physically correlated quantities.

A formal fit to the correlations in Figures 3.7a and 3.7b yield the following relationships:

$$Log(L_{\rm bol}/L_{\rm Edd}) = (1.04 \pm 0.62) log(L_{\rm FIR}) + (-13.67 \pm 5.40) \tag{3.3}$$

$$Log(L_{\rm bol}/L_{\rm Edd}) = (1.02 \pm 0.38) log(L_{\rm FIR}/L_B) + (-4.02 \pm 0.35) \tag{3.4}$$

The dispersion in Figures 3.7a and 3.7b is large. It is difficult to assess how much of the scatter is intrinsic or is due to the uncertainties in the derived quantities. The

Table 3.3: *Chandra* Observation Log

Galaxy Name (1)	OID (2)	Exposure Time (3)	R. A. (4)	DEC. (5)	Coordinate Catalog (6)
NGC0660	4010	5064	01 43 02.39	+13 38 43.9	*2MASS*
NGC1055	4011	5033	02 41 45.17	+00 26 38.1	*VLA*
NGC3125	4012	5153	10 06 33.98	-29 56 17.0	*2MASS*
NGC4013	4013	4897	11 58 31.37	+43 56 50.8	*2MASS*
NGC4102	4014	4541	12 06 23.05	+52 42 39.7	*VLA*
NGC4350	4015	4344	12 23 57.82	+16 41 36.1	*2MASS*
NGC4419	5283	5061	12 26 56.45	+15 02 50.9	*VLA*
NGC4527	4017	4897	12 34 08.50	+02 39 13.7	*VLA*
NGC4666	4018	4642	12 45 8.26	-00 27 50.2	*VLA*
NGC4713	4019	4904	12 49 57.89	+05 18 41.1	*2MASS*
NGC4750	4020	4935	12 50 07.40	+72 52 28.3	*2MASS*
NGC5005	4021	4900	13 10 56.28	+37 03 32.4	*VLA*
NGC5678	4022	4733	14 32 5.84	+57 55 10.0	*VLA*
NGC5954	4023	4146	15 34 35.16	+15 12 01.5	*VLA*
IC1218	4024	4638	16 16 37.10	+68 12 09.5	*2MASS*
NGC7465	4025	1579	23 02 00.96	+15 57 53.4	*2MASS*

Column Explanation: Col(1): Galaxy Common Name; Col(2): *Chandra* Observation Identification Number; Col(3): Exposure time in seconds; Col(4): Right Ascension of nucleus in hours, minutes, & seconds taken from the source in Column 6; Col(5): Declination of nucleus in degrees, minutes, & seconds, taken from the source in Column 6; Col(6): *VLA* Coordinates or *2MASS* coordinates used when extracting counts. *VLA* Coordinates came from the First Catalogе search, http://sundog.stsci.edu/cgi-bin/searchfirst. *2MASS* Coordinates came from NED.

bolometric luminosity estimated using the X-ray luminosity is highly uncertain as discussed in Section 3.3. In addition, the uncertainty and uniform applicability of the M_{BH} vs. σ relationship for our sample of galaxies will introduce additional errors. In addition, the nonsimultaneity of the X-ray, IR, and optical observations may also introduce additional scatter. Although the variability properties of low luminosity AGNs are not well known, some variability in several sources is found in at least the X-rays (e.g. Ptak et al. 1998). We regard the correlation in Figures 3.7a and 3.7b as preliminary. A larger sample and more extensive multiwavelength studies of the SEDs of LINERs would provide more accurate bolometric correction factors and allow us to better assess the origin of the scatter in Figure 3.7.

Table 3.4: X-ray Results of the Expanded Sample

Galaxy Name (1)	X-ray Class (2)	Hard Counts (3)	Hardness Ratio (4)	Count Rate 0.3-10keV (5)	L_X 2-10keV (6)	N_H^{MIN} $\times10^{23}$ (7)	N_H^{AVG} $\times10^{24}$ (8)	L_{bol}/L_{Edd} (9)
Table 3.3a: Proprietary X-ray Results								
NGC0660	II	5	-0.63	0.005 ±0.001	3.3E+38	···	···	4.0E-06
NGC1055	IV	<1	···	< 0.0004	<3.3E+37	6.7	9.7	···
NGC3125	I	137	-0.25	0.071 ± 0.004	4.7E+39	···	···	4.1E-03
NGC4013	IV	<1	···	<0.0003	<1.6E+37	11.0	10.2	···
NGC4102	III	80	-0.38	0.057 ± 0.004	3.1E+39	···	···	···
NGC4350	I	10	-0.13	0.005 ± 0.001	6.4E+38	···	···	1.8E-06
NGC4419	II	20	-0.20	0.010 ± 0.002	1.2E+39	···	···	3.9E-05
NGC4527	III	14	-0.30	0.008 ± 0.001	1.9E+39	···	···	2.9E-06
NGC4666	IV	<1	···	<0.0007	<1.2E+38	1.1	8.4	···
NGC4713	IV	<1	···	<0.0004	<1.3E+37	12.6	10.4	···
NGC4750	I	31	-0.58	0.030 ± 0.003	6.0E+39	···	···	···
NGC5005	III	27	-0.76	0.046 ± 0.003	3.1E+39	···	···	···
NGC5678	IV	<1	···	<0.0005	<1.5E+38	0.5	8.2	···
NGC5954	IV	<1	···	<0.0004	<1.7E+38	0.3	8.1	···
IC1218	IV	<1	···	<0.0003	<3.5E+37	6.4	9.5	···
NGC7465*	I	164	···	0.160 ± 0.011	···	···	···	···
Table 3.3b: SSD04 X-ray Statistics								
0248+4302	II	1	-0.85	0.001	1.8E+40[a]	···	···	···
1346+2650	III	52	-0.81	0.027	7.1E+41[a]	···	···	1.6E-04
2312-5919	III	286	0.07	0.011	1.1E+41[a]	···	···	···
2055-4250	III	65	-0.60	0.0072	7.2E+40[a]	···	···	···
IC1459*	III	1906	-0.50	0.13	2.6E+40[a]	···	···	7.1E-06
MRK266	I	148	-0.23	0.19	7.4E+40[a]	···	···	···
MRK273	III	671	0.15	0.026	1.1E+44[e]	···	···	5.3E-01
NGC0224*	II	51	-0.84	0.12	3.9E+37[a]	···	···	2.8E-07
NGC0253	II	254	-0.13	0.042	1.1E+38[a]	···	···	2.6E-06
NGC0404	II	25	-0.72	0.0076	2.1E+37[a]	···	···	7.5E-06
NGC0835	II	15	-0.47	0.0045	7E+39[a]	···	···	2.0E-06
NGC1052*	I	183	0.24	0.13	4.2E+41[b]	···	···	5.8E-04
NGC3031	I	76	-0.32	0.093	1.6E+40[c]	···	···	6.9E-05
NGC3079	II	95	-0.08	0.0078	6.8E+39[a]	···	···	4.1E-06
NGC3368	II	1	-0.78	0.0045	2.8E+39[a]	···	···	5.3E-05
NGC3623	IV	<2	···	<0.0081	<4E+38[a]	N/A	7.2	···
NGC4125	III	35	-0.74	0.0042	4.2E+38[a]	···	···	3.6E-07
NGC4278*	I	35	-0.68	0.21	1.2E+40[c]	···	···	2.1E-06
NGC4314	II	5	-0.70	0.0021	1.4E+38[a]	···	···	2.3E-06
NGC4374	III	153	-0.70	0.036	1.3E+39[c]	···	···	2.2E-07
NGC4486*	I	1948	-0.66	0.3	3.3E+40[a]	···	···	2.9E-06
NGC4569	II	10	-0.60	0.0296	2.6E+39[c]	···	···	1.8E-05
NGC4579*	I	8278	-0.39	0.81	8.9E+40[c]	···	···	3.4E-04
NGC4696	III	39	-0.59	0.0022	1.3E+40[a]	···	···	8.9E-06
NGC5194	III	49	-0.79	0.018	1.1E+41[d]	···	···	3.7E-03
NGC5195	IV	<1	···	<0.0009	<7.1E+37[c]	3.4	8.9	···
NGC6240	III	1110	0.04	0.058	1.6E+44[f]	···	···	3.1E-02
NGC6500	I	1	-0.95	0.02	1.7E+40[a]	···	···	6.96E-06
NGC6503	II	11	-0.42	0.0029	4.6E+35[a]	···	···	3.7E-07
NGC7331	II	33	-0.56	0.0051	3.3E+38[a]	···	···	1.1E-06
UGC05101	I	150	-0.15	0.0072	7.7E+40[a]	···	···	···

Column Explanation: See X-ray Results of the Expanded Sample continued, Table 3.3c below **References:**[a] SSD04, [b] Guainazzi et al 2000, [c] Ho et al. 2001, [d] Fukazawa et al. 2001, [e] Xia et al. 2002, [f] Vignati et al. 1999.

Table 3.5: X-ray Results of the Expanded Sample continued

Galaxy Name (1)	X-ray Class (2)	Hard Counts (3)	Hardness Ratio (4)	Count Rate 0.3-10keV (5)	L_X 2-10keV (6)	$N_H{}^{MIN}$ $\times 10^{23}$ (7)	$N_H{}^{AVG}$ $\times 10^{24}$ (8)	L_{bol}/ L_{Edd} (9)
Table 3.3c: H01 X-ray Statistics								
NGC 2787	III	NA	NA	0.0053	2.0E+38	···	···	1.4E-06
NGC 2841	II	NA	NA	0.0035	1.8E+38	···	···	1.9E-07
NGC 3489	II	NA	NA	0.0061	1.7E+38	···	···	1.2E-06
NGC 3627	IV	NA	NA	<0.0017	<4.1E+37	5.5	9.3	···
NGC 3628	IV	NA	NA	<0.0017	<4.8E+37	4.7	9.2	···
NGC 3675	IV	NA	NA	<0.0017	<9.8E+37	1.6	8.5	···
NGC 4203	I	NA	NA	0.22	1.2E+40	···	···	4.1E-05
NGC 4321	IV	NA	NA	<0.0040	<3.9E+38	NA	7.3	1.6E-05
NGC 4494	I	NA	NA	0.012	7.2E+38	···	···	4.4E-06
NGC 4594	I	NA	NA	0.19	1.4E+40	···	···	3.4E-06
NGC 4826	IV	NA	NA	<0.0067	<7.2E+37	2.8	8.8	···

Column Explanation: Col(1): Galaxy Common Name, (*) galaxies experiencing pileup; Col(2): X-ray morphological Class; Col(3): Hard counts in the nucleus (2-8 keV) from an extraction region of radius 2" centered on the radio or *2MASS* nucleus, NA=Not Available; Col(4): Hardness Ratio: Defined here as (H-S)/(H+S) where H represents the hard counts (2-8 kev) and S represents the soft counts (0.3-2 keV) in the nucleus, NA=Not Available. Col(5): Countrate (counts/sec), NGC 7465 experienced severe pileup and could not be confidently analyzed; Col(6): X-ray luminosity in ergs s^{-1}; Col(7):Intrinsic absorption corresponding to upper limits for all non-detections in units of cm^{-2}. This is the column density required to obscure an AGN with luminosity equal to $L_X = 2 \times 10^{38}$ ergs s^{-1}, which is the minimum 2-10keV luminosity of all targets with detections of hard nuclear sources from this sample, H01, and SSD04; Col(8):Intrinsic absorption corresponding to upper limits for all non-detections in units of cm^{-2}. This is the column density required to obscure an AGN with luminosity equal to $L_X = 9.5 \times 10^{42}$ ergs s^{-1}, which is the average 2-10keV luminosity of all targets with detections of hard nuclear sources from this sample, H01, and SSD04; Col(9): Eddington ratio **References:** [a] SSD04, [b] Guainazzi et al 2000, [c] Ho et al. 2001, [d] Fukazawa et al. 2001, [e] Xia et al. 2002, [f] Vignati et al. 1999.

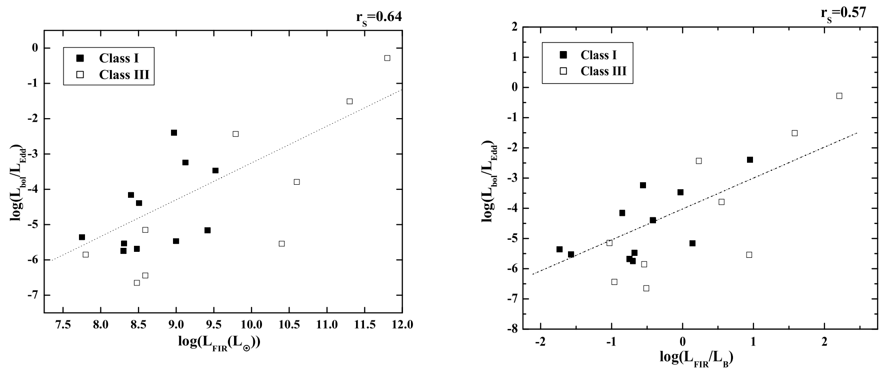

Figure 3.7: Eddington ratios vs. host galaxy properties

3.7a: Eddington Ratio as a function of the luminosity in the far-IR 3.7b: Eddington Ratio as a function of IR-brightness. A significant correlation that extends over seven orders of magnitude in L/L_{Edd} is found in both plots. The Spearman rank correlation coefficient is given in the upper right corner of each plot.

3.5 Discussion

3.5.1 Possible Connection between Black Hole Growth and Star Formation?

Figures 3.7a and 3.7b imply that either the mass accretion rate, or the radiative efficiency, or a combination of both, scales with the IR luminosity and IR-brightness of the galaxy. The majority of galaxies plotted in Figure 3.7 have extremely low accretion rates, well below the threshold at which the accretion flow is likely to take place via an Advection Dominated Accretion Flow (ADAF) model or other radiatively inefficient accretion models (Narayan, Mahadevan, & Quataert 1998). The smooth increase in L/L_{Edd} with respect to $L_{\mathrm{FIR}}/L_{\mathrm{B}}$ argues against the possibility that the accretion mode and therefore the radiative efficiency, changes significantly for the targets plotted in Figure 3.7. For operative purposes, in this paper, we assume constant radiative efficiency and explore the consequences.

The IR luminosities, as measured from IRAS, as well as the blue magnitudes are measured in a large aperture and therefore include the emission from the entire host galaxy in our sample of LINERs. The infrared emission from galaxies is usually attributed to thermal radiation from dust heated by young massive stars, the underlying old stellar population, and possibly an AGN (Rowan-Robinson & Crawford 1989). In the absence of an AGN, both the far-IR luminosity as well as the L_{FIR}/L_B ratio are widely used as star formation indicators (e.g., Keel 1993, Huang et al. 1996, Hunt & Malkan 1999). In starburst galaxies, both quantities can be used as a direct measure of the star formation rate (SFR; Lehnert & Heckman 1996; Meurer et al. 1997). Even in the case of early-type spiral galaxies, a comparison of Hα equivalent widths with IR-brightness suggests that the far-IR luminosity and L_{FIR}/L_B ratio can be used as a reliable star formation indicator (Usui, Saito, & Tomita 1998). In our sample of galaxies, the contributions to the IR emission from underlying old stars, the AGN, and the fraction of stellar light reprocessed by dust is unknown. However, given the low X-ray luminosities and Eddington ratios for our sample of LINERs, the contribution from the AGN to the far-IR luminosity is likely to be small. If we make the assumption that far-IR emission is predominantly associated with young massive stars, Figure 3.7 implies a link between black hole growth, as measured by the mass accretion rate, and the SFR, as measured by the far-IR luminosity and IR-brightness.

A correlation between mass accretion rate and SFR in LINERs may have important implications for our understanding of black hole growth and the connection between starbursts and AGNs. The well-known tight correlation between black hole mass and stellar velocity dispersion (Gebhart et al. 2000) implies that black hole and bulge formation and growth are intimately connected. In a study of narrow line Seyfert 1 (NLS1s) galaxies, Shemmer et al. (2004) find that the Eddington ratio is correlated with gas metallicity, implying a similar relationship between star formation, responsible for the gas metal enrichment, and the accretion rate. Unlike NLS1s, thought to represent an early phase in the lifetime of an AGN, LINERs are characterized by more massive black holes and low accretion rates, possibly representing the phase in galaxy evolution just before accretion "turns off". Figure 3.7 may suggest an evolutionary sequence, where IR-bright LINERs represent younger AGNs defined by higher mass accretion rates, evolving into lower accretion rate IR-faint LINERs, and finally, the normal quiescent galaxies with dormant black holes we see in our local Universe. Testing for systematic differences in the circumnuclear stellar populations in LINERs may prove vital to our understanding of galaxy evolution.

3.5.2 Speculations on AGN Fueling

The far-IR luminosity or Hα equivalent width is known to be roughly proportional to the CO emission from galactic and extragalactic molecular clouds (e.g., Mooney & Solomon 1988 ; Devereux & Young 1991; Young et al. 1996; Rownd & Young 1999) suggesting that the SFR rate in galaxies is proportional to the molecular gas mass (e.g., Mooney & Solomon 1988). CO-line observations for the majority of our sample do not exist in the literature. If the scaling between the far-IR luminosity and the CO emission holds for the host galaxies in our sample, Figure 3.7a suggests the intriguing possibility that the mass accretion rate scales with the host galaxy's fuel supply.

AGN fueling has been a longstanding question. While it is widely accepted that the onset of activity results from the feeding of the black hole by the gas reservoir of the host galaxy, there is no consensus on which mechanism is responsible for removing angular momentum and driving the gas infall down to scales of less than a parsec (see reviews by Martini 2004 and Wada 2004). A number of mechanisms for removing the angular momentum of the gas have been proposed. Among these mechanisms, galaxy interactions (eg Toomre & Toomre, 1972; Shlosman et al. 1989, 1990; Hernquist & Mihos, 1995) and galactic bars (e.g. Schwarz 1984; Shlosman, Frank & Begelman 1989; Knapen et al. 1995) are prime candidates for facilitating the transfer of mass from large to small scales. However, despite many years of observational effort, no strong correlations between the presence of any of the proposed large scale fueling mechanisms in low luminosity AGNs have been found. For example, the majority of recent observations show either a marginal or no clear excess of bars or interactions in galaxies harboring low luminosity AGNs as compared with normal galaxies (e.g. Ho, Fillipenko, & Sargent 1997a, Mulchaey & Regan 1997, Corbin 2000, Schmitt 2001). If Figure 3.7 implies that the mass accretion rate scales with fuel supply over seven orders of magnitude in L/L_{Edd}, then the fueling mechanism responsible must be compatible with this result. Of the targets plotted in Figure 3.7, two of the LINERs contain bars and the two with the most extreme $L_{\rm FIR}$ and $L_{\rm FIR}/L_{\rm B}$ values are interacting systems, suggesting that the large scale phenomenon does not have a significant impact on the fueling of the AGN . If different mechanisms are responsible for AGN fueling over the range of Eddington ratios plotted in Figure 3.7, it would be unexpected to see such a smooth trend in mass accretion rate with fuel supply. Rather one would expect the galaxies in Figure 3.7 to occupy well-defined regimes in $L/L_{\rm Edd}$ vs. $L_{\rm FIR}$ or $L_{\rm FIR}/L_{\rm B}$ based on the fueling mechanism responsible for accretion onto a black hole. We reiterate that the conclusions drawn from Figure 3.7 are highly speculative and based on limited data. More rigorous and extensive multi-wavelength observations are critical to validate our results.

3.6 Summary and Conclusions

We have examined the properties of a sample of nearby IR-bright LINERs using proprietary and archival X-ray observations from *Chandra*. Our main results are as follows.

1. Twenty-eight out of 55 LINERs (51%) show compact hard nuclear cores coincident with the radio or *2MASS* nucleus, with a luminosity L_X (2-10keV) $\geq 2 \times 10^{38}$ ergs s^{-1}. The nuclear 2-10 keV luminosity for this expanded sample of galaxies ranges from $\sim 2 \times 10^{38}$ ergs s^{-1} to $\sim 2 \times 10^{44}$ ergs s^{-1}.

2. We find that the most IR-faint LINERs are exclusively AGNs. The fraction of LINERs containing AGNs appears to decrease with IR-brightness and increase again at the highest values of $L_{\rm FIR}/L_{\rm B}$.

3. Of the LINERs with hard X-ray nuclear cores and observations at Hα wavelengths, only 33% (8/24) show broad lines. Similarly, only roughly half of the LINERs observed in the radio (8/14) show a flat spectrum radio core. These findings emphasize the need for high-resolution X-ray imaging observations in the study of IR bright LINERs.

4. We find a surprising trend in the Eddington ratio as a function of $L_{\rm FIR}/L_{\rm B}$ and $L_{\rm FIR}$ that extends over seven orders of magnitude in $L/L_{\rm Edd}$. This may imply a fundamental link between mass accretion rate, as measured by the Eddington ratio, and star formation rate (SFR), as measured by the IR-brightness. The correlation may further indicate that the accretion rate scales with fuel supply, a finding that has important implications for AGN fueling in low luminosity AGNs.

Chapter 4: THE LINK BETWEEN STAR FORMATION AND ACCRETION IN LINERS: A COMPARISON WITH OTHER AGN SUBCLASSES

This Chapter was published by S. Satyapal, R. P. Dudik, B. O'Halloran, & M. Gliozzi, 2005, ApJ, 633, 86

4.1 Introduction

The correlation between L_{bol}/L_{Edd} and L_{FIR}, L_{FIR}/L_B presented in Chapter 3 was based on a limited sample of 20 LINERs with confirmed AGNs in their nucleus. In an effort to confirm and assess the statistical significance of this correlation, in this paper we present a study of the 25 remaining LINERs in the *Chandra* archive for which stellar velocity dispersion-derived black hole masses are available. Of these LINERs, 13 show hard nuclear point sources consistent with an AGN. In addition, to assess whether the correlation is unique to LINERs or whether it extends to other AGN subclasses, in this paper we combine our data with published FIR measurements, bolometric luminosity and black hole mass estimates of additional galaxies that belong to other AGN subclasses.

This paper is organized as follows. In Section 4.2, we summarize the properties of the new *Chandra* archival sample presented in this paper, along with a description of additional samples of the various AGN subclasses included in our analysis. In Section 4.3, we summarize the observations and data analysis procedure employed for both our *Chandra* and *ISO* observations, followed by a description of our results, including a discussion of our correlations for the various AGN subclasses in Section 4.4. In Section 4.5, we discuss the implications of our correlations, followed by a summary of our major conclusions in Section 4.6.

4.2 The Sample

In this paper, we expand our previously published sample of LINERs and include in our analysis data from other AGN subclasses in the literature. In order to include additional AGNs, we must be able to estimate the mass of the black hole and the bolometric luminosity of the AGN. Black hole masses in AGNs are derived primarily through: 1) resolved stellar kinematics, 2) reverberation mapping, or 3) applying the correlation between optical bulge luminosity and central black hole mass determined in nearby galaxies. Dynamical estimates of the central mass are the most reliable but they exist for only a handful of AGNs (e.g., see review by Ferrarese & Ford 1999). In the absence of dynamical estimates, black hole mass estimates based on reverberation mapping observations are generally accepted to be accurate to within a factor of 3 (e.g., Peterson et al. 2004). Since the optical light from the bulge is often overwhelmed by that from the AGN, black hole mass estimates based on large aperture measurements of the optical luminosity are less reliable. In this work, we conservatively included a selection of AGNs for which the black hole mass was derived either through dynamical estimates, reverberation mapping, or host galaxy bulge luminosity *only* if the host galaxy was clearly resolved. In addition, in order to be included in our analysis, IRAS FIR fluxes and reliable bolometric luminosities must be available for all galaxies. Since the number of such objects is limited, we emphasize that these samples are not complete in any sense and are therefore subject to selection biases. Each sample is discussed separately below. The assumptions employed in estimating black hole masses and bolometric luminosities are discussed in each case.

4.2.1 LINER Sample

We searched the *Chandra* archive for all galaxies classified as LINERs in the multifrequency LINER catalog from Carillo et al. (1999) which were not previously published in our earlier works (Galaxies that are classified as LINERs using *either* the Heckman (1980) or the Veilleux & Osterbrock (1987) diagnostic diagrams are included). Of the 43 newly available galaxies, only 25 had stellar velocity dispersions and FIR fluxes published in the literature. These galaxies are nearby (1 to 215 Mpc; d_{median}=13 Mpc), and comprise a wide range of FIR luminosities (5.87×10^6 $L_\odot$ to 3.26×10^{10} $L_\odot$, infrared-to-blue ratios (0.01 to 2.81), and Hubble types. We combine this sample with the compilation presented in Papers I and II. The entire *Chandra* sample consists of a total of 82 galaxies. In this paper we refer to the combined sample as the *"comprehensive LINER sample"*, and the sample from this paper alone as the *"archival LINER sample"*. The basic properties of the archival LINER sample are summarized in Table 4.1 and Figure 4.1. Following the treatment described in Papers I and II (see Section 4.3), LINERs that displayed a dominant hard nuclear point source are classified as AGN-LINERs. Black hole masses for these sources were determined using the correlation between the stellar velocity dispersion and black hole mass (see Table 4.1; Ferrarese & Merritt 2000; Gebhardt et al. 2000) demonstrated to hold for nearby AGNs (Ferrarese et al. 2001; McLure & Dunlop 2002). While all of the LINERs in the archival LINER sample possess black hole mass estimates, seven AGN-LINERs from Chapter 3 do not have this data. They have therefore been excluded from those plots requiring such estimates. We note that of the 25 LINERs in the archival LINER sample, 13 display hard nuclear point sources consistent with an AGN and are used in the main study of this work. We refer to these AGNs as the *"archival AGN-LINER sample"*. As in Chapter 3, the bolometric luminosity of all targets was calculated using the formula $L_{bol} = 34\times\ L_X$(2-10keV), determined from the spectral energy distribution(SED) measurements of seven low luminosity AGNs from Ho 1999 (see Chapter 3 for details).

Of the 82 LINERs in our comprehensive LINER sample, 41 are AGN-LINERs, 34 of which have published black hole masses. Since AGN-LINERs with published black hole masses are the main study of this paper, we refer to the sample of all AGN-LINERs with published black hole masses included in this work as the *"comprehensive AGN-LINER sample"*. The galaxy properties were taken from the NASA/IPAC Extragalactic Database (NED). We note that the comprehensive LINER sample published in this work includes the complete set of LINERs from the Carillo et al. (1999) catalog with published black hole mass estimates that exist in the *Chandra* archive.

4.2.2 Seyfert Sample

The Seyfert galaxies included in our analysis were taken from the sample compiled by Woo & Urry (2002). Six of the galaxies in this sample were excluded because they are cross-listed in other AGN-subclass samples we include in this work (2 are Narrow Line Seyfert1s, 2 are LINERs, and 2 are radio loud AGNs). Only those objects with both 60 and 100 μm and blue magnitudes available in NED were selected. These include 12 Seyfert 1 galaxies with black hole masses derived from reverberation mapping (Kaspi et al. 2000, or Onken & Peterson 2002), 2 Seyfert 1s with M_{BH} derived through

Table 4.1: Properties of the Archival Sample

Galaxy Name (1)	Distance (Mpc) (2)	Hubble Type (3)	log L_{FIR} (4)	log (L_{FIR}/L_B) (5)	log (M_{BH}) (6)
AGN-LINERs					
NGC0315	66	E	9.4	-0.69	9.12
NGC2681	13*	SAB(rs)0	8.8	-0.30	7.75
NGC3169	20*	SA(s)a	9.8	0.30	7.86
NGC3245	22*	SA(r)0	9.2	-0.08	8.39
NGC3718	17*	SB(s)a	8.7	-0.46	7.93
NGC4258	7*	SAB(s)bc	9.4	0.06	7.16
NGC4261	35*	E2-3	8.9	-0.96	8.84
NGC4410A	97	Sab?	9.7	0.001	8.73
NGC4457	17*	SAB(s)0	9.4	0.35	6.95
NGC4552	17*	E	8.0	-1.44	8.57
NGC4565	10*	SA(s)b?	9.2	0.14	7.56
NGC6482	52*	E	8.8	-1.01	8.92
3C218	215	(R')SA0	10.2	-0.23	8.88
Non-AGN-LINERs					
NGC2541	11*	SA(s)cd	8.5	0.08	5.81
NGC2683	6*	SA(rs)b	8.5	-0.01	7.36
NGC4410B	97	S0	9.8	0.45	8.23
NGC4150	10*	SA(r)0	8.3	0.01	7.36
NGC4438	17*	SA(s)0	9.4	0.02	5.19
NGC4459	17*	SA(r)0	9.0	-0.19	7.85
NGC4501	17*	SA(rs)b	10.0	0.39	7.64
NGC4548	17*	SBb(rs)	9.2	-0.20	7.68
NGC4550	17*	SB0	7.8	-0.92	6.79
NGC4736	4*	SA(r)ab	9.3	0.28	7.07
NGC5846	29*	E0-1	7.8	-1.94	8.59
NGC5866	15*	S03	9.4	0.05	7.49

Columns Explanation: Col(1):Common Source Names; Col(2): Distance. Since most of these galaxies are nearby, we have taken distances (marked *) from Tully 1988 who derived distances based on the Virgo infall model. All others were calculated using redshift for H_0= 75 km $s^{-1}Mpc^{-1}$; Col(3): Morphological Class; Col(4): Far-infrared luminosities (in units of solar luminosities: $L_\odot$) correspond to the 40-500μm wavelength interval and were calculated using the IRAS 60 and 100 μm fluxes according to the prescription: L_{FIR}=$1.26\times10^{-14}(2.58f_{60}+f_{100})$ in W m^{-2} (Sanders & Mirabel 1996).; Col(5): L_B: B magnitude see Carrillo et al (1999); Col(6): Mass of central black hole calculated using the stellar velocity despersion in the formula: $M_{BH} = 1.2(\pm0.2)\times10^8\ M_\odot(\sigma_e/200\ \mathrm{km\ s^{-1}})^{3.75(\pm0.3)})$ (from Ferrarese & Merritt 2000; Gebhardt et al. 2000a; Tremaine et al. 2002). Velocity dispersions are taken from the Hypercat database available online at http://www-obs.univ-lyon1.fr/hypercat.

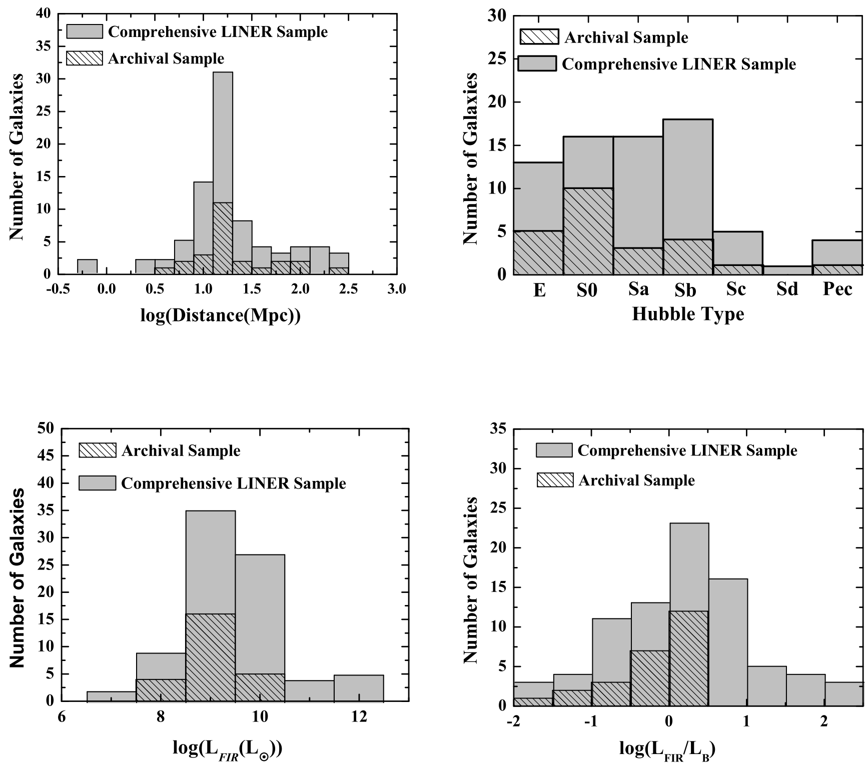

Figure 4.1: Comprehensive LINER sample statistics

Characteristics of the comprehensive *Chandra* sample of LINERs from this paper and Chapter 3. The solid bins correspond to the entire sample from this work and Chapter 3 (the *"comprehensive LINER sample"*). The striped bins correspond to the LINERs from this paper only (the *"archival LINER sample"*). Most galaxies in the comprehensive LINER sample are nearby and span a wide range of luminosities, IR-brightness ratios, and Hubble types. Note that not all galaxies have Hubble classifications available in the literature and have therefore been excluded from that plot.

their optical luminosity, and the remaining Seyfert 1s and 2s with M_{BH} derived from stellar velocity dispersion measurements. All Seyferts are nearby, spanning a distance range similar to that spanned by our LINER sample (d=4 to 136 Mpc; d_{median} = 56 Mpc). Bolometric luminosities were determined in virtually all cases by integrating all available flux points in the well-sampled SED. We note that since the two galaxies with black hole mass estimates derived from their optical luminosity are nearby, spatially resolved observations of their nuclear optical luminosity were possible.

4.2.3 Radio-Quiet Quasar Sample

The radio-quiet quasars (RQQ) included in our analysis were also taken from Woo & Urry (2002). Again, only those objects with firm 60 and 100 μm IRAS detections and blue magnitudes available in NED were selected. Ten out of 15 of these objects have M_{BH} derived from reverberation mapping, and the remaining 5 have M_{BH} derived through their optical luminosity. Bolometric luminosities were determined through either direct flux integration of the SED or by flux-fitting the appropriate RQQ template SED (Elvis et al. 1994) to the available flux points. The RQQ sample spans a distance range from z=0.06 to z=0.29, with a median z=0.11.

4.2.4 Radio-Loud AGN Sample

In radio-loud AGNs, the stellar light is often overwhelmed by the nonthermal contribution from the AGN. As a result, black hole mass estimates based on the host galaxy's bulge luminosity are unreliable. We therefore use the sample of radio-loud AGNs from Marchesini et al. (2004), which includes only those objects in the complete sample of 53 RLQs in the 3CR catalog (Spinrad et al. 1985) with clearly resolved host galaxies. We have included only those objects with firm IRAS detections and blue magnitudes, and of these 17, three additional galaxies have been excluded because they exist in our comprehensive AGN-LINER sample. The final radio-loud sample comprises 4 radio galaxies exhibiting Fanaroff-Riley type I (FR I) radio morphology, 5 objects exhibiting FR II morphology (Fanaroff & Riley 1974), and 5 radio-loud quasars. The sample spans a distance range from z=0.017 to z=1.436, with a median distance of z=0.07. Black hole masses were derived either through stellar velocity dispersion measurements or through the host galaxy's optical luminosity. Bolometric luminosities were obtained from the rest-frame monochromatic luminosity at $5100\mathring{A}$ (McLure & Dunlop 2001) using the bolometric correction from Elvis et al. (1994).

We note that several LINERs are radio-loud (e.g. Ho 1999; Terashima et al. 2003) and are found to exhibit weak radio jets (e.g. Yuan et al. 2002, Nagar et al. 2004). Alternatively, several radio galaxies that display either FR I or FR II radio morphologies also exhibit weak optical emission lines with LINER-like line ratios (e.g Tadhunter et al. 1993, Lewis et al. 2003). Strictly speaking, our LINER sample and the radio-loud AGN sample may not therefore be distinct AGN subclasses. However, in order to assess the incidence of possible selection biases, to enlarge the statistics, and to include radio-loud quasars (RLQs) with redshifts overlapping with the redshift range of the RQQs, we include this sample in our analysis.

4.2.5 Narrow Line Seyfert 1 Sample

A subset of Seyfert galaxies display narrow permitted optical lines (NLS1s; Osterbrock & Pogge 1985), appear to accrete at close to the Eddington rate and have smaller mass black holes for a given luminosity compared to regular Seyfert 1s (e.g. Borosson 2002, Grupe et al. 2004). In order to expand our sample to include low values of M_{BH} and high L_{bol}/L_{Edd} values, we include the sample of NLS1s from Grupe et al.

2004, which consists of a complete sample of 110 soft X-ray selected AGNs. Of the 51 NLS1s in this sample, only 12 have 60 and 100 μm IRAS detections and 4 more have 100 μm IRAS upper limits. Of these 16 galaxies, 2 were excluded because they overlap with our RQQ sample. Black hole masses were calculated using the Hβ line width and 5100 $\AA$ luminosity using the empirical relation from Kaspi et al. (2000). Bolometric luminosities were estimated by using a combined power-law model fit with exponential cutoff to the optical-UV data (See Grupe et al. 2004 for details). Our final NLS1 sample consists of 14 objects with distances that range from z=0.02 to z=0.14, with a median distance of z=0.045.

The entire AGN sample included in our analysis, which we refer to as *"The Expanded AGN sample"*, consists of: 52 Seyfert galaxies, 14 radio-loud AGNs, 15 RQQ, and 14 NLS1. Combined with our comprehensive AGN-LINER sample, the total number of galaxies in our analysis is 129. We emphasize again that the basis for selection of objects in the expanded AGN sample is on the availability of reliable black hole mass, bolometric and FIR luminosities. The sample therefore should not be viewed as complete in any sense. Black hole masses, bolometric luminosities, and Eddington ratios for all objects included in our expanded AGN sample are listed in Tables 4.2, 4.3, and 4.4.

4.3 Observations and Data Reduction Procedure

4.3.1 *Chandra* Observations

Archival *Chandra* observations of all LINER targets presented in this study were obtained and analyzed according to the perscription given in Chapter 2.2. For fourteen of the twenty-five sources the detected counts in the 0.3-8 keV range were sufficient to perform detailed spectral fits. Of these fourteen objects, eleven are

Table 4.2: Expanded AGN Sample Properties: Published AGN-LINERs[+]

Galaxy Name (1)	z (2)	$\log(M_{BH})^a$ (3)	$\log(L_{bol})^a$ (4)	$\log(L_{FIR})$ (5)	$\log(L_{FIR}/L_B)$ (6)	$\log(L_{bol}/L_{Edd})$ (7)
NGC3125	0.0029	5.77	41.5	9.0	0.95	-2.39
NGC 4350	0.0040	7.99	40.4	8.3	-0.70	-5.75
NGC1052	0.0049	8.29	43.2	9.1	-0.56	-3.24
NGC3031	-0.0001	7.79	41.7	8.4	-0.85	-4.16
NGC4278	0.0022	9.20	41.6	8.5	-0.75	-5.68
NGC4486	0.0044	9.48	42.1	8.3	-1.57	-5.53
NGC4579	0.0051	7.85	42.5	9.5	-0.03	-3.47
NGC6500	0.0100	8.82	41.8	9.4	0.14	-5.16
NGC 4203	0.0036	7.90	41.6	8.5	-0.42	-4.39
NGC 4494	0.0045	7.65	40.4	7.7	-1.73	-5.36
NGC 4594	0.0034	9.04	41.7	9.0	-0.68	-5.47
NGC4527	0.0058	8.25	40.3	9.9	0.94	-5.54
NGC4125	0.0045	8.50	40.2	8.6	-0.96	-6.44
NGC4374	0.0035	9.20	40.6	8.5	-0.51	-6.65
NGC4696	0.0099	8.60	41.7	8.8	-1.11	-5.05
NGC5194	0.0015	6.90	42.6	9.8	0.23	-2.43
MRK273	0.0378	7.74	45.6	11.8	2.21	-0.28
CGCG162-010	0.0633	9.07	43.4	10.6	0.55	-3.79
NGC6240	0.0245	9.15	45.7	11.3	1.58	-1.51
IC1459	0.0056	9.00	41.9	8.6	-1.03	-5.15
NGC 2787	0.0023	7.59	39.8	7.8	-0.54	-5.85

Columns Explanation: Col(1):Common Source Names; Col(2): Redshift; Col(3): Log of the mass of central black hole ($M_\odot$), * Mass of the Central black hole was calculated using the suggested formulation of Grupe & Mathur 2004: $\log(M_{BH}) = 5.17 + \log(R_{BLR}) + 2[\log FWHM(H\beta)\text{-}3]$, where R_{BLR} is the radius of the broad-line region (BLR) and is in units of light days. R_{BLR} may be calculated using the monochromatic luminosity at 5100 $\AA$ (λL_{5100}) in units of watts: $\log(R_{BLR}) = 1.52 + 0.70(\log(\lambda L_{5100})\text{-}37)$. Monochromatic luminosities at 5100 $\AA$ were taken from Grupe & Mathur 2004; Col(4): Log of the bolometric Luminosites in ergs s^{-1}; Col(5): Log of the far-infrared luminosities (in units of solar luminosities: $L\odot$) correspond to the 40-500μm wavelength interval and were calculated using the IRAS 60 and 100 μm fluxes according to the prescription: $L_{FIR}=1.26\times10^{-14}(2.58f_{60}+f_{100})$ in W m^{-2} (Sanders & Mirabel 1996), Col(6): L_B: B magnitude taken from the Nasa/Ipac Extragalactic Database (NED); Col(7): Log of the Eddington ratio. **References:** [a] Woo & Urry 2002 and references therein; [+] Includes only those AGN-LINERs with black hole mass estimates from Papers I and II. Combined with the AGN-LINERs in the archival LINER sample listed in Table 4.1, this represents the "comprehensive AGN-LINER sample discussed in the text.

Table 4.3: Expanded AGN Sample Properties: Seyferts

Galaxy Name (1)	z (2)	$\log(M_{BH})^a$ (3)	$\log(L_{bol})^a$ (4)	$\log(L_{FIR})$ (5)	$\log(L_{FIR}/L_B)$ (6)	$\log(L_{bol}/L_{Edd})$ (7)
Type 1 Seyferts						
NGC 1566	0.005	6.92	44.5	10.2	0.30	-0.57
NGC 3227	0.004	7.64	43.9	9.6	0.34	-1.88
NGC 3516	0.009	7.36	44.3	9.6	0.13	-1.17
NGC 3783	0.010	6.94	44.4	10.0	0.47	-0.63
NGC 3982	0.004	6.09	43.5	9.6	0.57	-0.65
NGC 3998	0.003	8.95	43.5	8.2	-0.65	-3.51
NGC 4151	0.003	7.13	43.7	9.2	0.27	-1.50
NGC 4593	0.009	6.91	44.1	9.9	0.10	-0.92
NGC 5548	0.017	8.03	44.8	9.9	0.26	-1.30
NGC 6814	0.005	7.28	43.9	9.8	0.64	-1.46
NGC 7469	0.016	6.84	45.3	11.3	1.51	0.34
Mrk 10	0.029	7.47	44.6	10.4	0.24	-0.96
Mrk 79	0.022	7.86	44.6	10.3	0.65	-1.39
Mrk 509	0.034	7.86	45.0	10.6	-0.27	-0.93
Mrk 590	0.026	7.20	44.6	10.1	0.27	-0.67
Mrk 817	0.032	7.60	45.0	10.7	0.98	-0.71
IC 4329A	0.016	6.77	44.8	10.1	0.73	-0.09
UGC 3223	0.016	7.02	44.3	10.1	0.69	-0.85
Akn 120	0.032	8.27	44.9	10.3	0.37	-1.46
Type 2 Seyferts						
NGC 513	0.002	7.65	42.5	8.4	0.81	-3.23
NGC 788	0.014	7.51	44.3	9.4	-0.22	-1.28
NGC 1068	0.004	7.23	45.0	10.9	0.98	-0.35
NGC 1320	0.009	7.18	44.0	9.7	0.54	-1.26
NGC 1358	0.013	7.88	44.4	9.4	-0.21	-1.61
NGC 1386	0.003	7.24	43.4	9.2	0.51	-1.96
NGC 1667	0.015	7.88	44.7	10.7	0.92	-1.29
NGC 2273	0.006	7.30	44.1	9.2	0.33	-1.35
NGC 3185	0.004	6.06	43.1	8.9	0.36	-1.08
NGC 4258	0.001	7.62	43.5	9.0	0.06	-2.27
NGC 5273	0.004	6.51	43.0	8.6	-0.14	-1.58
NGC 5347	0.008	6.79	43.8	9.5	0.36	-1.08
NGC 6104	0.028	7.60	43.6	10.2	0.46	-2.10
NGC 7213	0.006	7.99	44.3	9.6	-0.11	-1.79
NGC 7603	0.030	8.08	44.7	10.4	0.54	-1.52
NGC 7743	0.006	6.59	43.6	9.2	0.01	-1.09
Mrk 1	0.016	7.16	44.2	10.2	1.27	-1.06
Mrk 3	0.014	8.65	44.5	10.3	1.07	-2.21
Mrk 270	0.010	7.60	43.4	8.9	0.01	-2.33
Mrk 348	0.015	7.21	44.3	9.9	0.54	-1.04
Mrk 533	0.029	7.56	45.2	11.1	1.20	-0.51
Mrk 573	0.017	7.28	44.4	10.0	0.43	-0.94
Mrk 622	0.023	6.92	44.5	10.2	0.81	-0.50
Mrk 686	0.014	7.56	44.1	9.6	0.24	-1.55
Mrk 917	0.024	7.62	44.8	10.8	1.33	-0.97
Mrk 1040	0.017	7.64	44.5	10.4	0.77	-1.21
Mrk 1066	0.012	7.01	44.6	10.6	1.36	-0.56
Mrk 1157	0.015	6.83	44.3	10.1	0.79	-0.66
UGC 3995	0.016	7.69	44.4	9.8	0.14	-1.40
UGC 6100	0.029	7.70	44.5	10.2	0.49	-1.32
IC 5063	0.011	7.74	44.5	10.2	0.77	-1.31
F 341	0.016	7.15	44.1	9.8	0.54	-1.12
II ZW55	0.025	8.23	44.5	10.7	1.25	-1.79

Columns Explanation: Col(1):Common Source Names; Col(2): Redshift; Col(3): Log of the mass of central black hole ($M_\odot$), * Mass of the Central black hole was calculated using the suggested formulation of Grupe & Mathur 2004: $\log(M_{BH}) = 5.17 + \log(R_{BLR}) + 2[\log \mathrm{FWHM}(H\beta)\text{-}3]$, where R_{BLR} is the radius of the broad-line region (BLR) and is in units of light days. R_{BLR} may be calculated using the monochromatic luminosity at 5100 $\AA$ (λL_{5100}) in units of watts: $\log(R_{BLR}) = 1.52 + 0.70(\log(\lambda L_{5100})\text{-}37)$. Monochromatic luminosities at 5100 $\AA$ were taken from Grupe & Mathur 2004; Col(4): Log of the bolometric Luminosites in ergs s^{-1}; Col(5): Log of the far-infrared luminosities (in units of solar luminosities: $L\odot$) correspond to the 40-500μm wavelength interval and were calculated using the IRAS 60 and 100 μm fluxes according to the prescription: L_{FIR}=$1.26\times10^{-14}(2.58f_{60}+f_{100})$ in W m^{-2} (Sanders & Mirabel 1996), Col(6): L_B: B magnitude taken from the Nasa/Ipac Extragalactic Database (NED); Col(7): Log of the Eddington ratio. **References:** [a] Woo & Urry 2002 and references therein

Table 4.4: Expanded AGN Sample Properties: RL AGNs, RQ AGNs, & NLS1s

Galaxy Name (1)	z (2)	$\log(M_{BH})$ (3)	$\log(L_{bol})$ (4)	$\log(L_{FIR})$ (5)	$\log(L_{FIR}/L_B)$ (6)	$\log(L_{bol}/L_{Edd})$ (7)
Radio Quiet Quasars						
PG 0157+001	0.164	7.70^a	45.6^a	$12.1^\dagger$	1.17	-0.18
PG 0923+201	0.190	8.94^a	46.2^a	11.7	1.02	-0.82
PG 1202+281	0.165	8.29^a	45.4^a	11.1	0.42	-1.00
PG 1402+261	0.164	7.29^a	45.1^a	$11.1^\dagger$	0.40	-0.26
PG 1444+407	0.267	8.06^a	45.9^a	$11.2^\dagger$	0.26	-0.23
PG 0804+761	0.100	8.24^a	45.9^a	$10.6^\dagger$	0.15	-0.41
PG 1211+143	0.085	7.49^a	45.8^a	11.0	0.46	0.22
PG 1229+204	0.064	8.56^a	45.0^a	10.4	0.35	-1.65
PG 1351+640	0.087	8.48^a	45.5^a	11.2	0.64	-1.08
PG 1411+442	0.089	7.57^a	45.6^a	10.4	0.04	-0.09
PG 1426+015	0.086	7.92^a	45.2^a	10.8	0.39	-0.83
PG 1613+658	0.129	8.62^a	45.7^a	$11.5^\dagger$	1.02	-1.06
PG 1617+175	0.114	7.88^a	45.5^a	10.8	0.40	-0.46
PG 1700+518	0.292	8.31^a	46.6^a	$11.9^\dagger$	0.63	0.15
PG 2130+099	0.061	7.74^a	45.5^a	10.6	0.37	-0.37
Radio Loud AGN						
3C 031	0.017	7.89^b	42.0^b	9.8	0.09	-4.00
3C 84	0.018	9.28^b	44.0^b	10.7	0.62	-3.35
3C 338	0.030	9.23^b	42.3^b	9.8	-0.60	-4.99
3C 465	0.030	9.32^b	42.6^b	9.8	-0.34	-4.81
3C 088	0.030	8.53^b	42.4^b	9.9	0.34	-4.20
3C 285	0.079	8.46^b	41.5^b	10.8	0.80	-5.08
3C 327	0.105	9.00^b	42.4^b	11.2	0.93	-4.72
3C 390.3	0.056	8.41^b	44.9^b	10.3	-0.01	-1.64
3C 402	0.025	8.18^b	42.4^b	9.9	0.52	-3.85
3C 47	0.425	8.52^b	45.6^b	$12.0^\dagger$	1.41	-1.06
3C 138	0.759	8.73^b	45.9^b	$12.3^\dagger$	1.78	-0.96
3C 249.1	0.312	9.48^b	45.7^b	$11.1^\dagger$	-0.15	-1.90
3C 298	1.436	10.15^b	47.4^b	$13.2^\dagger$	1.22	-0.89
3C 380	0.692	9.37^b	46.4^b	$11.9^\dagger$	0.49	-1.10
Narrow Line Type 1 Seyferts						
NGC 4051	0.002	$5.13^\star$	42.6^c	9.1	1.18	-0.68
Mrk 142	0.045	$6.77^\star$	44.6^c	10.2	0.80	-0.31
Mrk 335	0.026	$6.90^\star$	45.2^c	<9.8	...	0.21
Mrk 478	0.077	$7.44^\star$	45.9^c	10.9	0.65	0.34
Mrk 493	0.032	$6.31^\star$	44.6^c	10.3	0.62	0.22
Mrk 684	0.046	$6.80^\star$	45.4^c	10.4	0.63	0.45
Mrk 766	0.013	$6.29^\star$	44.2^c	10.2	1.07	-0.16
Mrk 1044	0.017	$6.34^\star$	44.2^c	9.6	0.61	-0.24
Ton S 180	0.062	$6.85^\star$	45.7^c	<10.4	<0.99	0.76
RX J0323.2-4931	0.071	$6.85^\star$	44.6^c	<10.5	<0.95	-0.33
RX J1034.6+3938	0.044	$5.81^\star$	44.5^c	10.3	...	0.62
RX J2301.8-5508	0.140	$7.44^\star$	45.5^c	11.3	...	-0.07
PG 1244+026	0.049	$6.08^\star$	44.8^c	10.2	...	0.57
MS 2254-36	0.039	$6.60^\star$	44.3^c	<10.3	...	-0.43

Columns Explanation: Col(1):Common Source Names; Col(2): Redshift; Col(3): Log of the mass of central black hole ($M_\odot$), * Mass of the Central black hole was calculated using the suggested formulation of Grupe & Mathur 2004: $\log(M_{BH}) = 5.17 + \log(R_{BLR}) + 2[\log \mathrm{FWHM}(H\beta)\text{-}3]$, where R_{BLR} is the radius of the broad-line region (BLR) and is in units of light days. R_{BLR} may be calculated using the monochromatic luminosity at 5100 $\AA$ (λL_{5100}) in units of watts: $\log(R_{BLR}) = 1.52 + 0.70(\log(\lambda L_{5100})\text{-}37)$. Monochromatic luminosities at 5100 $\AA$ were taken from Grupe & Mathur 2004; Col(4): Log of the bolometric Luminosites in ergs s^{-1}; Col(5): Log of the far-infrared luminosities (in units of solar luminosities: $L\odot$) correspond to the 40-500μm wavelength interval and were calculated using the IRAS 60 and 100 μm fluxes according to the prescription: $L_{FIR}=1.26\times10^{-14}(2.58f_{60}+f_{100})$ in W m^{-2} (Sanders & Mirabel 1996), except † where FIR luminosities correspond to rest-frame values taken from Haas et al. (2003) or Haas et al. (2004); Col(6): L_B: B magnitude taken from the Nasa/Ipac Extragalactic Database (NED); Col(7): Log of the Eddington ratio. **References:** [a] Woo & Urry 2002 and references therein; [b] Marchesini, Celotti, & Ferrarese 2004 and references therein; [c] Grupe & Mathur 2004.

classified as AGN-LINERs. Spectral fitting on these objects was also performed as described in Chapter 2.2. We note here that several of the galaxies in our archival sample have been previously analyzed and published by various authors (e.g. Worrall et al. 2003, Donato et al. 2004, Terishima & Wilson, 2003). We have reanalyzed all of these galaxies in a homogeneous way in order to ensure consistancy in the data reduction proceedure.

4.3.2 AGN Detection Rate

Twenty-eight LINERs from the expanded LINER sample display a hard compact nuclear X-ray point source coincident with the *VLA* or *2MASS* nucleus. The minimum 2-10 keV luminosity of those objects displaying hard nuclear cores in the entire sample is 2×10^{38} ergs s^{-1} (NGC 2787; H01). Young supernova remnants, X-ray-binaries (XRBs), and/or hot diffuse gas from starburst-driven winds are known to emit X-rays, however these sources are weak and/or are usually spatially extended at the distances of our objects. For example, while intergalactic XRBs are known to reach luminosities of $\sim 10^{38}$ ergs s^{-1} (McClintock & Remillard 2003), typical XRBs have luminosities up to 10^{37} ergs s^{-1} (White, Nagase, & Parmar 1995). Several tens to over ten thousand XRBs, concentrated in a spatial extent of only a few tens of parsecs, would be required to produce the luminosities of the hard nuclear point sources, which is highly implausible. Moreover, the detection of a single hard nuclear point source coincident with the *VLA* or *2MASS* nucleus is highly suggestive of an AGN. Therefore, in this paper, we define AGN-LINERs as all LINERs displaying hard nuclear cores with luminosites L_X (2-10keV) $\geq 2 \times 10^{38}$ ergs s^{-1}.

4.3.3 *ISOPHOT-S* Observations

We searched the *ISOPHOT-S* archive for 6.2 μm emission feature observations of all galaxies presented in this work. Twenty one objects with previously unpublished 6.2 μm feature fluxes were found. The spectra for all but two galaxies were obtained by operating the PHT-S aperture in rectangular chopping mode - NGC 4102 and Mrk 79 were observed with PHT-S in triangular chopping mode. The 24" $\times$ 24" ISOPHOT aperture corresponds to the central 0.5 kpc for the nearest source to $\leq$ 60 kpc for the most distant sources presented here. In 87% of the sources with published or archival 6.2 μm PHT-S observations, the central 1 kpc nuclear region is contained within the ISOPHOT beam. Nuclear star formation in the vast majority of galaxies originates from the central few hundred parsecs (e.g. Surace & Sanders 1999; Scoville et al. 2000). Indeed the MIR continuum and PAH emission as well as the FIR flux is within the ISOPHOT beam for a large number of galaxies of comparable redshift range to our sample (e.g Lutz, Veilleux & Genzel, 1999, Lutz et al.,1998, Rigopoulou et al., 1999). Even for the nearest galaxies, imaging observations by Clavel et al. (2000) of 14 spatially extended nearby Seyferts demonstrate that, on average, 75% of the total 6.75μm continuum flux is contained within the ISOPHOT aperture.

4.4 Results

4.4.1 AGN Detection Rate and X-ray Luminosities of AGN-LINERs

In Chapter 3 we defined AGN-LINERs as those objects which display a hard nuclear point source, with a 2-10 keV luminosity $\geq 2 \times 10^{38}$ ergs s^{-1}, coincident with the *VLA* or *2MASS* nucleus. Of the 25 galaxies in the archival LINER sample, 13 meet this criterion. Combining these statistics with those from Papers I and II, we find

Table 4.5: *Chandra* Observation Log

Galaxy Name (1)	OID (2)	Exposure Time (3)	R. A. (4)	DEC. (5)	Coordinate Catalog (6)
AGN-LINERs					
NGC0315	4156	54127	00 57 48.887	+30 21 08.84	*2MASS*
NGC2681	2060	79579	08 53 32.751	+51 18 49.38	*VLA*
NGC3169	1614	1953	10 14 15.36	+03 27 57.40	*VLA*
NGC3245	2926	9633	10 27 18.389	+28 30 26.59	*VLA*
NGC3718	3993	4911	11 32 34.848	+53 04 4.56	*VLA*
NGC4410A	2982	34721	12 26 28.20	+09 01 10.80	*2MASS*
NGC4258	2340	693512	18 57.533	+47 18 14.06	*VLA*
NGC4261	834	31465	12 19 23.227	+05 49 29.89	*VLA*
NGC4457	3150	36433	12 28 59.022	+03 34 14.58	*VLA*
NGC4552	2072	53492	12 35 39.804	+12 33 22.91	*VLA*
NGC4565	3950	54495	12 36 20.772	+25 59 15.78	*VLA*
NGC6482	3218	18430	17 51 48.81	+23 04 19.0	*2MASS*
3C218	576	18364	09 18 05.675	-12 05 44.30	*VLA*
NONAGN-LINERs					
NGC2541	1635	1927	08 14 40.07	+49 03 41.2	*2MASS*
NGC2683	1636	1738	08 52 41.292	+33 25 18.74	*VLA*
NGC4150	1638	1738	12 10 33.3	+30 24 05.50	*VLA*
NGC4410B	2982	34721	12 26 29.59	+09 01 09.4	*2MASS*
NGC4438	2883	25073	12 27 45.567	+13 00 32.87	*VLA*
NGC4459	2927	9835	12 28 59.976	+13 58 43.47	*VLA*
NGC4501	2922	13823	12 31 59.175	+14 25 12.98	*VLA*
NGC4548	1620	2655	12 35 26.43	+14 29 46.8	*2MASS*
NGC4550	1621	1880	12 35 30.60	+12 13 15.3	*2MASS*
NGC4736	808	47366	12 50 53.064	+41 07 13.65	*VLA*
NGC5846	788	24091	15 06 29.294	+01 36 20.39	*VLA*
NGC5866	2879	23686	15 06 29.475	+55 45 47.60	*VLA*

Column Explanation: Col(1): Galaxy Common Name; Col(2): *Chandra* Observation Identification Number; Col(3): Exposure time in seconds; Col(4): Right Ascension of nucleus in hours, minutes, & seconds taken from the source in Column 6; Col(5): Declination of nucleus in degrees, minutes, & seconds, taken from the source in Column 6; Col(6): *VLA* Coordinates or *2MASS* coordinates used when extracting counts. *VLA* Coordinates come from the First Cataloge search, http://sundog.stsci.edu/cgi-bin/searchfirst. *2MASS* Coordinates came from NED.

that 50% (41/82) of LINERs have AGN nuclei. As in Papers I and II, we assume that young supernova remnants, X-ray binaries, or hot diffuse gas from starburst driven winds are unlikely to be the source of the detections we observe, since these sources of emission are usually weak and/or spatially extended. Moreover, detection of a single, dominant hard X-ray point source coincident with the *VLA* or *2MASS* nucleus is highly suggestive of an AGN.

We assume in this work that LINERs that do not display dominant hard nuclear X-ray point sources do not harbor AGNs ("*Non-AGN-LINERs*" listed in Tables 4.1, 4.5 & 4.6). These galaxies either display off-nuclear X-ray sources of comparable brightness to the nuclear source or no nuclear X-ray source. Galaxies that display multiple sources emit primarily in the soft X-rays and are most likely to be morphologically consistent with starburst galaxies, expected to contain a large population of young stars and/or X-ray binaries. Galaxies that lack a hard nuclear source either 1) lack an energetically significant AGN or 2) contain highly obscured AGN with column densities reaching $\sim 10^{24}$ cm^{-2}.

From Table 4.6, the 2-10 keV luminosities of the AGN-LINERs in our archival LINER sample range from $\sim 2 \times 10^{38}$ to $\sim 1 \times 10^{42}$ ergs s^{-1}, well within the span of luminosities of the comprehensive AGN-LINER sample ($\sim 2 \times 10^{38}$ to $\sim 2 \times 10^{44}$ ergs s^{-1}). As in Chapter 3, the majority of objects occupy the 10^{39} to 10^{41} ergs s^{-1} luminosity range.

The majority of the 2-10 keV X-ray luminosities listed in Table 4.6 were calculated assuming a generic power-law model with photon index $\Gamma = 1.8$ using the Galactic absorption given in Table 4.6. Fourteen of the twenty-five LINERs had counts sufficient for an XPEC spectral analysis, allowing us to gauge the accuracy of our generic power-law model. Combing these fits with the 3 spectral fits from Chapter

3, we find that the photon index for AGN-LINERs ranged from ~ 0.7 to 2.0 with an average of 1.6. This range in photon index is consistent with the values found in a larger sample of low luminosity AGNs (Terashima et al. 2002).

Two of the fourteen galaxies (NGC 4410A & 3C218 - both AGN-LINERs) were well fit by a single power-law model with absorption fixed at the Galactic value. For seven of the fourteen galaxies (2 Non-AGN-LINERs and 5 AGN-LINERs) one additional component (either an intrinsic absorption or a thermal component) was required before an acceptable χ^2_{red} was obtained. With respect to the thermal component, for all galaxies with low signal-to-noise (all except NGC 2681) the abundance was fixed at the Galactic value. In the case of NGC 2681 the abundance was first left free to vary, which resulted in a best fit value of 0.8. However, the spectral data for this galaxy were not good enough to estimate the errors on the abundance parameter when it was left free to vary. The abundance for NGC 2681 was therefore fixed at the best fit value. In these nine cases, the XSPEC luminosity was less than a factor of 4 different from the generic luminosities calculated using our generic power-law model. The X-ray spectra of the AGN-LINERs NGC 4258, NGC 0315, & NGC 4261, on the other hand, were well fit with more complex models that are described and shown below. In the case of NGC 0315 and NGC 4261, the XSPEC luminosity differed by factors of only 3 and 4 respectively from the generic calculation. However, in the case of NGC 4258, whose spectrum shows severe absorption in the soft band, the XSPEC-derived luminosity differs by a factor of nearly 15 from that derived using the generic power law model. In addition, though the luminosities derived through the XSPEC and generic models roughly agree in the case of NGC 4261, the flat power law component, Γ=0.71, differs greatly from the Γ=1.8 described by our generic model. These results lead us to conclude that our generic model is appropriate only in so far as the spectrum is simple, requiring few additional components. Lastly, NGC 5846 (a Non-AGN-LINER) and NGC 6482 (an AGN-LINER) were fit using a thermal component and absorption fixed at the Galactic value. In both cases, the spectra in the hard band (2-10 keV) were poorly constrained and characterized by large errors. The fits for NGC 5846 and NGC 6482 are representative of the 0.3-2.0 keV band *only* and say nothing about the hard band (2-10 keV) luminosity associated with the power-law component and thus the accuracy of the luminosity derived from the generic power-law model. We therefore choose to adopt the luminosities derived from the generic power-law model for these two galaxies until better spectral data for the two galaxies can be obtained. The specific parameters and models for these fourteen galaxies are given in Table 4.7.

4.4.2 Spectral Fits for Individual Objects

NGC 4258: This galaxy's spectrum was initially fit with a single power-law model with $\Gamma = 1.4^{+0.5}_{-0.3}$ and absorption column density fixed at the Galactic value. The resulting poor fit (${\chi^2}_{\rm red} = 2.1$, 70 d.o.f.) in addition to the clear absence of soft counts indicated the need for an additional absorption component. The resulting intrinsic absorption for the best fit model was $N_{\rm H} = (6.6\ ^{+2.1}_{-1.3}) \times 10^{22}$ cm^{-2}. The model was further improved with the addition of a thermal component (kT = $0.83^{+0.4}_{-0.7}$ keV, $Z/Z_{\odot} = 1.0$), which is significant at greater than the 99% confidence level. This model yielded an acceptable fit (${\chi^2}_{\rm red} = 0.50$ (67 d.o.f.)). The spectrum for this galaxy is shown in Figure 4.2a.

NGC 4261: The spectrum for this galaxy was initially fit with a single power law model with $\Gamma = 0.7^{+0.8}_{-0.7}$ and absorption column density fixed at the Galactic value. The resulting poor fit (${\chi^2}_{\rm red} = 7.1$, 71 d.o.f.) in addition to the clear absence of soft energies, as well as a large deficit in the 1.4 to 4 keV energy range indicated the need for two additional components. As per Gliozzi et al. 2003, the model was improved with the addition of a thermal component (kT $= 0.61^{+0.03}_{-0.02}$ keV, $Z/Z_{\odot}$ =1.0) as well as a partial covering fraction ($N_{\rm H}$ = (5.3 $^{+3.7}_{-2.8}$) $\times$ 10^{22} cm^{-2}, Covering Fraction = $85^{+0.2}_{-0.6}$%), both of which are significant at the 99% confidence level. This final model yielded an acceptable fit (${\chi^2}_{\rm red}$ = 0.69 (67 d.o.f.)). The spectrum for this galaxy is shown in Figure 4.2b.

NGC 0315: This galaxy's spectrum was initially fit with a single power law model with $\Gamma = 1.6^{+0.1}_{-0.2}$ and absorption column density fixed at the Galactic value. The resulting poor fit (${\chi^2}_{\rm red}$ = 1.5, 166 d.o.f.) in addition to the clear absence of soft energies indicated the need for an additional absorption component. The resulting intrinsic absorption for the best fit model was $N_{\rm H}$ = (8.0 $^{+1.0}_{-2.0}$) $\times$ 10^{21} cm^{-2}. The model was further improved with the addition of a thermal component (kT $= 0.54^{+0.3}_{-0.5}$ keV, $Z/Z_{\odot}$ = 1.0), which is significant at greater than 99% confidence level. This model yielded an acceptable fit (${\chi^2}_{\rm red}$ = 0.58, 162 d.o.f.). The spectrum and model for this galaxy is shown in Figure 4.2c.

Our spectral analysis suggests that for the vast majority of AGN-LINERs in the comprehensive AGN-LINER sample, our generic power-law model is likely to yield reasonable 2-10 keV luminosities. In those targets with accurate spectral fits (excluding NGC 5846 and NGC 6482), we have adopted the XSPEC-derived luminosities in all of our calculations and plots.

4.4.3 Correlation between Eddington Ratio and FIR Luminosity and IR Brightness in AGN-LINERs

In Figures 4.3a and 4.3b we plot $L_{\rm bol}/L_{\rm Edd}$ versus $L_{\rm FIR}$, $L_{\rm FIR}/L_{\rm B}$ for the 34 out of 41 AGN-LINERs in our comprehensive LINER sample that have black hole estimates.

Table 4.6: Results of the Archival LINER Sample

Galaxy Name (1)	$N_{\rm H}$ cm^{-2} (2)	Hard Counts (3)	Count Rate (4)	Hardness Ratio (5)	log ($L_{X-\rm Generic}$) (6)	log ($L_{X-\rm Xspec}$) (7)	log $L_{\rm bol}/L_{\rm Edd}$ (8)
AGN-LINERs							
NGC0315	5.87	1862	0.084±0.001	-0.18	41.22	41.67	-4.02
NGC2681	2.42	103	0.012±0.001	-0.78	38.92	38.74	-5.89
NGC3169	2.66	150	0.080±0.007	0.92	40.09	...	-4.49
NGC3245	2.13	17	0.007±0.001	-0.53	39.16	...	-5.98
NGC3718	1.08	609	0.227±0.007	0.09	40.44	40.06	-3.65
NGC4258	1.51	1541	0.239±0.006	0.86	39.62	40.80	-3.04
NGC4261	1.52	545	0.069±0.002	-0.50	40.51	41.15	-4.41
NGC4410A	1.71	251	0.036±0.001	-0.60	41.14	41.24	-4.06
NGC4457	1.80	61	0.013±0.001	-0.74	39.22	39.22	-4.64
NGC4552	2.57	219	0.032±0.001	-0.74	39.55	39.62	-6.70
NGC4565	1.32	543	0.035±0.001	-0.43	39.09	39.34	-4.29
NGC6482[a]	7.67	17	0.022±0.001	-0.92	40.47	...	-5.02
3C218	4.93	202	0.033±0.001	-0.34	41.82	42.15	-3.30
NONAGN-LINERs							
NGC2541	4.60	<1	<0.001	...	<37.60	...	...
NGC2683	3.10	14	0.009±0.002	0.87	38.06	...	...
NGC4150	1.63	<1	<0.001	...	<37.16	...	...
NGC4410B	1.71	1	<0.001	-0.80	38.51	...	...
NGC4438	2.64	53	0.028±0.001	-0.85	39.50	37.54	...
NGC4459	2.72	9	0.006±0.001	-0.70	38.84	...	...
NGC4501	2.47	30	0.006±0.001	-0.33	38.90	...	...
NGC4548	2.35	17	0.010±0.002	0.26	39.05	...	...
NGC4550	2.60	<2	<0.001	...	<37.68	...	...
NGC4736	1.43	446	0.068±0.001	-0.72	38.68	38.72	...
NGC5846[a]	4.27	7	0.008±0.001	-0.92	39.44	...	...
NGC5866	1.47	22	<0.001	0.34	37.69	...	...

Notes: *a* Luminosities derived from the generic power-law model rather than the Xspec model are adopted for these two galaxies in all of our plots and calculations. See Section 4.4.1 for details. **Columns Explanation:** Col(1):Common Source Names; Col(2): Galactic $N_{\rm H}$(in units of$\times$ 10^{20} cm^{-2}); Col(3): Hard counts in the nucleus (2-8 keV) from an extraction region of radius 2" centered on the radio or *2MASS* nucleus; Col(4): Countrate (counts/sec) in the 0.3-10 keV band; Col(5): Hardness Ratio: Defined here as (H-S)/(H+S), where H represents the hard counts (2-8 keV) and S represents the soft counts (0.3-2 keV) in the nucleus; Col(6): Log of the X-ray luminosity (2-10keV) in ergs s^{-1} calculated using our generic model; Col(7): Log of the X-ray luminosity (2-10keV) in ergs s^{-1} calculated using the Xspec model; Col(8): Log of the Eddington ratio.

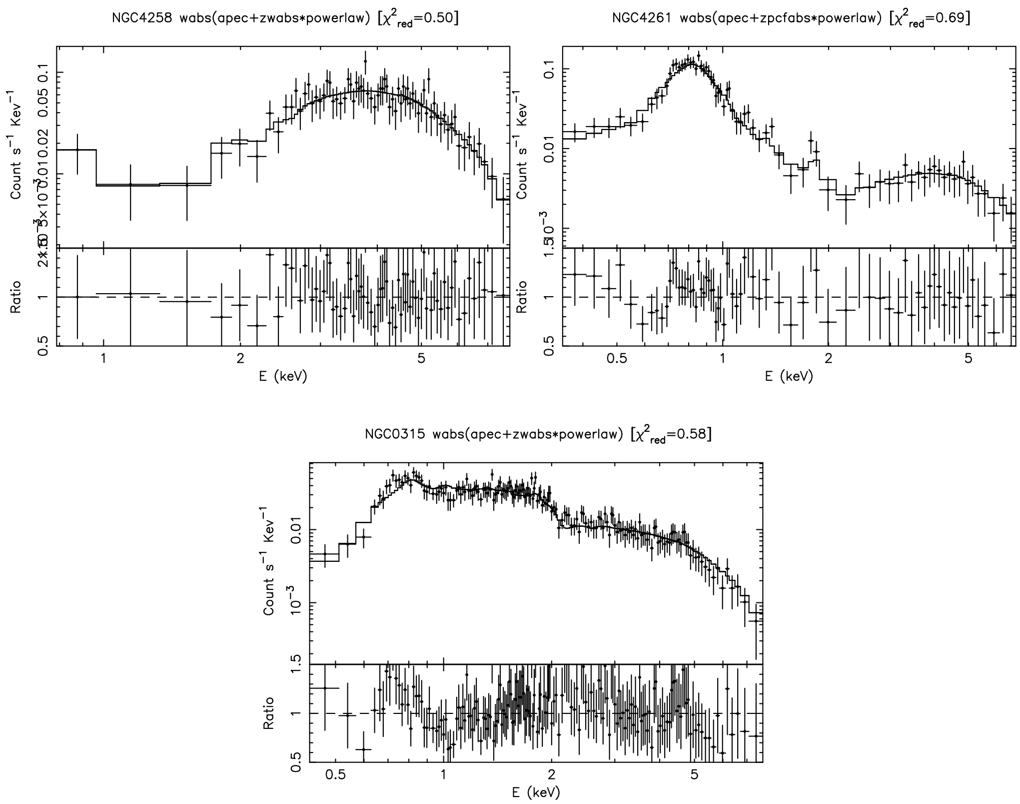

Figure 4.2: X-ray spectral fits for selected LINERs

4.2a: Best fit model for Non-AGN-LINER, NGC 4261, 4.2b: Best fit model for AGN-LINER, NGC 4258, 4.2c:Best fit model for AGN-LINER, NGC 0315.

Table 4.7: Results of Spectral Analysis

Galaxy Name (1)	Model[b] (2)	kT (3)	N_H^{Add} (4)	Γ (5)	χ^2_{red}/d.o.f. (6)
NGC0315[a]	IV	$0.54^{+0.03}_{-0.05}$	$0.8^{+0.1}_{-0.2}$	$1.60^{+0.14}_{-0.24}$	0.58/162
NGC2681[a]	III	0.73 ± 0.06	...	$1.57^{+0.47}_{-0.57}$	0.47/29
NGC3718[a]	II	...	$0.8^{+0.4}_{-0.3}$	$1.48^{+0.42}_{-0.35}$	0.43/45
NGC4258[a]	IV	$0.83^{+0.37}_{-0.73}$	$6.6^{+2.1}_{-1.3}$	$1.44^{+0.52}_{-0.34}$	0.50/67
NGC4261[a,c]	VI	$0.61^{+0.03}_{-0.02}$	$5.3^{+3.7}_{-2.8}$	$0.71^{+0.80}_{-0.71}$	0.69/67
NGC4410A[a]	I	...	...	1.73 ± 0.14	0.36/51
NGC4438	III	0.77 ± 0.06	...	$1.19^{+0.67}_{-0.48}$	0.93/22
NGC4457[a]	III	0.69 ± 0.13	...	$1.57^{+0.70}_{-0.57}$	0.38/15
NGC4552[a]	III	$0.75^{+0.06}_{-0.08}$	...	$1.62^{+0.16}_{-0.14}$	0.64/59
NGC4565[a]	II	...	0.2 ± 0.06	$1.92^{+0.23}_{-0.21}$	0.66/71
NGC4736	III	$0.67^{+0.07}_{-0.06}$	...	$1.60^{+0.09}_{-0.08}$	0.48/46
NGC5846	V	$0.65^{+0.17}_{-0.14}$	...	...	0.46/13
NGC6482[a]	V	0.80 ± 0.06	...	...	0.57/15
3C218[a]	I	...	...	$1.17^{+0.24}_{-0.23}$	0.31/26

Notes: *a*: indicates AGN-LINERs, *b*: I=wabs(powerlaw), II=wabs(zwabs(powerlaw)), III=wabs(apec+powerlaw), IV=wabs(apec+zwabs(powerlaw)), V=wabs(apec), VI=wabs(apec+zpcfabs(powerlaw)), *c* The fit for NGC 4261 also required a partial covering fraction of $0.85^{+0.15}_{-0.62}$%. **Columns Explanation:** Col.(1): Common Source Names, ; Col.(2): Spectral model (see note); Col.(3): Plasma temperature in keV; Col.(4): Absorption column density at the redshift of the source in units of 10^{22}cm^{-2}; Col(5): Photon index; Col(6): reduced χ^2 and degrees of freedom.

As can be seen, the original correlations are reinforced by our expanded AGN-LINER sample, extending over seven orders of magnitude in L_{bol}/L_{Edd}. Employing a Spearman rank correlation analysis (Kendall & Stuart 1976) to assess the statistical significance of our correlation yields a correlation coefficient of $r_S = 0.50$ between L_{bol}/L_{Edd} and L_{FIR}/L_B with a probability of chance correlation of 2.9×10^{-3}, indicating a significant correlation. In the case of L_{bol}/L_{Edd} and L_{FIR}, the Spearman rank test gives a correlation coefficient of $r_S = 0.62$ with a probability of chance correlation of 7.8×10^{-5}, again indicating a significant correlation. The Spearman rank correlation technique has the advantage of being non-parametric, robust to outliers and does not presuppose a linear relation.

The correlations presented in Figures 4.3a and 4.3b appear to be primary and are unlikely to be induced by either distance effects or correlations between any individually observed quantities used to calculate the Eddington ratio. The 2-10 keV X-ray and FIR fluxes for the entire sample of AGN-LINERs show no correlation

(r_S = 0.03), suggesting that the correlations shown in Figures 4.3a and 4.3b are fundamental. We also conducted a Spearman partial correlation analysis on our datasets to check whether spurious correlations may have been produced by distance effects. The partial correlation describes the relationship between two variables when the third variable is held constant. The partial Spearman rank correlation coefficient between L_{bol}/L_{Edd} and L_{FIR}, L_{FIR}/L_B holding the distance fixed was higher in both cases (P_S = 0.69 and P_S= 0.64, respectively), suggesting that the Eddington ratio and FIR luminosity and IR-brightness ratio in AGN-LINERs are indeed physically correlated quantities.

A formal fit to the plots in Figures 4.3a and 4.3b yields the following relationships:

$$\log(L_{\mathrm{bol}}/L_{\mathrm{Edd}}) = (1.15 \pm 0.19)\log(L_{\mathrm{FIR}}) + (-14.92 \pm 1.75) \tag{4.1}$$

$$\log(L_{\mathrm{bol}}/L_{\mathrm{Edd}}) = (1.13 \pm 0.22)\log(L_{\mathrm{FIR}}/L_B) + (-4.13 \pm 0.19) \tag{4.2}$$

The dispersion in the plots displayed in Figures 4.3a and 4.3b is significant (rms scatter of 0.99 and 1.06 dex in L_{bol}/L_{Edd} for Figures 4.3a and 4.3b, respectively). In Chapter 3, we pointed out the difficulty in assessing how much of the scatter is intrinsic or due to the uncertainties in the derived quantities. The uncertainty in the X-ray luminosity derived from our power-law model, the uncertainty in the bolometric correction factor for the LINER class, the uncertainty and uniform applicability of the M_{BH} vs. σ relationship for this sample of LINERs, and the non-simultaneity of the observations will all introduce some scatter. If we assume that the uncertainty in the black hole mass estimate is 0.3 dex (Tremaine et al. 2002) and that there is no X-ray, optical, or FIR variability in this sample of LINERs, then the uncertainty in L_{bol} would need to be a factor of ~ 5 if the scatter is entirely due to the uncertainties in the derived quantities plotted in Figures 4.3a and 4.3b. The bolometric luminosity

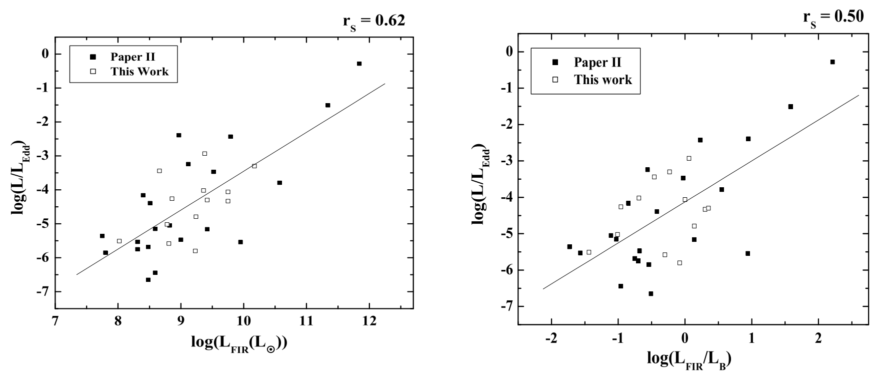

Figure 4.3: Correlations between host galaxy and black hole properties for AGN-LINERs

Correlation between L_{bol}/L_{Edd} verses L_{FIR} (a) L_{FIR}/L_B (b) for the entire set of 34/41 AGN-LINERs that have black hole estimates in our comprehensive LINER sample. There is a significant correlation in each plot that extends over seven orders of magnitude in L/L_{Edd}. The Spearman rank correlation coefficients are given in the upper right corner of each plot.

in our sample of LINERs, estimated using the X-ray luminosity (see Section 4.2), is certainly uncertain within this factor, if not more. The bolometric correction factor used in this work relies on the average SED of only 7 low luminosity AGNs presented by Ho (1999) since more extensive studies of the SEDs of LINERs are nonexistent. Indeed, the correction factor for these 7 objects varies by a factor of 6 ($L_{bol} = 11 \times L_X$(2-10 keV) to $L_{bol} = 69 \times L_X$(2-10 keV)). In addition, there is some uncertainty in adopting a generic power-law model to calculate the X-ray luminosity. As described in section 4.1, detailed spectral fits of the X-ray spectrum of a few of the targets in the archival LINER sample show that the derived luminosities can deviate substantially from the generic power law-derived luminosities. Given these uncertainties, it is entirely plausible that the scatter in Figures 4.3a and 4.3b is not intrinsic and can be completely attributable to the uncertainties in the derived quantities.

4.4.4 Correlation between Eddington Ratio and FIR Luminosity in other AGN Subclasses

In Figure 4.4 we plot L_{bol}/L_{Edd} versus L_{FIR} for the entire expanded AGN sample included in this paper. We highlight all targets with redshift $z > 0.1$ as open symbols in the plot since distance effects may spuriously reinforce the correlation. Interestingly, the original correlation is in general reinforced by our expanded AGN sample, extending in this case over almost nine orders of magnitude in L_{bol}/L_{Edd}. For the various AGN subclasses, the origin of the optical luminosity is likely to vary tremendously. For example, massive ellipticals are often the hosts of many radio-loud AGNs and LINERs. In these cases, a significant fraction of the blue luminosity is likely to originate from the host galaxy. On the other hand, in RQQ for example, the bulk of the optical luminosity is likely to originate from an optically thick accretion disk. We therefore choose to plot the FIR luminosity only in our investigation of possible correlations.

Employing a Spearman rank correlation analysis to the entire 129 galaxies plotted in Figure 4.4 yields a correlation coefficient of $r_S = 0.65$ between L_{bol}/L_{Edd} and L_{FIR} with a probability of chance correlation of 6.9×10^{-17}, indicating a significant correlation. The best-fit linear relationship to the entire dataset is:

$$\log(L_{\rm bol}/L_{\rm Edd}) = (1.22 \pm 0.14) \log(L_{\rm FIR}) + (-14.14 \pm 1.38) \tag{4.3}$$

Apart from the overall correlation, there are correlations between the quantities plotted in Figure 4.4 for each AGN subclass. We list the Spearman rank correlation coefficients between L_{bol}/L_{Edd} and L_{FIR} for each AGN subclass in Table 4.8. Figure 4.4 shows that the different AGN subclasses occupy distinct regions in the L_{bol}/L_{Edd} and L_{FIR} plane. Most notably, the Seyferts, RQQs, and NLS1s in general display a shallower slope and larger intercept than do the LINERs and radio-loud AGNs. For example, the best-fit linear relationship to the entire Seyfert dataset is:

$$\log(L_{\mathrm{bol}}/L_{\mathrm{Edd}}) = (0.66 \pm 0.11)\log(L_{\mathrm{FIR}}) + (-7.81 \pm 1.09) \tag{4.4}$$

which is significantly different from the best-fit linear relationship for the LINER dataset (Equation 1). In addition, the scatter in the Seyfert dataset displayed in Figure 4.4 is significantly less than that in the LINER dataset (0.5 dex in $L_{\mathrm{bol}}/L_{\mathrm{Edd}}$ compared with 1.09 dex in the Seyfert and LINER datasets, respectively). This may be the result of the fact that the bolometric luminosity, obtained by direct flux integration of a well-sampled SED, is much more reliable in the Seyferts compared with the LINERs.

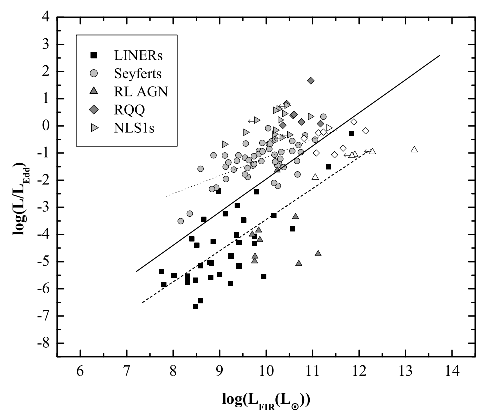

Figure 4.4: Correlations between L/L_{Edd} and L_{FIR} for all AGNs

Correlation between $L_{\mathrm{bol}}/L_{\mathrm{Edd}}$ verses L_{FIR} for the entire set of AGNs presented in this work. This includes the 34/41 AGN-LINERs that have black hole estimates. This plot shows a significant correlation that extends over almost nine orders of magnitude in L/L_{Edd}. The best-fit linear relationship to the entire dataset is displayed by the solid line. The dashed and dotted lines correspond to the best-fit line applied only to the LINER, and Seyfert datasets, respectively. The Spearman rank correlation coefficients for the different datasets are give in Table 4.8.

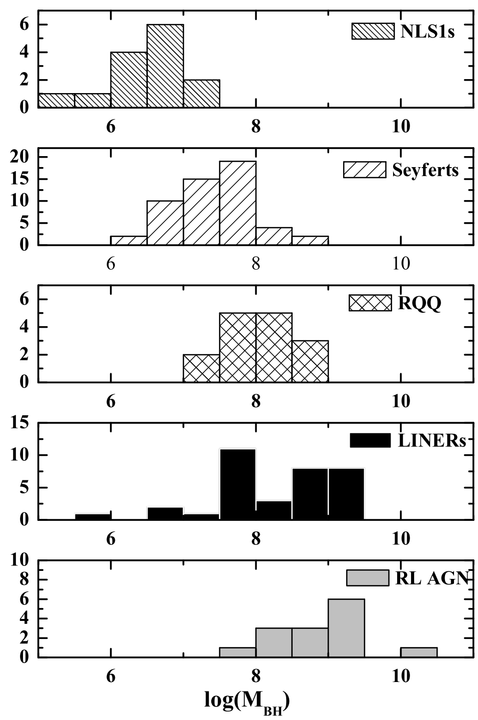

Figure 4.5: Black hole masses

Black hole masses for the entire set of AGNs presented in this work.

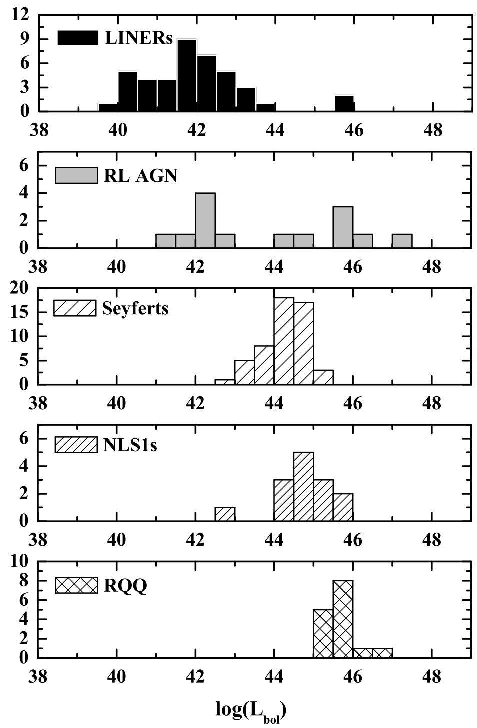

Figure 4.6: Bolometric luminosities

Bolemetric luminosities for the entire set of AGNs presented in this work.

If the different AGN subclasses occupy distinct regions of the plot in Figure 4.4, this may be an important result. This means that for a given L_{FIR}, Seyferts, RQQ, and NLS1s tend to show higher values of L_{bol}/L_{Edd} than LINERs. A spurious result may be obtained if L_{bol} is systematically underestimated in the LINERs or if L_{Edd} i.e., M_{BH} - is systematically overestimated relative to the Seyferts, RQQ, and NLS1s. Figures 4.5 & 4.6 show the distributions of black hole masses and bolometric luminosities for each AGN subclass. The plot clearly shows that each AGN subtype shows different distributions of black hole masses and bolometric luminosities. Radio-loud AGNs and LINERs tend to have more massive black holes than Seyferts and NLS1s have the least massive black holes. A formal Kolmogorov-Smirnov (K-S) test between the black hole masses of Seyferts and LINERs, for example, demonstrates that the two distributions are significantly different, with a probability of being drawn from the same population of less than 0.00046%. This result is unlikely to be spurious. NLS1s most likely contain lower mass black holes than standard Seyferts which is why they display narrow lines (e.g. Peterson et al. 2000; Wandel & Boller (1998)). Likewise, the hosts of radio-loud AGNs and LINERs are often massive ellipticals, which are typically more massive than spirals - the hosts of most standard Seyferts (e.g. Ho, Filippenko, & Sargent 2003). Figure 4.7 shows that the bolometric luminosities of the LINERs are lower than that of the other AGN subclasses. A formal K-S test between the bolometric luminosities of Seyferts and LINERs, for example, demonstrates that the two distributions are significantly different, with a probability of being drawn from the same population of less than 3%. Again, this result is unlikely to be spurious. Most of the LINERs in our sample are low luminosity AGNs, which do contain less luminous nuclei than standard Seyferts (e.g. Koratkar et al. 1995, Terashima et al. 2003), radio galaxies, and certainly quasars. We thus conclude that there is a real separation between the different AGN subclasses in the L_{bol}/L_{Edd} and L_{FIR} plane.

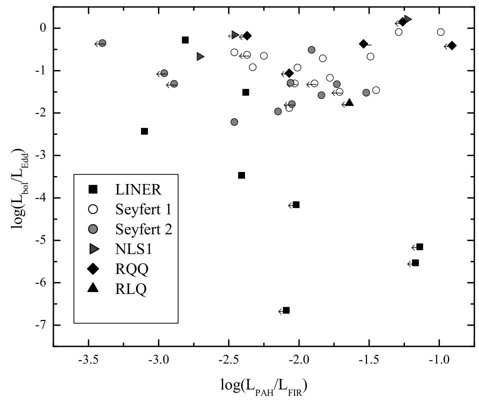

Figure 4.7: 6.2 μm PAH test

Plot of the ratio the bolometric luminosity to the Eddington luminosity as a function of the ratio of the 6.2μm PAH luminosity and L_{FIR} for all of the galaxies in our expanded AGN sample with 6.2μm data. No correlation is found between these two quantities, implying that the contribution from the AGN to L_{FIR} is indeed minimal.

4.4.5 *ISOPHOT-S* PAH Feature Luminosities and $L_{\rm PAH}$ /$L_{\rm FIR}$ Ratios

In Table 4.9, we list the 6.2 μm emission feature fluxes and upper limits for all objects in the expanded AGN sample with archival or previously published *ISO* observations. Of the 21 observations we reduced in this work, we report only 4 firm detections. Combined with published fluxes, there are a total of 28 firm detections of the 6.2 μm emission feature in our expanded AGN sample.

The FIR luminosity used to construct Figures 4.3 and 4.4 can include or be entirely from thermally reprocessed radiation from the AGN. In this case, the FIR luminosity will increase with AGN power as measured by the Eddington ratio. Such an increase can induce the correlation between $L_{\rm bol}/L_{\rm Edd}$ and L_{FIR} displayed in Figures 4.3 and 4.4, invalidating any implied association between the SFR and the mass accretion rate. Since the PAH feature flux is found to be directly proportional to the FIR

Table 4.8: Spearman Rank Coefficients

AGN type (1)	r_S (2)	P_S (3)
ALL	0.65	6.9×10^{-17}
LINERs	0.62	7.8×10^{-5}
Seyferts	0.49	2.0×10^{-4}
RQQ	0.19	0.50
RL AGN	0.70	5.2×10^{-3}
NLS1s	0.31	0.27

Columns Explanation: Col(1):AGN subclass; Col(2): Spearman rank correlation coefficient between L_{bol}/L_{Edd} and L_{FIR} for each AGN subtype; Col(3): Probability that the correlation would occur by chance.

flux in normal and starburst galaxies but is absent or weak in galaxies dominated by AGNs (e.g., Genzel et al. 1998, Rigopoulou et al. 1999, Clavel et al. 2000), we can use our 6.2 μm emission feature fluxes to investigate whether the fraction of L_{FIR} increases with L_{bol}/L_{Edd} in our expanded AGN sample. Figure 4.7 shows the relationship between L_{PAH} /L_{FIR} and L/L_{Edd}. If the fraction of the FIR luminosity increases with Eddington ratio, then we should see a decrease in L_{PAH} /L_{FIR} with L_{bol}/L_{Edd}. Although the data are limited, Figure 4.7 reveals no correlation, strongly suggesting that the correlation between L_{bol}/L_{Edd} and L_{FIR} for this sample of AGNs is NOT an artifact of an increasing contribution to the FIR emission from dust heated by an AGN with Eddington ratio.

4.5 Discussion

4.5.1 L_{FIR} as a SFR Indicator

Since the FIR luminosity is widely used as a direct measure of the SFR in galaxies (Kennicutt 1998; Lehnert & Heckman 1996; Meurer et al. 1997; Kewley et al. 2002), the correlations presented in D05 and expanded upon in Figures 4.3 and 4.4 hint at the possibility of a fundamental link between accretion onto the black hole and the

SFR in the host galaxy. The reliability of using L_{FIR} to estimate the SFR rests on the assumption that dust heating is dominated primarily by the radiation field from young stars and that the dust surrounding these stars absorbs all of the optical/ultraviolet (OUV) radiation and reemits it in the FIR. While this may be a good assumption in optically thick intensely star forming galaxies, it may not hold for all galaxies in our sample. In converting the FIR luminosity to a SFR in our expanded AGN sample of galaxies, the following questions need to be addressed: 1) What fraction of L_{FIR} arises from dust at large distances from and heated primarily by the AGN? 2) What is the contribution from old stars to L_{FIR}? 3) How much of the bolometric luminosity from young stars is emitted in the FIR?

What fraction of the FIR luminosity in AGNs arises from dust at large distances from and heated primarily by the AGNs

There is general agreement that the AGN radiation field, which heats the dust to higher temperatures than does the starburst, is responsible for the near-IR and MIR emission in AGNs (e.g., Wilkes et al. 1999; van Bemmel & Dullemond 2003; Farrah et al. 2003). The FIR emission, however, can in principle arise from starburst-heated dust as well as cooler dust heated by and located farther from the AGN. For nearby quasars, several studies claim that the entire near-IR, MIR, and FIR SED can be explained purely by AGN heating (e.g. Sanders et al. 1989, Kuraszkiewicz et al. 2003, Siebenmorgen et al. 2004). However, these studies do not rule out the possibility that starbursts provide the dominant heating source in powering the FIR. Indeed, detailed modeling of the SEDs of hyperluminous AGNs ($L_{\rm FIR} > 10^{13} L_\odot$) suggest that star formation provides the dominant heating source behind their FIR emission (Rowan Robinson 2000), and the lack of correlation between the MIR and FIR of several well-studied PG quasars strongly suggests that the two wavelength regimes are dominated by different heating sources (Haas et al. 1999). In addition, if AGN heating dominates the cooler FIR-emitting dust, then there should be a correlation between quasar OUV and FIR luminosity which is not seen (e.g., McMahon et al. 1999; Isaak et al. 2002; Priddey et al. 2003). In Seyfert galaxies, the spatially extended distribution of the FIR emission as well as the similarity between their IR SEDs with starbursts suggests that the AGN is not responsible for the bulk of their FIR emission (Espinosa et al. 1987). The IR properties of LINERs are currently not well-studied but since their central AGNs are generally weak, it is unlikely that they provide the dominant heating source behind their FIR emission. Furthermore the lack of correlation between the 2-10 keV X-ray and FIR fluxes for the AGN-LINERs plotted in Figures 4.3a and 4.3b (section 4.2) strongly suggests that FIR is not related to the AGNs in our sample of LINERs. In addition, the relationship between L_{PAH} $/L_{FIR}$ and L_{bol}/L_{Edd} discussed in Section 4.4 argues against AGN heating being the primary mechanism behind the FIR for the galaxies plotted in Figure 4.7. If L_{FIR} is dominated by AGN heating, then L_{PAH} $/L_{FIR}$ should decrease with AGN power, as measured by the Eddington ratio. Although the data are limited, this may be the most definitive discriminator between the relative contributions of starbursts and AGNs to the FIR emission in AGNs. We make the explicit assumption in this work that AGN heating of the dust is not responsible for the bulk of the FIR emission for all galaxies in our expanded AGN sample and explore the consequences. More extensive studies of the PAH feature in AGNs with Spitzer can help confirm this assumption.

What is the contribution from old stars to L_{FIR} and is the dust opacity high in our sample?

A significant fraction of the galaxies in our expanded AGN sample are bulge-dominated. Some studies indicate that in early-type galaxies, the general stellar radiation field may make a significant contribution to the dust heating and that the dust opacity may be small (e.g., Sauvage & Thuan 1994; Mazzei & de Zotti 1994). Contrary to these findings, a detailed comparison of the Hα and FIR emission in a large sample of normal galaxies suggests that the FIR emission *can* be associated primarily with star formation and that the widely adopted SFR- L_{FIR} calibration ratio usually applied to starbursts from Kennicutt (1998) can be applied in all Hubble types, including early-type spirals (Kewley et al. 2002). The ambiguity in the contribution to the dust heating by old stars affects the calibration of the SFR in terms of L_{FIR}. Since our expanded AGN sample was inhomogenously constructed and spans a large range in luminosity and Hubble types, it may not be appropriate to apply the Kennicutt (1998) SFR- L_{FIR} calibration derived for starbursts for all objects in the sample. Instead, we chose to adopt the calibration ratio from the recent work by Bell (2003). Using a large and diverse sample of normal and starburst galaxies and multiple SFR indicators, they find that the old underlying stellar population's contribution to L_{FIR} increases as the galaxy's luminosity decreases. Using their calibration ratio, the host galaxy's SFR can be calculated:

$$\mathrm{SFR_{FIR}}(M_\odot \mathrm{yr}^{-1}) \frac{1.75 f L_{\mathrm{FIR}}}{6.38 \times 10^9 \mathrm{L}_\odot} = \frac{f L_{\mathrm{FIR}}}{3.63 \times 10^9 \mathrm{L}_\odot}, \tag{4.5}$$

where

$$f = \begin{cases} 1 + \sqrt{5.71 \times 10^8\,\mathrm{L}_\odot / L_{\mathrm{FIR}}} & L_{\mathrm{FIR}} > L_c \\ 0.75(1 + \sqrt{5.71 \times 10^8 \mathrm{L}_\odot / L_{\mathrm{FIR}}}) & L_{\mathrm{FIR}} \leq L_c, \end{cases} \tag{4.6}$$

and $L_c = 5.71 \times 10^{10} L_\odot$. $L_{\rm FIR}$ is the luminosity corresponding to the FIR flux as defined above, and the factor of 1.75 in Equation 6 converts this to a luminosity representative of the full ($8 - 1000\,\mu$m) mid- to far-infrared spectrum (for details see Bell 2003).

The resulting SFR agrees to within a factor of 2 of the SFR derived using the Kennicutt (1998) calibration for all galaxies in our expanded AGN sample with the exception of only two LINERs with elliptical hosts, where slightly more discrepant factors are seen (~ 3 and 6). Bell points out that agreement with the Kennicutt (1998) value arises because of the competing effects of the contribution of old stars, which reduces the derived SFR, and the reduction in dust opacity with decreasing luminosity, which increases the derived SFR. In calculating SFRs, we stress that we have made the explicit assumption in this work that AGN heating plays an insignificant role in the FIR emission in our expanded AGN sample.

4.5.2 The SFR-Accretion Rate Connection

The discovery of the correlation between black hole mass and stellar velocity dispersion (Gebhardt et al. 2000, Ferrarese & Merritt 2000) has spawned numerous speculations on the connection between the growth of black holes and the formation of galactic bulges. A number of theoretical models have attempted to explain the relationship, invoking radiative or mechanical feedback from the black hole on the gas supply in the bulge (e.g., Silk & Rees 1998; Haehnelt, Natarajan, & Rees 1998; Blandford 1999; King 2003; Wyithe & Loeb 2003), merger-driven starbursts with black hole accretion (e.g. Haehnelt & Kauffman 2000), and stellar captures by the accretion disk feeding the hole (e.g., Zhao, Haehnelt & Rees 2002). However, the case remains ambiguous which one is correct or, for that matter, whether there really is a causal connection between the birth and growth of black holes and the formation and evolution of galaxies. Most previous studies have focused on expanding the number of black hole and bulge mass estimates in the various AGN subclasses in an attempt to reconstruct the accretion and star formation history in galaxies during various phases of accretion activity. If black holes grow primarily when they are accreting–i.e., when they are AGNs, a complementary and more direct constraint to theoretical models is to determine the relationship between the mass accretion rate and the spheroidal star formation rate in the various manifestations of nuclear activity in galaxies. If there is a constant ratio between the accretion rate and the star formation rate (SFR) associated with the bulge, with a proportionality constant independent of time, galaxy type, merger status, and accretion activity, this can have a tremendous impact on our understanding of galaxy formation and evolution.

Using the SFR calibration ratio described above, together with an assumption of the radiative efficiency of accretion, we can convert Figure 4.4 to a plot of SFR vs. mass accretion rate, $\dot{M}$ in our sample of galaxies. Making the first order assumption that all AGNs in our sample have a radiative efficiency η =0.1, the standard factor used for a geometrically thin, optically thick accretion disk (Shukura & Sunyaev 1973, Narayan & Yi 1995), we plot in Figure 4.8 the SFR vs. $\dot{M}$ for our expanded AGN sample. A linear fit yields the following relationships for the AGN-LINER class:

$$\log \mathrm{SFR} = (0.45 \pm 0.06) \log \dot{M} + (1.46 \pm 0.25), \tag{4.7}$$

where SFR and $\dot{M}$ are both in units of $\mathrm{M_\odot yr^{-1}}$.

From Figure 4.8, there is a clear distinction in slope and intercept between the various AGN subclasses. The regression line for the Seyfert class is:

$$\log \mathrm{SFR} = (0.89 \pm 0.07) \log \dot{M} + (1.68 \pm 0.12), \tag{4.8}$$

Table 4.9: Properties of the *ISO* sample

Galaxy Name (1)	Distance (Mpc) (2)	Optical Class (3)	Hubble Type (4)	log L_{FIR} (5)	$F_{PAH-6.2}$ $\times 10^{-15}$ (6)
NGC3031	4	LINER/S1.5	SA(s)ab	8.4	<6.03
NGC5194	8	S2/LINER	SA(s)bc;pec	9.8	2.20 ± 0.18
NGC4486	17	L2	E+0-1;pec	8.3	<1.71
NGC4579	17	L1.9	SAB(rs)b	9.5	1.47 ± 0.16
NGC4374	18	L2	E1	8.5	<1.50
IC 1459	23	LINER	E3	8.6	<1.78
NGC6240	98	LINER	I0:;pec	11.3	4.52
MRK273	151	LINER	Ring galaxy	11.8	2.14^a
NGC4151	9	Sy1.5	SAB(rs)bc	9.1	<5.91
NGC3227	16	Sy1	SAB(s)pec	9.6	4.31 ± 0.24^b
NGC3982	16	Sy1	SAB(r)b	9.6	2.55 ± 0.25^b
NGC1566	20	Sy1	SAB(rs)bc	10.1	3.70 ± 0.49^b
NGC3516	36	Sy1	SB(s)0:	9.5	1.44 ± 0.24^b
NGC4593	36	Sy1	SB(rs)b	9.8	0.82 ± 0.16^b
NGC3783	39	Sy1.5	(R')SB(r)a	9.9	<0.71
IC 4329A	65	Sy1.2	SA0+: sp	10.0	8.87 ± 0.26^b
NGC 7469	66	Sy1.2	(R')SAB(rs)a	10.0	4.45 ± 0.40
NGC5548	68	Sy1	SA(s)0/a	9.9	$<0.51^b$
Mrk 79	89	Sy1.2	SBb	9.9	<0.71
Mrk 590	106	Sy1.2	SA(s)a:	10.1	1.11 ± 0.12^b
Mrk 817	127	Sy1.5	SBc	10.7	1.45 ± 0.16^b
Ark 120	130	Sy1	Sb/pec	10.2	1.23 ± 0.16^b
Mrk 509	139	Sy1.2	Compact	10.6	0.63 ± 0.08^b
NGC1386	12	Sy2	SB(s)0+	9.1	2.16 ± 0.24^b
NGC 1068	15	Sy2	(R)SA(rs)b;	10.8	<3.44
NGC5273	16	Sy2	SA(s)0	8.6	0.71 ± 0.11^b
NGC7213	24	Sy2 LINER	SA(s)0;	9.6	<1.77
IC 5063	46	Sy2	SA(s)0+:	10.2	<0.34
Mrk3	56	Sy2	S0	10.3	0.64 ± 0.11^b
NGC1667	60	Sy2	SAB(r)c	10.7	3.56 ± 0.16^b
Mrk 1	64	Sy2	(R')S?	10.2	<0.13
Mrk 533	117	Sy2	SA(r)bc pec;	11.1	3.34 ± 0.23^b
UGC 6100	119	Sy2	Sa?	10.2	0.71 ± 0.08^b
NGC7603	120	Sy2	SA(rs)b	10.4	1.60 ± 0.17^b
NGC4051	8	Sy1.5/NLS	SAB(rs)bc	9.1	1.25 ± 0.24^b
Mrk 766	52	Sy1.5/NLS	(R')SB(s)a:	10.2	$<0.67^b$
PG2130+099	244	Sy1/RQQ	(R)Sa	10.6	<0.62
PG0804+761	400	Sy1/RQQ	···	10.6	<0.97
PG1613+658	516	Sy1/RQQ	Elliptical	11.5	<0.30
PG0157+001	677	Sy1/RQQ	Bulge/disc	12.1	<0.45
PG1700+518	1243	Sy1/RQQ	BALQSO	11.9	<1.02
3C 390.3	227	Sy1/RLQ	Opt.var.;BLRG	10.2	<0.24

Columns Explanation: Col.(1): Common Source Names; Col.(2): Distance in Mpc; Col.(3): Optical Classification/AGN Class; Col.(4): Hubble Type; Col.(5): Far-infrared luminosities (in units of solar luminosities: $L_\odot$) correspond to the 40-500μm wavelength interval and were calculated using the IRAS 60 and 100 μm fluxes according to the prescription of Sanders and Mirabel (1996), See Table 4.1 above; Col.(6): Flux of the 6.2μm PAH feature ($\times 10^{-15}$) in units of W m^{-2}. Upper limits correspond to 3σ values. **References:** a: fluxes from Spoon et al. (2002); b: fluxes from Clavel et al. (2000)

In Section 4.4.3, we showed that the apparent separation between the various AGN subclasses in the L_{bol}/L_{Edd} and L_{FIR} plane, which gives rise to the separation in the SFR and $\dot{M}$ plane seen in Figure 4.8, is not likely to be due to systematic effects in estimating $L_{\rm bol}$, $L_{\rm Edd}$, or $L_{\rm FIR}$ in our expanded AGN sample. Figure 4.9 shows the distribution of the SFR/$\dot{M}$ ratio for the sample. NLS1s and RQQ, generally considered to be characterized by very high accretion rates, generally have the smallest SFR/$\dot{M}$ values, followed by Seyferts, RL AGNs, and finally, LINERs. If we make the crude assumption that the FIR luminosity is at least loosely correlated with star formation in the bulge, at face value, Figures 4.8 and 4.9 imply that the growth of the black hole by accretion does not always match the growth of the bulge during all phases of galaxy evolution. Is there prodigious black hole growth without major star formation in the most highly accreting local sources compared with the weakly accreting sources?

Alternatively, the separation seen in Figures 4.8 and 4.9 could simply be an artificial consequence of our assumption that η is the same for all sources, while in fact the radiative efficiency for the objects at low $\dot{M}$ is likely to be much smaller (and possibly a decreasing function of $\dot{M}$; Narayan & Yi 1995). Such an effect would alter both the slope and intercepts of the regression lines displayed in Figure 4.8 as well as introduce greater dispersion in the RL AGNs and LINERs which span a greater range in L_{bol}/L_{Edd} consistent with what is seen in Figures 4.8 and 4.9. Indeed, a transition between a radiatively efficient, geometrically thin, optically thick accretion flow, and a radiatively inefficient, geometrically thick and optically thin flow is theoretically expected to occur at low values of $\dot{M}$ (Rees et al. 1982; Narayan & Yi 1995). Applying a single value for η to a sample of AGNs (as is commonly done in the literature), particulary in our sample where L_{bol}/L_{Edd} varies widely, is therefore likely to be incorrect. Most of the LINERs and many of the RL AGNs in our expanded AGN sample (see Tables 4.2, 4.4 and 4.6) have low L_{bol}/L_{Edd} values. If the accretion flow in those objects with low Eddington ratios is characterized by systematically lower η values compared with the rest of the sample, the separations seen in Figures 4.8 and 11 can be removed. If we adopt $\eta = 0.001$ for LINERs and the RL AGNs with low values of L/L_{Edd}, Figures 4.8 and 4.9 show that the SFR/$\dot{M}$ ratio becomes more consistent amongst the various AGN types. This value of η is consistent with radiatively inefficient accretion models (RIAF; Quataert 2003) and is in fact compatible with the values of η calculated directly based on the Bondi accretion rates and a detailed spatial analysis of a sample of radio galaxies with low Eddington ratios (Donato, Sambruna, & Gliozzi 2004). In order to truly understand the relationship between the mass accretion rate and the host galaxy SFR in the various AGN subclasses, it is necessary to determine the radiative efficiencies and decouple their effects on the derived mass accretion rates for the entire sample. However, our limited dataset and theoretical uncertainties do not allow us to expand further on this point, or to give any robust indication on the true value of η for all galaxies in our sample.

If there is a variation in the SFR/$\dot{M}$ ratio as function of AGN type and activity level, this may have an important consequence on our understanding of galaxy evolution and black hole growth. Using our expanded AGN sample, we can also investigate whether there are any systematic trends in the SFR/$\dot{M}$ ratio as a function of interaction status. Our sample includes 22 AGNs that are in either merging or interacting pairs. Several models assume black hole growth matches bulge growth exactly during a merger with subsequent growth of the bulge being regulated by AGN feedback (e.g. Haehnelt & Kauffman 2000). If this scenario holds, one might

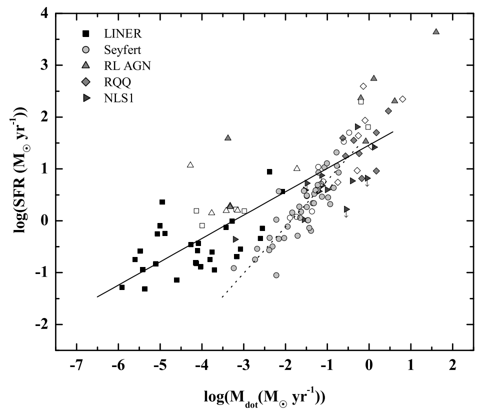

Figure 4.8: Star formation rate vs. mass accretion rate

Log plot of the Star Formation rate in $M_{\odot}\mathrm{yr}_{-1}$ as a function of the Mass Accretion Rate in $M_{\odot}\mathrm{yr}_{-1}$ for the '129 AGNs in our expanded AGN sample with black hole estimates. The dotted line represents the linear fit to the Seyfert data and the solid line represents the linear fit to the LINER data. AGNs that belong to merging or interacting systems are indicated by the open symbols.

expect to see variations in the SFR/$\dot{M}$ ratio as a function of AGN type, activity level, and merger status. Indeed, recent hydrodynamical simulations that simultaneously follow star formation and the growth of black holes during galaxy-galaxy collisions shows that SFR/$\dot{M}$ varies with time as energy released by the AGN expels enough gas to quench both star formation and further black hole growth (Di Matteo, Springel, & Hernquist 2005). In Figure 4.8, merging or interacting galaxies are indicated with open symbols. Apart from the fact that the merging or interacting galaxies are concentrated at high values of $\dot{M}$, there is no apparent distinction in their SFR vs. $\dot{M}$ relation. Clearly there are not enough data to make definitive conclusions. A more extensive analysis that includes a larger population of mergers would be required to address this important question.

There have been a few recent studies on the connection between the SFR and mass accretion rate in AGNs. Using the SDSS observations of 123,000 low redshift galaxies, Heckman et al. (2004) find that the global volume-averaged SFR/$\dot{M}$ ratio is approximately 1000 in bulge-dominated systems, in agreement with ratio of bulge to black hole mass implied by the M_{BH} vs. σ relationship (Marconi & Hunt 2003). This ratio is significantly higher than the the SFR/$\dot{M}$ ratio for the majority of galaxies in our sample, which target solely definitive AGNs (see Figure 4.9). For example, the average SFR/$\dot{M}$ ratio for the Seyfert and RQQ subclasses is approximately 100 - a value that can be compatible with the global ratio of 1000 if there is a duty cycle for the AGN of about 10%. Interestingly, Hao et al. (2005) recently found a significantly higher SFR/$\dot{M}$ ratio ($\sim$500) in a small sample of infrared-selected QSOs compared with the majority of AGNs in our expanded AGN sample. Since this ratio is determined in IR-bright QSOs, there is potentially enhanced star formation in these sources compared with the standard RQQ included in our sample.

We note that our estimate of the SFR is based on the total L_{FIR} from the host galaxy. As we have pointed out, the FIR emission can include an AGN contribution, a contribution from old stars, and probably, most importantly, star formation taking place in the disk, all of which would result in an overestimate to the bulge SFR. Indeed, in spiral hosts, the total FIR emission may be dominated by star formation in the disk (e.g., Fukugita et al. 1998; Benson et al. 2002; Hogg et al. 2002). Spatially resolved observations of the PAH emission in these galaxies - possibly the most robust indicators of the SFR in AGNs - can potentially provide a more accurate determination of bulge-dominated star formation. Future spectroscopic imaging observations of these features with *Spitzer* in a statistically significant sample of nearby AGNs can potentially provide important advances in our understanding of the observed correlation of the black hole and bulge mass and its relationship to the

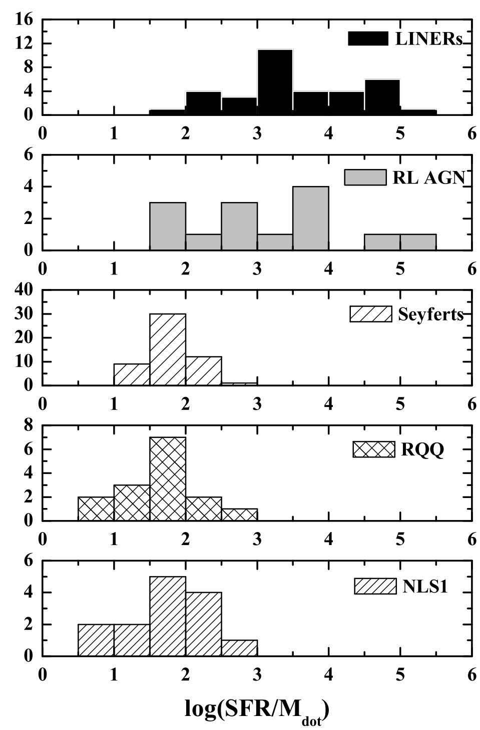

Figure 4.9: Histogram of SFR/$M_{\odot}$ for 129 AGNs

Histogram of the ratio of the star formation rate to the mass accretion rate for the 129 AGNs in this work that have black hole estimates.

birth, growth, and evolution of black holes and galaxies.

4.6 Conclusion

We have studied the relationship between the Eddington ratio, $L/L_{\rm Edd}$, as a function of the FIR luminosity, $L_{\rm FIR}$, of the host galaxy, found to be correlated over seven orders of magnitude in $L_{\rm bol}/L_{\rm Edd}$ in our previous work (Chapter 3), in a sample of 34 LINERs with confirmed hard X-ray nuclear point sources. This sample builds on our previously published proprietary and archival X-ray observations from *Chandra* by including the remaining 25 LINERs in the *Chandra* archive for which black hole masses and FIR luminosities have been previously published. We combined our sample with a larger sample of AGNs with reliable black hole masses and bolometric luminosities drawn from the literature. The entire sample discussed in this work consists of 129 confirmed AGNs: 34 AGN-LINERs, 52 Seyferts, 14 radio-loud AGNs, 15 QSOs, and 14 narrow line Seyfert 1s. Our main results are as follows.

1. Of the 25 LINERs presented in this article, 13 show compact hard nuclear cores coincident with the radio or *2MASS* nucleus, with a luminosity L_X (2-10 keV) $\geq 2 \times 10^{38}$ ergs s^{-1}. The nuclear 2-10 keV luminosities for the 25 galaxies range from $\sim 2 \times 10^{38}$ ergs s^{-1} to $\sim 1 \times 10^{42}$ ergs s^{-1}.

2. Combining these observations with our previously published work, we find that 50% (41/82) of LINERs have hard nuclear X-ray cores consistent with an AGN.

3. We find a significant correlation between the Eddington ratio as a function of $L_{\rm FIR}$ that extends over almost nine orders of magnitude in $L_{\rm bol}/L_{\rm Edd}$. Using archival and previously published observations of the 6.2 μm PAH feature, we find that it is unlikely that dust heating by the AGN dominates the

FIR luminosity in our sample of AGNs. Our results may therefore imply a fundamental link between the mass accretion rate ($\dot{M}$), as measured by the Eddington ratio, and star formation rate (SFR), as measured by the FIR luminosity.

4. Apart from the overall correlation, we find that the different AGN subclasses occupy distinct regions in the L_{FIR} and L_{bol}/L_{Edd} plane. This may imply a variation in the SFR/$\dot{M}$ ratio as function of AGN type and activity level. Although data are limited, there seems to be no systematic difference in the derived SFR/$\dot{M}$ ratio in AGNs that belong to merging or interacting pairs and those that do not.

5. Assuming that the radiative efficieny for accretion is 10% for all AGNs in the sample and that the FIR luminosity traces arises solely from dust heated by young stars, we determined the relationship between the mass accretion rate and the host galaxy's SFR. The average ratios of the SFR/$\dot{M}$ ratio for the Seyfert and RQQ subclasses are approximately 100 - a value that can be compatible with the global volume-averaged ratio of 1000 found in a large sample of bulge-dominated systems observed in the SDSS, if there is a duty cycle for the AGN of about 10%.

Chapter 5: MID-INFRARED FINE STRUCTURE LINE RATIOS IN ACTIVE GALACTIC NUCLEI OBSERVED WITH SPITZER IRS: EVIDENCE FOR EXTINCTION BY THE TORUS

This Chapter was published by R. P. Dudik, J. C. Weingartner, S. Satyapal, J. Fischer, & C. C. Dudley, 2007, ApJ, XX, XX

5.1 Introduction

The NLRs of AGNs have been studied extensively using optical spectroscopic observations. However, there have been very few systematic studies of the NLR using infrared spectroscopic observations. Infrared (IR) fine-structure emission lines have a number of special characteristics that have been regarded as distinct advantages, particularly in determining the electron density of the ionized gas very close to the central AGN. As mentioned in Chapter 1, infrared spectroscopic observations allow access to fine-structure lines from ions with higher ionization potentials than the most widely used optical diagnostic lines. This is important in many AGNs, where a significant fraction of the line emission from lower ionization species can originate in gas ionized by star forming regions. In addition, it is generally assumed that the density-sensitive infrared line ratios originate in gas with temperatures around 10^4 K and are less dependent on electron temperature variations, enabling a more straightforward determination of the electron density in the ionized gas. Finally, it has long been assumed that the IR diagnostic line ratios are insensitive to reddening corrections–a serious impediment to optical and ultraviolet observations, particularly in the NLRs of AGNs, where the dust composition and spatial distribution are highly uncertain. For these reasons, IR spectroscopic observations, especially since the era of the *Infrared Space Observatory* (*ISO*), have provided us with some of the most reliable tools for studying the NLRs in AGNs. However, while there are clear advantages of mid-IR fine-structure diagnostics in studying the physical state of the ionized gas, very little work has been done to investigate their robustness in determining the gas densities of the NLRs in a large sample of AGNs. The *Spitzer Space Telescope* Infrared Spectrometer (IRS), with its extraordinary sensitivity and spectral resolution, offers the opportunity to examine for the first time the physical state of NLR gas in a large sample of AGNs and particularly LINERs.

The focus of most previous comparative studies of the infrared fine-structure lines in AGNs has been on the excitation state of the ionized gas, in an effort to determine the existence and energetic importance of potentially buried AGNs and to constrain their ionizing radiation fields (Genzel et al. 1998, Lutz et al. 1999, Alexander & Sternberg 1999, Sturm et al. 2002, Satyapal, Sambruna, & Dudik 2004, Spinoglio et al. 2005). Remarkably, very little work has been done in the infrared on studying the line flux ratios traditionally used to probe the NLR gas densities in a significant number of AGNs. We present in this chapter the first systematic infrared spectroscopic study of the line flux ratios of [NeV] and [SIII] in order to 1) test the robustness of these line ratios as density diagnostics and 2) if possible, to probe the densities of the NLR gas in a large sample of AGNs from LINERs to Quasars.

5.2 The Sample

We searched the *Spitzer* archive for galaxies with an active nucleus and both high- and low-resolution Infrared Spectrometer (IRS; Houck et al. 2004) observations currently available. Only those galaxies with indisputable optical, X-ray, or radio signatures of active nuclei (such as broad Hα or X-ray or radio point sources) were included in our sample. The sample includes three AGNs subclasses: Seyferts, LINERs, and Quasars. The galaxies in this sample span a wide range of distances (4 to 400 Mpc; median = 21 Mpc), Hubble types, bolometric luminosities (log (L_{BOL}) $\sim$ 40 to 46, median = 43), and Eddington Ratios (log(L/L_{Edd}) $\sim$ -6.5 to 0.3; median= -2.5). The entire sample consists of 41 galaxies. The basic properties of the sample are given in Table 5.1. The black hole masses listed in Table 5.1 were derived using resolved stellar kinematics, if available, reverberation mapping, or by applying the correlation between optical bulge luminosity and central black hole mass determined in nearby galaxies only when the host galaxy was clearly resolved. Bolometric luminosities listed in Table 5.1 were calculated from the X-ray luminosities for most objects. For Seyferts, the relationship $L_{BOL} = 10 \times L_X$ was adopted (Elvis 1994). For LINERs we assumed $L_{BOL} = 34 \times L_X$, as derived from the spectral energy distribution of a sample of nearby LINERs from Ho (1999) (see also Dudik et al. 2005 and Satyapal et al. 2005, galaxies that are classified as LINERs using *either* the Heckman (1980) or Veilleux & Osterbrock (1987) diagnostic diagrams are included). The bolometric luminosities and black hole masses for quasars and radio galaxies were taken from Woo & Urry (2002) and Marchesini, Celotti, & Ferrarese (2004), respectively. A detailed discussion of our methodology and justification of assumptions for determining black hole masses and bolometric luminosities for the various AGN classes represented in Table 5.1 can be found in Satyapal et al. (2005) and Dudik et al. (2005). Table 5.1 also lists the

AGN type (1 or 2) for the galaxies in our sample based on the presence or absence of broad (full width at half max (FWHM) exceeding 1000 km s^{-1}) Balmer emission lines in the optical spectrum. We emphasize that the selection basis for the objects in our sample was on the availability of high resolution IRS *Spitzer* observations. The sample should therefore not be viewed as complete in any sense.

5.3 Data Analysis and Results

The 41 observations presented in this work are archived from various programs, including the *SINGS* Legacy Program, and therefore contain both mapping and staring observations. We present the data analysis and reduction details for these observations in Chapter 2.2. In Tables 5.2 and 5.3 we list the line fluxes and statistical errors from the SH and LH observations for the [NeV] 14.3μm and 24.3μm lines, the [SIII] 18.1μm and 33.5μm lines, as well as the 6.2μm PAH emission feature. For all galaxies with previously published fluxes, we list in Tables 5.2 and 5.3 the published flux values. Our values differ by no more than a factor of 1.9, much less in most cases, from the Weedman et al. (2005) or Armus et al. (2004, 2006) published values.

Abundance-independent density estimates can readily be obtained using infrared fine-structure transitions from like ions in the same ionization state with different critical densities. The density diagnostics available in the IRS spectra of our objects are: [NeV] 14.32μm, 24.32 μm ($n_{crit} \sim 4.9 \times 10^4$ cm^{-3}, and 2.7×10^4 cm^{-3}, where n_{crit} = A_{ul}/γ_{ul}, with A_{ul} the Einstein A coefficient and γ_{ul} the rate coefficient for collisional de-excitation from the upper to the lower level), [NeIII] 15.55μm, 36.04 μm ($n_{crit} \sim 3 \times 10^5$ cm^{-3}, and 5×10^4 cm^{-3}, Giveon et al. 2002), and [SIII]18.71μm, 33.48 μm ($n_{crit} \sim 1.5 \times 10^4$ cm^{-3}, and 4.1×10^3 cm^{-3}). The results are very insensitive to the shape of the ionizing continuum. Since the [NeIII] 36μm line was either not detected

Table 5.1: Properties of the Sample

Galaxy Name (1)	Distance (Mpc) (2)	Hubble Type (3)	log (M_{BH}) (4)	log (L_X) (5)	log (L/L_{Edd}) (6)	AGN Type (7)
Seyferts						
NGC4151	13	SABab	7.13^a	42.7^b	-1.53	1^r
NGC1365	19	SBb	7.64^b	41.3^d	-3.42	2^s
NGC1097	15	SBb	...	40.7^e	...	...
NGC7469	65	SABa	6.84^a	44.3^a	0.34	1^t
NGC4945	4	SBcd	7.35^b	42.5^f	-1.97	2^u
Circinus	4	SAb	7.72^b	42.1^g	-2.74	2^v
Mrk 231	169	SAc	7.24^c	42.2^h	-2.16	...
Mrk3	54	S0	8.65^a	43.5^a	-2.21	2^w
Cen A	3	S0	7.24^b	41.8^i	-2.54	2^x
Mrk463	201	Merger	...	43.0^j	...	2^y
NGC 4826	8	SAab	6.76^b	...	...	...
NGC 4725	16	SABab	7.40^b	...	...	2^r
1 ZW 1	245	Sa	...	43.9^k	...	...
NGC 5033	19	SAc	7.39^b	41.4^l	-3.13	1^r
NGC1566	20	SABbc	6.92^a	43.5^a	-0.57	1^t
NGC 2841	9	SAb	8.21^a	42.7^a	-2.64	...
NGC 7213	24	SA0	7.99^a	43.30^a	-1.79	...
LINERs*						
NGC4579	17	SABb	7.85^b	41.0^b	-3.47	...
NGC3031	4	SAab	7.79^b	40.2^b	-4.16	...
NGC6240	98	Merger	9.15^b	44.2^b	-1.52	2^z
NGC5194	8	SAbc	6.90^b	41.0^b	-2.43	2^r
MRK266NE	112	Merger	...	40.9^b	...	2^t
NGC7552	21	SBab	6.99^b	...	...	...
NGC 4552	17	...	8.57^b	39.6^b	-5.52	...
NGC 3079	15	SBc	7.58^b	40.1^m	-4.05	...
NGC 1614	64	SBc	6.94^b	...	...	...
NGC 3628	10	SAb	7.86^b	39.9^n	-4.58	...
NGC 2623	74	Pec	6.83^b	...	...	2^{aa}
IRAS23128-5919	178	Merger	...	41.0^b	...	2^{bb}
MRK273	151	Merger	7.74^b	44.0^o	-0.31	2^t
IRAS20551-4250	171	Merger	7.52^c	40.9^b	-3.23	...
NGC3627	10	SABb	7.16^b	39.4^p	-4.33	2^r
UGC05101	158	S	...	40.9^b	...	1^{cc}
NGC4125	18	E6	8.50^b	38.6^b	-6.47	...
NGC 4594	10	SAa	9.04^b	40.1^q	-5.47	...
Quasars						
PG 1351+640	353	...	8.48^a	44.5^a	-1.08	...
PG 1211+143	324	...	7.49^a	44.8^a	0.22	1^t
PG 1119+120	201	...	...	...	...	1^y
PG 2130+099	252	Sa	7.74^a	44.47^a	-0.37	1^y
PG 0804+761	400	...	8.24^a	44.93^a	-0.41	1^{dd}
PG 1501+106	146	E	...	...	...	1^y

Columns Explanation: Col(1):Common Source Names; Col(2): Distance (for H_0= 75 km $s^{-1}Mpc^{-1}$); Col(3): Morphological Class; Col(4): Mass of central black hole in solar masses; Col(5): Log of the hard X-ray luminosity (2-10keV) in erg s^{-1}. Col(6): log of the Eddington Ratio. (* = We include all galaxies that are classified as LINERs using *either* the Heckman (1980) or Veilleux & Osterbrock (1987) diagnostic diagrams. Col(6): AGN type based on the presence or absence of broad Balmer emission lines.) **References:**[a]Woo & Urry 2002, [b] Satyapal et al. 2005, [c] Tacconi et al. 2002, [d] Risaliti et al. 2005, [e] Terashima et al. 2002, [f] Guainazzi et al. 2000, [g] Smith & Wilson 2001, [h] Gallagher et al. 2002, [i] Evans et al. 2004, [j] Imanishi & Terashima et al. 2004, [k]Gallo et al. 2004 , [l] Terashima et al. 1999, [m] Cappi et al. 2006, [n] Roberts, Schurch, & Warwick 2001, [o] Balestra et al. 2005, [p]Georgantopoulos et al 2002, [q] Dudik et al. 2005, [r] Ho et al. 1997, [s] Storchi-Bergmann, Mulchaey, & Wilson, 1992, [t] Veron-Cetty & Veron 2003, [u] Marconi et al. 2000, [v]Oliva et al. 1994, [w] Khachikian & Weedman 1974, [x] Veron-Cetty & Veron 1986[y] Dahari & De Robertis 1988, [z] Andreasian, Khachikian, & Ye, 1987, [aa] Laine et al. 2003, [bb] Duc, Mirabel, & Maza 1997, [cc] Sanders et al. 1988, [dd] Thompson 1992.

or was outside the wavelength range of the LH module in virtually all galaxies, we omit any analysis of the [NeIII] line ratio from this work.

5.4 The [NeV] Line Flux Ratios

In Figure 5.1 we plot the calculated $14\mu m/24\mu$ line luminosity ratio as a function of electron density n_e for gas temperatures $T = 10^4\,K$, $10^5\,K$, and $10^6\,K$. We include only the five levels of the ground $2s^2 2p^2$ configuration and neglect absorption and stimulated emission. The results are nearly identical if only the lowest three levels of the ground term are included. We adopt collision strengths from Griffin & Badnell (2000) and radiative transition probabilities from Galavis, Mendoza, & Zeippen (1997).

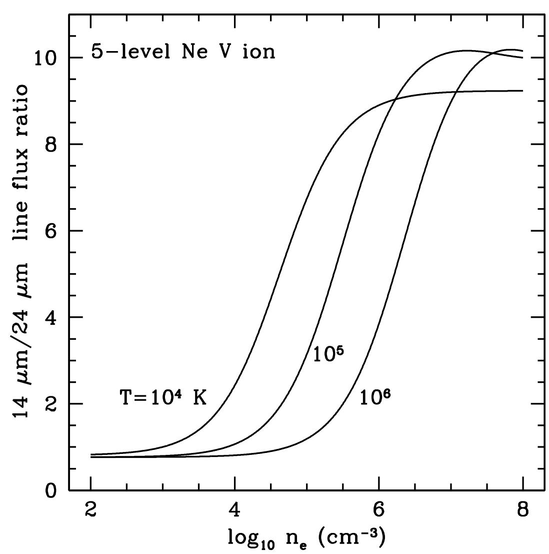

Figure 5.1: [NeV] line ratio vs. density

[NeV] $14\mu m/24\mu m$ line flux ratio versus electron density, n_e, for gas temperatures $T = 10^4\,K$, $10^5\,K$, $10^6\,K$.

In Table 5.2, we list the observed [NeV] line flux ratios and their associated calibration uncertainties. In calculating the upper and lower limits on the ratios, R_{MAX} and R_{MIN}, shown in Table 5.2, we did not propagate the errors in quadrature as would be appropriate for statistical uncertainties, but propagated them as follows:

$$R_{MAX} = \frac{F[\mathrm{NeV}]_{14} + 0.15(F[\mathrm{NeV}]_{14})}{F[\mathrm{NeV}]_{24} - 0.15(F[\mathrm{NeV}]_{24})} \tag{5.1}$$

$$R_{MIN} = \frac{F[\mathrm{NeV}]_{14} - 0.15(F[\mathrm{NeV}]_{14})}{F[\mathrm{NeV}]_{24} + 0.15(F[\mathrm{NeV}]_{24})} \tag{5.2}$$

We note that this is conservative, since some components of the calibration errors should cancel in the ratio. Both line fluxes were measured for 19 galaxies. In what follows we compare the line flux ratios measured in all but one, MKN 266, for reasons that are discussed in detail in Section 5.5.2. Of these 18 AGNs, 13 have ratios that are consistent with the low density limit to within the uncertainties, while only 2, both Type 1, have ratios significantly above it. The remaining 3, all Type 2, have ratios significantly below the low-density limit. Interestingly, we note that a similar range of ratios was also measured with the ISO SWS (Sturm et al. 2002, Alexander et al. 1999). There are several possible explanations for this finding. The observed, unphysically low ratios could result from artifacts introduced by variations in the slit sizes from which the line fluxes are obtained, from calibration uncertainties, or from substantial mid-IR extinction. Alternatively, perhaps important physical processes were neglected in calculating the theoretical ratios. In addition, errors in the collisional rate coefficients for the [NeV] transitions associated with the mid-infrared lines may be important. We explore these scenarios in the following sections.

Observational Effects: Because the IRS LH slit is larger than the SH slit, if the [NeV] emission is extended, or multiple AGNs are present, the 14/24 μm line ratio will be artificially reduced. However, since the ionization potential of [NeV] is ~ 97 eV, we expect that the [NeV]-emitting gas is ionized by the AGN radiation field only and is concentrated very close to the central source. Virtually all of the [NeV] fluxes presented in this work were obtained from IRS staring observations. Thus it is impossible to determine whether the emission is extended using *Spitzer* observations alone. However, a number of galaxies have been observed at 14 and 24 μm by ISO. In Table 5.2 we list in addition to our *Spitzer* [NeV] fluxes, all available [NeV] fluxes from ISO. The ISO aperture at 14 and 24 μm (14"×27") is much larger than either the SH or LH slits. In Figure 5.2 we plot the ratio of the [NeV] flux measured by ISO to that measured by *Spitzer* for both the 14 and 24 μm lines. The ranges of the [NeV] line flux ratios are consistent with the instrument uncertainties and are similar for all galaxies in the sample. Only the 14μm ratio for Mrk 266 falls outside of the expected range. This strongly suggests that the [NeV] emission is indeed compact and originates in the NLR and that the ratios are *not* affected by aperture variations, except for Mrk 266 which is discussed in detail in Section 5.5.2.

If the data were affected by aperture variations we would expect to see an overall systematic increase of the 14μm/24μm line ratio with distance(See Figure 5.3). The Spearman rank correlation coefficient (r_S, Kendall & Stuart 1976) corresponding to this plot is -0.069 (with a probability of chance correlation of 0.78), where a coefficient of 1 or -1 indicates a strong correlation and a coefficient of 0 indicates no correlation. Thus we find that there is no correlation between the [NeV] ratio and distance in our sample. However this does not completely rule out aperture effects, if the size of the [NeV] emitting region increases with the bolometric luminosity of the AGN and the sample displays a significant trend in bolometric luminosity with distance. In this case, a correlation between the [NeV] ratio and distance would not be apparent since

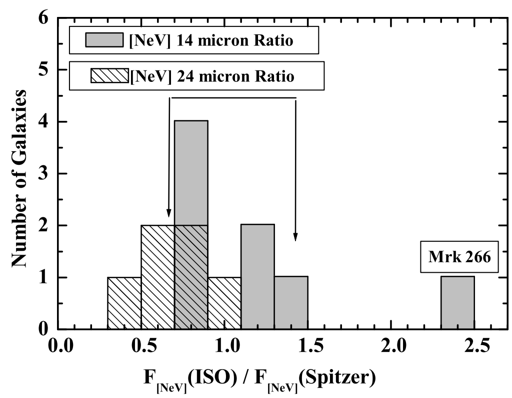

Figure 5.2: *ISO* and *Spitzer* [NeV] line fluxes

Ratio of the *ISO* to *Spitzer* [NeV] 14μm and 24μm fluxes for those galaxies with overlapping observations. The range indicated with arrows is that corresponding to the absolute flux calibration for *ISO* (20%) and *Spitzer* (15%). Within the calibration uncertainties of the instrument, the [NeV] fluxes are virtually the same for all of the galaxies except Mrk 266 (See Section 5.5.2). This strongly suggests that the [NeV] emission is compact and originates in the NLR. We note that Sturm et al. 2002 find that the [NeV] 24μm detection for NGC 7469 is questionable. The *ISO* to *Spitzer* ratio for this galaxy (0.43) is the lowest shown here.

aperture variations would affect all galaxies in the same way, regardless of distance. However this scenario is unlikely since the size of the [NeV]-emitting region would have to increase proportionately with distance in order to remain extended beyond the slit for all galaxies. Nevertheless, we checked for this possibility, both by examining the [NeV] ratio vs. bolometric luminosity and by plotting the ratio vs. distance, binning the galaxies according to their bolometric luminosity. We find neither to be correlated over 5 orders of magnitude in L_{BOL}. Thus, in the case of the [NeV] line flux ratio, we find no indication that ratios below the low density limit are artifacts of aperture effects.

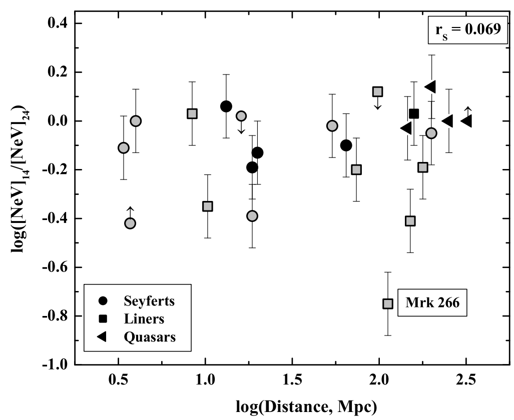

Figure 5.3: [NeV] ratio vs. distance

The [NeV] 14μm/24μm ratio as a function of distance. Open symbols signify Type 1 AGNs, Filled symbols signify Type 2 AGNs. The error bars shown here mark the calibration uncertainties on the line ratio. If the ratio were indeed affected by aperture variations we would expect a systematic increase of the ratio with distance. As can be seen here, this is not the case, and we find no indication that the low ratio is attribuable to aperture effects.

We point out that the [NeV] 24μm IRS line fluxes in the small overlapping sample plotted in Figure 5.2 are systematically higher than the corresponding *ISO*-SWS fluxes, despite the smaller IRS slit. This indicates that one or both of the instruments is affected by systematic errors more severe than are indicated by the calibration uncertainty estimates. The SWS band 3D that includes the [NeV] 24μm line was characterized by strong fringing effects that when combined with the narrow range of the line scan mode introduced sometimes large uncertainties in the baseline fitting, and therefore the line flux measurement accuracy. In contrast, the baseline fitting over the entire *Spitzer* IRS SH and LH full spectra can be much more accurate. Moreover pointing accuracy and stability are an order of magnitude improved over that obtained by ISO. We therefore assume in the sections that follow that the adopted conservative *Spitzer* IRS calibration uncertainties are accurate characterizations of the IRS measurements. Importantly, *regardless of which instrument is used, [NeV] ratios consistent with the low density limit have been observed in a number of sources with both ISO* (e.g. Sturm et al. 2002 NGC 1365, NGC 7582, NGC4151, NGC 5506; Alexander et al. 1999, NGC 4151) and *Spitzer* (Weedman et al. 2005, Haas et al. 2005, and this work).

Extinction: We consider the possibility that mid-IR differential extinction toward the [NeV]-emitting regions is responsible for the low [NeV] line ratios. Adopting the low-density limit (LDL) for the intrinsic value of the ratio ([NeV]14μm/24μm ~0.83 for $n_e \leq 200$ cm^{-3}) for galaxies with ratios below the LDL, the observed line ratio gives a *lower limit* to the extinction, for a given MIR extinction curve. We examined the visual extinctions corresponding to the mid-IR differential extinction derived using three separate extinction curves: 1) the Draine (1989) extinction curve amended by the more recent ISO SWS extinction curve toward the Galactic center for 2.5-10μm (Lutz et al. 1996), 2) the Chiar & Tielens (2006) extinction curve for the Galactic Center using 2.38-40μm ISO SWS observations of a bright IR source in the Quintuplet cluster (GCS3-I) 3) the Chiar & Tielens (2006) extinction curve for the local ISM using 2.38-40μm ISO SWS observations of a WC-type Wolf-Rayet (WR) star (WR98a). The Draine (1989) and Lutz et al. (1996) extinction curve yields $A_V \sim 3$ to 99 mag (See Table 5.2). However, these values result from an extinction law that is unexplored beyond 10μm. The Chiar & Tielens (2006) Galactic center extinction curve cannot explain the observed [NeV] ratios since the extinction at 24μm is greater than the extinction at 14μm, so we do not discuss it further. The visual extinction resulting from their local ISM extinction curve is unrealistically high ($A_{V median}$=500mag). The calculated extinction obtained using the Draine (1989), Lutz et al. (1996), and Chiar & Tielens (2006) local ISM extinction curves are given in Table 5.2.

The A_V derived from the two extinction curves described above are extremely high in many cases. Even if the extinction is calculated from the upper limit on the ratio to the LDL for the three galaxies whose upper limits are below the LDL, the corresponding visual extinction is still very high (for the Draine 1989 and Lutz et al. 1996 extinction curve A_V = 21, 26, and 30 mag for these three galaxies; for the Chiar and Tielens extinction curve A_V = 260, 330, and 370 mag). However, we caution the reader that the actual *value* for extinction is highly uncertain. Indeed very little is known about the 8-40μm extinction curve in AGNs. Specifically, the 10 and 18 μm silicate features in this band are the source of inconsistency. Even within the AGN class, extinction may vary dramatically from 8-40μm because of variations in the silicate features due to differences in grain size, porosity, shape, composition, abundance, and location in each galaxy. Hao et al. (2005) show that in five AGNs (4 of which are in our sample), both silicate features vary considerably in strength and width. Sturm et al. (2005) also show that the standard ISM silicate models do not accurately fit NGC 3998, a LINER with silicate emission. Sturm et al. (2005) suggest that increased grain size and possibly the presence of crystalline silicates such as clino-pyroxenes may improve the fit, but that clearly circumnuclear dust in AGNs has very different properties than dust in the Galactic ISM (see also Maiolino et al. 2001a, 2001b, but Weingartner & Murray 2002 for an alternative view). Chiar & Tielens (2006) even show that the GC observations and the local ISM observations within the Galaxy deviate from each other most dramatically in the wavelength region between the two silicate absorption features. In their observations, this is the region between $\sim$ 12-15μm -directly overlapping with the 14μm values in which we are interested. Because of irregularity of the silicate features in the mid-IR, it is very difficult to interpret the true extinction there. Moreover, in addition to the uncertainty in the extinction law, the geometry of the obscuring material is unknown and can vary substantially from galaxy to galaxy. The most that can be said here for the galaxies with ratios below the LDL is that if extinction is responsible for the low ratios, then the extinction must be less at 24μm than at 14μm.

Physical Processes: It is possible that important physical processes have been neglected in calculating the [NeV] line luminosity ratio as a function of electron density shown in Figure 5.1. We consider three physical processes that may affect the line ratios:

(1) A source of gas heating in addition to photoionization (e.g., shocks, turbulence) that may yield gas temperatures substantially higher than 10^4 K. As can be seen in Figure 5.1, higher gas temperatures do not yield significantly lower line ratios in the low-density limit, but could explain the generally low values of the ratios that lie above the LDL.

(2) Pumping from the ground term to the first excited term, e.g., by O III resonance lines. The specific energy density required for this to significantly affect

the line ratio exceeds $10^{-14}\,\mathrm{erg\,cm^{-3}\,Hz^{-1}}$, which is implausibly large by orders of magnitude.

(3) Absorption and stimulated emission within the ground term, which could be important if, e.g., a large quantity of warm dust yielding copious 24μm continuum emission is located close to the [NeV]-emitting region. Figures 5.4a through 5.4e show the line ratio as a function of the specific energy density at 24 μm, $u_\nu(24\mu\mathrm{m})$. We display results for electron density $n_e = 10^2$, 10^3, 10^4, 10^5, and $10^6\,\mathrm{cm^{-3}}$; gas temperature $T = 10^4$, 10^5, and 10^6 K; and ratio of the specific energy density at 14 and $24\mu m$, $u_\nu(14\mu m)/u_\nu(24\mu m) = 0.4$, 1.0, and 1.8 (values were chosen to reproduce the observed range of the 14μm/24μm continuum flux ratios; see Section 5.5).

For the moment, assume that the NeV is located sufficiently far from the source of the 14 and 24μm continuum emission to treat the source as a point. If hot dust within or near the inner edge of the torus is responsible for this emission, then this assumption requires that the distance to the NeV, r_{Ne}, be large compared with the dust sublimation radius, $r_{\mathrm{sub}} \sim 1\,\mathrm{pc}\,L_{\mathrm{bol,\,46}}^{1/2}$ (Ferland et al. 2002); $L_{\mathrm{bol,\,46}}$ is the bolometric luminosity in units of $10^{46}\,\mathrm{erg\,s^{-1}}$. In this case, we can obtain a simple estimate of $u_\nu(24\mu m)$ at the location of the [NeV]-emitting region from the observed specific flux $F_\nu(24\mu m)$, the distance to the galaxy D, and r_{Ne}:

$$u_\nu(24\mu m) \sim \frac{1}{c} F_\nu(24\mu m) \left(\frac{D}{r_{\mathrm{Ne}}}\right)^2 \quad . \tag{5.3}$$

With $r_{\mathrm{Ne}} = 100\,\mathrm{pc}$, $u_\nu(24\mu m)$ estimated in this way ranges from $\approx 10^{-24}\,\mathrm{erg\,cm^{-3}\,Hz^{-1}}$ to somewhat less than $10^{-20}\,\mathrm{erg\,cm^{-3}\,Hz^{-1}}$ for the galaxies in our sample. These can be compared to the results of Hönig et al. (2006), who modeled the infrared emission from clumpy tori. They presented plots of F_ν at a distance of 10 Mpc from an AGN with bolometric luminosity $L_{\rm bol} = 4 \times 10^{45}\,{\rm erg\,s^{-1}}$. Extrapolating to a distance of 100 pc, we find $u_\nu(24\mu m)$ as large as a few times $10^{-21}\,{\rm erg\,cm^{-3}\,Hz^{-1}}$, close to the estimate for the most luminous AGNs in our sample.

From Figures 5.4a through 5.4e, we see that the infrared continuum can only reduce the line ratio significantly at $r_{\rm Ne} \approx 100\,{\rm pc}$ if $T \gtrsim 10^5\,{\rm K}$ when $n_e \sim 10^2\,{\rm cm^{-3}}$ and $T \gtrsim 10^6\,{\rm K}$ when $n_e \sim 10^3\,{\rm cm^{-3}}$. However, the NeV, as a high-ionization species, may lie closer to the central source than does the bulk of the narrow line region. If $r_{\rm Ne} \approx 10\,{\rm pc}$, then $u_\nu(24\mu m)$ increases by a factor ~ 100. In this case, the observed low line ratios can be explained by this mechanism with $T \sim 10^4\,{\rm K}$, if $n_e \sim 10^2\,{\rm cm^{-3}}$. Higher values of electron density would require higher gas temperatures.

In Section 5.5.1, we suggest that the [NeV]-emitting region may lie within the torus. In this case, absorption and stimulated emission within the ground term are probably important. For the high-luminosity objects, these may even dominate over collisional excitation and de-excitation. At these central locations, gas temperatures $T \sim 10^6\,{\rm K}$ may be natural (Ferland et al. 2002). Relatively high densities may also be expected, in which case the infrared continuum may not appreciably depress the line ratio (see Figure 5.4d).

Adopting the Mathews & Ferland (1987) spectrum and $T \approx 10^6\,{\rm K}$, the ionization parameter $U \equiv n_\gamma / n_e \sim 10^{-3}$ in order for a substantial fraction of the Ne to be NeV; n_γ is the number density of H-ionizing photons. For this spectrum, $n_\gamma \approx 1.7 \times 10^3 L_{\rm bol,\,46}\, r_{\rm Ne,\,100}^{-2}\,{\rm cm^{-3}}$, where $r_{\rm Ne,\,100} = r_{\rm Ne}/100\,{\rm pc}$. If $r_{\rm Ne} = 1\,{\rm pc}$, then either (1) $n_e \sim 10^{10} L_{\rm bol,\,46}\,{\rm cm^{-3}}$ or (2) the nuclear continuum is filtered through a far-UV/X-ray-absorbing medium before reaching the [NeV]-emitting region.

If absorption and stimulated emission are indeed relevant processes in [NeV] line production, we might expect a relationship between the [NeV] line flux ratio and

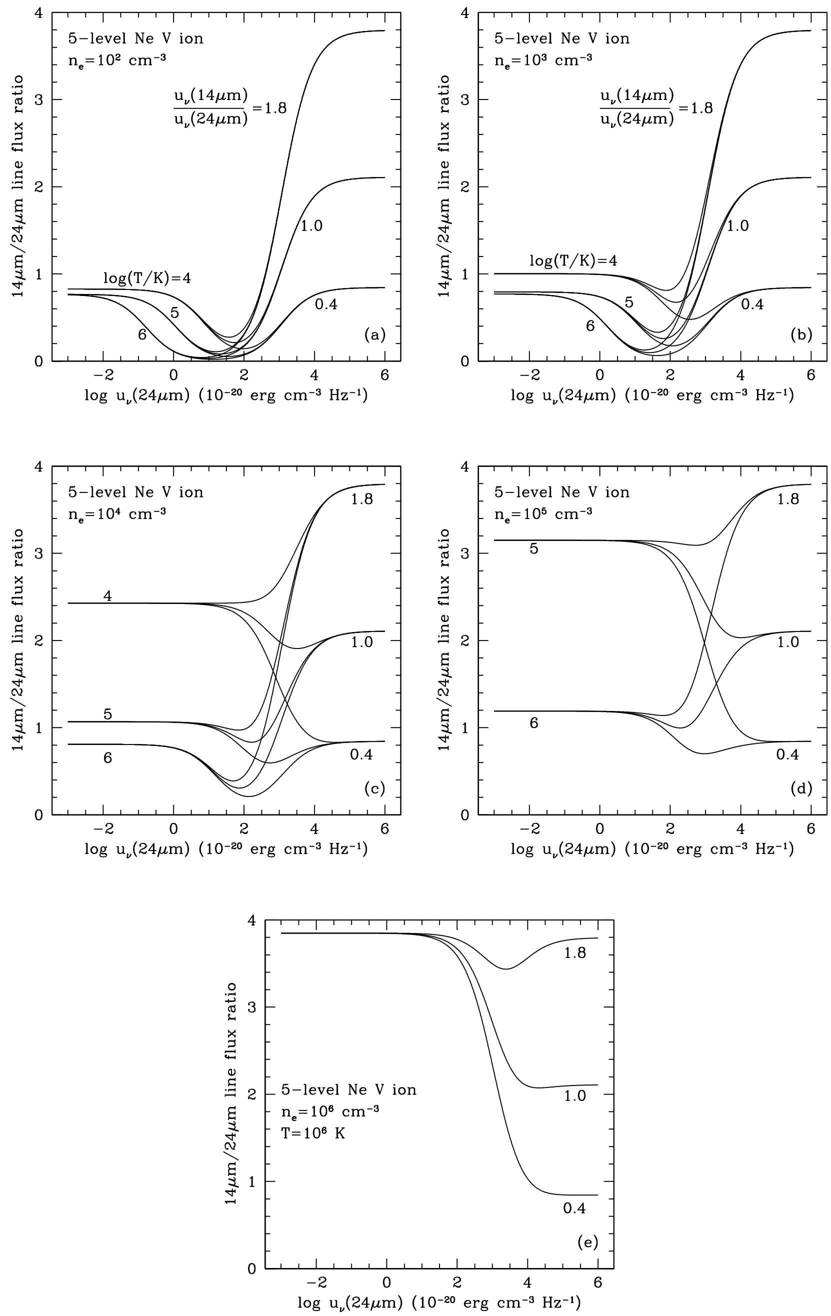

Figure 5.4: [NeV] line ratio vs. specific energy density

The [NeV] line ratio as a function of the specific energy density at 24μm, $u_\nu(24\mu\text{m})$, for temperatures, T = 10^4, 10^5, 10^6 K, for 14μm/24μm continuum ratios of 0.4, 1.0, and 1.8, and finally for electron densites, n$_e$ = 10^2, 10^3, 10^4, 10^5, 10^6 cm^{-3}.

the 24 μm continuum luminosity that is consistent with one of the curves shown in Figures 5.4a through 5.4e. In Figure 5.5 we plot this relationship for the [NeV] emitting galaxies in our sample. As can be seen in Figure 5.5, we find no relationship between the [NeV] line flux ratio and the 24μm continuum luminosity for our sample of galaxies. The Spearman rank correlation coefficient for this plot is -0.01 (probability of chance correlation = 0.95), indicating no correlation. As a result, as can be seen from Figures 5.4a and 5.4b, stimulated emission and absorption at low densities can be ruled out as possible scenarios because the scatter plot shown in Figure 5.5 does not follow the model predictions. Here we have assumed that the location of the [NeV]-emitting region relative to the source of the 24μm continuum emission is uniform among the galaxies in the sample. Variations in the location might obscure any correlation in these plots. Figures 5.4c and .4d reveal that, for some values of n_e, T, and $u_\nu(14\mu m)/u_\nu(24\mu m)$, the line ratio is very insensitive to the value of $u_\nu(24\mu m)$. In these cases, the line ratio remains above ~ 0.8. Thus, although absorption and stimulated emission may be contributing processes to [NeV] production, *another mechanism is required to explain the low (<0.8) [NeV] line flux ratios in our sample.*

Computed Quantities: Finally, it is possible that there is significant error in the adopted collisional rate coefficients. The accuracy of collisional strengths of infrared atomic transitions has been a longstanding question. We adopt the collisional rate coefficients from the state of the art IRON project (Hummer et al. 1993) which produced the most up-to-date and accurate collision strengths for a large database of atomic transitions. While these calculations have been questioned based on recent ISO observations of nebulae (Clegg et al. 1987, Oliva et al. 1996, Rubin et al. 2002, Rubin 2004), it is likely that the discrepancies between the observational and theoretical values can be explained by inaccuracies in the fluxes employed (van Hoof

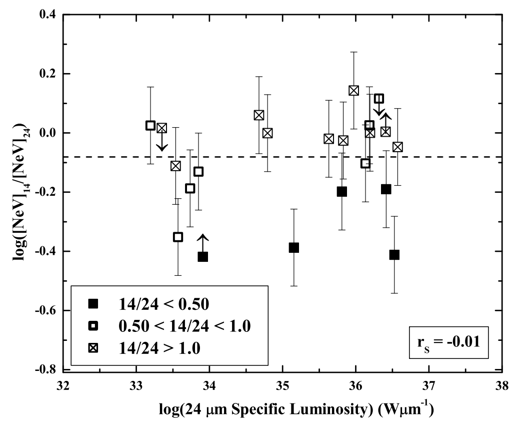

Figure 5.5: [NeV] line ratio vs. 24μm specific luminosity

The observed [NeV] line ratio as a function of the 24μm specific luminosity for our sample of galaxies. The error bars shown here represent the calibration uncertainties on the [NeV] line flux ratio as in Figure 3. The symbol type indicates the 14μm/24μm continuum ratio.

et al. 2000). Uncertainties in the collisional rate coefficients for the [NeV] transitions are unlikely to exceed 30% (van Hoof et al. 2000). It is therefore unlikely that the low critical densities implied by our data can be attributed to uncertainties in the theoretical values of the [NeV] collisional strengths.

5.5 Extinction Effects of the Torus and AGN Unification

Although low electron densities, high gas temperatures, and/or high infrared radiation densities may play a role in lowering the [NeV] line flux ratio, we argue that differential infrared extinction to the [NeV] emitting region due to dust in the obscuring torus is responsible for the low line ratios in at least some AGNs. Clearly, this requires that there is significant extinction at mid-IR wavelengths, and specifically toward

Table 5.2: [NeV] Line Fluxes and Derived Extinction

Galaxy Source (1)	[NeV] 14.32 SH (2)	[NeV] 14.32 ISO (3)	[NeV] 24.32 LH (4)	[NeV] 24.32 ISO (5)	[NeV] Ratio (6)	A_V LDL (D&L) (7)	A_V HDL (D&L) (8)	A_V LDL (C&T) (9)	A_V HDL (C&T) (10)
Seyferts									
NGC4151	7.77[a]	5.50[c]	6.77[a]	5.60[c]	$1.15^{+0.41}_{-0.30}$	···	126	···	1686
NGC1365	2.20±0.06	2.50[c]	5.36±0.06	3.90[c]	$0.41^{+0.14}_{-0.11}$	45	189	570	2519
NGC1097	<0.05	···	<0.18	···	···	···	···	···	···
NGC7469	1.16[a]	<1.50[c]	1.47[a]	0.63[c*]	$0.79^{+0.28}_{-0.21}$	3	149	41	1990
NGC4945	0.28±0.03	<0.50[d]	<0.75	···	>0.38	···	···	···	···
Circinus	23.94±0.61	31.70[c]	24.00±3.90	21.80[c]	$1.00^{+0.35}_{-0.26}$	···	135	···	1799
Mrk 231	<0.44[a]	<1.50[e]	<0.69[a]	···	···	···	···	···	···
Mrk3	6.45[a]	4.60[c]	6.75[a]	3.40[c]	$0.96^{+0.34}_{-0.25}$	···	138	···	1835
Cen A	2.32[a]	2.70[c]	2.99[a]	2.00[c]	$0.77^{+0.27}_{-0.20}$	4	150	56	2005
Mrk463	1.83[b]	1.40[c]	2.04[b]	···	$0.90^{+0.32}_{-0.23}$	···	141	···	1886
NGC 4826	···	···	···	···	···	···	···	···	···
NGC 4725	<0.09	···	0.09±0.03	···	<1.04	···	···	···	···
1 ZW 1	<0.11[a]	0.27[c]	<0.10[a]	···	···	···	···	···	···
NGC 5033	0.07±0.02	···	0.11±0.02	···	$0.65^{+0.23}_{-0.17}$	16	161	198	2146
NGC1566	0.16±0.05	···	0.22±0.04	···	$0.74^{+0.26}_{-0.19}$	7	153	92	2041
NGC 2841	<0.04	···	<0.03	···	···	···	···	···	···
NGC 7213	<0.04	···	<0.09	···	···	···	···	···	···
LINERs									
NGC4579	<0.06	···	<0.03	···	···	···	···	···	···
NGC3031	<0.06	···	<0.04	···	···	···	···	···	···
NGC6240	0.51[b]	<1.00[e]	<0.39[b]	···	<1.31	···	···	···	···
NGC5194	0.41±0.04	<0.20[c]	0.39±0.09	···	$1.06^{+0.37}_{-0.28}$	···	131	···	1751
MRK266**	0.21±0.02	0.50[f]	1.19±0.06	···	$0.18^{+0.06}_{-0.05}$	100	240	1254	3203
NGC7552	<0.11	···	<0.83	···	···	···	···	···	···
NGC 4552	<0.06	···	<0.07	···	···	···	···	···	···
NGC 3079	<0.07[a]	···	<0.14[a]	···	···	···	···	···	···
NGC 1614	<0.28	···	<1.49	···	···	···	···	···	···
NGC 3628	<0.06	···	<0.34	···	···	···	···	···	···
NGC 2623	0.30±0.04	···	0.47±0.07	···	$0.63^{+0.22}_{-0.14}$	17	163	218	2167
IRAS23128	0.22±0.02	<0.40[e]	0.34±0.10	···	$0.65^{+0.23}_{-0.22}$	16	161	203	2152
MRK273	1.06±0.05	0.82[e]	2.74±0.19	···	$0.39^{+0.14}_{-0.10}$	49	192	617	2565
IRAS20551	<0.06	<0.25[e]	<0.25	···	···	···	···	···	···
NGC3627	0.08±0.01	···	0.19±0.05	···	$0.45^{+0.16}_{-0.12}$	40	184	504	2453
UGC05101	0.52[b]	<1.50[e]	0.49[b]	···	$1.06^{+0.37}_{-0.28}$	···	131	···	1750
NGC4125	<0.03	···	<0.07	···	···	···	···	···	···
NGC 4594	<0.03	···	<0.04	···	···	···	···	···	···
Quasars									
PG1351···	<0.04	···	<0.07	···	···	···	···	···	···
PG1211···	0.04±0.007	···	<0.04	···	>1.01	···	···	···	···
PG1119···	0.30±0.06	···	0.22±0.02	···	$1.39^{+0.49}_{-0.36}$	···	115	···	1531
PG2130···	0.42±0.03	···	0.42±0.05	···	$1.00^{+0.35}_{-0.26}$	···	135	···	1798
PG0804···	<0.06	···	<0.07	···	···	···	···	···	···
PG1501···	0.78±0.02	···	0.83±0.02	···	$0.94^{+0.33}_{-0.25}$	···	138	···	1846

Columns Explanation: Col(1):Common Source Names; Col(2)-(3): 14.32 μm [NeV] line flux and statistical error in units of 10^{-20} W cm^{-2} from *Spitzer* and *ISO* respectively; Col(4)-(5): 24.31 μm [NeV] line flux and statistical error in units of 10^{-20} W cm^{-2} from *Spitzer* and *ISO* respectively; Col(6): [NeV] Line Ratio used in plots and calculations; Col(7): Extinction required to bring ratios below the low-density limit (LDL) up to the LDL, calculated using the Draine (1989) extinction curve amended by the more recent *ISO* SWS extinction curve toward the Galactic center for 2.5-10μm (Lutz et al. 1996); Col(8): Extinction required to bring ratios below the low-density limit (LDL) up to the high-density limit (HDL), calculated same as Col(7), Col(9): Extinction required to bring ratios below the low-density limit (LDL) up to the LDL, calculated using the Chiar & Tielens (2006) extinction curve for the local ISM, Col(10): Extinction required to bring ratios below the low-density limit (LDL) up to the high-density limit (HDL), calculated same as Col(9) $*$ Sturm et al. 2002 find that the [NeV] 24μm detection for NGC 7469 is a questionable one, $**$ As discussed in detail in Section 5.5.2, ratio for Mrk 266 is affected by aperture variations and has been excluded here. **References for Table 5.2:** [a] Weedman et al. 2005, [b] Armus et al. 2004 & 2006, [c] Sturm et al. 2002, [d] Verma et al. 2003, [e] Genzel et al. 1998, [f] Prieto & Viegas 2000

Table 5.3: SIII Line Fluxes and Derived Extinction

Galaxy Source	[SIII] 18.71 SH	[SIII] 18.71 ISO	[SIII] 33.48 LH	[SIII] 33.48 ISO	[SIII] Ratio	A_v LDL (D&L)	A_v HDL (D&L)	A_v LDL (C&T)	A_v HDL (C&T)	PAH 6.2 SL2
(1)	(2)	(3)	(4)	(5)	(6)	(7)	(8)	(9)	(10)	(11)
Seyferts										
NGC4151	7.50[a]	5.40[c]	6.57[a]	8.10[c]	$1.14^{+0.40}_{-0.30}$	···	···	···	···	168.1
NGC1365	5.73±0.05	13.50[c]	27.20±0.38	36.10[c]	$0.21^{+0.07}_{-0.05}$	···	···	···	···	132.3
NGC1097	2.18±0.02	···	11.40±0.23	···	$0.19^{+0.07}_{-0.05}$	···	···	···	···	151.7
NGC7469	7.70[a]	9.20[c]	9.80[a]	10.40[c]	$0.79^{+0.28}_{-0.20}$	···	···	···	···	415.0
NGC4945	3.18±0.03	6.30[d]	38.70±1.80	51.40[d]	$0.08^{+0.03}_{-0.02}$	···	···	···	···	671.7
Circinus	19.10±0.70	35.20[c]	56.30±3.31	93.20[c]	$0.37^{+0.13}_{-0.10}$	···	···	···	···	1018.4
Mrk 231	<0.47[a]	<3.00[e]	<2.30[a]	<3.00[e]	···	···	···	···	···	175.6
Mrk3	5.55[a]	···	5.25[a]	···	$1.06^{+0.37}_{-0.28}$	···	83	···	72	18.4
Cen A	4.54[a]	6.40[c]	14.80[a]	22.30[c]	$0.31^{+0.11}_{-0.08}$	···	···	···	···	220.8
Mrk463	1.50[b]	<0.80[c]	1.35[b]	1.20[c]	$1.11^{+0.39}_{-0.29}$	···	81	···	70	55.4
NGC 4826	3.39±0.03[f]	···	4.61±0.08[f]	···	$0.74^{+0.26}_{-0.19}$	···	96	···	82	66.2
NGC 4725	0.02±0.02[f]	···	0.11±0.02[f]	···	$0.23^{+0.08}_{-0.06}$	23	135	20	116	3.7
1 ZW 1	<0.11[a]	<0.50[c]	<0.18[a]	<1.00[c]	···	···	···	···	···	22.2
NGC 5033	0.85±0.11	···	2.42±0.10	···	$0.35^{+0.12}_{-0.09}$	···	···	···	···	33.9
NGC1566	0.55±0.05[f]	···	0.55±0.06[f]	···	$1.00^{+0.35}_{-0.26}$	···	85	···	73	61.0
NGC 2841	0.22±0.04[f]	···	0.29±0.03[f]	···	$0.75^{+0.26}_{-0.20}$	···	95	···	82	10.9
NGC 7213	0.47±0.05	···	0.59±0.06	···	$0.80^{+0.28}_{-0.21}$	···	···	···	···	28.7
LINERs										
NGC4579	0.32±0.06[f]	<0.78[g]	0.24±0.03[f]	<1.20[g]	$1.33^{+0.47}_{-0.35}$	···	75	···	65	17.3
NGC3031	0.61±0.03	···	0.09±0.09	···	$0.67^{+0.24}_{-0.18}$	···	···	···	···	23.4
NGC6240	1.99[b]	<4.00[e]	2.63[b]	4.50[e]	$0.76^{+0.27}_{-0.20}$	···	95	···	81	399[b]
NGC5194	1.06±0.05[f]	1.00[d]	1.48±0.03[f]	4.60[d]	$0.72^{+0.25}_{-0.19}$	···	96	···	83	26.4
MRK266**	1.00±0.13	···	4.65±0.09	···	$0.21^{+0.08}_{-0.06}$	25	138	22	118	23.1
NGC7552	17.11±0.08[f]	24.60[d]	13.38±0.41[f]	41.10[d]	$1.28^{+0.45}_{-0.33}$	···	77	···	66	872.0
NGC 4552	0.07±0.03[f]	···	0.06±0.02[f]	···	$1.29^{+0.45}_{-0.34}$	···	76	···	66	21.5
NGC 3079	1.25[a]	6.80[g]	6.08[a]	6.60[g]	$0.21^{+0.07}_{-0.05}$	···	···	···	···	620.3
NGC 1614	9.63±0.27	···	11.60±0.43	···	$0.83^{+0.29}_{-0.15}$	···	91	···	79	508.5
NGC 3628	2.14±0.03	···	15.80±0.33	···	$0.14^{+0.05}_{-0.04}$	···	···	···	···	430.4
NGC 2623	0.88±0.05	···	3.16±0.20	···	$0.28^{+0.10}_{-0.07}$	16	129	14	111	128.6
IRAS23128	2.62±0.12	0.89[e]	2.11±0.18	2.80[e]	$1.24^{+0.44}_{-0.32}$	···	78	···	67	90.1
MRK273	1.24±0.07	<0.82[e]	3.88±0.40	2.30[e]	$0.32^{+0.11}_{-0.08}$	12	124	10	107	69.2
IRAS20551	0.66±0.06	0.30[e]	1.18±0.13	1.40[e]	$0.56^{+0.20}_{-0.15}$	···	105	···	90	38.3
NGC3627	0.38±0.03[f]	···	0.57±0.09[f]	···	$0.67^{+0.24}_{-0.18}$	···	99	···	85	153.8
UGC05101	0.98[b]	<1.40[e]	1.30[b]	2.50[e]	$0.75^{+0.27}_{-0.20}$	···	95	···	82	190[b]
NGC4125	···[f]	···	0.06±0.05[f]	···	···	···	···	···	···	14.9
NGC 4594	0.39±0.03	···	1.24±0.13	···	$0.32^{+0.11}_{-0.08}$	···	···	···	···	14.2
Quasars										
PG1351···	0.34±0.06	···	<0.13	···	>2.70	···	···	···	···	29.6
PG1211···	<0.06	···	<0.08	···	···	···	···	···	···	25.8
PG1119···	<0.13	···	0.19±0.06	···	<0.71	···	···	···	···	8.7
PG2130···	<0.19	···	0.34±0.06	···	<0.55	···	···	···	···	26.9
PG0804···	<0.06	···	<0.21	···	···	···	···	···	···	27.4
PG1501···	0.67±0.15	···	0.41±0.05	···	$1.64^{+0.58}_{-0.43}$	···	68	···	59	19.2

Columns Explanation: Col(1):Common Source Names; Col(2)-(3): 18.71 μm [SIII] line flux and statistical error in units of 10^{-20} W cm^{-2} from *Spitzer* and *ISO* respectively; Col(4)-(5): 33.48 μm [SIII] line flux and statistical error in units of 10^{-20} W cm^{-2} from *Spitzer* and *ISO* respectively; Col(6):[SIII] line flux ratio used for plots and calculations; Col(7)-(8): Extinction required to bring ratios below the low-density limit (LDL) up to the LDL and up to the high-density limit (HDL) respectively, calculated using the Draine (1989) extinction curve amended by Lutz et al. (1996); Col(9)-(10): Extinction required to bring ratios below the low-density limit (LDL) up to the LDL and up to the HDL respectively, calculated using the Chiar & Tielens (2006) extinction curve for the Galactic Center; Col(7)-(10): For those galaxies with distances greater than 55 Mpc that are not effected by aperture variations** The ratios for Mrk 266 are excluded (See Section 5.5.2 for details); Col(11): 6.2 μm PAH line flux in units of 10^{-21} W cm^{-2} **References for Table 5.3:**[a] Weedman et al. 2005, [b] Armus et al. 2004 & 2006, [c] Sturm et al. 2002, [d] Verma et al. 2003, [e] Genzel et al. 1998, [f] Dale et al. 2006, [g] Satyapal et al. 2004.

the [NeV]-emitting regions. Is this reasonable? If there is significant extinction, it is possible that: 1) the [NeV]-emitting region originates much closer to the central source than previously recognized, close enough to be extinguished by the central torus in some galaxies, 2) the [NeV]-emitting portion of the NLR is obscured by dust in the host galaxy or in the NLR itself, or 3) some combination of these scenarios. We explore these possibilities in the following analysis.

5.5.1 The [NeV] originates in gas interior to the central torus.

In the conventional picture of an AGN, the broad line region (BLR) is thought to exist within a small region interior to a dusty molecular torus while the NLR originates further out. This of course is the paradigm invoked to explain the Type 1/Type 2 dichotomy. However there have been multiple optical spectroscopic studies that contradict the assumption that the observational properties of the NLR are not dependent on the viewing angle and the inclination of the system, suggesting that some of the narrow emission lines originate in gas interior to the torus. For instance, Shuder and Osterbrock (1981) and Cohen (1983) showed that narrow high ionization forbidden lines such as [Fe VII] λ 6374 (requiring photons with energies $\geq$ 100eV to ionize) are stronger relative to the low ionization lines in Seyfert 1 galaxies (including intermediate Seyferts, 1.2, 1.5 etc.) than in Seyfert 2 galaxies, suggesting that some of the emission is obscured by the torus. In addition, [FeX] λ 6374 and [NeV] λ 3426 have also been shown to be less luminous in Type 2 objects than in Type 1 objects (Murayama & Taniguchi, 1998a; Schmitt 1998, Nagao et al. 2000, 2001a, 2001b, 2003, Tran et al. 2000, see also Jackson and Browne (1990) for narrow line radio galaxies and quasars.) These findings may imply that the emission lines of species with the highest ionization potentials originate closer to the AGN than those of lower ionization species such as [OII]λ3727, [SII]$\lambda\lambda$6716, 6731, [OI] λ6300 etc. and therefore may be partially obscured by the central torus.

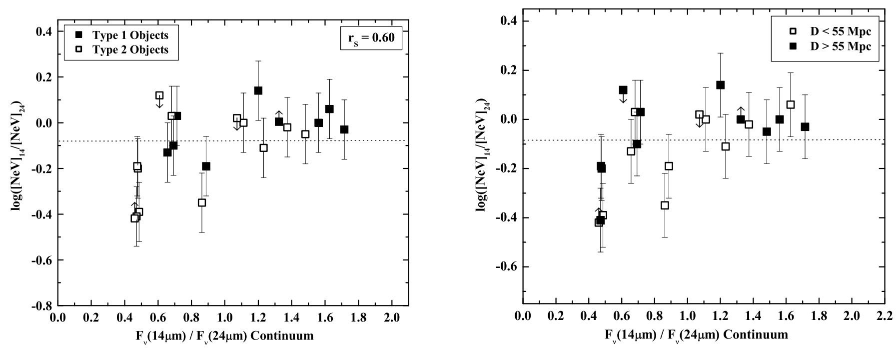

Figure 5.6: [NeV] line ratio vs. continuum ratio

The [NeV] line ratio vs. the $F_\nu(14\mu m)/F_\nu(24\mu m)$ continuum ratio for our sample. In both plots, the error bars mark the calibration uncertainties on the line ratio. There is a correlation between the line and continuum ratios which suggests that extinction affects the observed line flux ratios. 6a) The majority of galaxies with ratios below the LDL are Type 2 objects, implying that the extinction toward the [NeV]-emitting region may be due to the torus. 6b) The correlation shown here is not an artifact of aperture vatiations between the SH and LH slits. The correlation holds when only the most distant galaxies are considered.

If there is considerable extinction to the line-emitting regions due to the torus, one may expect the mid-infrared continuum to be similarly obscured. To test this scenario we divided our sample into Type 1 or Type 2 objects based on the presence or absence of broad (full width at half max (FWHM) exceeding 1000 km s^{-1}) Balmer emission lines in the optical spectrum. The spectral classification for the [NeV]-emitting galaxies is given in Table 5.1. In Figure 5.6a, we plot the [NeV] 14μm/24μm line flux ratio versus the 14μm/24μm continuum ratio of the [NeV] emitting galaxies in our sample. Assuming there is no correlation between the electron density and the continuum shape, a correlation between the line flux and continuum ratios would suggest that the mid-IR extinction associated with the torus (such as that found by Clavel et al. 2000) affects the observed line flux ratios. As can be seen, there is a correlation between the line and continuum ratios for galaxies with [NeV] emission. Moreover we note that the 3 nuclei with ratios significantly below the LDL are all Type 2 AGNs, while the 2 that lie significantly above this limit are Type 1 AGNs, suggestive that the extinction of the [NeV]-emitting region in Type 2 AGNs may be due to the torus. We note that the error bars displayed in Figure 5.6 are based on a conservative estimate (15%) of the absolute calibration error on the flux (see Section 5.3). Moreover, we have adopted the most conservative approach in propagating the error (see Section 5.4) for each line ratio. We further note that two of the three nuclei with ratios below the LDL were also observed in high-accuracy peak-up mode, resulting in a pointing accuracy on the continuum for these galaxies of 0.4". The third galaxy, NGC 3627, was observed in high resolution mapping mode over 15" X 22". We extracted the spectra and found that the full map and the single slit fluxes agree to within 10%. Thus pointing errors do not appear to be responsible for the low ratios in these galaxies. Finally we find that the ratios for the all galaxies except Mrk 266 are not sensitive to the line-fitting or flux extraction methods that we have employed.

The Spearman rank correlation coefficient for Figure 5.6 is 0.60 (with a probability of chance correlation of 0.008), indicating a significant correlation between the [NeV] line flux ratios and the mid-IR continuum ratio. We note that some AGNs are known to contain prominent silicate emission features (Hao et al. 2005, Sturm et al. 2005) which have not been disentangled from the underlying continuum in this study. Because of this, the 14μm or 24μm flux may be overestimated in some cases making intrinsic value of the continuum at 14μm and 24μm somewhat uncertain. However only one galaxy plotted in Figure 5.6 is currently known to contain such features (PG1211+143, Hao et al. 2005). Variations in n_e and the underlying continuum shape will also add scatter to the correlation, as will differences in extinction to the line- and continuum-producing regions. We should note that the correlation seen in Figure 5.6 is not an artifact of aperture variations between the LH and SH slit. The correlation holds when only the most distant galaxies (closed symbols in Figure 5.6b) are considered.

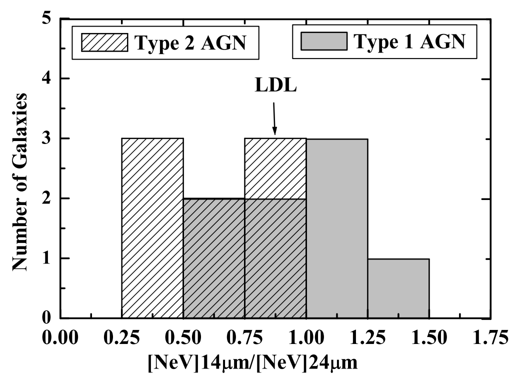

Figure 5.7: [NeV] line ratios for Type 1 and Type 2 AGNs

Histogram of the [NeV] 14μm/24μm line flux ratio as a function of AGN type. The [NeV] line ratios for Type 2 AGNs are consistently lower than those from Type 1 AGNs.

Independent of this correlation, *our most important finding is that the [NeV] line flux ratio is significantly lower for Type 2 AGNs than it is for Type 1 AGNs.* Figure 5.7 shows the relative [NeV] flux ratios for the Type 1 and Type 2 objects in our sample. The mean ratios are 0.97 and 0.72 for the eight Type 1 and ten Type 2 AGNs, respectively, with uncertainties in the mean of about 0.08 for each. Interestingly, although the sample size is limited, precluding us from drawing firm statistically significant conclusions, there is a similar suggestive trend seen in the sample of AGNs observed by Sturm et al. (2002) with *ISO*-SWS. That is, in their work, the two galaxies with the lowest [NeV] flux ratios are NGC 1365 and NGC 7582, both Type 2 AGNs. The galaxy with the highest ratio in their work is TOL 0109-383 , a Type 1 AGN.

If indeed the torus obscures the IR [NeV] emission in Type 2 objects, one would expect the optical/UV [NeV] emission in these objects to be obscured as well. We searched the literature for optical/UV detections of [NeV] λ3426 for all of the galaxies in our sample and found five galaxies with observations at this wavelength. Four of these galaxies (Mrk 463, Mrk 3, NGC 1566, and NGC 4151) were detected at [NeV] λ3426; the other (NGC 3031) was not detected (see, Kuraszkiewicz et al. 2002, 2004 and Forster et al. 2001 for optical/UV fluxes). Of the four galaxies with optical/UV [NeV] detections, two are Type 1 galaxies (NGC 1566 & NGC 4151) and, surprisingly, two are Type 2 galaxies (Mrk 3 and Mrk 463). If the Type 2 galaxies Mrk 3 and Mrk 463 had [NeV] emitting regions interior to the torus, then the optical/UV lines in these objects should not be detected due to severe obscuration. We note that Mrk 3 and Mrk 463 have some of the highest X-ray luminosities (both $\sim 10^{43}$ erg s^{-1}) in the sample and mid-IR [NeV] ratios that are comparable to similarly luminous Type 1 objects–consistent with little or no obscuration in the mid-IR for these Type 2 galaxies. This finding may imply that, in the most powerful AGNs, the [NeV] emitting region is pushed beyond the torus because the radiation field is so intense, while lines with higher ionization potentials than [NeV] (such as [NeVI], [FeX] etc.) are still concealed by the torus. More data, both from the mid-IR and from the optical/UV, are needed to further test this hypothesis.

5.5.2 The [NeV]-emitting region is obscured by the host galaxy or dust in the NLR.

While the correlation in Figures 5.6a and 5.6b are very promising explanations for the observed [NeV] line ratios, it is not completely clear why some Type 2 galaxies appear obscured and others may not. Perhaps the [NeV] emission is attenuated by dust in the NLR itself or elsewhere in the host galaxy. Indeed, it is well-known that dust does exist in the NLR (e.g., Radomski et al. 2003, Tran et al. 2000) and that it can be extended and patchy (e.g Alloin et al. 2000; Galliano et al. 2005; Mason et al. 2006). In addition, dust in the host galaxy could be responsible for the extinction seen here. For completeness, we have conducted a detailed archival analysis of all of the galaxies in our sample with [NeV] ratios close to or below the LDL in order to see if there is additional evidence for high extinction either in the host galaxy or within the NLR. We find that the majority of galaxies with low densities do indeed have well-known dust lanes, large X-ray inferred column densities, or other properties indicative of extinction.

Cen A: This nearby (D = 3.4Mpc) early type (S0) galaxy at one time devoured a smaller gas-rich spiral galaxy (Israel 1998, Quillen et al. 2006). There is clear evidence for substantial obscuration toward the nucleus of Cen A. For example, the central region is veiled by a well known dense dust lane thought to be a warped thin disk (Ebneter & Balick 1983, Bland et al. 1986, 1987, Nicholson et al. 1992, Sparke 1996, Israel 1998, Quillen et al. 2006). Schreier et al. (1996) find V-band extinction averaging 4-5 mag and infrared observations by Alonso & Minniti yield A_V values exceeding 30 mag in some regions. Thus, it is plausible that there are regions toward the nucleus of Cen A that are obscured even at infrared wavelengths.

NGC 1566: The optical nuclear spectrum of this nearby galaxy is known to vary dramatically over a period of months, changing its optical classification from a Type 2 object to a Type 1 object and back again (Pastoriza & Gerola 1970, de Vaucouleurs 1973, Penfold 1979, Alloin et al. 1985). The narrow optical lines in this object also show prominent blue wings and the radio properties of this galaxy are more consistent with a Type 2 object than a Type 1 object (Alloin et al. 1985). HST continuum imagery reveals spiral dust lanes within 1" of the nucleus (Griffiths et al. 1997) which might be responsible for the Type 1/Type 2 variability. Baribaud et al. (1992) find hot dust which lies just outside the broad line region in this galaxy and a large covering factor that might explain the steep continuum of the AGN. Ehle et al. (1996) find $N_H \sim 2.5 \times 10^{20}$ cm^{-2} from ROSAT X-ray observations of this galaxy.

NGC 2623: This galaxy's tidal tails are evidence of a merger event, however infrared observations reveal a single symmetric nucleus, implying that the merging galaxies have coalesced. Multi-color, near infrared observations reveal strong concentrations of obscuring material in the central 500 pc.(Joy & Harvey 1987; Lipari et al. 2004). Lipari et al. (2004) also find an optically obscured nucleus with V-band extinction ≥ 5 mag.

IRAS 23128-5919: This galaxy is also in the late stages of a merger. The nuclei of the two galaxies are 4kpc apart and have not yet coalesced. The northern nucleus is a starburst. The southern nucleus is a known AGN, though its optical classification, Seyfert or LINER, is unclear (Duc, Mirabel, & Maza 1997; Charmandaris et al. 2002; Satyapal et al. 2004). IRAS 23128-5919 is an ultraluminous infrared galaxy (ULIRG), clearly consistent with the presence of substantial dust towards the nucleus. Optical spectroscopy of the southern nucleus indicates very large (1500 km s^{-1}) blue asymmetries in the Hβ and [OIII] lines. This blue wing could be a signature of extinction toward the far side of an expanding region, where the red wing is preferentially obscured. (Johansson & Bergvall 1988).

Mrk 273: This galaxy is also a ULIRG, so significant dust obscuration toward the nucleus is expected. Near-IR imaging and high resolution radio observations show evidence for a double nucleus in this galaxy separated by less than 1 kpc (Ulvestad & Wilson 1984; Mazzarella et al. 1991; Majewski et al. 1993). However, high resolution Chandra observations reveal only the northern of the two nuclei, suggesting that this galaxy is hosting only one AGN and that perhaps the other "nucleus" is in fact a portion of the southern radio jet. The soft X-ray emission from the northern nucleus is obscured by column densities of at least 10^{23} cm^{-2} (Xia et al. 2002). Although the X-ray-emitting regions are physically distinct from the NLR and some of the obscuration at X-ray wavelengths likely arises in dust-free gas within the sublimation radius, the high column density derived may be consistent with high extinction toward the central regions of this galaxy. Though Xia et al (2002) find that the X-ray morphology of the AGN in Mrk 273 is consistent with a Seyfert, Colina et al. (1999) find that it has a LINER optical spectrum, thus implying that some LINER galaxies are in fact heavily absorbed powerful AGN. The soft diffuse X-ray halo in combination with the radio morphology found by Carilli & Taylor (2000) may suggest a circumnuclear starburst surrounding the northern AGN nucleus, again consistent with substantial obscuration toward the AGN.

NGC 3627: This nearby galaxy (D $\sim$ 10Mpc) is thought to have had tidal interactions with NGC 3628, a neighboring galaxy in the Leo Triplet, some 8×10^8 years ago which caused an intense burst of star formation in the nuclear regions around the same time (Rots 1978, Zhang et al. 1993, Afanasiev & Sil'chenko 2005). Zhang et al. (1993) also discovered an extremely dense molecular bar (mass $\geq 4 \times 10^8$ M$_\odot$) and

Chemin et al. (2003) uncovered a warped disk using Hα observations, both evidence of the tidal interaction. In their spectral fitting to the BeppoSAX observation of NGC 3627, Georgantopoulos et al. (2002) find intrinsic column densities of $\sim 1.5 \times 10^{22}$ cm^{-2} which, like Mrk 273, may suggest substantial extinction to other regions near the nucleus.

NGC 7469: This is a well-known, extensively-studied galaxy with strong, active star formation surrounding a Seyfert 1 nucleus. Meixner et al. (1990) find dense molecular gas (2×10^{10} M$_{\odot}$), two orders of magnitude above the Galactic value, within the central 2.5kpc of the nucleus. 3.3μm imaging of the galaxy reveals that 80% of the PAH emission comes from an annulus $\sim$ 1"-3"in radius around the central nucleus, indicating that there is an elongated region of material that shelters the PAH from the harsh radiation field of the AGN (Cutri et al. 1984, Mazzarella et al. 1994). [OIII] line asymmetries may corroborate the presence of a dense obscuring medium, revealing a blue wing resulting when the redshifted gas is obscured by the star forming ring (Wilson et al. 1986). In addition, Genzel et al. (1995) find variation in the NIR emission attributable to extinction and estimate the extinction from the CO observations of Meixner et al. (1990) to be A$_V$ $\sim$ 10 mag.

NGC 1365: This nearby (D = 18.6 Mpc) AGN is known to be circumscribed by embedded young star clusters. The galaxy also contains a prominent bar with a dust lane that penetrates the nuclear region (Phillips et al. 1983, Lindblad et al. 1996 & 1999, Galliano et al. 2005). Like NGC 7469, NGC 1365 shows a peak at 3.5μm implying PAH emission in spite of the harsh AGN radiation field (Galliano et al. 2005). The large Hα/Hβ ratio found by Alloin et al. (1981) implies substantial extinction toward the emission line regions, ranging from 3-4 mag. Observations with ASCA and ROSAT imply high intrinsic column densities toward the X-ray emitting regions, suggesting possibly high obscuration towards other regions near the nucleus (Iyomoto et al. 1997, Komossa & Schulz (1998), see also Schulz et al. 1999). Komossa & Schulz show that the ratio of Hα to both the mid-IR and X-ray radiation is substantially different in NGC 1365 compared with typical Seyfert 1 galaxies, possibly suggesting inhomogenous obscuration (Schultz et al. 1999). In an XMM X-ray study of NGC 1365, Risaliti et al. (2005) also find a heavily absorbed Seyfert nucleus. The blueshifted X-ray spectral lines imply high column densities of 10^{23} cm^{-2} or more.

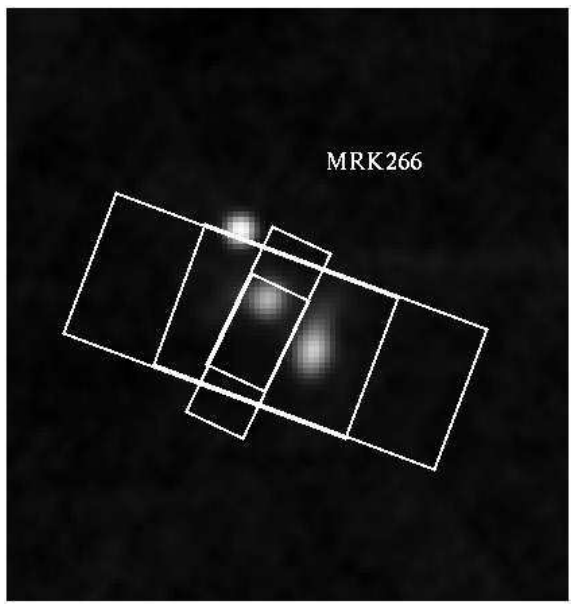

Figure 5.8: Mrk 266: aperture effects

20 cm image of Mrk 266 taken from NED (http://nedwww.ipac.caltech.edu/). As can be seen here, the SH slit (from which the 14μm line is extracted) overlaps with a third radio source, while the LH slit (from which the 24μm line is extracted) encompasses the southwestern nucleus and part of the northeastern nucleus.

Mrk 266 (NGC 5256): This luminous infrared galaxy is the only galaxy for which aperture effects most likely account for the low 14μm/24μm ratio. Mrk 266 contains a very complicated structure which includes at least two bright nuclei, a Seyfert and a LINER, that are 10" apart–a signature of a merger in progress. The morphology of the northeast LINER nucleus is extremely controversial (Wang et al. 1997; Kollatschny & Kowatsch 1998; Satyapal et al. 2004, 2005; Ishigaki et al. 2000; Davies, Ward, & Sugai 2000). Mazzarella et al. (1988) find three non-thermal radio structures, two that coincide with the nuclei and one between the two nuclei. Mazzarella et al. (1988) suggest that the two nuclear structures are associated with classical AGNs and are in the stage of a violent interaction in which the center of gravity of the collision produces a massive burst of star formation with supernovae or shocks which are responsible for the third nonthermal radio source. As can be seen in Figure 5.8, the SH slit, which provides the 14μm flux, overlaps with this third radio source, while the LH slit, responsible for the 24μm flux, encompasses the southwestern nucleus, the third radio source, and part of the northeastern nucleus. In this case the two lines observed originate in physically distinct regions that do not each encompass all potential sources of [NeV] emission, resulting in an unphysical 14μm/24μm ratio. This is not to say that Mrk 266 does not suffer from extinction at all. Indeed the possible presence of a circumnuclear starburst implies that there may be substantial extinction (Ishigaki et al. 2000; Davies, Ward, & Sugai 2000). We have verified that this is the only distant galaxy in our sample with a complicated nuclear structure that will result in aperture effects.

5.5.3 Can the [NeV] line flux ratio be used as a density diagnostic?

Our analysis reveals that extinction towards parts of the NLR in some objects is significant and cannot be ignored at mid-IR wavelengths. In fact, it is quite possible that extinction affects the [NeV] line flux ratios of those galaxies with ratios above the low density limit (LDL) and the amount of extinction in all cases is highly uncertain. In addition to extinction, the temperature of the [NeV] emitting gas is unknown. If the [NeV] emission originates within the walls of the obscuring central torus, which may be the source of extinction in many of our galaxies, we might expect the temperature of the gas to reach 10^6 K (Ferland et al. 2002). If, on the other hand, the [NeV] emission comes from further out in the NLR and is instead attenuated by the intervening material, we might expect the temperature of the gas to be closer to 10^4 K. As shown in Figure 5.1, the electron densities inferred from the [NeV] line flux ratios are sensitive to temperature when such large temperature variations are considered. Based on the calculations shown in Figure 5.1, the low ratios could indicate that the densities in the [NeV] line emitting gas are typically ≤ 3000 cm^{-3} for T = 10^4 K. However, if the [NeV] gas is characterized by temperatures as high as T = 10^5 K to 10^6 K, densities as high as 10^5 cm^{-3} would be consistent with our measurements. We note that the [NeV] line flux ratios for the galaxies in our sample (especially the Type 1 AGNs) all cluster around a ratio of ≈ 1.0. Two separate conclusions may be drawn from this finding: 1) That the temperatures of the gas are low ($\sim 10^4$ K) and that the electron density is relatively constant over many orders of magnitude in X-ray Luminosity and Eddington Ratio for these AGNs, or 2) That the temperature of the gas is high (10^5 K to 10^6 K) and that the AGNs here sample a wide range of electron densities (from 10^2 cm^{-3} to 10^5 cm^{-3}). Since gas temperature, electron density, mid-IR continuum, and extinction are all unknown for these objects, the electron density cannot be determined here.

5.6 The SIII Line Flux Ratios

In Figure 5.9 we plot the $18\mu m/33\mu m$ line ratio as a function of electron density n_e. As with [NeV], we only consider the five levels of the ground configuration when computing the line ratio and we plot the relationship for gas temperatures of $T = 10^4$ K and 10^5K. We adopt collision strengths from Tayal & Gupta (1999) and radiative transition probabilities from Mendoza & Zeippen (1982).

In Table 5.3, we list the observed [SIII] line flux ratios for the galaxies in our sample. As with the [NeV] ratios, the [SIII] ratios in many galaxies listed in Table 5.3 are well below the theoretically allowed value of 0.45 for a gas temperature of $T = 10^4$ K (13/33 detections). Again we explore the observational effects and the theoretical uncertainties that could artificially lower these ratios.

Aperture Effects: The ionization potential of [SIII] is $\sim$ 35 eV and therefore the [SIII] emission may arise from gas ionized by either the AGN or young stars. In Table 5.3 we list, in addition to our *Spitzer* [SIII] fluxes, all available [SIII] fluxes from ISO. Unlike [NeV], the [SIII] fluxes from ISO are significantly larger than the *Spitzer* fluxes for most galaxies. In Figure 5.10 we plot the *ISO* to *Spitzer* flux ratios for the 18μm and 33μm the [SIII] lines. As can be seen here, the [SIII] emission extends beyond the *Spitzer* slit for many galaxies (6 out of 9 for [SIII] 18μm and 11 out of 13 for [SIII] 33μm). Similarly, when we compare the [SIII] flux arising from a single slit centered on the nucleus to the flux arising from a more extended region obtained using mapping observations (Dale et al. 2006), we find that in most cases the fluxes from the extended region are much larger than the nuclear single-slit fluxes. Galaxies with fluxes from Dale et al. (2006) are not included in Figure 5.10 since the extraction aperture for these galaxies is comparable to the 18μm *ISO* slit. We point out that the value for this ratio is dependent on the orientation of the *Spitzer* slit relative to the *ISO* slit and on the distance of each object. We also note that IRAS20551 and IRAS23128 are point sources with *Spitzer* 18μm fluxes greater than the *ISO* fluxes from Genzel et al. (1998), however they fall within the Genzel et al. (1998) quoted errors of 30% and the Spitzer calibration error of 15%. Figure 5.10 suggests that the [SIII] emission may be produced in the extended, circumnuclear star forming regions associated with many AGNs and that *aperture effects need to be considered in our analysis of the [SIII] ratio for nearby objects.* The contribution from star formation

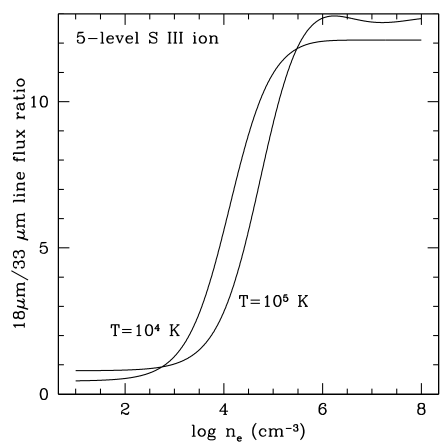

Figure 5.9: [SIII] line ratio vs. electron density

[SIII] 18μm33μm line flux ratio versus electron density n_e, for gas temperatures $T = 10^4$ K and 10^5 K.

to the [SIII] lines can be estimated using the strength of the PAH emission, one of the most widely used indicators of the star formation activity in galaxies (e.g. Luhman et al. 2003; Genzel et al. 1998; Roche et al. 1991; Rigopoulou et al. 1999, Clavel et al.

2000; Peeters, Spoon, & Tielens 2004). We examined the [SIII] 18.71 μm/PAH 6.2 μm and [SIII] 33.48 μm/PAH 6.2 μm line flux ratios in 7 starburst galaxies observed by *Spitzer* and found them to be comparable to the analogous ratios in our entire sample of AGNs as shown in Figure 5.11. This suggests that the bulk of the [SIII] emission originates in gas ionized by young stars. We note that the apertures of the SH and LH IRS modules are smaller than that of the SL2 module, which may artificially raise the line ratios plotted in Figure 5.11 for nearby galaxies compared with the more distant ones. However, the fact that the line ratios plotted in Figure 5.11 span a very narrow range suggests that the [SIII] line emission has a similar origin in starbursts and in AGNs. Thus, we assume that the bulk of the [SIII] emission originates in gas ionized by young stars and that the electron densities derived using these lines taken from slits of the same size (such those galaxies coming from Dale et al. 2006 mapping observations) or from the most distant galaxies are representative of the gas density in star forming regions.

Extinction: We have shown that aperture effects are the likely explanation for why many of the [SIII] ratios for the galaxies in our sample fall below the LDL. However, there are three galaxies in the sample with ratios below the LDL that are distant enough (D>55 Mpc, corresponding to projected distances greater than 1.2 by 3 kpc and 3 by 6 kpc for the SH and LH slits, respectively) that aperture effects may not be as important (NGC 2623 & Mrk 273, Mrk 266 has been excluded since it is known to be affected by aperture variations See Section 5.5.2). Extinction may be the explanation for the low ratios in these galaxies. However, even though the SH and LH slits likely cover the entirety of the NLR at these distances, we note that these three galaxies contain well-known, large circumnuclear starbursts (See Section 5.5.2 for the individual galaxy summaries) which may produce extremely extended

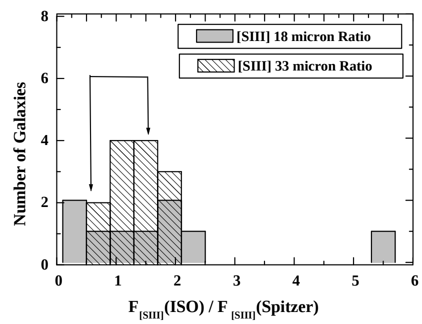

Figure 5.10: *ISO* and *Spitzer* [SIII] line fluxes

The ratios of the [SIII] flux from *ISO* and *Spitzer* for the 18μm and 33μm lines. The range indicated with arrows is that corresponding to the absolute flux calibration for *ISO* (20%) and *Spitzer* (15%). The [SIII] emission is indeed extended beyond the *Spitzer* slit for many galaxies, suggesting that the [SIII] emission may be produced in star forming regions. We note that IRAS20551 and IRAS23128 are point sources with *Spitzer* 18μm fluxes greater than the *ISO* fluxes from Genzel et al. 1998, however they fall within the Genzel et al. (1998) quoted errors of 30% and the Spitzer calibration error of 15%. Galaxies with fluxes from Dale et al. 2006 are not included in this plot since the extraction aperture for these galaxies is comparable to the 18μm *ISO* slit.

[SIII] emission. It is therefore still possible that the line ratios in these galaxies are artificially lowered by aperture variations between the SH and LH slits. However, in addition to these three distant galaxies, NGC 4725 from Dale et al. (2006) has a [SIII] ratio below the low density limit. The low [SIII] ratio (<0.45) in this case cannot be attributed to aperture variations since the extraction region is the same for both the 18 and 33μm lines. Thus, for completeness, the extinction derived using the extinction curves given in Section 5.4 from the observed [SIII] line ratio for these four sources are given in Table 5.3. The Draine (1989) and Lutz et al. (1996) extinction curve calculations yield extinction values that range from $\sim$ 12 to 25 mag. The Chiar and Tielens (2006) extinction curve for the Galactic Center may also be used since, unlike [NeV], the extinction at the longer wavelength line (33μm) is greater than that at the shorter wavelength line (18μm). The values derived from this method are quite similar, ranging from $\sim$ 10 to 22 mag. The Chiar and Tielens (2006) extinction curve from the local ISM cannot be used here since it only extends to 27.0μm. **Computed Quantities:** As with NeV, there may be uncertainties in the computed SIII infrared collisional rate coefficients. However, there is generally less controversy surrounding the [SIII] coefficients and these values are widely accepted.

Our analysis suggests that aperture effects severely influence the [SIII] line flux ratios in most cases and that the observed flux is likely dominated by star forming regions. Figure 5.12, a plot of the [SIII] line ratio as a function of distance, illustrates the influence of aperture effects on the [SIII] line ratio. Most of the galaxies at distances <55 Mpc with [SIII] fluxes extracted from apertures of different sizes (i.e. NOT the Dale et al. (2006) galaxies) are below the LDL. On the other hand, galaxies at larger distances and galaxies with fluxes from Dale et al. (2006) are generally above the LDL. Thus, for the most distant galaxies in our sample and the galaxies

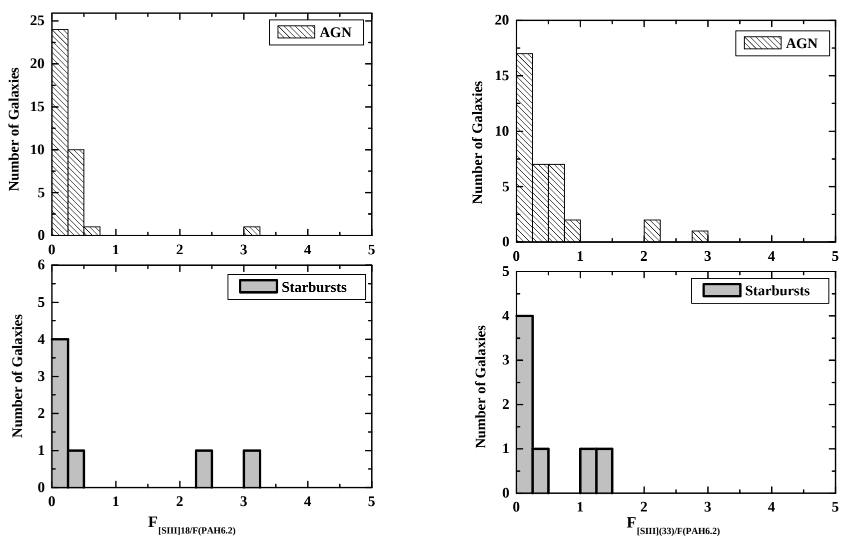

Figure 5.11: [SIII]/PAH for AGNs and starbursts

Distribution of the [SIII]33μm/PAH 6.2μm and the [SIII]18μm/PAH 6.2μm line flux ratios for our sample of AGNs and a small sample of starburst galaxies observed by *Spitzer*. It is apparent that the line ratios of the AGNs are comparable to the corresponding ratios in starbursts, suggesting that the bulk of the [SIII] emission originates in star forming regions and not the NLRs in our sample of AGNs.

with fluxes from Dale et al. (2006) where the aperture for the 18 and 33 μm lines are equal, aperture effects are not problematic, but extinction, as can be seen from Mrk 273, NGC2623, and NGC 4725 in Figure 5.12, needs to be considered. As with the [NeV] line ratio, the [SIII] line ratio is NOT a tracer of the electron density in our sample. In conclusion, the ambiguity of the intrinsic [SIII] line ratio is primarily the result of aperture variations. However there is at least one case (NGC 4725) where aperture effects cannot explain the low ratio, implying that, in addition to aperture variations, extinction likely plays a role in lowering the [SIII] line flux ratios.

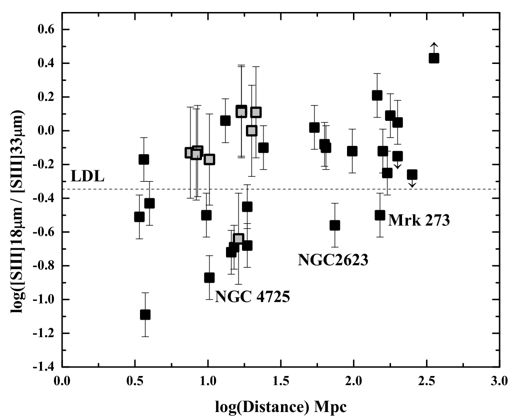

Figure 5.12: [SIII] line ratios vs. distance

The [SIII] 18μm/33μm line ratio as a function of distance. The error bars shown here mark the calibration uncertainties on the line ratio. Dale et al. (2006) quote 30% calibration error which is shown here for those galaxies. For the rest of the sample the calibration error is 15% as per the Spitzer handbook. Most of the galaxies at distances <55 Mpc with [SIII] fluxes extracted from apertures of different sizes (i.e. not the Dale et al. (2006) galaxies) are below the LDL. However, for the most distant galaxies in our sample and the galaxies with fluxes from Dale et al. (2006) where the aperture for the 18 and 33 μm lines are equal, aperture effects are not problematic, but extinction needs to be considered (see Mrk 273, NGC2623, and NGC 4725 above).

5.7 Summary

We report in this paper the [NeV] 14μm/24μm and [SIII]18μm/33μm line flux ratios, traditionally used to measure electron densities in ionized gas, in an archival sample of 41 AGNs observed by the *Spitzer Space Telescope.*

1. We find that the [NeV] 14μm/24μm line flux ratios are low: approximately 70% of those measured are consistent with the low density limit to within the calibration uncertainties of the IRS.

2. We find that Type 2 AGNs have lower [NeV] 14μm/24μm line flux ratios than Type 1 AGNs. The mean ratios are 0.97 and 0.72 for the eight Type 1 and ten Type 2 AGNs, respectively, with uncertainties in the mean of about 0.08 for each.

3. For several galaxies, the observed [NeV] line ratios are below the theoretical low density limit. All of these galaxies are Type 2 AGNs.

4. We discuss the physical mechanisms that may play a role in lowering the line ratios: differential mid-IR extinction, low density, high temperature, and high mid-IR radiation density.

5. We argue that the [NeV]-emitting region likely originates interior to the torus in many of these AGNs and that differential infrared extinction due to dust in the obscuring torus may be responsible for the ratios below the low density limit. We suggest that the ratio may be a tracer of the torus inclination angle to our line of sight.

6. Our results imply that the extinction curve in these galaxies must be characterized by higher extinction at 14μm than at 24μm, contrary to recent

studies of the extinction curve toward the Galactic Center.

7. A comparison between the [NeV] line fluxes obtained with *Spitzer* and *ISO* reveals that there are systematic discrepancies in calibration between the two instruments. However, our results are independent of which instrument is used; [NeV] line flux ratios are consistently lower in Type 2 AGNs than in Type 1 and [NeV] line flux ratios below the LDL are observed with both ISO and Spitzer.

8. Our work provides strong motivation for investigating the mid-IR spectra of a larger sample of galaxies with *Spitzer* in order to test our conclusions.

9. Finally, an analysis of the [SIII] emission reveals that it is extended in many or all of the galaxies and likely originates in star forming gas and NOT the NLR. Since there is a variation in the apertures between the SH and LH modules of the IRS, we cannot use the [SIII] line flux ratios to derive densities for the majority of galaxies in our sample.

Chapter 6: CURRENT WORK: A *SPITZER* MID-IR SPECTROSCOPIC SURVEY OF A LARGE SAMPLE OF LINERS–A SEARCH FOR THE BIG BLUE BUMP

This Chapter is in preparation by R. P. Dudik, S. Satyapal, & D. Marcu, 2007

6.1 Introduction

In this Chapter, We present an extensive mid-Infrared (mid-IR) analysis of an archival sample of LINERs observed by Spitzer. In Chapters 3 and 4, the X-ray analysis shows an AGN detection rate in LINERs of $\sim 50\%$. We find that the majority of these AGN-LINERs contain active black holes with very low accretion rates, corroborating some of the previous studies discussed in Chapter 1. This study investigates the mid-Infrared properties of a large sample of LINERs. We use the high-ionization mid-IR [NeV] 14 or 24μm lines to search for AGNs in LINERs. Presence of either of these lines (ionization potential = 97eV) constitutes strong evidence for an active black hole, since [NeV] is not readily produced by HII regions, the ionizing source in star forming regions. Therefore, the central goal of this study is to search for AGNs in LINERs using the diagnostic power of [NeV], and to compare the mid-IR AGN detection rate with those from other bands.

This Chapter is structured as follows. Section 6.2 summarizes the properties of the *Spitzer* sample. Section 6.3 describes the data reduction and analysis for the mid-IR observations and present the mid-IR line fluxes for the sample. In Section 6.4

the mid-IR AGN detection rate is presented and in Section 6.5 this mid-IR detection rate is compared with other multi-band AGN indicators. In Section 6.6 the mid-IR line ratios in LINERs are examined and these ratios are compared with others from a sample of standard AGNs. Finally, a summary of the major conclusions is given in Section 6.7.

6.2 Sample Selection and Data Analysis

The optical spectroscopic definitions of LINERs have changed since the discovery and classification of these objects by Heckman (1980). Veilleux & Osterbrock (1987) redefined LINERs in order to minimize some of the observational effects associated with optical spectroscopy such as reddening, line blending, and abundance sensitivities. Ho, Filippenko, & Sargent (1997, hereafter H97) further refined these definitions to distinguish a new class of objects called "Transition Objects," (TO) with ratios of [OI] to Hα intermediate between LINERs and HII regions. Because the extraction aperture often varies from study to study and because the line ratios from the most distant galaxies will naturally come from larger intrinsic extraction regions, what is a LINER (or even a TO or HII region) in one optical observation may have a very different classification in another smaller-aperture observation. As a result, the definition of a "true" LINER is somewhat ambiguous and depends largely on the aperture size and the distance to the object. In addition, objects will often adhere to three of the four line-ratio criteria, but display a characteristic HII or Seyfert ratio for the fourth. These objects are, by definition, intermediary between LINERs and Seyferts or LINERs and HII regions. Therefore, while the chosen classification scheme for this investigation is that of Veilleux & Osterbrock (1987), all of the objects in the sample must also adhere to all four LINER criteria, thus making the sample selection more robust.

As emphasized in Chapter 1, the majority of LINERs are luminous in the far-IR (FIR) and span a wide range of far-IR to optical B-band ratios (IR-brightness ratios, Dudik et al. 2005, Satyapal 2005). Therefore a critical criterion for any statistically significant, representative sample of these objects is inclusion of both IR-bright and luminous infrared LINERs. As a result, the sample of LINERs presented here is derived from the Polamar survey of bright nearby galaxies (containing predominantly IR-faint LINERs, H97) *and* the Veilleux et al. (1995, hereafter V95) sample of luminous infrared galaxies (containing IR-bright LINERs). A subsequent search of the *Spitzer* archive for the subset of LINERs with high-resolution Infrared Spectrometer (IRS; Houck et al. 2004) observations yielded 67 available galaxies. The resulting sample of galaxies span a wide range of distances (2 to 276 Mpc; median = 28 Mpc), Hubble types, far-IR luminosities (log (L_{FIR}) $\sim$ 41 to 45, median = 43, Far-IR luminosities correspond to the 40-500μm wavelength interval and were calculated using the IRAS 60 and 100 μm fluxes according to the prescription: L_{FIR}=$1.26\times10^{-14}(2.58f_{60}+f_{100})$ in W m^{-2} (Sanders & Mirabel 1996)), and IR-brightness ratios (L_{FIR}/L_B $\sim$ 0.02 to 158, median = 1). The basic properties of the sample are given in Figure 6.1 and Tables 6.1 and 6.2. We note that the objects presented here were selected based on their LINER classification, their Far-IR properties and the availability of high resolution IRS *Spitzer* observations. Therefore the sample should not be viewed as complete in any sense.

The 67 observations presented in this work are archived from various programs, and therefore contain both mapping and staring observations. All of the staring observations presented were analyzed as per the prescription in Chapter 2.2. However the mapping observation presented in this study were analyzed slightly differently. In order to isolate the nuclear region in the mapping observations, fluxes were extracted from a single slit (instead of 3 slits, e.g. Chapter 2.2) coinciding with the radio or *2MASS* nuclear coordinates. The surrounding slits were also checked to ensure that detections of some of the high ionization lines presented were not missed either because of incorrect nuclear coordinates or because of low signal-noise characteristic of many the mapping observations. In all cases final fluxes presented from mapping observations resulted from the single, nuclear slit. In Table 6.3 we list the line fluxes, statistical errors, and upper limits from the SH and LH observations for the [NeII] 12μm, [NeV] 14μm, [NeIII] 15μm, [NeV] 24μm and the [OIV] 26μm lines.

6.3 Mid-IR Detection Rate

The Mid-IR band is abundant with emission lines from ions with a wide range of ionization potentials. Most of these lines have relatively low ionization potentials and are characteristic of prototypical starbursts as well as AGNs (Genzel et al. 1998, Alexander et al. 1999, Lutz 2002, Sturm et al. 2002, Satyapal et al. 2004). However, with an ionization potential of 97eV, the [NeV] 14.3 and 24.3μm lines are not readily produced by the HII regions surrounding young stars–the dominant energy source in starbursts. Conversely, the accretion disk of an active black hole is capable of producing ionizing UV photons needed to generate these mid-IR [NeV] lines. In light of this, detection of the mid-IR [NeV] emission lines as an alternate to optical and X-ray diagnostics is proposed as means to detect buried AGNs in LINER galaxies.

[NeV] emission is detected in 26 of the 67 galaxies in this sample, yielding an AGN detection rate in LINERs of 39%. The fluxes of the 14 and 24μm [NeV] detections are given in Table 6.2. The [NeV] spectra, as well as the [NeIII] 15.6μm and [OIV]μm spectra, when available, are shown in Figure 6.2. Because the sample is made up of

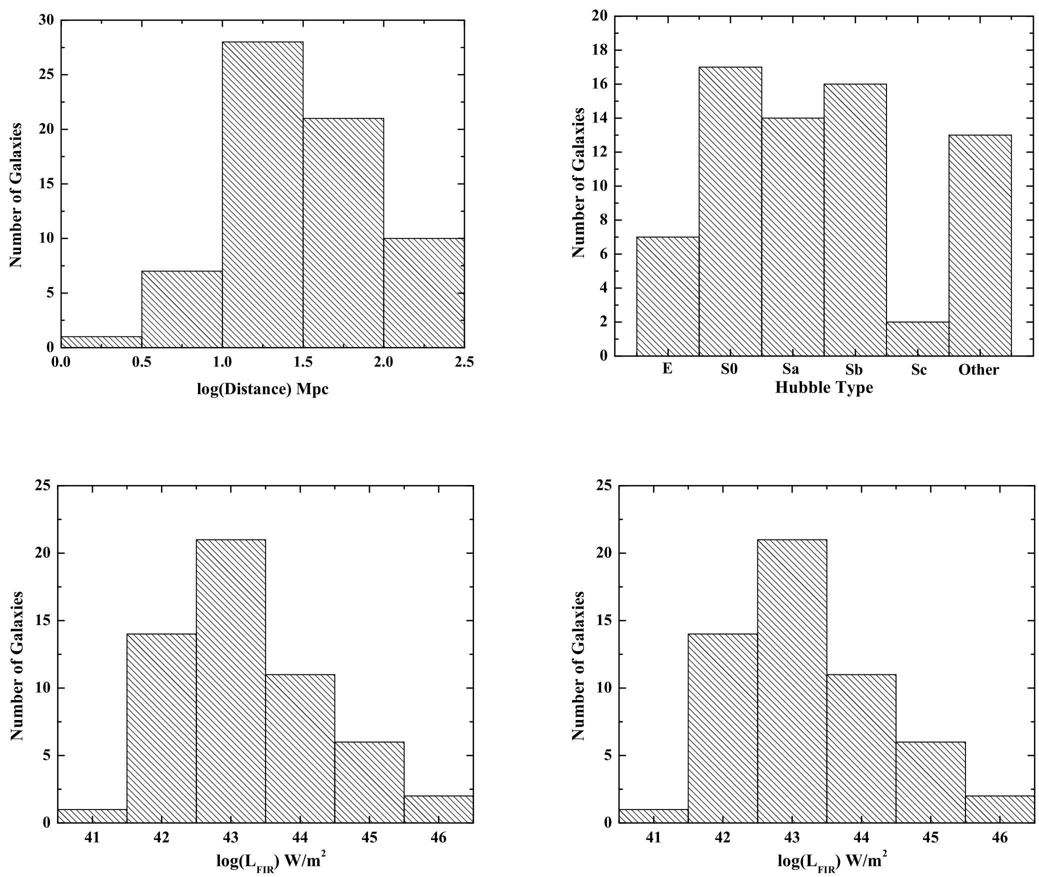

Figure 6.1: Statistics of the sample

Characteristics of the *Spitzer* sample of LINERs. Most galaxies are nearby and span a wide range of far-IR luminosities, IR-brightness ratios, and Hubble types.

Table 6.1: Properties of the H97 Sample

Galaxy Name (1)	Distance (Mpc) (2)	Hubble Type (3)	$\frac{[OIII]}{H_\beta}$ (4)	$\frac{[OI]}{H_\alpha}$ (5)	$\frac{[NII]}{H_\alpha}$ (6)	$\frac{[SII]}{H_\alpha}$ (7)	log L_{FIR} (8)	$\frac{L_{FIR}}{L_B}$ (9)
NGC1052	18	E4	2.01	0.71	1.20	1.72	42.25	-0.59
NGC1055	13	SBb	···	0.06	0.66	0.41	43.46	0.66
NGC1961	53	SABc	1.18	0.21	1.96	1.07	44.21	0.28
NGC266	62	SBab	2.38	0.28	2.36	1.27	43.50	-0.11
NGC2681	13	SAB0/a	1.73	0.19	2.36	0.75	42.91	0.13
NGC2787	13	SB0	1.41	0.55	1.61	1.41	41.83	-0.64
NGC2841	12	SAb	1.86	0.17	1.83	1.14	42.89	-0.32
NGC3166	22	SAB0/a	2.71	0.27	2.57	1.32	43.34	0.17
NGC3169	20	Saa	2.88	0.28	2.07	1.45	43.40	0.31
NGC3190	22	SAa	2.06	0.34	3.47	1.82	43.14	0.13
NGC3226	23	E2 pec	2.22	0.59	1.45	1.36	41.95	-0.69
NGC3368	8	SABab	1.83	0.18	1.11	0.97	42.76	-0.02
NGC3507	20	SBb	0.98	0.18	1.10	0.94	···	···
NGC3521	7	SABbc	1.00	0.23	0.64	0.88	43.27	0.39
NGC3642	28	SAbc	1.32	0.18	0.71	1.04	42.98	-0.20
NGC3884	92	SA0/a	2.24	0.58	2.07	1.12	···	···
NGC3998	22	SA0	1.98	0.53	1.08	0.99	42.24	-0.71
NGC4036	25	SA0	1.85	0.46	2.25	1.81	42.43	-0.64
NGC404	2	SA0	1.26	0.17	0.44	0.99	40.94	-0.34
NGC4143	17	SAB0	2.15	0.71	1.75	1.39	···	···
NGC4203	10	SAB0	1.57	1.22	1.84	1.42	41.70	-0.52
NGC4261	35	E2	2.44	0.49	2.60	1.29	42.45	-0.98
NGC4278	10	E1	1.31	0.41	1.22	1.48	41.66	-0.81
NGC4314	10	SBa	0.72	0.18	1.01	0.57	42.38	-0.01
NGC4394	17	SBb	2.80	0.44	1.08	0.98	42.53	-0.20
NGC4438	17	SA0/a	1.59	0.27	1.64	1.51	42.99	-0.15
NGC4450	17	SAab	2.12	0.67	1.94	2.15	42.73	-0.31
NGC4457	17	SAB0/a	0.87	0.19	1.04	0.90	42.98	0.24
NGC4486	17	E0	1.89	0.30	2.12	1.30	41.77	-1.77
NGC4548	17	SBb	1.12	0.23	1.38	1.06	42.89	-0.13
NGC4594	20	SAa	1.57	0.18	2.19	1.07	43.31	-0.82
NGC4596	17	SB0	1.00	0.27	1.48	1.16	42.03	-0.71
NGC4736	4	SAab	1.47	0.24	2.15	1.39	42.92	0.27
NGC474	33	SA0	2.41	0.21	0.47	1.01	41.87	-1.25
NGC5005	21	SABbc	2.27	0.65	4.94	3.31	43.92	0.46
NGC5195	9	IA0	1.22	0.55	5.43	2.00	42.96	0.29
NGC5353	38	SA0	1.22	0.19	1.71	0.83	42.66	-0.58
NGC5371	38	SABbc	2.07	0.28	2.36	1.48	43.84	0.27
NGC5850	29	SBb	2.38	0.22	1.69	1.43	42.89	-0.35
NGC5982	39	E3	1.08	0.49	2.42	0.71	42.12	-1.12
NGC5985	39	SABb	2.65	0.30	3.08	1.51	43.32	-0.20
NGC6500	40	SAab	1.40	0.23	0.73	0.96	43.00	-0.09
NGC7626	46	E	1.62	0.22	2.35	1.28	42.33	-1.05

Columns Explanation: Col(1):Common Source Names; Col(2): Distance, = taken from H97 ; Col(3): Hubble Type; Col(4): [OIII] to H_β ratio taken from H97; Col(5): [OI] to H_α ratiotaken from H97; Col(6): [NII] to H_α ratio taken from H97; Col(7): [SII] to H_α ratio taken from H97; Col(8): Log of the far-IR luminosity in units of ergs s^{-1}, Far-infrared luminosities correspond to the 40-500μm wavelength interval and were calculated using the IRAS 60 and 100 μm fluxes according to the prescription: L_{FIR}=$1.26\times10^{-14}(2.58f_{60}+f_{100})$ in W m^{-2} (Sanders & Mirabel 1996); Col(9): IR-brightness Ratio (L_{FIR}/L_B)

Table 6.2: Properties of the V95 Sample

Galaxy Name (1)	Distance (Mpc) (2)	Hubble Type (3)	$\frac{[OIII]}{H_\beta}$ (4)	$\frac{[OI]}{H_\alpha}$ (5)	$\frac{[NII]}{H_\alpha}$ (6)	$\frac{[SII]}{H_\alpha}$ (7)	log L_{FIR} (8)	$\frac{L_{FIR}}{L_B}$ (9)
UGC556	62	S	0.63	0.14	0.59	0.49	44.16	1.47
IR01364-1042	193	LIRG	1.62	0.35	0.95	0.59	45.13	···
NGC660	11	SBa	2.19	0.08	1.00	0.43	43.74	1.32
IIIZw35	110	LIRG	1.17	0.21	1.02	0.49	44.94	···
IR02438+2122	93	LIRG	2.57	0.20	1.35	0.29	44.46	···
NGC1266	29	SB0	1.20	0.35	3.72	1.62	43.82	1.74
ugc5101	157	S	2.29	0.11	1.32	0.35	45.27	1.95
NGC4666	20	SABc	1.20	0.06	1.29	0.60	44.06	0.83
UGC8387	93	Im	0.69	0.11	0.66	0.40	44.95	1.86
NGC5104	74	Sa	1.10	0.09	0.85	0.48	44.41	1.37
NGC5218	39	SBb	0.44	0.13	0.85	0.47	43.86	0.93
Mrk273	151	Ring	2.82	0.14	1.02	0.58	45.44	1.82
Mrk848	161	S0	1.15	0.09	0.76	0.45	45.11	···
NGC5953	26	SAa	1.82	0.06	0.78	0.40	43.72	···
IR15335-0513	109	LINER	0.56	0.20	1.17	0.46	44.60	···
IR16164-0746	109	LINER	1.02	0.25	1.00	0.44	44.85	···
NGC6240	98	I0	1.17	0.37	1.23	1.10	45.09	1.50
NGC6286	73	Sb	0.56	0.15	0.83	0.60	44.58	1.54
ESO593-IG008	195	Double	0.65	0.10	2.82	0.59	45.17	···
NGC7130	65	Sa	2.40	0.26	0.91	0.48	44.64	1.26
ZW453.062	100	LIRG	1.07	0.14	1.20	0.48	44.66	1.82
NGC7591	66	SBbc	1.10	0.10	0.95	0.39	44.37	1.03
IR23365+3604	258	Sba	0.50	0.07	0.66	0.43	45.45	2.19
IR04259-0440	62	E-S0	1.66	0.14	0.72	0.51	43.91	···

Columns Explanation: Col(1):Common Source Names; Col(2): Distance, calculated assuming H_0 = 75 km s^{-1} Mpc^{-1}; Col(3): Hubble Type; Col(4): [OIII] to H_β ratio taken from V95; Col(5): [OI] to H_α ratiotaken from V95; Col(6): [NII] to H_α ratio taken from V95; Col(7): [SII] to H_α ratio taken from V95; Col(8): Log of the far-IR luminosity in units of ergs s^{-1}, Far-infrared luminosities correspond to the 40-500μm wavelength interval and were calculated using the IRAS 60 and 100 μm fluxes according to the prescription: L_{FIR}=$1.26\times10^{-14}(2.58f_{60}+f_{100})$ in W m^{-2} (Sanders & Mirabel 1996); Col(9): IR-brightness Ratio (L_{FIR}/L_B)

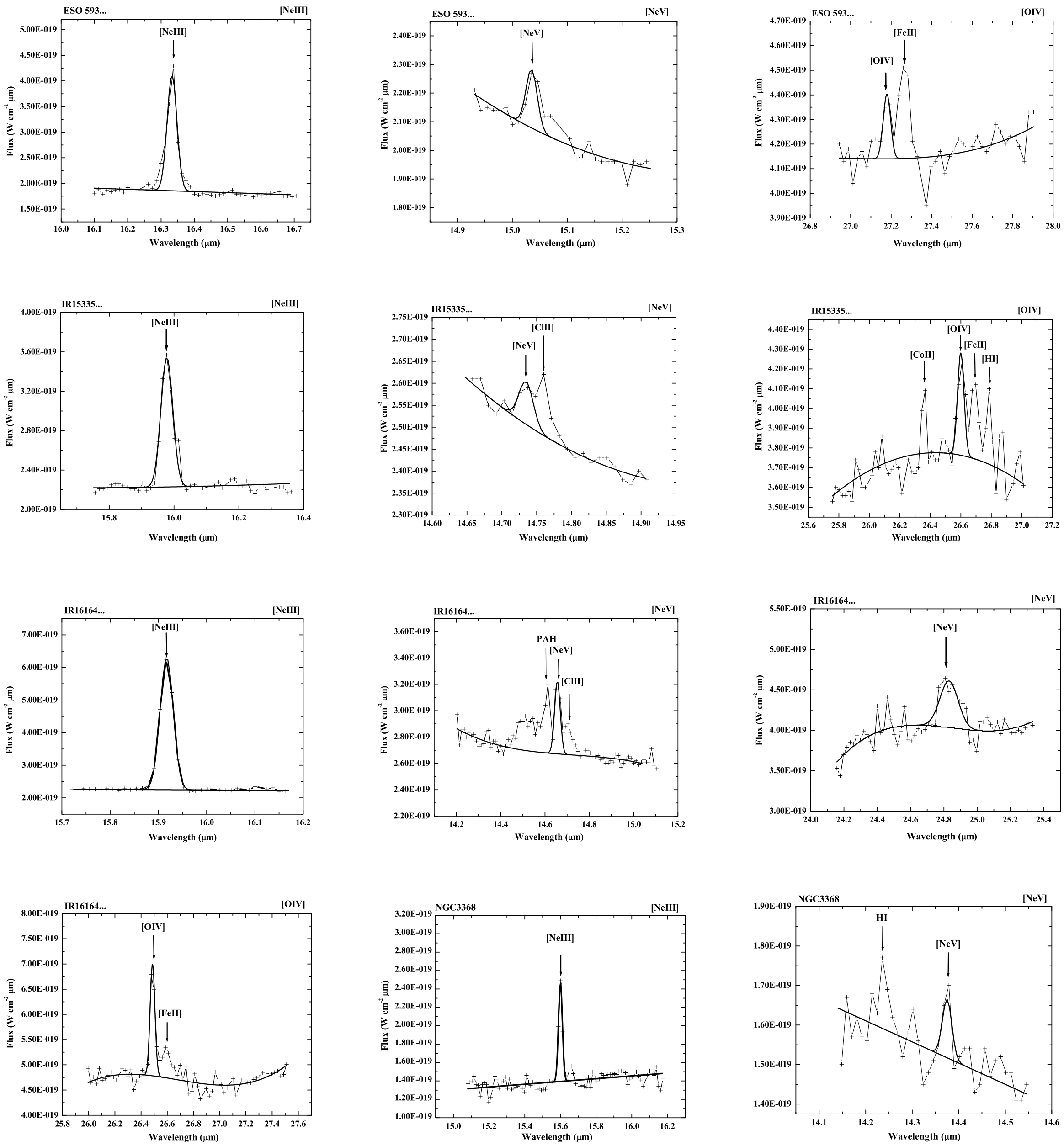

Figure 6.2: Spectra of AGN-LINERs

[NeIII]15, [NeV]14, [NeV]24, and [OIV]26 μm spectra for the [NeV] emitting galaxies in our sample.

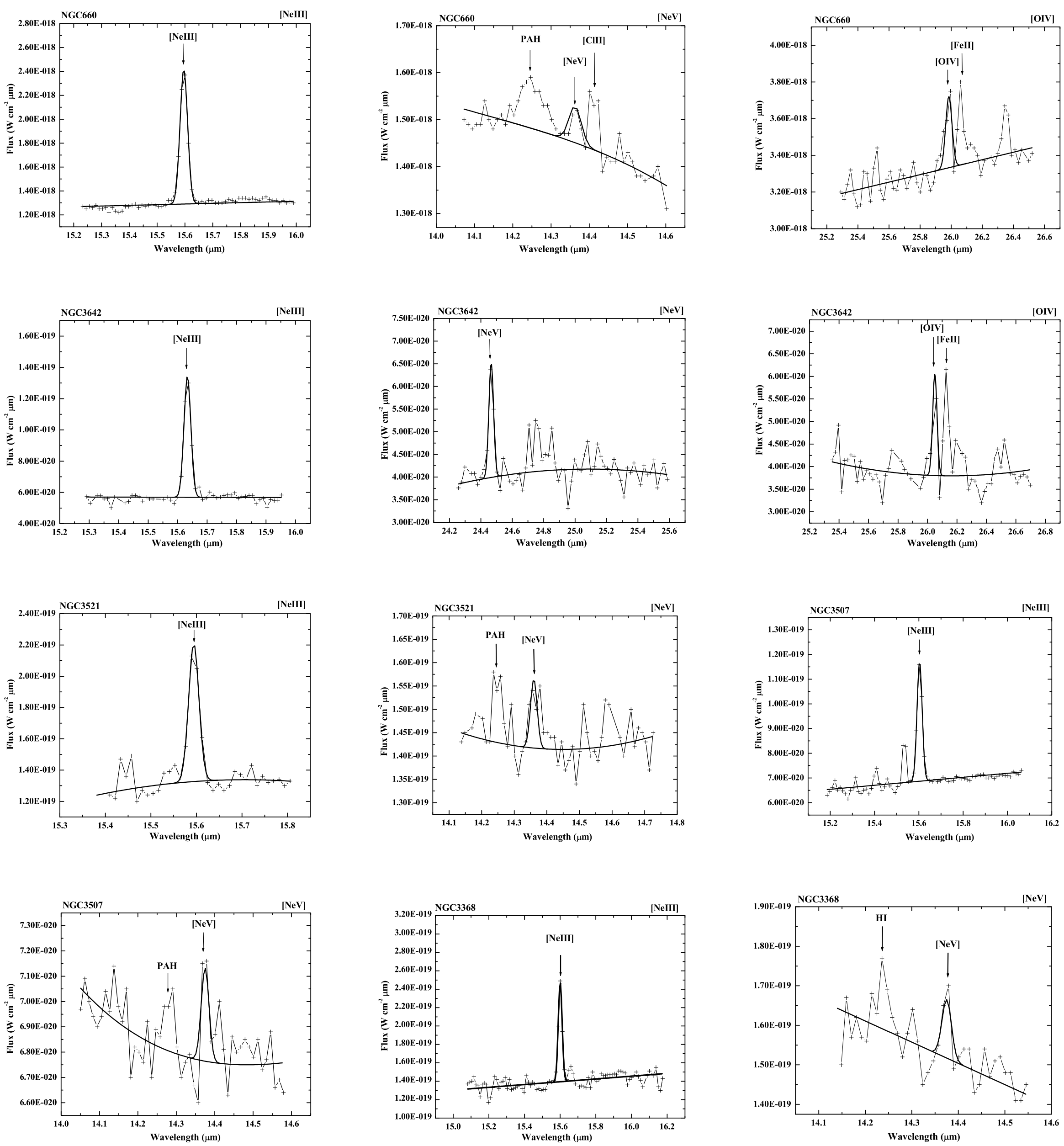

Figure 6.2 Spectra Continued.

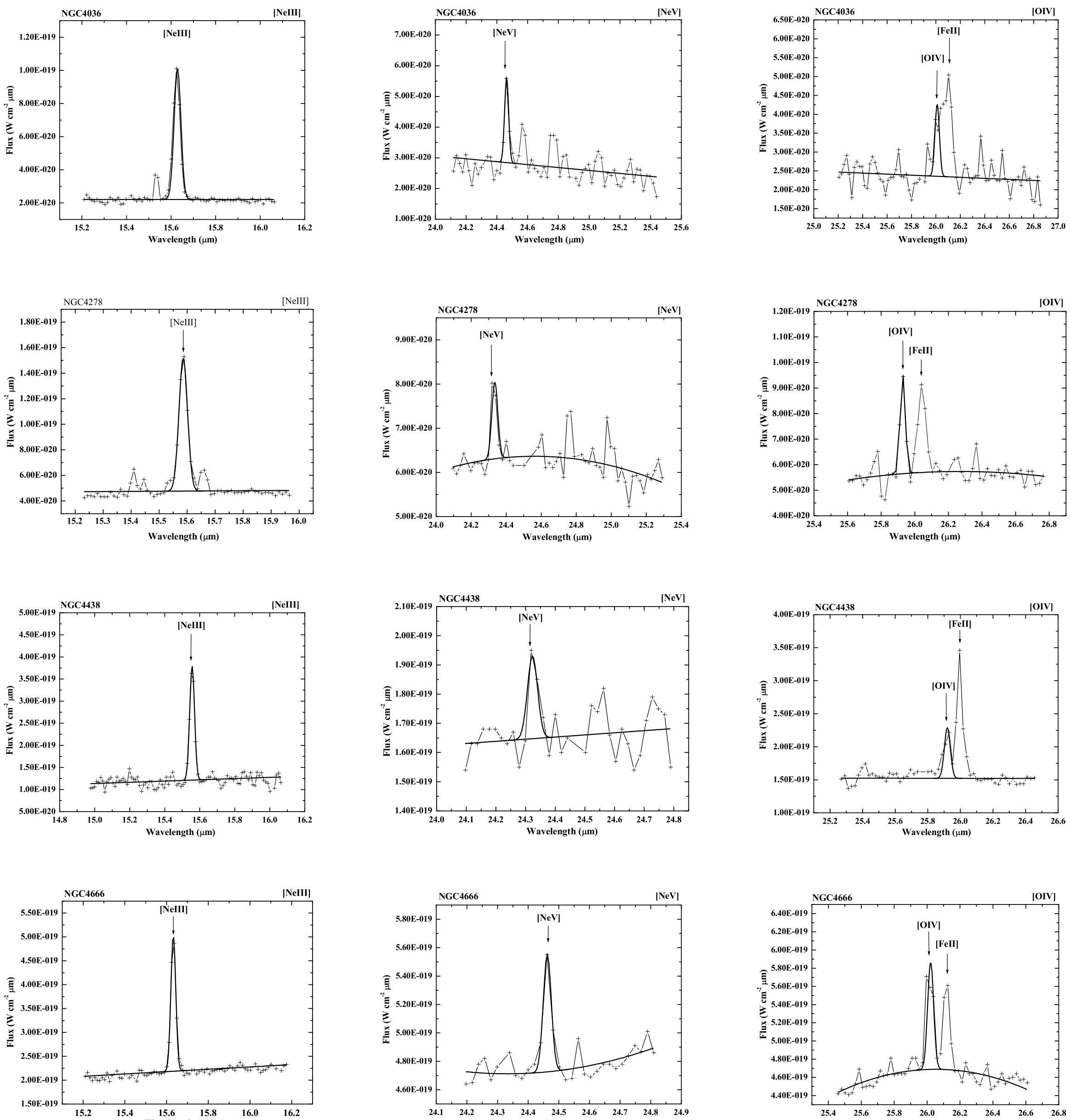

Figure 6.2 Spectra Continued.

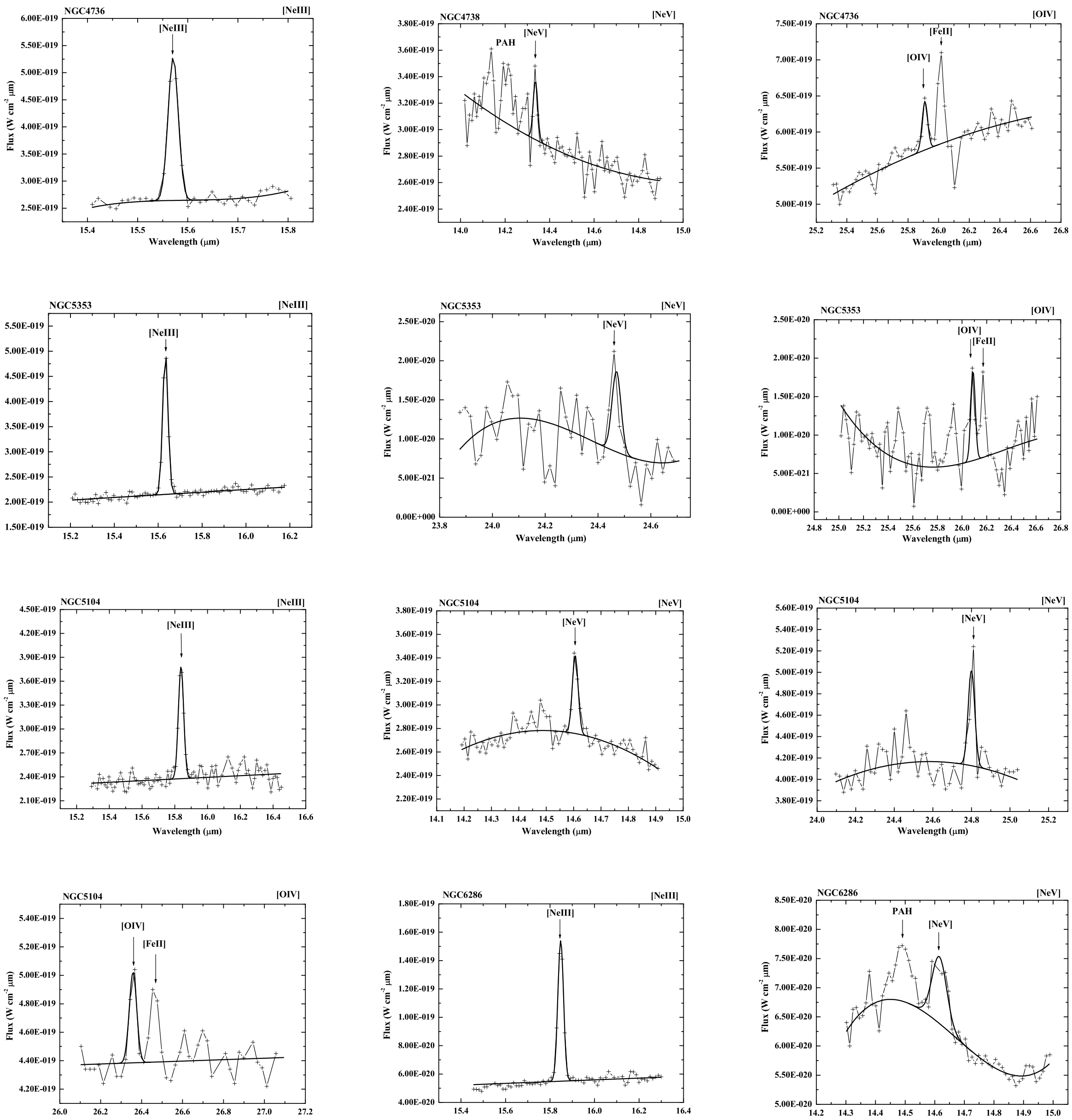

Figure 6.2 Spectra Continued.

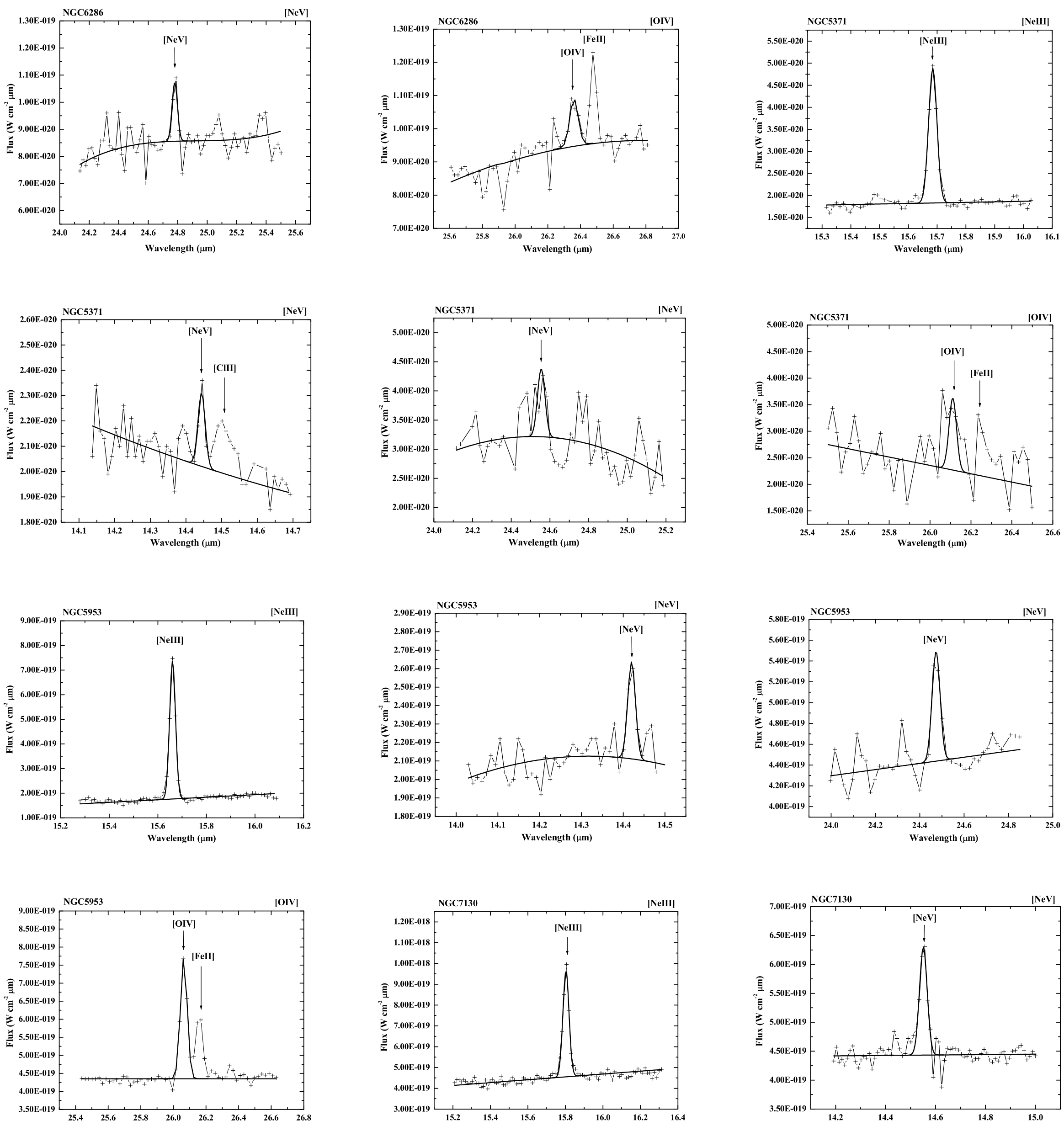

Figure 6.2 Spectra Continued.

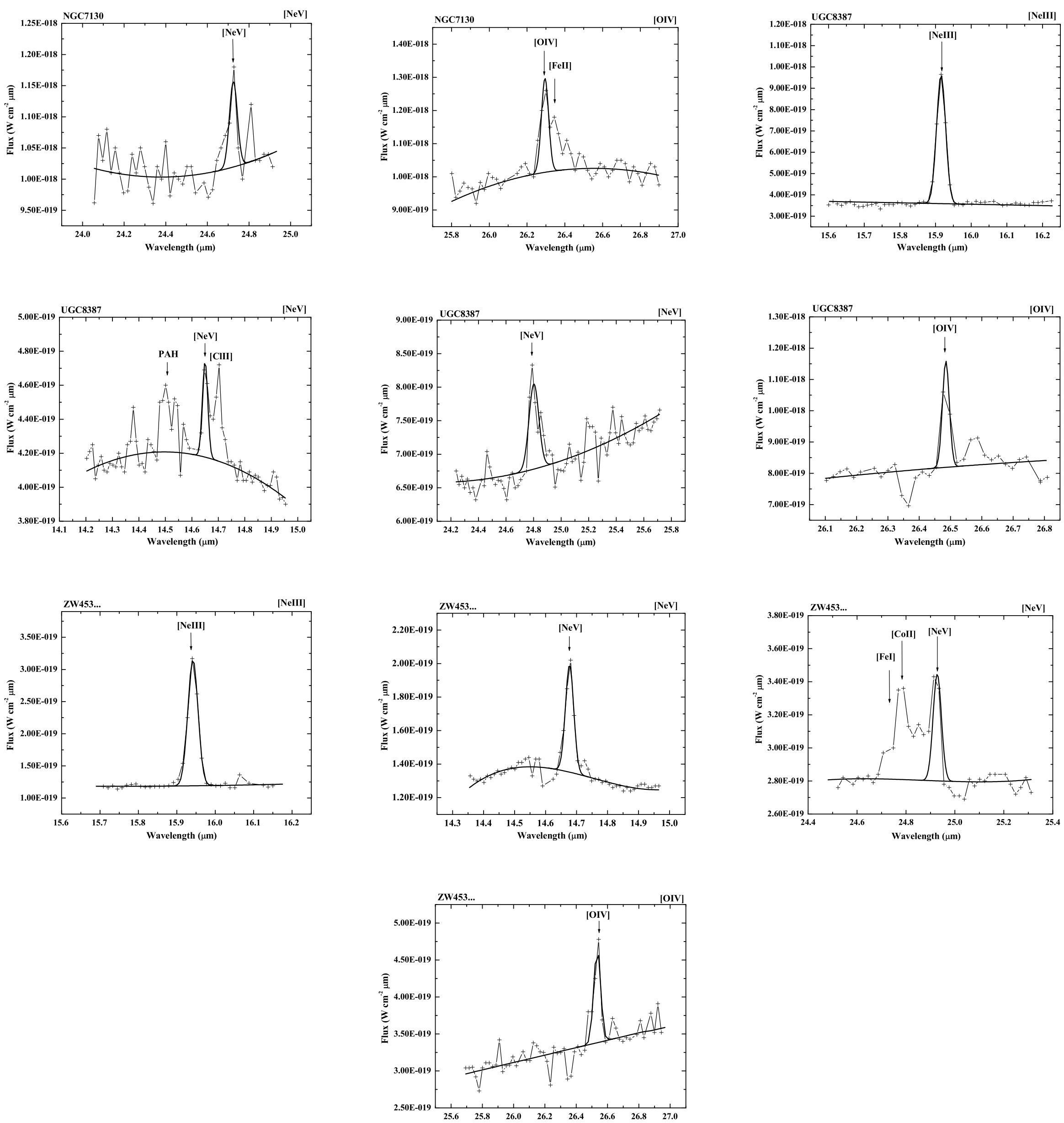

Figure 6.2 Spectra Continued.

a random assortment of available archival observations with variable signal to noise (S/N) and, in some cases, limited sensitivity, the AGN detection rate of 39% may be lower than it would be were the observing times for some galaxies longer. Figure 6.3 shows the detection rate as a function of the [NeV]14μm 3σ sensitivity. Some of the galaxies in the sample show [NeV]24μm emission but not 14μm emission. These galaxies have been included in the detection rate for each luminosity bin since, as shown by Satyapal et al. (2007, in prep), the [NeV]14μm and 24μm luminosities show a tight relationship in standard AGNs, with a slope close to 1. In Section 6.5 (and Chapter 5) we explore some of the instrumental effects and physical processes that may result in [NeV]14μm non-detections but clear 24μm detections. We estimated what the detection rate would be if the galaxies in this sample were observed long enough to detect a [NeV] 14μm line with luminosity $\log(L[NeV]_{14}) = 38$ erg s^{-1}, the lowest luminosity line detected in a sample of standard AGNs from Dudik et al. (2007). The detection rate for a $\log(L[NeV]_{14})$ sensitivity of ~ 38 erg s^{-1} or better is 33% (13 out of 39 galaxies), less than the over-all detection rate for the entire sample. The 33% mid-IR detection rate for a luminosity threshold of 10^{38} erg s^{-1} initially implies that the detection rate would not improve given more sensitive observations. Excluding galaxies with [NeV]24μm detections will only lower the detection rate for the 10^{38} erg s^{-1} luminosity threshold to 18%. Interestingly, the galaxies with the most sensitive observations ([NeV] sensitivities better than 10^{38} erg s^{-1},) are FIR-faint, possibly creating a bias. The detection rate as a function of L_{FIR} is explored further in Section 6.

We checked to see if our [NeV] detection rate was a function of either distance or Hubble type (See Figures 6.4 and 6.5). For some galaxies the Hubble type could not be determined because the available observations lacked sufficient spatial resolution

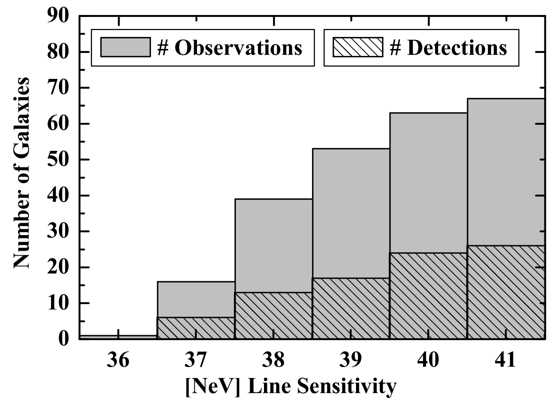

Figure 6.3: Detection rate vs. line sensitivity

Detection Rate as a function of [NeV] Line Sensitivity. We find a [NeV] detection rate of 39%. At a luminosity threshold of 10^{38} erg s^{-1} we find a detection rate of no more than 33% implying that better sensitivity observations would not yield a higher detection rate. Although, the galaxies with the best sensitivity are faint in the FIR possibly inducing a bias. This possibility is explored further in Section 6.

to determine the classification. These galaxies are denoted as a question mark in Figure 6.5. Though the sample is incomplete, prohibiting any significant statistical analysis, the detection rate is highest in mergers and galaxies with relatively large distances. These findings do not agree with the findings of Ho et al. (1999) and Nagar et al. (2002, 2005) who find the optical AGN detection rate highest in ellipticals and early-type spirals. In fact some of the lowest detection rates are found in galaxies with these Hubble types.

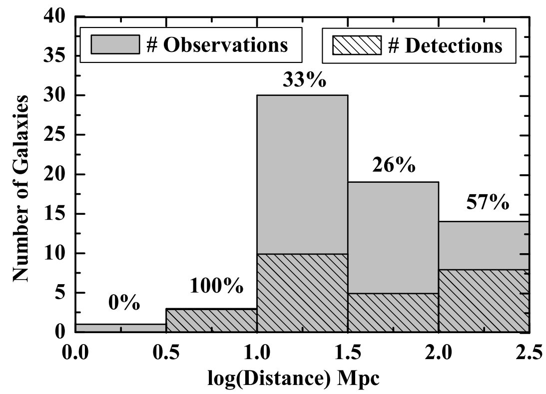

Figure 6.4: Detection rate vs. distance

[NeV] Detection rate as a function of distance. Though the sample is limited, this plot indicates that the detection rate highest for the most distant AGNs.

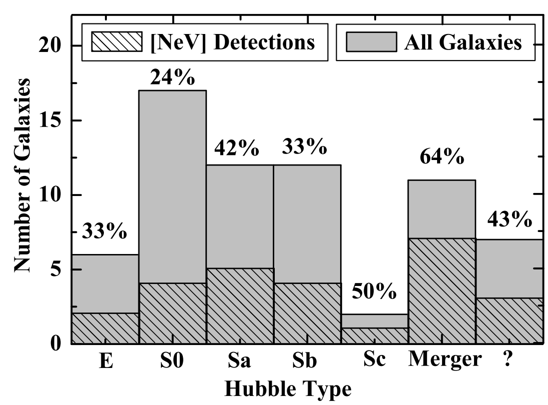

Figure 6.5: Detection rate vs. Hubble type

[NeV] Detection rate as a function of Hubble type. For some galaxies the spatial resolution was insufficient to determine Hubble Type. These galaxies are denoted by a question mark. Mergers have the highest detection rate of all Hubble classes.

6.4 Mid-IR vs. Optical, X-ray, and Radio AGN Diagnostics

6.4.1 Optical Observations

As mentioned in Chapter 1, in the conventional picture of an AGN, the broad line region is thought to exist within a small region interior to a dusty molecular torus. When viewed above the confines of the torus (face-on), Doppler broadened (FWHM exceeding 1000 km s^{-1}) Balmer emission lines are visible in the optical spectrum. These broad permitted lines are the most widely used AGN indicators used in optical studies of LINERs. Broad Hα measurements exist in the literature for 84% (56 of 67) of the galaxies in our sample and result in an optical detection rate of 30%. Broad Hα results taken from the literature are given in Table 6.4 along with the corresponding [NeV] detection information. As can be seen from Table 6.4, there is very little consistency between the detection of [NeV] and the presence of Broad Hα in the optical spectrum. In fact, 26% of galaxies with optical and IR measurements show [NeV] emission lines with luminosity of $\geq 10^{37}$ ergs s^{-1}, but no broad Hα component. In addition, and perhaps most interestingly, for the same sub-sample of galaxies with both optical and IR data, 20% show broad Hα but no evidence of [NeV] with luminosity $\geq 10^{37}$ ergs s^{-1}. If the IR and optically detected AGN-LINERs are totaled for galaxies with multi-wavelength observations, the detection rate is at least 54%.

6.4.2 X-ray Observations

The standard model for AGNs includes an accretion disk that primarily emits in the optical and UV bands. The hard X-ray (2-10keV) emission in AGNs is believed

Table 6.3: Mid-IR Line Fluxes-H97 and V95

Galaxy Name (1)	[NeII] 12μm (2)	[NeIII] 15μm (3)	[NeV] 14μm (4)	[NeV] 24μm (5)	[OIV] 26μm (6)
NGC1052	21.0±0.3	12.4±0.2	0.54±0.15	2.5±0.4	2.1±0.5
NGC1055	28.3±0.3	2.7±0.2	<0.12	<0.37	<0.4
NGC1961	23.8±0.7	2.1±0.3	<0.13	<0.61	<0.3
NGC266	1.5±0.1	1.1±0.1	<0.03	<0.16	<0.2
NGC2681	8.5±0.5	3.4±0.2	<0.1	<0.27	2.3±0.4
NGC2787	1.5±0.1	1.0±0.1	<0.03	<0.12	<0.3
NGC2841	4.5[a]	5.4[a]	<0.4	<0.31	0.7[a]
NGC3166	7.9±0.4	3.8±0.4	<0.52	0.75±0.22	1.4±0.3
NGC3169	29.1±0.8	4.8±0.1	<0.08	<0.24	1.5±0.2
NGC3190	5.7±0.3	3.5±0.5	<0.57	<0.75	<1.3
NGC3226	2.0±0.2	1.9±0.1	<0.14	<1.4	<1.4
NGC3368	5.3±0.2	2.9±0.2	0.38±0.12	<2.0	<0.4
NGC3507	3.9±0.1	1.3±0.1	0.09±0.02	<0.14	<0.2
NGC3521	2.9±0.4	2.5±0.2	0.38±0.12	<1.6	<1.9
NGC3642	9.8±0.4	2.3±0.1	<0.07	0.90±0.17	1.2±0.3
NGC3884	2.1±0.1	1.1±0.1	<0.04	<0.11	<0.1
NGC3998	12.2±0.1	7.8±0.2	<0.10	<1.8	<1.5
NGC4036	5.1±0.1	3.0±0.1	<0.02	0.90±0.16	0.9±0.2
NGC404	3.7±0.1	1.8±0.1	<0.05	<0.18	0.8±0.2
NGC4143	3.2±0.1	2.3±0.1	<0.04	<0.15	0.6±0.2
NGC4203	1.8±0.1	2.1±0.1	<0.03	<0.30	<0.5
NGC4261	5.4±0.2	2.6±0.2	<0.03	<0.23	1.2±0.4
NGC4278	5.6±0.1	4.0±0.1	<0.03	0.70±0.14	1.6±0.1
NGC4314	11.3±0.3	1.9±0.2	<0.05	<0.33	<0.4
NGC4394	1.7±0.3	1.2±0.3	<0.16	<0.11	0.7±0.1
NGC4438	22.2±0.8	8.6±0.5	<0.21	1.1±0.19	3.5±0.5
NGC4450	3.8±0.9	2.5±0.6	<0.71	<1.46	1.8±0.7
NGC4457	8.9±0.2	3.2±0.1	<0.03	<0.15	2.1±0.5
NGC4486	7.8±0.1	7.9±0.2	<0.10	<0.94	2.4±0.4
NGC4548	2.5±0.2	1.5±0.1	<0.05	<3.5	2.3±0.4
NGC4594	9.5[a]	8.2[a]	<0.32	<0.40	2.4[a]
NGC4596	1.1±0.1	1.7±0.1	<0.03	<0.32	<0.2
NGC4736	11.9±2.6	6.7±0.4	1.1±0.32	<1.7	3.1±1.0
NGC474	<0.5	<0.2	<0.09	<0.37	<0.7
NGC5005	41.8±0.7	13.3±0.7	<0.14	<0.39	<0.8
NGC5195	21.7±3.4	5.4±0.4	<1.14	<3.4	<6.2
NGC5353	3.3±0.4	2.0±0.3	<0.39	0.44±0.13	0.5±0.1
NGC5371	2.0±0.1	1.1±0.04	0.07±0.02	0.56±0.17	0.6±0.2
NGC5850	7.0±0.3	1.8±0.4	<0.54	<0.10	<0.1
NGC5982	4.5±0.4	<0.6	<0.15	<0.10	<0.1
NGC5985	5.1±0.5	0.8±0.2	<0.45	<0.08	<0.1
NGC6500	5.4±0.1	2.6±0.1	<0.02	<0.21	<0.2
NGC7626	1.0±0.1	0.5±0.1	<0.03	<0.27	<0.4

Table 6.3 Continued: Mid-IR Line Fluxes

Galaxy Name (1)	[NeII] 12μm (2)	[NeIII] 15μm (3)	[NeV] 14μm (4)	[NeV] 24μm (5)	[OIV] 26μm (6)
UGC556	35.3±1.3	8.0±0.1	<0.18	<0.30	<0.4
IR01364-1042	9.3±0.2	2.2±0.2	<1.18	<1.4	<1.5
NGC660	367 ±5.1	36.8±0.8	3.1±0.56	<10.0	19.8±4.6
IIIZw35	3.6±0.1	0.6±0.1	<0.49	<2.4	<3.7
IR02438+2122	18.6±0.6	1.6±0.2	<1.63	<2.2	<1.8
NGC1266	20.9±0.8	5.3±0.7	<0.80	<2.9	<6.6
ugc5101	55.2±2.5[b]	23.9±1.4[b]	5.2±0.70[b]	4.9±1.0[b]	5.5±1.4[b]
NGC4666	38.3±0.7	8.3±0.4	<0.15	2.4±0.4	5.4±0.5
UGC8387	105±0.9	18.9±0.7	1.43±0.33	11.4±2.4	11.2±1.8
NGC5104	44.3±0.5	5.4±0.5	1.77±0.36	3.8±0.5	2.9±0.6
NGC5218	145.0±1.8	10.6±0.5	<0.18	<0.44	<1.6
Mrk273	43.2±0.4[c]	34.3±0.5[c]	10.6±0.47[c]	27.4±1.9[c]	56.9±1.8[c]
Mrk848	61.4±0.4	14.3±0.3	<0.09	<0.92	<0.8
NGC5953	56.0±0.7	16.8±0.2	1.2±0.26	4.7±1.1	17.5±1.4
IR15335-0513	35.1±0.4	6.0±0.2	0.23±0.04	<0.83	2.7±0.5
IR16164-0746	45.4±0.4	13.7±0.2	1.8±0.22	3.8±0.7	10.2±1.4
NGC6240	193±3.7[b]	70.4±2.4[b]	5.1±0.90[b]	<3.9	27.2±0.7[b]
NGC6286	18.5±0.2	3.1±0.1	0.33±0.11	0.99±0.20	0.9±0.2
ESO 593-IG008	38.4±1.3	8.2±0.2	0.50±0.11	<0.42	1.2±0.3
NGC7130	58.8±0.8	20.6±0.5	2.12±0.31	6.6±1.0	13.3±1.2
ZW453.062	25.3±0.2	6.5±0.1	7.2±0.64	2.6±0.4	10.1±2.0
NGC7591	34.8±0.4	4.1±0.4	<0.30	<0.76	<0.4
IR23365+3604	8.6[d]	0.7[d]	<0.80[d]	<0.54[d]	<2.0[d]
IR04259-0440	12.3±5.3	<1.0	<0.73	<8.5	<5.2

Columns Explanation: Col(1): Common Source Names; Col(2) - (6): Fluxes in units of 10^{-21} W cm^{-2}. 3 σ upper limits are reported for nondetections. **References for Table 3** [a] Dale et al. 2006, [b] Armus et al. 2004 & 2006, [c] Dudik et al. 2007, [d] Farrah et al. 2007

to result from inverse compton scattering of these lower energy optical and UV accretion disk photons. Because the hard X-rays are not efficiently produced in normal star-forming regions, a hard nuclear X-ray point source coincident with the nucleus of a galaxy constitutes strong evidence for the presence of an AGN. We searched the literature for X-ray classifications and X-ray luminosities for all of the galaxies in our sample. 58% (39 of 67) of galaxies have published X-ray luminosities and morphologies from either *Chandra*, *XMM*, or *ASCA*. We have excluded those galaxies observed by either *ROSAT* or *Einstein* since these lower-spatial resolution observations were limited to the soft X-ray band (0.2-4keV) so that the classifications of the X-ray sources are ambiguous and the luminosites could be contaminated or dominated by star forming regions. The published X-ray information for these galaxies is given in Table 6.4. Like the optical AGN-detections, IR-detections of

AGNs do not necessarily agree with the X-ray observations of AGNs. Indeed 41% of AGNs detected in the X-rays show *no* evidence of a [NeV] line with luminosity $\geq 10^{37}$ ergs s^{-1} in the mid-IR. In addition 17% of IR-detected AGNs, show no definitive evidence of an AGN with 2-10keV luminosity $\geq 10^{38}$ erg s^{-1} in the hard X-rays . The detection rate of galaxies observed in the hard X-ray band is 56%–higher than the maximum [NeV]-based detection rate. If the AGNs detected via either the IR or hard X-ray methods are combined for galaxies with multi-wavelength observations, the total detection rate is 74%. Similar to the published optical data, the available X-ray information is limited to primarily IR-faint galaxies since many of the luminous infrared galaxies in our sample have not been observed in the 2-10keV band. Longer exposure times for some of the X-ray observations may yield a higher all around detection rate for the sample.

From the analysis thus far, it is clear that multi-wavelength X-ray and IR observations yield the highest AGN-detection rate. However it is worthwhile to examine the combined X-ray and optical detection rate for the sample of AGNs to look for consistency in these measurements. All galaxies with detected broad Hα except one also have a hard X-ray point source consistent with an AGN. The anomolous galaxy (NGC4438) shows multiple sources of comparable luminosity in the X-rays and a luminosity $\sim 10^{37}$ erg s^{-1}. On the other hand, we find that 26% of galaxies with both observations show an AGN-like X-ray morphology and no broad line component in the optical band. This is expected since the broad optical lines are extinguished by the torus in edge-on (view through the torus) AGNs, where-as the hard X-rays are less susceptible to absorption and can be detected in edge-on sources. The combined detection rate for galaxies with both optical and X-ray observations is at least 61%, which may increase with more sensitive X-ray observations for some galaxies.

6.4.3 Radio Observations

A flat spectrum, compact nuclear radio source or any signature of a radio jet emanating from the nucleus of a galaxy are the two primary indicators of the presence of an active black hole in radio observations (Nagar et al. 2002, 2005). Very high spatial resolution observations are essential for uncovering radio jets in the nucleus of galaxies and such published observations are very rare. Therefore we searched the literature for observations of either a flat spectrum nuclear radio source or evidence of radio jets in the nucleus of galaxies in our sample. In particular Nagar et al.(2005, hereafter N05) conducted a high resolution radio imaging survey of the majority of low luminosity Seyferts (LLAGNs) and LINERs in the H97 catalog of galaxies. In this study N05 find over 50% of LLAGNs and LINERs host AGNs. However, while this survey covers 91% of the IR-faint galaxies in the sample, it includes only one galaxy that is IR luminous. A subsequent search for any other radio observations with the spatial resolution to confirm a compact nuclear radio source yielded an additional 5 observations.

While this sample of radio observations is lacking IR-luminous galaxies, precluding any statistically significant results for a representative sample of LINERs, a radio-based AGN detection rate of 46% is found for LINERs. This is lower than the radio-based detection rate reported by Nagar et al. (2002, 2005), because LL Seyferts are included in that sample. It is clear from Table 6.4 that the IR observation and the radio observation agree in very few cases (42%, 19/45 galaxies). In fact the radio data does not agree very well with even the optical data (only 62% of cases (27 of 43) agree). Though data is limited, the radio observations seem to agree best with X-ray observations (75% of cases, 24 out of 32 cases).

Table 6.4: Multiwavelength Statistics: H97 and V95

Galaxy Name (1)	[NeV] Detect? (2)	Broad Hα? (3)	Optical Ref. (4)	X-ray Detect? (5)	log(L_X) erg s^{-1} (6)	X-ray Ref. (7)	Radio Detect? (8)	Radio Ref. (9)
NGC1052	Yes	Yes	A	AGN	40.78	G	...	...
NGC1055	No	No	A	nonAGN	<37.52	H	No	S
NGC1961	No	No	A	nonAGN	...	I	No	S
NGC266	No	Yes	A	AGN	40.88	J	Yes	S
NGC2681	No	Yes	A	AGN	38.94	G	No	S
NGC2787	No	Yes	A	AGN	38.30	K	Yes	S
NGC2841	No	No	A	nonAGN	38.26	K	Yes	S
NGC3166	Yes	No	A	...	...	...	No	S
NGC3169	No	No	A	AGN	41.41	J	Yes	S
NGC3190	No	No	A	...	...	...	Yes	S
NGC3226	No	Yes	A	AGN	39.62	G	Yes	S
NGC3368	Yes	No	A	nonAGN	39.45	L	No	S
NGC3507	Yes	No	A	nonAGN	38.31	G	No	S
NGC3521	Yes	No	A	...	...	...	...	...
NGC3642	Yes	Yes	A	...	...	...	No	S
NGC3884	No	Yes	A	...	...	...	...	...
NGC3998	No	Yes	A	AGN	41.67	M	Yes	S
NGC4036	Yes	Yes	A	...	...	...	No	S
NGC404	No	No	A	nonAGN	37.32	L	No	S
NGC4143	No	Yes	A	AGN	40.04	J	Yes	S
NGC4203	No	Yes	A	AGN	40.08	K	Yes	S
NGC4261	No	No	A	AGN	40.65	G	Yes	S
NGC4278	Yes	Yes	A	AGN	40.09	K	Yes	S
NGC4314	No	No	A	nonAGN	38.15	L	No	S
NGC4394	No	No	A	...	...	...	No	S
NGC4438	Yes	Yes	A	nonAGN	37.54	N	No	S
NGC4450	No	Yes	A	AGN	40.35	M	Yes	S
NGC4457	No	No	A	AGN	39.22	N	No	S
NGC4486	No	No	A	AGN	40.52	L	Yes	S
NGC4548	No	No	A	nonAGN	39.05	N	Yes	S
NGC4594	No	No	A	AGN	38.86	K	...	...
NGC4596	No	No	A	nonAGN	38.65	G	No	S
NGC4736	Yes	No	A	nonAGN	38.72	K	Yes	S
NGC474	No	No	A	...	...	...	No	S
NGC5005	No	Yes	A	AGN	39.49	H	No	S
NGC5195	No	No	A	nonAGN	37.85	K	No	S
NGC5353	Yes	No	A	...	...	...	Yes	S
NGC5371	Yes	No	A	...	...	...	No	S
NGC5850	No	No	A	non-AGN	39.83	O	No	S
NGC5982	No	No	A	...	...	...	No	S
NGC5985	No	No	A	...	...	...	No	S
NGC6500	No	No	A	AGN	40.23	L	Yes	S
NGC7626	No	No	A	nonAGN	41.51	P	Yes	S

Table 6.4 Continued: Multiwavelength Statistics

Galaxy Name (1)	[NeV] Detect? (2)	Broad Hα? (3)	Optical Ref. (4)	X-ray Detect? (5)	log(L_X) erg s^{-1} (6)	X-ray Ref. (7)	Radio Detect? (8)	Radio Ref. (9)
UGC556	No	...	...	...	...	...	...	...
IR01364-1042	No	...	...	...	...	...	...	...
NGC660	Yes	No	A	nonAGN	38.52	H	No	S
IIIZw35	No	No	B	...	...	...	AGN?	T
IR02438+2122	No	...		...	...	...	AGN?	T
NGC1266	No	...		...	...	...	...	...
UGC5101	Yes	Yes	B	AGN	40.89	L	AGN	T
NGC4666	Yes	...		nonAGN	<38.08	H	...	...
UGC8387	Yes	...		...	...	...	...	...
NGC5104	Yes	...		...	...	...	...	...
NGC5218	No	Yes	B	...	...	...	...	...
Mrk273	Yes	No	B	AGN	42.18	G	...	...
Mrk848	No	No	C	...	...	...	...	...
NGC5953	Yes	No	C	nonAGN	<38.69	Q	...	...
IR15335-0513	Yes	...		...	...	...	...	...
IR16164-0746	Yes	...		...	...	...	...	...
NGC6240	Yes	No	D	AGN	42.04	G	...	...
NGC6286	Yes	...		...	...	...	No	T
ESO593-IG008	Yes	...		...	...	...	...	...
NGC7130	Yes	No	E	AGN	40.49	G	...	...
ZW453.062	Yes	No	C	...	...	...	...	...
NGC7591	No	No	B	...	...	...	...	...
IR23365+3604	No	No	B	AGN	41.52	R	No	T
IR04259-0440	No	No	F	...	...	...	...	...

Columns Explanation: Col(1): Common Source Names; Col(2): Galaxies with [NeV] Detected; Col(3): Galaxies with Broad Hα detected; Col(4): Reference for Broad Hα; Col(5): Galaxies with AGN-like nuclei in the X-rays; Col(6): X-ray luminosity in erg s^{-1} Col(7): Reference for X-ray morphology and luminosity. Col(8): Galaxies with compact flat spectrum radio cores. Col(9): Reference for radio morphology. **References for Table 4** A - H97; B - Veron-Cetty & Veron 2003; C - Goncalves, Vron-Cetty, & Vron, 1999; D - Andreasian & Khachikian 1987; E - Phillips 1983 F - Kewley et al. 2001; G - Gonzalez-Martin et al. 2006; H - Dudik et al. 2005; I - Colbert & Ptak 2002; J - Terashima et al. 2003; K - Ho et al. 2001; L - Satyapal et al. 2004; M - Terashima et al. 2000; N - Satyapal et al. 2005; O - Georgantopoulos, Georgakakis, & Koulouridis 2005; P - Philip et al. 2006; Q - Guainazzi, Matt, & Perola, 2005; R - Teng et al. 2005; S - Nagar, Falcke & Wilson 2005; T - Baan & Klockner 2006

We note that X-ray binary sources are also known to display compact flat spectrum radio sources (Fender & Belloni 2004) and compact starbursts can produce radio emission that mimics AGN spectra (Condon et al. 1991).

6.4.4 Multi-wavelength AGN Detection Rate in LINERs

The combined detection rate for galaxies with optical, X-ray and IR observations is at least 74%. The radio data has been excluded from this calculation because of insufficient data for IR-luminous galaxies. Inclusion of radio data will only increase this detection rate as may more optical and X-ray observations of luminous far-IR sources. Regardless, the detection rate is rather high considering that many previous studies using single bands have reported AGN-detection rate in LINERs of $\leq 50\%$ (e.g. Ho et al. 1999, 2001; Nagar et al. 2005; Satyapal et al. 2004, 2005; Dudik et al. 2005). Such a high detection rate is due primarily to the inconsistency between the IR and both the X-ray and optical AGN detection methods. In the following section possible causes for this inconsistency are explored.

The multi-wavelength data presented here stem from an assortment of observations with variable signal to noise and a wide range of sensitivites. However, from Section 6.4 it is not clear that, given better S/N, the IR observations would match either the X-ray or optically detected AGNs in our sample. We explored whether the IR, optical, and X-ray detection rates in LINERs were related to the host galaxy's properties. In Figure 6.6 shows the multi-band, AGN detection rates as a function of the host galaxys far-IR luminosity (L_{FIR}).

Figure 6.6 clearly shows that the optical AGN-detection rate decreases with L_{FIR}, while the [NeV] AGN detection rate increases with L_{FIR}. Though data is limited at large L_{FIR}, the X-ray-based detection rate seems to be unrelated to L_{FIR}. Excess dust

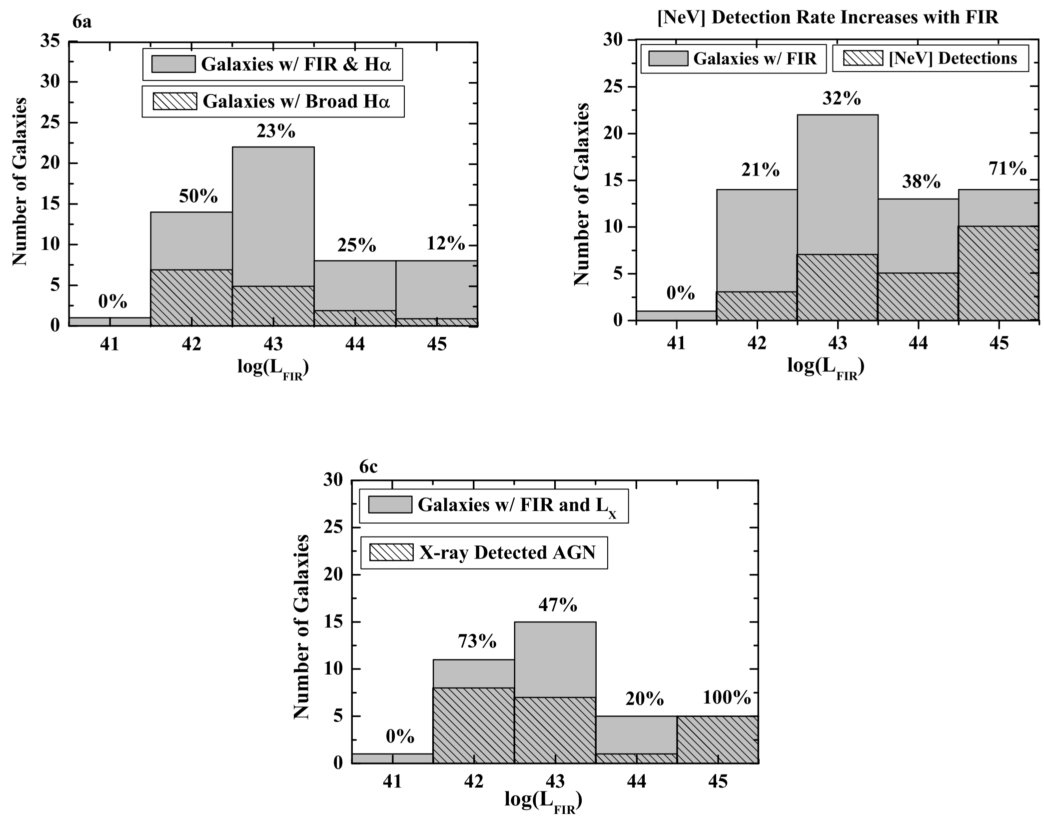

Figure 6.6: Hα, [NeV] and X-ray detection rate vs. FIR

Optical, IR, and X-ray detection rates as a function of far-IR luminosity. As can be see from these plots, the optical AGN-detection rate decreases with L_{FIR}, while the [NeV] AGN detection rate increases with L_{FIR}. On the other hand, the X-ray-based detection rate seems unrelated to L_{FIR}.

in LINERs with large L_{FIR} may therefore explain the broad Hα deficiency in these galaxies. In fact, near-infrared spectroscopic studies of infrared luminous galaxies show broad Paα lines are detected in some IR-luminous galaxies, suggesting that the broad-line region is present, but attenuated by dust in the optical band (Veilleux, Sander, & Kim 1999).

A dust-obscured broad-line region can easily explain the absence of broad Hα detections at large L_{FIR}, but it does not explain the absence of [NeV] at low L_{FIR}, especially in galaxies *with* broad Hα. In Section 6.4 the [NeV] AGN detection rate was estimated for a limiting [NeV] luminosity of L[NeV]$_{14}$ = 10^{38} erg s^{-1} (lowest L([NeV]) in AGNs from Dudik et al. 2007). However, assuming that the [NeV] luminosity scales with the bolometric luminosity of the AGN, the [NeV] in some AGNs may be much lower than 10^{38} erg s^{-1}. If this is the case, low sensitivity and/or S/N may explain the missing [NeV] in optically detected AGNs.

We tried to estimate the [NeV] 14μm luminosity for galaxies with non-detection using the [NeIII] 15μm luminosity, which is almost universally detected in the sample (64 out of 67). The [NeV] 14μm luminosity has been found to be tightly correlated with the [NeIII] 15μm luminosity in a large sample of standard AGNs (Gorjian et al 2006, hereafter G06). In Figure 6.7a plots the [NeV] 14μm luminosity as a function of the [NeIII] 15μm luminosity for all of the detections in our sample and also shows a very tight correlation. The best-fit linear relation for this plot is:

$$\log(L_{[\mathrm{NeV}]14}) = (1.03)\log(L_{[\mathrm{NeIII}]15}) - 2.26 \tag{6.1}$$

Employing a Spearman rank correlation analysis (Kendall & Stuart 1976) to assess the statistical significance of this correlation yields a correlation coefficient of r_S = 0.96, with a probability of chance correlation of 7.8×10^{-11}, indicating a significant

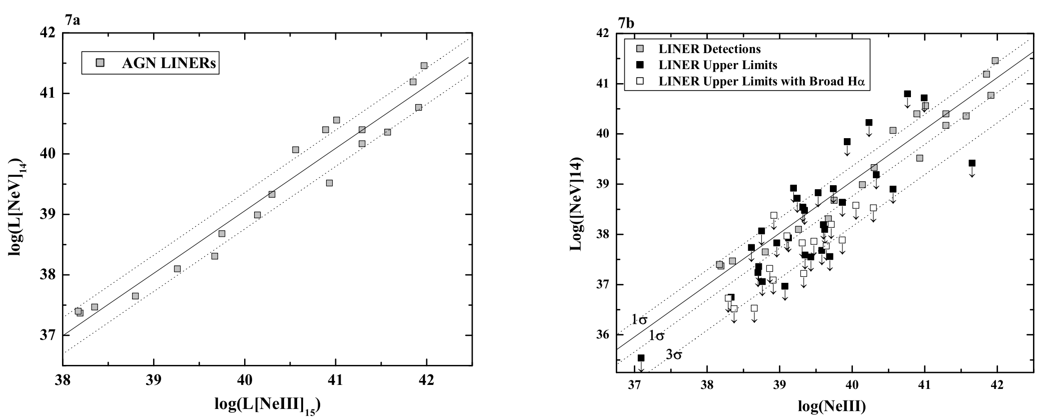

Figure 6.7: [NeIII] vs. [NeV] detections and non-detections

7a. log(L$[\mathrm{NeV}]_{14}$) in erg s^{-1} vs. log(L$[\mathrm{NeIII}]_{15}$)in erg s^{-1} for all of the AGN-LINERs for our sample, 7b. log(L$[\mathrm{NeV}]_{14}$) vs. log(L$[\mathrm{NeIII}]_{15}$) for both detection and upper limits for our sample. Surprisingly, the majority of line sensitivities (21 of 38) fall below the lowest standard-deviation fit, implying that sensitivity is *not responsible* for the missing [NeV] in these objects.

correlation. The dotted lines represent the standard deviation of fit. The standard deviation of 0.30 is much larger than the calibration error of 15% for all of the fluxes in the plot (max calibration error = 0.07).

In Figure 6.7b we also plot the 3σ [NeV] luminosity sensitivites for the non-detections in our sample on the [NeIII]-[NeV] correlation for the detections. Surprisingly, the majority of line sensitivities (21 of 38) fall below 1σ and at least 12 galaxies have [NeV] line sensitivities consistent with or below 3σ. This implies that sensitivity is *not responsible* for the missing [NeV] in these objects. Some of these galaxies may actually be non-AGN-LINERs, incapable of producing [NeV]. However, 13 of the 21 galaxies with [NeV] upper limits below 1σ and 6 of the 12 galaxies with upper limits below 3σ *do* have broad Hα, implying that they *are* AGNs.

Figure 6.6 implies that the majority of [NeV] detections are in galaxies with large L_{FIR} and Figure 6.7 implies that some of the galaxies without [NeV] may have very different ionizing SEDs from LINERs with [NeV]. Interestingly, the optically identified AGN-LINERs that do not show [NeV] represent the IR-faint population of LINERs. If detection of [NeV] is dependant on the FIR luminosity of the AGN, then the calculations of the detection rate as a function of line sensitivity may be biased toward IR-faint LINERs as suggested in Section 6.4. In this case the detection rate for [NeV] luminosity sensitivities better than 10^{38} may be off since non-[NeV] producing galaxies are included in the caluculation. In Figures 6.8a and 6.8b we plot the [NeV] detection rate as a function of line sensitivity for galaxies with $L_{FIR} < 10^{43.5}$ erg s^{-1} and $L_{FIR} \geq 10^{43.5}$ erg s^{-1} respectively, where 43.5 erg s^{-1} is the mean $\log(L_{FIR})$ for the sample. As can be seen from these plots the detection rate for a luminosity threshold of 10^{38} erg s^{-1} is dramatically different for FIR-faint objects (29%) than for FIR luminous objects (50%). Indeed FIR luminous objects yield a detection rate that is closer to previous X-ray-based estimates (Dudik et al. 2005, Satyapal et al. 2005). The total detection rate for IR-faint and IR-luminous galaxies are $\sim 28\%$ and $\sim 51\%$ respectively. These percentages are very close to the detection rate at the threshold luminosity reaffirming that sensitivity is likely not responsible for the missing [NeV]. We note there may be biases in this sample as well. The luminosity sensitivity ranges in 6.8a and 6.8b are very different. IR-faint objects show a sensitivity range of log(L[NeV]) from 36 to 39 much lower than the range for IR-bright objects (37-41), with the majority of objects having log(L[NeV]) > 40 erg s^{-1}. Thus whether the overall detection rate would increase given more sensitive observations is inconclusive.

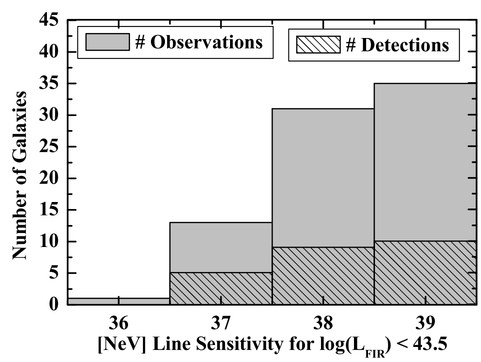

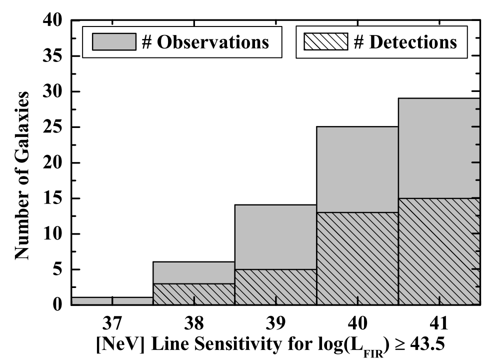

Figure 6.8: [NeV] line sensitivities as a function of detection rate and L_{FIR}

8a. log(L[NeV]$_{14}$) in erg s^{-1} line sensitivity as a function of detection rate for galaxies with $L_{FIR} < 43.5$. 8b. log(L[NeV]$_{14}$) in erg s^{-1} line sensitivity as a function of detection rate for galaxies with $L_{FIR} \geq 43.5$. As can be seen from these plots, the detection rate for a luminosity threshold of 10^{38} is dramatically different for FIR-faint objects (29%) than for FIR luminous objects (50%), implying that the overall detection rate of 74% given earlier in this section is likely underestimated.

6.5 Nature of [NeV] Detections in LINERs

As mentioned in Chapter 1, the observed nuclear SEDs in at least some LINERs are known to be different from standard AGNs (Ho 1999), deficient in the optical/UV photons normally associated with emission from an optically thick, geometrically thin accretion disk (Lasota et al. 1996). If these optical/UV photons are absent or deficient in AGN-LINERs, a corresponding deficit in the [NeV] line would be observed. However it is unclear whether this optical/UV deficit in some or all LINERs is intrinsic or if it is due to heavy extinction toward the optical/UV continuum (Satyapal et al. 2004). In fact, Figure 6.7 suggests that the LINER population is not homogeneous and that likely both scenarios are at work. If this is the case, two types of LINERs would emerge: 1) those that can and do produce [NeV] because the optical/UV photons are there, but obscured and 2) those that cannot produce [NeV] due to a shortage of the optical/UV photons needed to create the ion. For at lease 6 galaxies in the sample, there is evidence of AGN activity in the nucleus in the form of broad permitted lines in the optical spectrum. However, these same 6 galaxies show no [NeV] in the mid-IR spectrum and show no evidence that this [NeV] would appear given longer, more sensitive observations. At the same time, [NeV] is detected in at least 26 other sources, some of which show *no* evidence for AGN activity in any other band. Detailed photoionization models are required to assess the ionizing SED in these galaxies and to confirm that a UV-deficient radiation field is required to replicate the mid-IR line fluxes.

Table 6.5: NeV Line Flux Ratios

Galaxy Name (1)	$\frac{[NeV]_{14}}{[NeV]_{24}}$ (2)	Galaxy Name (3)	$\frac{[NeV]_{14}}{[NeV]_{24}}$ (4)
NGC1052	0.22	UGC5101	1.06
NGC3166	<0.70	NGC4666	<0.06
NGC3368	>0.19	UGC8387	0.13
NGC3507	>0.69	NGC5104	0.47
NGC3521	>0.23	Mrk273	0.39
NGC3642	<0.08	NGC5953	0.25
NGC4036	<0.03	IR15335···	>0.28
NGC4278	<0.04	IR16164···	0.46
NGC4438	<0.19	NGC6240	>1.31
NGC4736	>0.66	NGC6286	0.33
NGC5353	<0.89	ESO593···	>1.19
NGC5371	0.13	NGC7130	1.10
NGC660	>0.31	ZW453.062	0.80

Columns Explanation: Col(1) and Col(3): Common Source Names; Col(2) and Col(4): [NeV]14μ / [NeV]24μ line flux ratio

6.5.1 Evidence for Mid-IR Extinction

Traditionally, ratios of infrared fine-structure transitions from like ions in the same ionization state with different critical densities have been used to provide abundance-independent density estimates for the ionized gas from which they arise. However, as demonstrated in Chapter 5, we find that the ratio of [NeV]14μm/[NeV]24μm in some AGNs result in ratios that are below the theoretical low density limit. By ruling out aperture effects and theoretical uncertainties, we argue that differential infrared extinction due to dust in the obscuring torus may be responsible for the ratios below the low density limit. If the LINERs in our sample suffer severe extinction toward the optical/UV band, one might expect the mid-IR line fluxes to be similarly effected.

The low density limit for the [NeV]14μm/[NeV]24μm ratio is 0.83. Table 6.5 lists the [NeV] ratio for all of the LINERs in our sample. Clearly, the majority LINERs in the sample with [NeV] detections have ratios far below the theoretical limit. Figure 6.9 shows the [NeV] 24μm luminosity vs. [NeV] 14μm luminosity for LINERs and a sample of standard AGNs. Of the 26 LINERs with [NeV] detections, 15 have ratios that are consistent with the low density limit to within the calibration error, while only 4 LINERs have ratios significantly above it. From Figure 6.9, it is clear that LINERs show [NeV] line flux ratios well below standard AGNs. The average [NeV]14μm/[NeV]24μm ratio in LINERs where both lines are detected is 0.49. The same ratio for our sample of standard AGNs is 0.98. Assuming that extinction is responsible for the anomalous ratios (Dudik et al. 2007), these results require that the extinction curve in LINER galaxies must be characterized by higher extinction at 14μm than at 24μm.

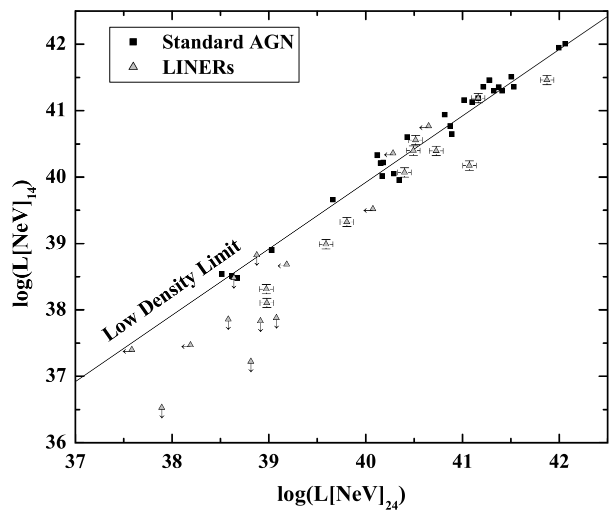

Figure 6.9: L[NeV]14μm vs. L[NeV]24μm

The [NeV] 14μm luminsity to [NeV] 24μm luminosity for all of the detections in our sample as well as a sample of standard AGNs. The majority of LINERs in our sample (15/26) have ratios well below the low density limit. This may imply severe extinction toward the [NeV] 14μm emitting region in these galaxies. The error bars in this plot represent the calibration error of 15%

In Figure 6.10 the [NeIII]15μm luminosity as a function of the [NeV]14μm luminosity is re-ploted for LINERs and the large sample of standard AGNs from G06.

G06 find a very tight correlation between L[NeIII]$_{15}$ and L[NeV]$_{14}$ in these standard AGNs. If the [NeV] 14μm line is effected by extinction in LINERs, and all else being similar in LINERs and standard AGNs, one would expect the [NeV] $_{14}$ /[NeIII] $_{15}$ ratio to be lowered compared with unaffected galaxies. Figure 6.10 suggests this is indeed the case, with LINERs showing a very different relationship between [NeV] and [NeIII] than standard AGNs. Of the two galaxies from G06 that overlap with the LINER slope, one (NGC 3079) is a LINER and the other (Cen A) was shown in Dudik 2007 to have a line ratio consistent with the low density limit. We note that we have chosen the [NeIII] 15μm and [NeV] 14μm line since they are obtained from the same IRS module so as to avoid aperture effects that may result from ratios of lines from different sized apertures. If aperture effects due to the variable distances of the objects in both this sample and the G06 sample were at work, the opposite effect on the [NeV]/[NeIII] ratio presented in Figure 6.10 would be expected, with [NeIII] much lower for nearby LINERs than for the distant galaxies in the G06 sample (2.4-300Mpc for LINERs vs. 4-3000 Mpc for G06). The best fit relation for the LINER population is given in Section 6.6, Equation 1. The best fit relation for the G06 sample is given by:

$$\log(L_{[\mathrm{NeV}]14}) = (1.06)\log(L_{[\mathrm{NeIII}]15}) - 2.99. \qquad (6.2)$$

Clearly the slopes for both correlations are very similar, implying that the relation holds for both objects. However the y-intercept for standard AGNs is larger than that for LINERs, implying that [NeV] 14μm luminosity is deficient in LINERs.

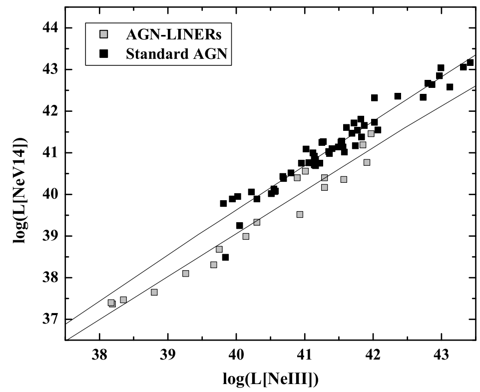

Figure 6.10: [NeV] vs. [NeIII] for LINERs and standard AGNs

Log(L[NeV]$_{14}$) in erg s^{-1} vs. log(L[NeIII]$_{15}$)in erg s^{-1} for all of the AGN-LINERs for our sample as a well as a sample of standard AGNs from G06. We note the slopes for both correlations are very similar, implying that the relation holds for both objects. However the y-intercept for standard AGNs is larger than that for LINERs, implying that [NeV] 14μm luminosity is deficient in LINERs.

6.5.2 Unique SEDs for [NeV]-detected AGN-LINERs ?

The analysis thus far lends credence to the theory that the optical/UV deficit in AGN LINERs with [NeV] is not intrinsic, but rather due to heavy obscuration in these particular LINERs. On the other hand, one could argue that the anomalous L[NeIII]$_{15}$ to L[NeV]$_{14}$ relationship in LINERs when compared to standard AGNs suggests a different intrinsic SED in LINERs; one in which [NeV] *can* be produced but at lower luminosities because of a shortage in ionizing photons. If this were the case, the [NeV] 24μm line flux should be similarly effected. In Figure 6.11a the [NeV] 24μm luminosity as a function of the [OIV] 26μm luminosity is plotted for both LINERs and standard AGNs (AGNs taken from Dudik et al. 2007, Haas et al. 2005, and Sturm et al. 2002 which overlap with the G06 sample as well as AGN-ULIRGs from Farrah et al. 2007, hereafter DHSF sample). Since these two lines are close in wavelength, the line flux ratio is insensitive to extinction. In this case as in Figure 6.10 we have chosen [OIV] since it is obtained from the same IRS module to avoid aperture effects due to ratios of lines from apertures of different sizes. As can be seen, both LINERs and standard AGNs follow a very similar trend in both the plot and the [NeV] 24μm/[OIV] 26μm line ratio. However, the mean ratio for LINERs is much larger than that for the DHSF sample ($\sim$ 0.7 vs. 0.4 respectivly), implying that LINERs have larger ratios of [NeV]/[OIV] than standard AGNs. Some differences between this LINER sample and the DHSF AGN sample may spring from differences in the line fitting and line de-blending techniques for the [OIV]26μm line, which is strongly blended in some cases with an [FeII] 26μm line.

Aperture effects due to the variable distances of the objects in both the LINER sample and the DHSF sample could artificially raise this ratio in the most nearby objects since the [OIV] may be spatially extended. In this scenario AGNs in this sample and in the DHSF sample would have similar ratios. In Figure 6.11b we plot the [NeV] 24μm luminosity vs. [OIV] 26μm luminosity for the galaxies from the DHSF sample that also overlap with the 10 -160 Mpc distance range of the [NeV]24μm emitting LINERs. A similar inconsistency is found between the means in the new nearby AGN sample and the LINER sample (0.41 and 0.70 respectively), implying that aperture effects due to distance are likely not the cause of the discrepancy in line ratios.

A Kolmogorov-Smirnov statistical test shows significant differences in the distributions of the [NeV]24μm to [OIV]26μm ratios between LINERs and standard AGNs, but with mean values within their 1σ standard deviations (1σ for both samples $\sim$0.30). These results suggest that the LINERs and the DHSF AGNs represent different populations in their [NeV]24μm/[OIV]26μm ratios. However the limited

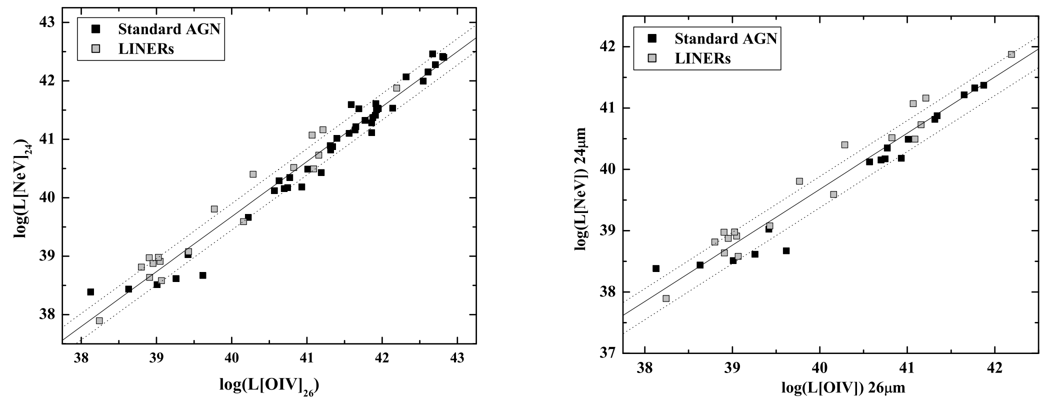

Figure 6.11: [NeV]24μm vs. [OIV]26μm

6.11a. The [NeV] 24μm luminosity to [OIV] 26μm luminosity for all of the detections in our sample as well as a sample of standard AGNs. 6.11b. The [NeV] 24μm luminosity to [OIV] 26μm luminosity for all of the detections in our sample and a sample of standard AGNs with the same distance range as the LINERs. We find that aperture effects are likely not the cause of the discrepancy between LINER and AGN [NeV]/[OIV] ratios.

sample size, the variability in SED shape for all of the AGN subclasses included in the DHSF sample, and differences in line de-blending methods for [OIV] (and [FeII]) between this sample and the AGN sub-samples from DHSF preclude any definitive conclusion on this subject. If these results intimate that LINERs have different SED shapes from standard AGNs, then the ratios of [NeV]/[OIV] in LINERs suggest that the lower energy 55eV photons are deficient in these objects or that the 97eV photons are more abundant as compared with standard AGNs. In any case, our results imply that LINERs are severely effected by extinction as evidenced by their [NeV]14/[NeV]24 μm ratios and supported by their both their [NeV]14/[NeIII]15 and [NeV]24/[OIV]26 ratios. Detailed photoionization models are needed to confirm any SED differences further and will be the subject of future work.

6.6 Conclusions

An archival mid-IR spectroscopic study of 67 LINERs was conducted in order to search for mid-IR detected AGNs and to compare the mid-IR derived detection rate with those from the optical, X-ray and radio bands. In addition the line ratios in AGN-LINERs were compared with those from as sample of standard Seyferts and quasars. Our main results are as follows.

1. The [NeV] 14 and/or 24 μm line is detected in 26 of the 67 galaxies in our sample. We find a mid-IR detection rate of 39%. There is no evidence that this detection rate would improve given more sensitive observations.

2. Very little consistency exists between the detection of [NeV] and either the presence of Broad Hα or the presence of a hard X-ray point source. The consistency is worse for optical observation. 26% of galaxies with optical and IR measurements show [NeV] emission lines, but no broad Hα component. More surprisingly 20% show broad Hα but no evidence of [NeV] , for the same sub-sample of galaxies with both optical and IR data.

3. Using the combined X-ray, optical, and IR statistics, an AGN-detection rate in LINERs of at least 74% is found. Better sensitivity X-ray and IR observations and inclusion of radio data will only increase this detection rate.

4. We re-examined whether longer observing times for IR observations may yield a higher mid-IR AGN detection rate for each band and further consistency between optical and IR observations. However, multiple tests of possible biases indicates that even with longer observing times, [NeV] would *not* be detected in at least 6 broad Hα detected AGN-LINERs. In light of this we suggest that LINERs are *not* homogeneous, and in fact constitute two alternate subclasses:

LINERs that produce [NeV] and LINERs that lack [NeV] because they are deficient in ionizing optical/UV photons.

5. The intrinsic nature of the [NeV] detections was examined to see if these lines were affected by an “optical/UV deficit.” Instead, using ratios of [NeV]14μm/[NeV]24μm, LINERs with [NeV] detections are shown to likely suffer severe extinction toward the [NeV]14μm line emitting region. In addition, a plot of of [NeIII]15μm vs. [NeV]14μm shows that LINERs have consistently lower [NeV] relative to [NeIII] than standard AGNs.

6. The anomalous [NeIII]15μm, [NeV]14μm relationship could be explained if the SEDs of all LINERs were different from standard AGNs, in which case, the [NeV] 24μm line would obey a similar behavior to the 14μm line. However, instead the [NeV] 24μm to [OIV] 26μm relationship is higher in LINERs than in standard AGNs. Using a K-S test, the sample of standard AGNs (which includes Seyferts, Radio Galaxies, and ULIRGs) is found to have different [NeV]24/[OIV]26 ratios from LINERs. However, limited sample size among other things, preclude any definitive results on this subject. Detailed photoionization modeling is critical to confirm any differences in SED shape and will be the subject of future work.

Chapter 7: CONCLUSIONS

In this Thesis I have studied the nuclear properties of Low Ionization Nuclear Emission-line Regions in order to diagnose the ionizing source responsible for their unusual optical line ratios, determine the accretion properties of those that are AGNs, and finally to study the overall SEDs of these objects. I have used a multi-wavelength X-ray and mid-IR approach to answer some fundamental questions that compliment and extend previous work. A summary of the main conclusions of this study are as follows:

Q: What is the ionization mechanisms responsible for the optical line ratios in LINERs? What fraction of LINERs are AGNs?

A: . Based on optical studies, the percentage of LINERs hosting AGNs is 23% (Ho et al. 1997). Our investigation has shown that this percentage is significantly underestimated. We have shown (Chapters 3,4,6) that using combined X-ray imaging and mid-IR spectroscopic observations, the AGN detection rate is at least $\sim$ 75%, implying that the majority of LINERs are AGNs. The AGN detection rate may in fact be higher if the sensitivity of the X-ray and IR observations are improved. Our study demonstrates that optically studies are insensitive to finding the vast majority of LINERs with active black holes. This is particulary true in the most infrared-bright objects which constitute the dominant population of LINERs. .

Q: What are the luminosities and accretion properties of those LINERs found to contain AGNs?

A: In Chapters 3 and 4 we conducted an extensive analysis of the overall luminosities and accretion properties of AGN-LINERs. We find that the X-ray luminosities of LINERs range from 10^{38} to 10^{44} erg s^{-1}. Using the X-ray luminosities of the AGNs to estimate the bolometric luminosities and the published stellar velocity dispersions to estimate the black hole mass, we calculated the Eddington ratio for our sample of LINERs. We find that LINERs, which are known to have the largest black hole masses. also have relatively low accretion rates. The Eddington ratios (L/L_{EDD}) in LINERs range from $\log(L/LEDD) \sim$ -7 to -2, as compared to ratios ranging from$\sim$ -3 to nearly 2 in a sample of standard AGNs (Seyferts, RLQ, RQQ, NLS1s). With the largest black hole masses and low Eddington ratios, our studies may suggest that LINERs represent the population of AGNs just before accretion onto the black hole ceasesa finding that could have a tremendous impact on studies concerning the formation and evolution of black holes and galaxies.

Q: How do the accretion properties in AGN-LINERs compare with the properties of the host galaxy?

A: In Chapters 3 we find we have found an intriguing correlation between the Eddington ratio, L/L_{EDD}, which is a proxy for accretion rate normalized to the Eddington rate, and the far-infrared (far-IR) luminosity, L_{FIR}, as well as the IR-brightness ratio, L_{FIR}/L_B, of the host galaxy that extends over seven orders of magnitude in L/L_{EDD}. This trend implies that either the mass accretion rate or the radiative efficiency, or a combination of both, scales with the far-IR luminosity and IR-brightness ratio of the host galaxy. Since the far-IR luminosity is a widely-used measure of the star formation rate in galaxies, this correlation may imply a fundamental link between the growth of the black hole and the buildup of the host galaxy. These findings support the proposition for a causal connection between the birth and growth of black holes and the formation and evolution of galaxies.

In Chapter 4 we explored whether the correlation extends to other AGN subclasses or whether it is characteristic of only LINERs. We expanded the sample to include 140 AGNs, including LINERs, Seyferts, Narrow line Seyfert 1s (NLS1s), Radio quiet quasars (RQQ), and Radio-loud AGNs (RL AGNs) and found that the correlation is reinforced for the entire AGN sample, extending over almost nine orders of magnitude in Eddington ratio. Interestingly, there is a distinct variation in the slope of the relationship for the various AGN subclasses. If the Eddington ratios are converted to accretion rates assuming a uniform raditive efficiency, the distinct slopes are reinforced. However if the radiative efficiency is varied and is assumed to be particularly low for LINERs, all of the AGN subclasses have consistent slopes. Without accurate estimates for the radiative efficiency it is unclear if the discrepancy between subclasses is intrinsic or artificial. If the discrepancy is intrinsic this result may imply that the growth of the bulge does not always match the growth of the black hole at all times in a galaxys evolution.

Q: How are the SEDs of LINERs characterized in the mid-IR? Is the optical/UV deficit found in LINERs intrinsic? Or due to severe extinction toward the optical/UV continuum?

A: In Chapter 6 we find that the LINER class is likely not homogeneous, and may constitute two mid-IR defined subclasses: AGN-LINERs that produce [NeV] and AGN-LINERs that do not. The LINERs that *do not* produce [NeV] are likely deficient in the optical/UV photons needed to produce this line, however there is clear optical and X-ray evidence that these LINERs *are* AGNs. LINERs that *do* produce [NeV] seem to be severely effected by extinction toward the [NeV] 14μm emitting region. Indeed their [NeV]14μm/[NeV]24μm line flux ratio is well below the theoretical low density limit. They also show anomalous [NeIII] 15μm to [NeV]14μm ratios with lower L[NeV]$_{14}$ than standard AGNs. This could be easily explained if the SEDs of all LINERs were different from standard AGNs, in which case, the [NeV] 24μm line should obey a similar behavior to the 14μm line. However, instead we find that the [NeV] 24μm line relative to [OIV] 26μm in these galaxies is higher in LINERs than in standard AGNs. Using a K-S test, we find that our sample of standard AGNs, which includes Seyferts, Radio Galaxies, and ULIRGs, have different [NeV]24/[OIV]26 ratios. However, limited sample size among other things, preclude any definitive results on this subject. Detailed photoionization modeling is critical to confirm any differences in SED shape and will be the subject of future work.

Appendix A: SMART High Resolution Data Analysis

A.1 Loading the Data

1. Load SMART in the folder where your data is located.
    - Remember that:
      ch0 = SL (SL2 = 5.2-7.7μm, SL1 = 7.4-14.5μm),
      ch1 = SH (9.9-19.6μm),
      ch2 = LL (LL2=14-21.7μm, LL1=19.5-38μm)
      ch3 = LH (18.7-37.2μum)

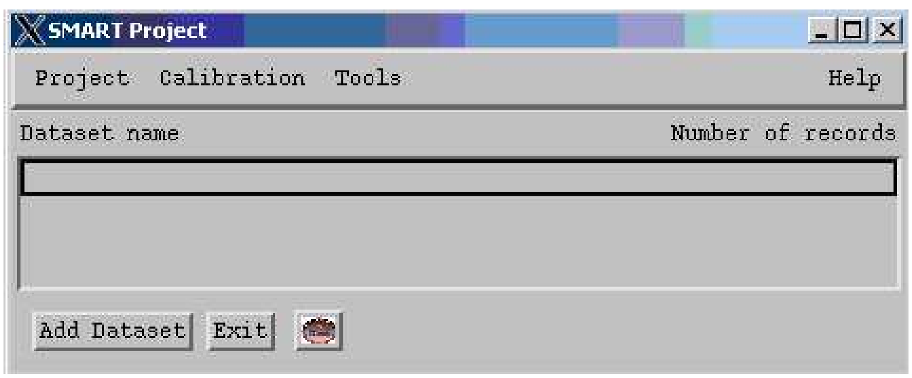

Figure A.1: SMART Project gui

    - Click: Add Dataset
    - For now, call this dataset "1"
    - Click ok
    - Click on the dataset you just made called "1" to highlight it
    - Click Add records/Edit Dataset the following gui will pop up:

2. We are now going to browse the entire galaxy file from leopard

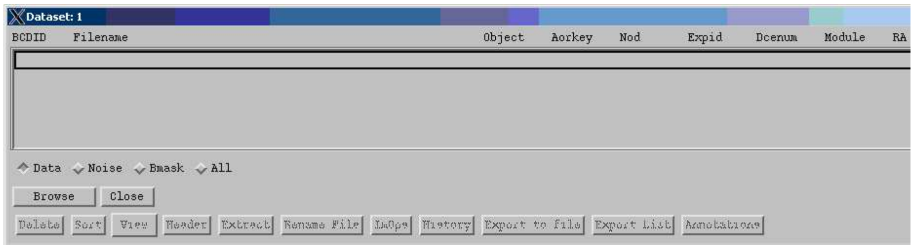

Figure A.2: Dataset gui

- click browse and the following gui will pop up:
- In the left corner of the second gui type *.fits
- Press Enter/Return Key on keyboard
- To select all fits, hold down the shift button and click the down arrow to highlight all of the files.
- Click OK
- The Dataset GUI should look like this now:

3. Now we are going to view the first spectrum:

   - Click on the first coa2d file or the coa2d file you are interested in. This will be the only file with information in all columns.

IMPORTANT: If you have a dedicated background file you will have to load it here along with the spectrum. To do this you must highlight both of these files at once by holding down the Control key and clicking on both files.

FYI: *For Mapping observation you will need to use leopard to find the coordinates of the first file you are interested in looking at and find that file in the DATASET gui. The coordinates in leopard are NOT always EXACTLY the same as what shows up in the gui (and the fits file), BUT THEY SHOULD BE VERY VERY CLOSE. The difference results because the coordinates in leopard are calculated, whereas the coordinates from the fits file are the final coordinates. For Staring observations the two slits are AWAYS centered on the PIs requested position (usually the nucleus).*

   - Click Extract and the following gui will pop up:

4. We are not going to do background subtraction with High Res. Observations.

   - Click Full
   - Click Extract. The following gui will pop up:

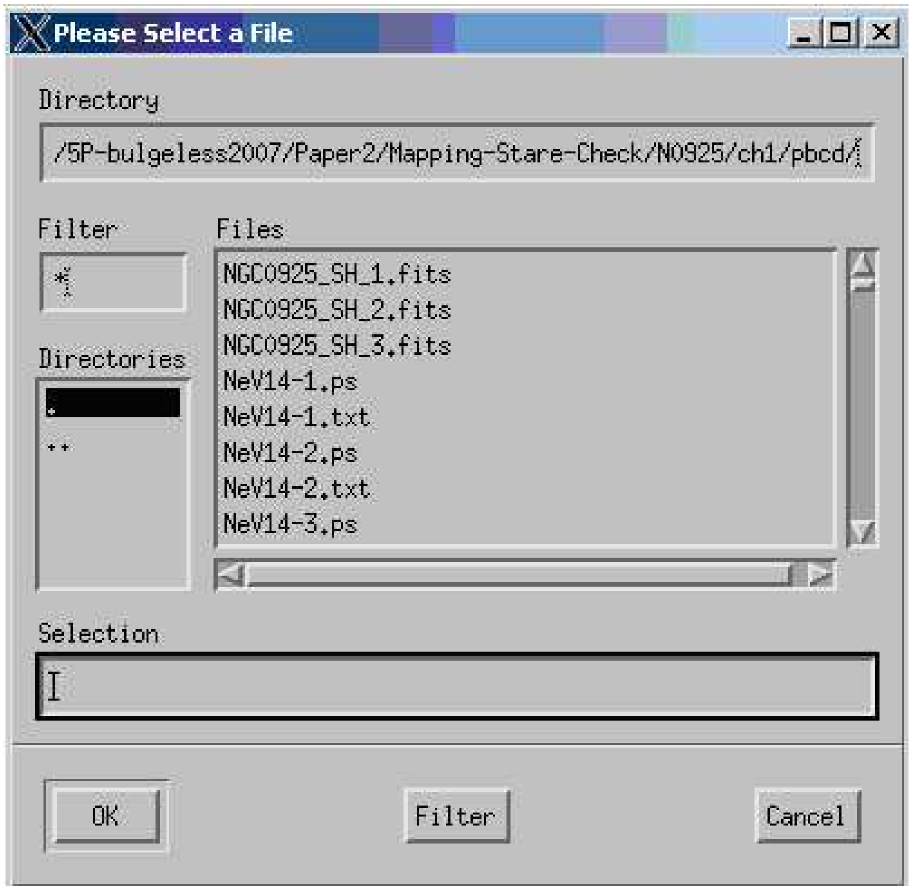

Figure A.3: File gui

FYI: *The other buttons on this gui will allow you to define the source by using only part of the emission from the entire slit. Manual Source extraction might be useful for Low Res. Observations, when you want to use part of the slit to subtract the background. I am not going to go over this here. This method cannot be used for High Res. Observations because the slit is too small.*

If you have a dedicated back ground file, follow Step a otherwise go to Step b.

a. Dedicated File Background Subtraction
   - If you have a dedicated background file you should have loaded it with the spectral image.
   - Click image

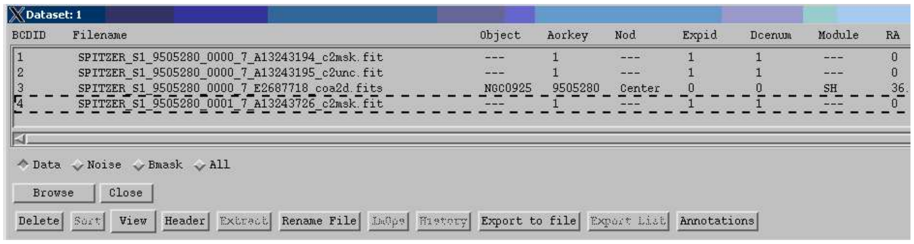

Figure A.4: Dataset gui 2

- The same gui should now show a box which gives you the option of choosing the dedicated background file. BE CAREFUL TO CHOOSE THE APPROPRIATE FILE. One file is your spectrum and the other is the bkg file.
- Once the bkg file is selected click EXIT.

b. No dedicated Background file/No Sky subtraction

- With "None" selected at the top, click EXIT
- The following Gui should pop up:

A.2 Zapping Bad Data

1. View the Spectra.

   - In the second row of the SMART IDEA gui called 'Orders', click on All
   - Click on the style button on the left panel. When the Style gui pops up click connected and red (These are my preferences but you can choose what you want here)next click Apply
   - The spectrum should pop up in the window.

2. Zapping Spectra: Zapping bad data is very complicated and might take some practice. As a rule you want to zap as little as possible because the noise determines the goodness of your fit. However it is also critical that you zap bad pixels and drooping spectra at the edge of the order so that you do not end up with false detections or nondetections that should be detections. At the edges of each order the detector goes a little crazy and causes what is known as drooping. Much of this artifact is fixed through the pipeline prior to download, but there is often some residual drooping. Zapping the ends of these orders is very important especially when they overlap with the line you are interested in. This happens a lot with the NeV14 and 24μm lines.

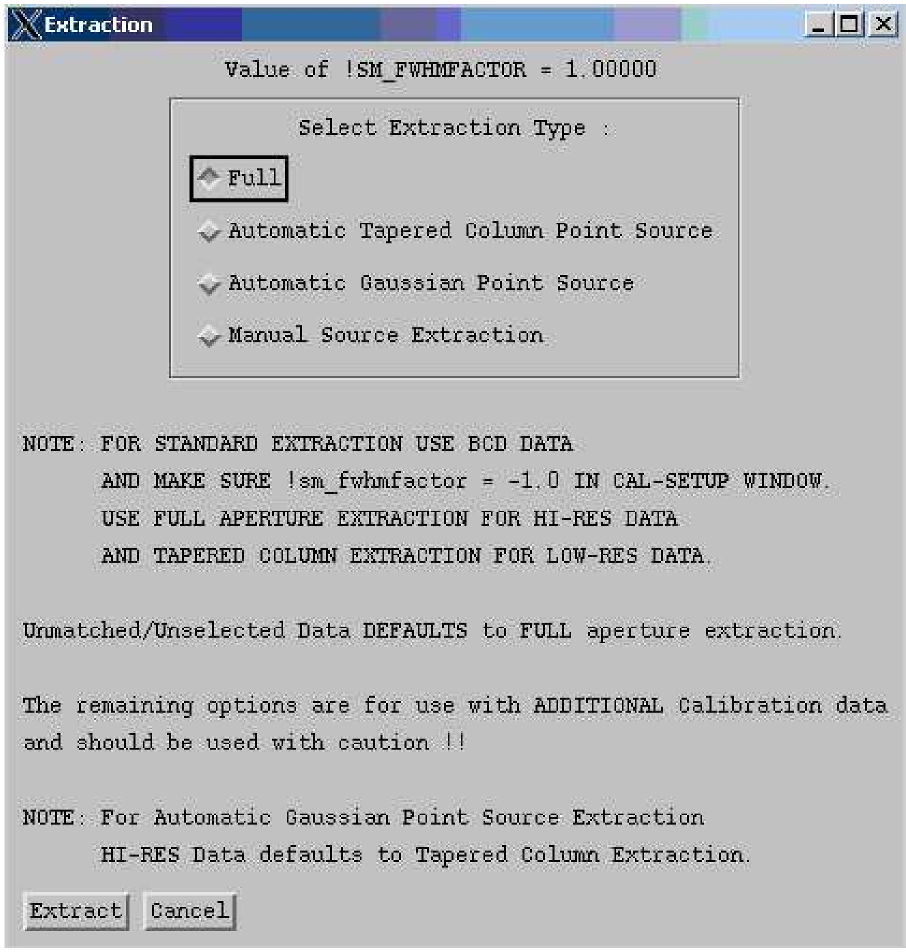

Figure A.5: Extraction gui

- To zap simply right click and drag a box over the data points you want to zap.
- A gui will pop up that looks like this:
- Click zap in the left-most column.
- This will DELETE those data points.

3. Examples of points to zap:

   A. Points with flux densities below 0 are usually residual drooping

   B. The very edge of each order suffers drooping. In the image below, the white arrow points to the spectra that need to be zapped. The green arrow points to what the spectra should look like. This is the middle of

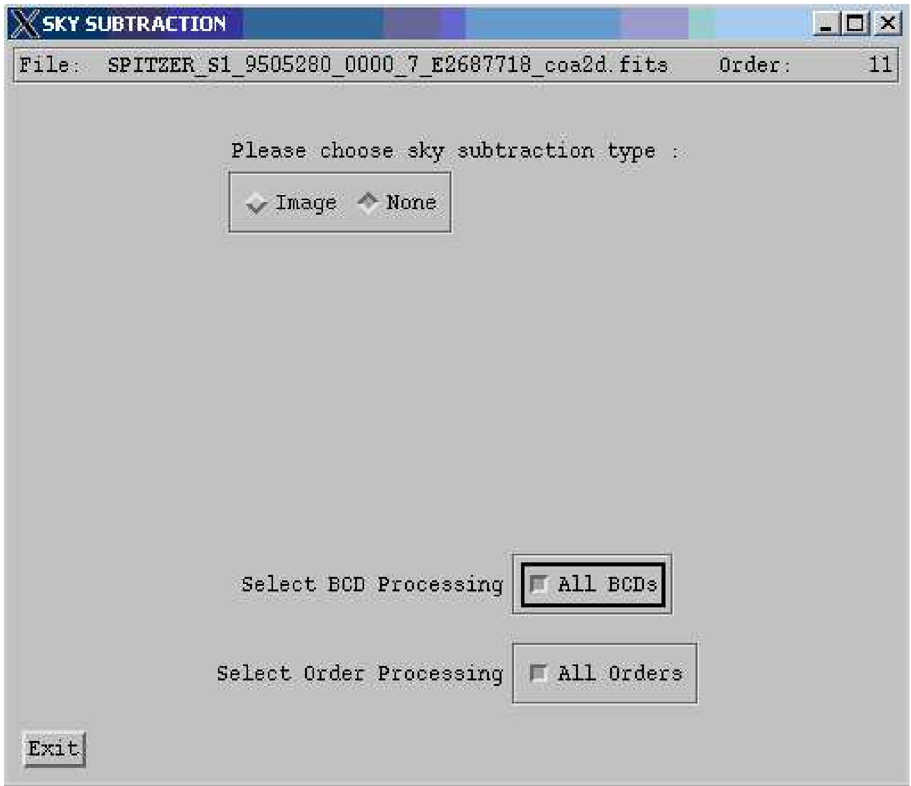

Figure A.6: Sky Subtraction gui

an order where there are no real artifacts. Basically you want to zap until the edge of the overlapping order that suffers drooping effects maintains a similar flux density to the order that does not suffer the drooping effect

C. Huge variations in flux held up by only 1 data point are usually caused by a bad pixel. These points need to be zapped.

4. Averaging over the orders: In order to fit spectral lines you will have to average over the orders. It is very important to do this AFTER you zap.

   - To average right click a box over the ENTIRE spectrum.
   - The APPLICATIONS gui will pop up.
   - Click Average and the following gui will pop up:
   - Click Standard Clip Mean. This will average spectra with less than 2.5 sigma between the orders.
   - Click the X at the type right corner of the gui. This will close the gui and average the spectra.

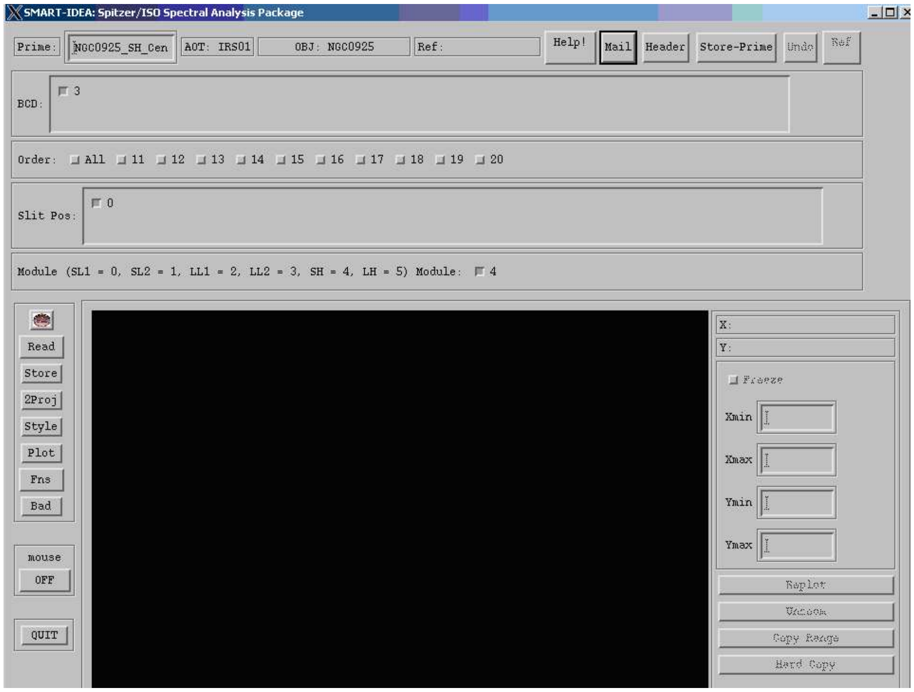

Figure A.7: SMART Idea gui

You will be spending most of your time with this gui

IMPORTANT: One you have finished zapping and averaging you should SAVE YOUR WORK!!!! Once you have saved you spectra you can load it as many times as you want, but if you dont save it you will have to do all of the zapping, etc. over again!

5. Saving your spectra:

   - At the top right corner of the SMART IDEA gui Click Store Prime
   - On the left column Click Store
   - When the gui pops up with your stored data, click on the last spectrum in the listthis is the spectrum you just stored. Usually it will have a name like ZZZZZZZZZZ_NGCXX_SH.fits. The Zs are for all of the zaps you made.
   - Click "Choose and Apply function"
   - Click "Write to Disk", and immediately click "In Fits Table Format"
   - I always save my spectra in this form because there will be multiple spectra for the same object. You might find a better method. "nameofgalaxy_SH_1.fits" for Slit 1 and "nameofgalaxy_SH_2.fits" for Slit 2.

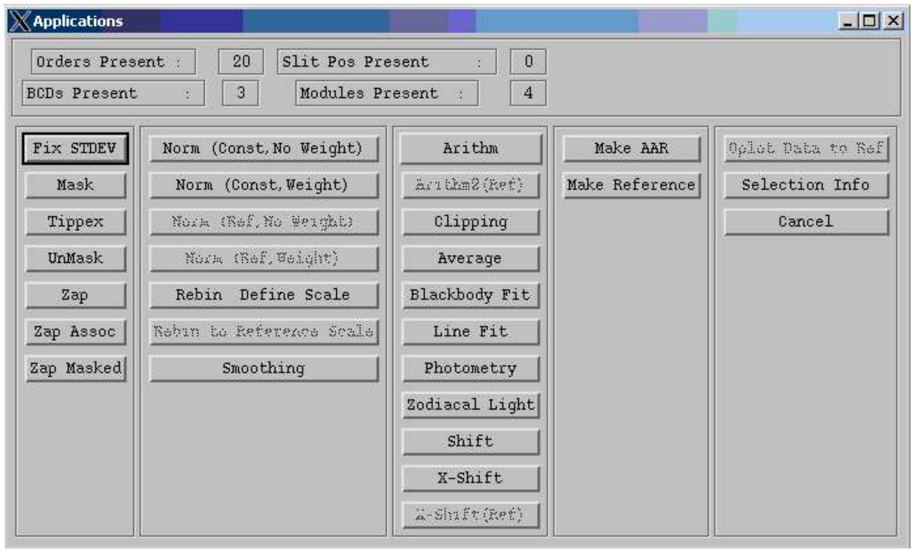

Figure A.8: Applications gui

A.3 Fitting Spectral Lines

1. Fitting luminous lines such as NeII, NeIII, SIII, and SiIIlines that are not blended.

   - Right click and drag a box around the line you are interested in. if you have to zoom in, you can **left click**, making a box around the line you are interested in. That will allow you to zoom in closer to the line. When you are ready to select the line, be sure to provide enough continuum so that the program can fit a baseline along the continuum. This is important because the baseline determines the noise. The LINE FIT gui will then pop up:
   - On the left column click "Order of baseline fit". (01,2,3, represent 1st 2nd 3rd etc. order polynomials) Choose the type of baseline that would best fit the noise. In the case above I would use "2"
   - The "Line fit" section should be automatically set to "single Gaussian" This is what I usually stick with.
   - Finally at the bottom, where it says "redshift" click on the button that says "z" and fill in the redshift of the source.
   - We are now ready to let the program fit this line: Click "Fit Baseline Line" This should fit the continuum and line.
   - A new gui should pop with the parameters of the fit. Click Record. This temporarily records the fit in SMART.

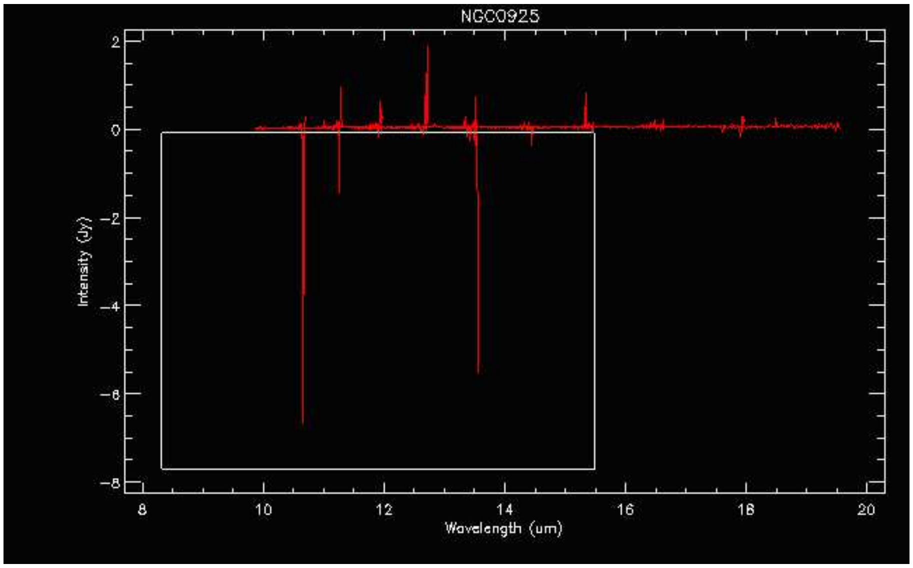

Figure A.9: Zapping 1

The white box shows points below zero. (drooping)

- To save the parameters to disk, click "save to disk" at the left bottom corner of the line fit gui
- To save a *ps image of the fit click hard copy on the right-most of the LINE FIT gui.

2. Fitting OIV and NeVblended lines: Fitting OIV or NeV is very similar to (1) for non-blended, strong lines. However, more often, these lines are very difficult to fit because they are not very luminous or non-existent in most objects. When a NeV line is on the line between a detection and a non-detection often you can fit it one way and it will be 2.5 sigma (a non-detection) or fit it another way and it will be 4 sigma (a detection). One thing you should always do is really look at the line and compare it with the noise. Does it look like noise or does it look like a detection? A line is ALWAYS held up by more than one data point and is often at least 3-5 data points. Your eye is very good at picking out the baseline, which is usually pretty uniform.

    - Once in the LINE FIT GUI (see step 1 first bullet above), choose the order of your baseline and the line fit as done above. Input the redshift.
    - Sometimes you can fit the NeV and OIV very easily as is done with the luminous lines in (1)
    - For blended lines you will have to manually fill in the line center and FWHM in the column on the right. You will also have to manually fit the

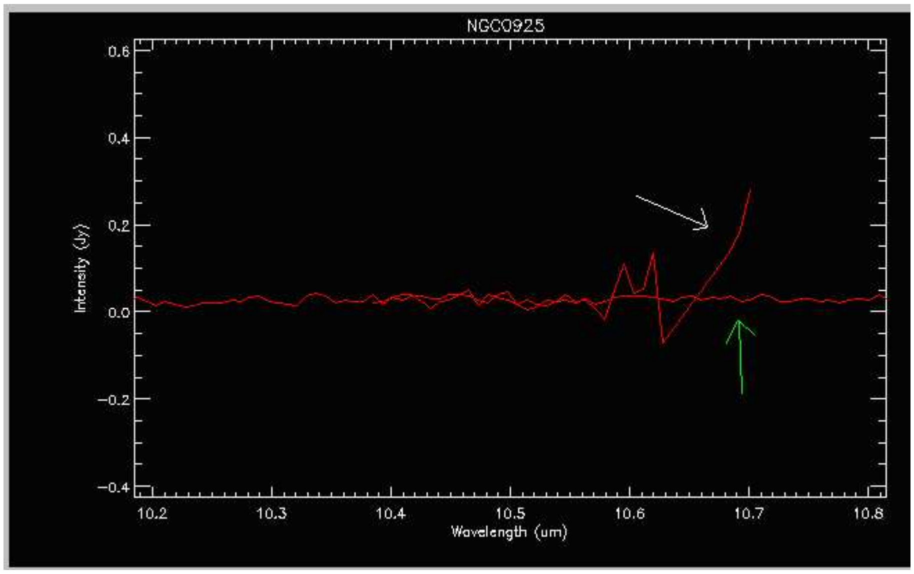

Figure A.10: Zapping 2

The edges of the orders need to be zapped

baseline because you dont want the program to consider the other lines as noisethis will increase the baseline and thus the error resulting in a non-detection when there should be a detection.

FYI *The "line list" button in the middle of the line fit gui can be very useful when manually fitting lines. This button will cause a gui to pop up showing all of the rest wavelengths of the lines that are available in the MIR as well as their redshifted wavelengths (as long as you have the redshift inputed before pressing the button). You can find your line and its redshifted wavelength and write it down. (or you could calculate it yourself which ever is easier)*

- To fit the baseline, manually right click two boxes on either side of the lines EXCLUDE THE NEV, THE PAH AND THE CLII TO AVOIID HAVING THESE CONSIDERED IN THE BASELINE FIT.
- Click Fit baseline under the spectral-view window.
- To fit the line you can do one of two things
  a. You can right click a box that cover the NeV line and click Fit Line under the spectra view window. BEWARE OF THIS METHOD. WE HAVE FOUND THAT SOMETIMES THIS RESULTS IN UNREALISTIC VALUES FOR THE ERROR ON THE FLUX. THUS INSTEAD OF WHAT SHOULD BE A NON DETECTION YOU GET A 7 SIGMA DETECTION. TRUST YOUR EYE!!!

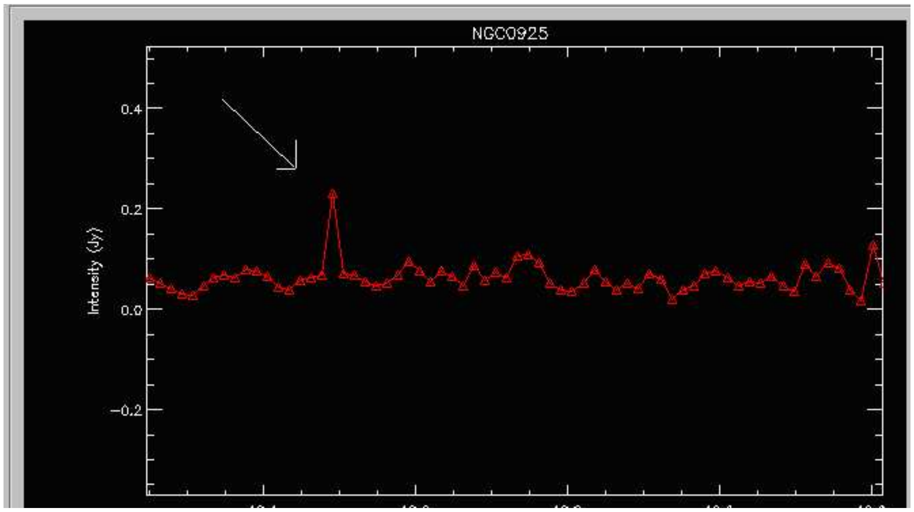

Figure A.11: Zapping 3

Bad Pixels such as these must be zapped

b. The second method is to fill in the line center and the FWHM on the left column and then click Fit Line under the spectral-view window. You might have to vary the FWHM and the line center to get an good fit. Remember that the gas containing the NeV and OIV might be slightly blue shifted or further redshifted depending on the environment. This means that the line might not fall right on the "redshifted line center. WE FIT ANYTHING WITHIN THE RESOLUTION ELEMENT AS A LINE ($R = \lambda/\Delta\lambda$ where λ is the rest wavelength of your line, $\Delta\lambda$ is the resolution element and R is the resolution of the instrument (600 for high resolution)) For the FWHM I always start with the resolution element (0.024um for NeV14um) and increase the FWHM until I get a good fit. **DONT FORGET TO SAVE YOUR FIT (SEE 1.)**

3. Fitting Non-Detections: The method for fitting non-detections (or upperlimits) is pretty standard. In principle you are just fitting the noise at the resolution element of the instrument. This method is very similar to fitting OIV and NeV lines.

- Once in the LINE FIT GUI (see step 1 first bullet above), choose the order of your baseline and the line fit as done above. Input the redshift.
- You can use the line list button in the middle of the LINE FIT gui to find the redshifted wavelength of your line (or you could just calculate it yourself)

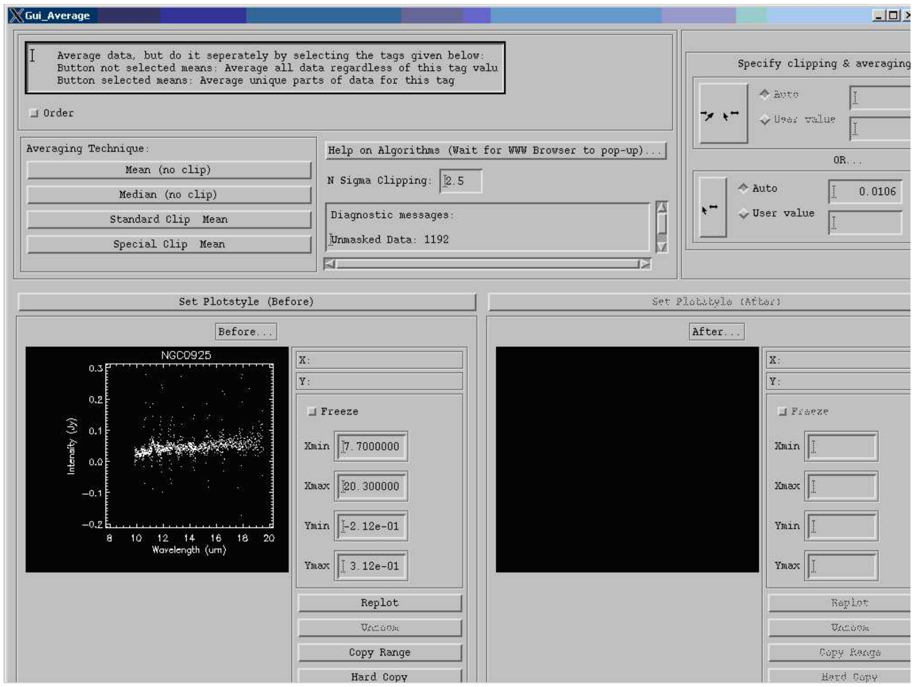

Figure A.12: Averaging gui

- In the "line center" section in the left column of the LINE FIT gui, click enter (which means manually enter) and fill in the redshifted wavelength of your line.
- In the line width FWHM section fill in the width to the resolution element. See (2) above.
- You should manually fit the baseline as in (2) if you have other lines (other than the one you are looking for) in the spectrum you have chosen. If the spectrum you have chosen is free of other possible detections, you can just click "Fit Baseline Line" at the center of the gui. This should fit the continuum and line automatically.
- An upper limit is defined as 3 * the error on the flux.
- SEE FIGURE BELOW FOR AN EXAMPLE OF A FIT FOR A NON-DETECTION

A.4 Full Spectrum for Publications

1. *Spectra Line fluxes for publications:* As you should know by now, every observation (mapping or staring) from every module (SL, SH, LL, or LH) comes

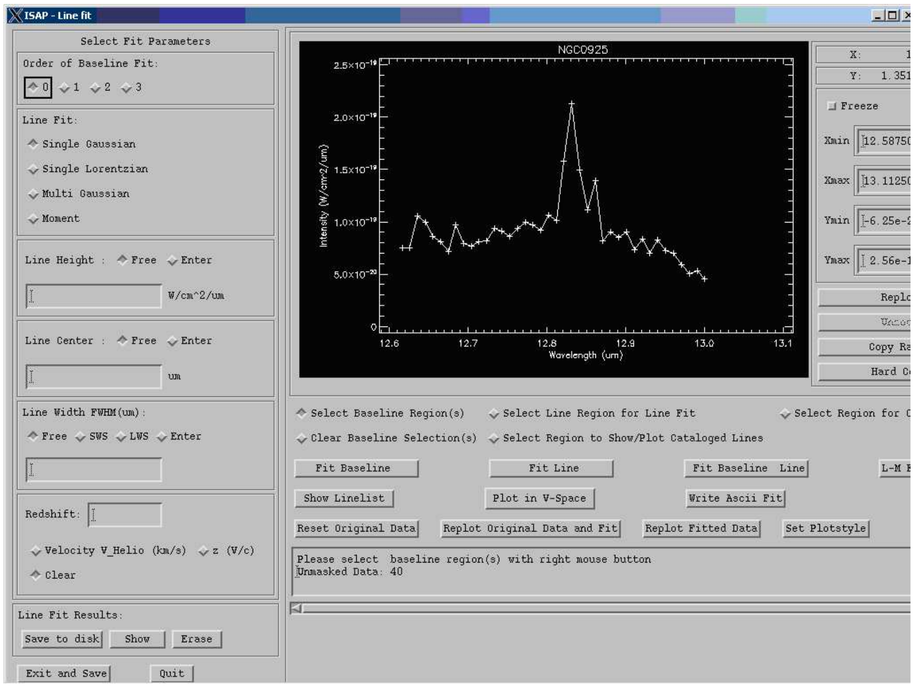

Figure A.13: Line Fit gui

with multiple observations. With staring observations there are two slits per module. In all of our publications we have ALWAYS extracted the fluxes from each slit individually rather than averaging the spectra from the two slits and then extracting the line flux. This is because the slits in both the mapping and staring observations occupy distinctly different regions of the sky–the slits cannot therefore be averaged unless the emission originates from a compact source that is contained entirely in each slit. If the emission is not uniformly distributed, averaging can underestimate the flux or give you an overall non-detection for a particular line, when in fact you have a detection in one slit but a non-detection in another. We follow the procedure below when extracting fluxes. You might find another method depending on your science, but we have found that this is the most conservative method. (See the Data Analysis section of Dudik et al. 2007 for more details)

- If the fluxes measured from the two slits differed by no more than the calibration error of the instrument, then the fluxes were averaged; otherwise, the slit with the highest measured line flux was chosen.
- If an emission line was detected in one slit, but not in the other, then the detection was selected. This is true for all of the high and low resolution staring and mapping observations.

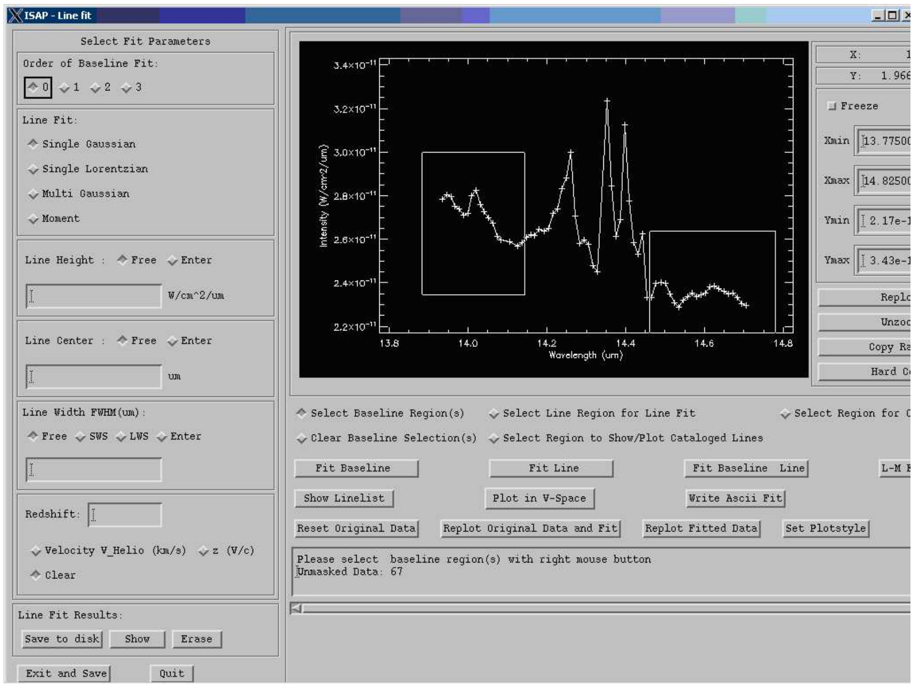

Figure A.14: An example of [NeV] blended with PAH and [ClII]

2. *Full Spectrum for Publications:* Here I will show you how to average two full SH or LH spectra. This might be useful for publication purposes but there are a couple of things I need to note here:

IMPORTANT: *Averaging full spectra will be very difficult and whether you can do it or not is STRONGLY dependent on the observation. For mapping observations the best way to create a full spectrum is to use CUBISM which I am not going to go over here. CUBISM uses an algorithm to average over overlapping slits (as opposed to coincident slits) which results in a much more accurate full spectrum then to use a standard averaging method as though the slits were coincident. For staring observations you CANNOT use CUBISM, thus the only way to create one full spectrum is to average the two slits. This can be done in SMART, but you must be careful.*

WARNINGS:

- Sometimes the continuum in two SH slits is not uniform. You cannot average these slits. This will be obvious when you overlap both spectra in SMART and they dont line up at all.
- LH and SH spectra should really not be averaged together. LH spectra come from much larger slits than SH spectra. Therefore the LH spectra will inevitably be higher in continuum flux than the SH slits. You can

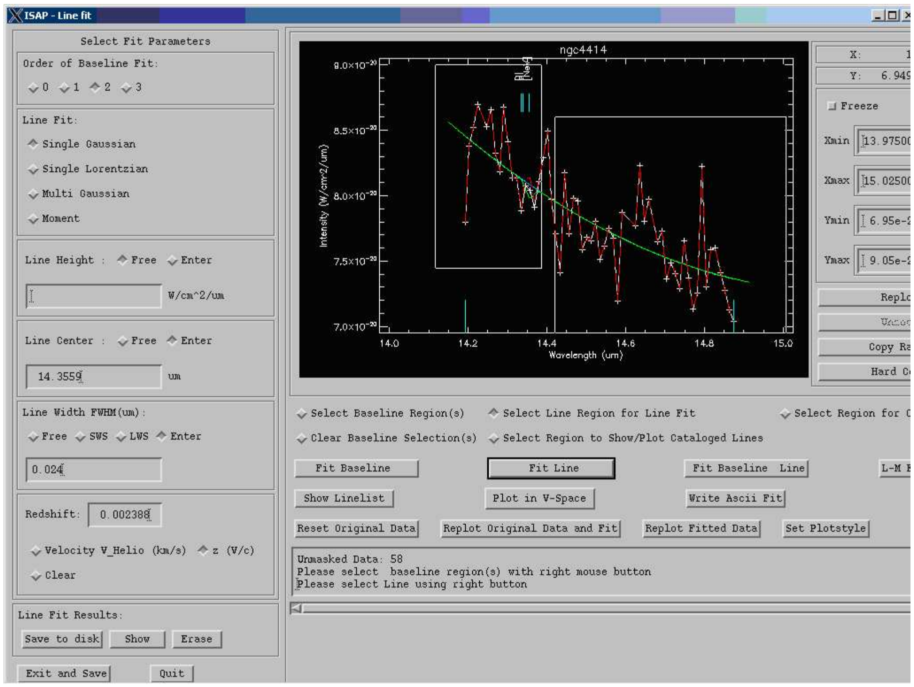

Figure A.15: An example of a fit for a non-detection

subtract a set value from the LH flux so that the two spectra line up, but the flux value on the Y-axis will not mean anything.

3. The following is the method for averaging two SH slits or two LH slits in SMART.

   - Once you have zapped all of the bad data points and saved two cleaned SH files in SMART (YOU HAVE FINISHED II.5. FOR BOTH SH), you can now load both files back into SMART
   - On the left column of the SMART IDEA gui click Read, immediately click AAR.fits
   - A gui will pop up asking you to please select a file. Select the first SH file that you already cleaned and click OK.
   - IF YOU CLICK "STORE" ON THE LEFT COLUMN OF THE IDEA GUI YOU SHOULD SEE YOUR FILE AS THE LAST FILE IN THE LIST HERE.
   - Load the second SH file in the same way: Click Read and immediately AAR.fits. Select the second SH file that you have cleaned and click OK.
   - Click on STORE.

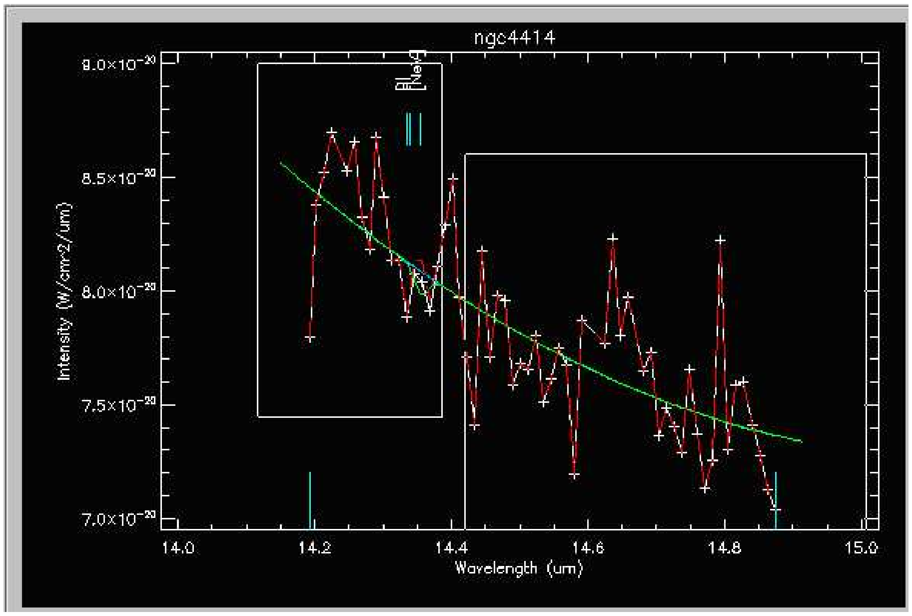

Figure A.16: An example of a fit for a non-detection

- Your two SH files should appear as the last two files in the Stored Data Sets gui.
- Click on the first SH file so that the diamond (or circle) is highlighted.
- Click "Choose and Apply Function", immediately click "Make Prime Data Set" *This will make the first SH file the "prime" data set that we will apply other functions to.*
- Go to "Store" again.
- Highlight the diamond (or circle) of the second SH file.
- Click "Choose and Apply Function", immediately click "Merge with Prime Data Set"
- In order to get both Spectra to appear in the SMART IDEA gui you must Click "ALL" under the BCD row and the SLIT Pos. row at the top of the SMART IDEA gui. This tells SMART to Plot both spectra together. Your spectra should now look like this:

NOTE *This is an example of a spectrum that can be averaged. The continuum in the two slits very obviously line up almost perfectly. This is not always the case. It just so happens that the continuum emission in this case seems to be relatively uniform.*

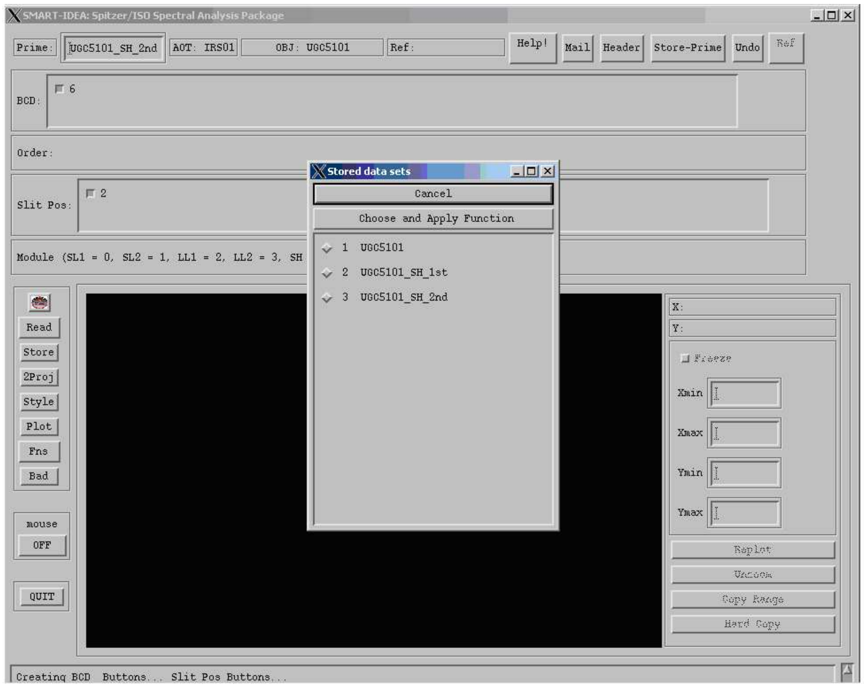

Figure A.17: Stored Data Sets gui within the SMART IDEA gui

- To average, Right click a box over both spectra to include everything.
- The Applications gui should pop up
- Click Average and the Averaging gui will pop up:

- Click Standard Clip Mean
- Click the X and the top right corner of the averaging gui to exit.
- The result of should show up in the SMART IDEA gui as such:

- Click Store Prime at the top right of the SMART IDEA gui
- Slick Store at the left of the SMART IDEA gui
- Click on the Merged Spectrum and highlight the associated diamond
- Click Click Choose and Apply Function
- Click "Write to Disk", and immediately click "In Fits Table Format"
- Save the Averaged Spectra.

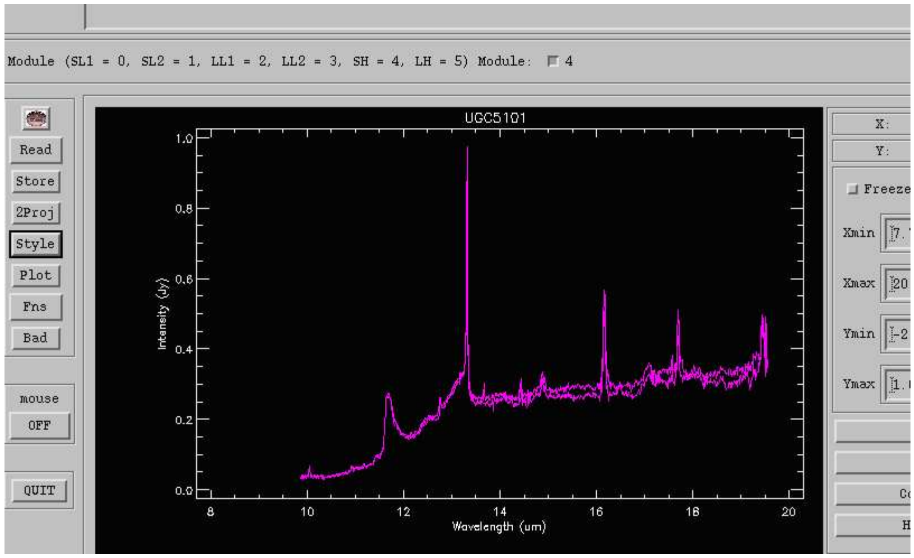

Figure A.18: Two spectra in SMART after they have been merged together

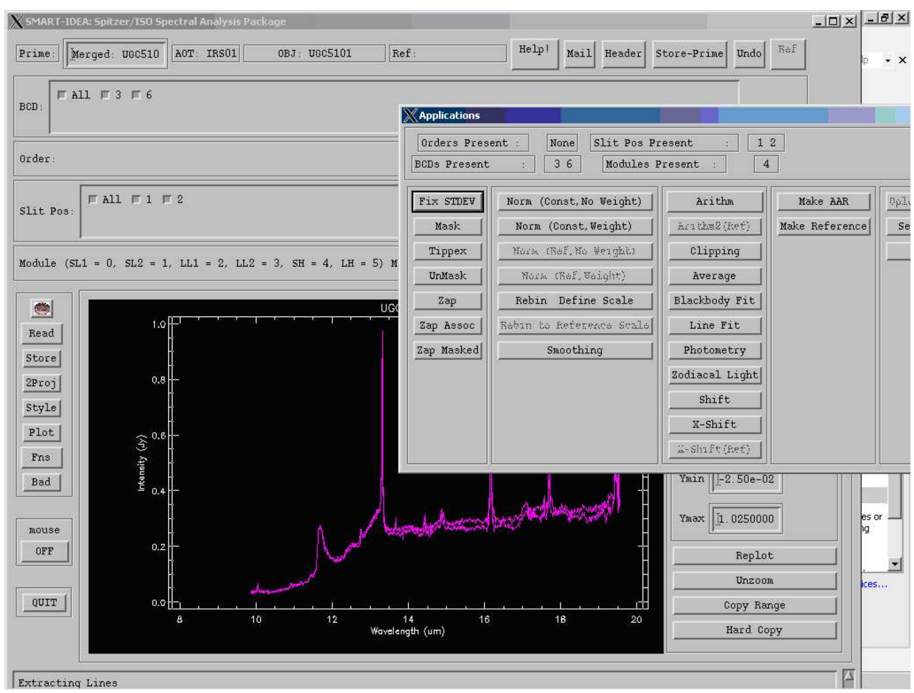

Figure A.19: Applications gui

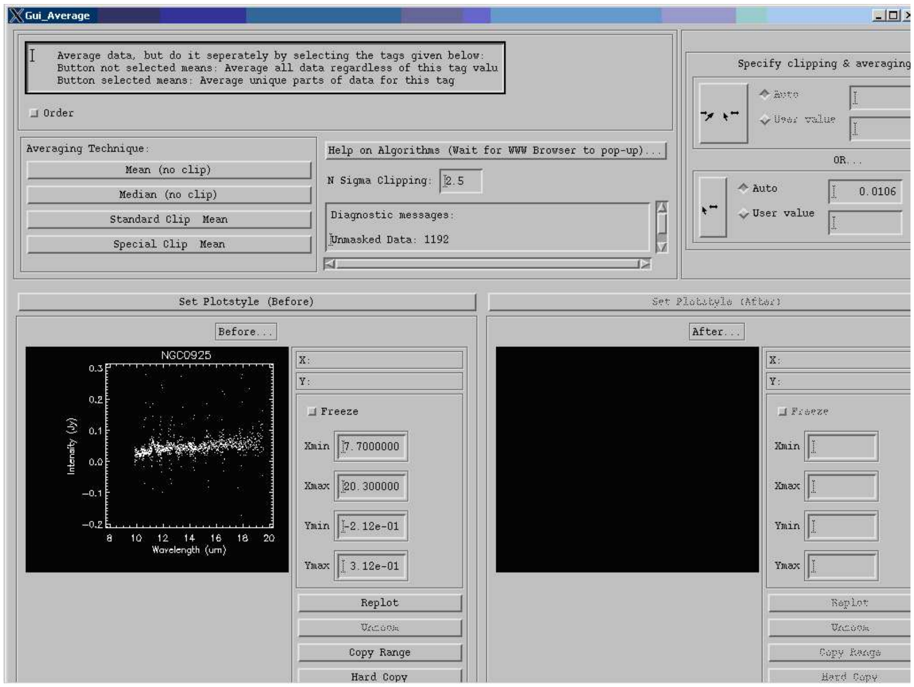

Figure A.20: Averaging gui

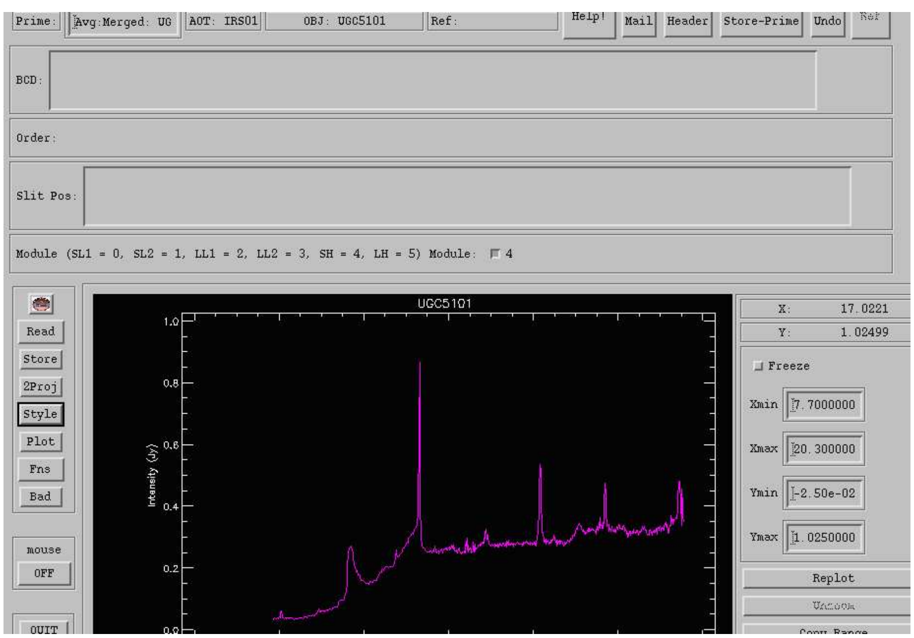

Figure A.21: Final merged spectra

Bibliography

Bibliography

[1] Adams, T. F. & Weedman, D. W., 1975, ApJ, 199, 19

[2] Arnaud, K. A., Dorman, B., Gordon, C., X-spec User's Guide for Version 12.3.1, 2007, http://heasarc.nasa.gov/xanadu/xspec/manual/manual.html

[3] Acosta-Pulido, J. A., Gabriel, C., & Castaneda, H. O. 2000, Exp. Astron., 10, 333

[4] Afanasiev, V. L. & Sil'chenko, 2005, A&A, 429, 825

[5] Alexander, T. & Sternberg, A., 1999, ApJ, 520, 137

[6] Alexander, T., Sturm, E., Lutz, D., et al. 1999, ApJ, 512, 204

[7] Alloin, D., Edmunds, M. G., Lindblad, P. O., & Pagel, B. E. J., 1981, A&A, 101, 377

[8] Alloin, D., Pantin, E, Lagage, P.O., & Granato, G. L., 2000, A&A, 363, 929

[9] Alloin, D., Pelat, D., Phillips, M., & Whittle, M., 1985, ApJ, 288, 205

[10] Andreasian, N. K. & Khachikian, E. Y., 1987, IAUS, 121, 541

[11] Armus, L., Bernard-Salas, J., Spoon,et al., H. W. W., et al. 2006, ApJ, 640, 204

[12] Armus, L., Charmandaris, V., Spoon, H. W. W., et al. 2004, ApJS, 154, 178

[13] Baan, W. A. & Klckner, H. R., 2006, A&A, 449, 559

[14] Balestra, I., Boller, T., Gallo, L., et al., 2005, A&A, 442, 469

[15] Baribaud, T., Alloin, D., Glass, I., & Pelat, D., 1992, A&A, 256, 375

[16] Bell, E. F. 2003, ApJ, 586, 794

[17] Benson, A. J., Frenk, C. S., & Sharples, R. M. 2002, ApJ, 574, 104

[18] Bland, J., Taylor, K, & Atherton, P. D., 1986, IAUS, 127, 417

[19] Bland, J., Taylor, K. & Atherton, P. D., 1987, MNRAS, 228, 595

[20] Blandford, R. D. 1999, in ASP Conf. Ser. 182, Galaxy Dynamics, ed. D. R. Merritt, M. Valluri, & J. A. Sellwood (San Francisco: ASP), 87

[21] Boroson, T. A. 2002, BAAS, 34, 1265

[22] Boroson, T. A. 2003, ApJ, 585, 647

[23] Botte, V., Ciroi, S., Rafanelli, P., & Di Mille, F. 2004, AJ, 127, 3168

[24] Capetti, A., Axon, D. J., & Macchetto, F., 1997, ApJ, 487, 560

[25] Capetti, A., Macchetto, F., Axon, D. J., Sparks, W. B., & Boksenberg, A., 1995, ApJ, 448, 600.

[26] Cappi, M, Panessa, F., Bassani, L., et al. 2006, 446, 459.

[27] Carilli, C. L., & Taylor, G. B., 2000, ApJ, 532, 95

[28] Carrillo, R., Masegosa, J., Dultzin-Hacyan, D., & Ordonez, R. 1999, Rev. Mex. AA, 35, 187

[29] Charmandaris, V., Laurent, O., Le Floch, E., 2002, A&A, 391, 429

[30] Chemin, L., Cayatte, V., Balkowski, C., et al., 2003, A&A, 405, 89

[31] Chiar, J. E. & Tielens, A. G. G. M., 2006, ApJ, 637, 774

[32] Clavel, J., Schulz, B., Altieri, B., et al., 2000, A&A, 357, 839

[33] Clegg, R.E.S, Harrington, J. P., Barlow, M. J., & Walsh, J. R.,1987, ApJ, 314, 551

[34] Cohen, R. D., 1983, ApJ, 273, 489

[35] Colina, L. Arribas, S., & Borne, K. D., 1999, ApJ, 527, 13

[36] Condon, J. J., Huang, Z. P., Yin, Q. F., & Thuan, T. X. 1991, ApJ, 378, 65

[37] Corbin, M. R. 2000, ApJ, 536, L73

[38] Crane, P. C. 1977, PhDT, 115

[39] Cutri, R. M., Rieke, G. H., Tokunaga, A. T., Willner, S. P. & Rudy, R. J., 1984, ApJ, 280, 521

[40] Dahari, O. & De Robertis, M. M., 1988, ApJS, 67, 249

[41] Dahlem, M., Petr, M. G., Lehnert, M. D., Heckman, T. M., & Ehle, M. 1997, A&A, 320, 731

[42] Dale, D. A., Smith, J. D. T., Armus, L, et al., 2006, astroph/0604007

[43] Davies, R., Ward, M., & Sugai, H., 2000, ApJ, 535, 735

[44] de Bruyn, A. G., & Wilson, A. S. 1978, A&A, 64, 433

[45] de Graauw, T., Haser, L. N., Beintema, D. A., Roelfsema, P. R., van Agthoven, H., 1996, A&A, 315, 49

[46] de Vaucouleurs, G., 1973, ApJ, 181, 31

[47] Devereux, N. A., & Young, J. S. 1991, ApJ, 371, 515

[48] Di Matteo, T., Springel, V., & Hernquist, L. 2005, preprint (astro-ph/0502199)

[49] Donato, D., Sambruna, R. M., & Gliozzi, M. 2004, ApJ, 617, 915

[50] Draine, B. T., 1989, Interstellar Extinction in the Infrared, Edited by B.H. Kaldeich, European Space Agency.

[51] Duc, P. A., Mirabel, I. F., & Maza, J., 1997, A&AS, 124, 533

[52] Dudik, R. P., Satyapal, S. Gliozzi, M. & Sambruna, R. M.2005, ApJ, 620, 113

[] udik, R. P., Weingartner, J. C., Satyapal, S., Fischer, J., Dudley, C. C., O'Halloran, B. 2007, ApJ, 664, 71

[53] Ebneter, K., & Balick, B., 1983, ASP, 95, 675

[54] Ehle, M., Beck, R., Haynes, et al., 1996, A&A, 306, 73

[55] Elvis, M., et al. 1994, ApJS, 95, 1

[56] Elvis, M.; Wilkes, B. J., McDowell, J. C., et al. 1994, ApJS, 95,1

[57] Espinosa, J. M., Rodriquez, R. J., & Jones, B. 1987, in Star Formation in Galaxies (Washington: NASA), 669

[58] Evans, D. A., Kraft, R. P., Worrall, D. M., et al., 2004, ApJ, 612, 786

[59] Fabian, A. C., 1989, ESASP, 296, 1097

[60] Falcke, H., Wilson, A. S., & Simpson, C., 1998, ApJ, 502, 199

[61] Falcke, H., Nagar, N. M., Wilson, A. S., Ho, L, C., & Ulvestad, J. S., 1999, astro-ph/9912436

[62] Falcke, H., Nagar, N. M., Wilson, A. S. & Ulvestad, J. S., 2000, ApJ, 542, 197

[63] Fanaroff, B. L., & Riley, J. M. 1974, MNRAS, 167, 31

[64] Farrah, D., Afonso, J., Efstathiou, A., Rowan-Robinson, M., Fox, M., & Clements, D. 2003, MNRAS, 343, 585

[65] Farrah, D., Bernard-Salas, J., Spoon, H. W. W., Soifer, B. T., & Armus, L., 2007, ApJ, 667, 149

[66] Fender, R. & Belloni, T., 2004, ARA&A, 42, 317

[67] Ferland, G. J., Martin, P. G., van Hoof, P. A. M., & Weingartner, J. C. 2002, in Workshop on X-ray Spectroscopy of AGN with Chandra and XMM-Newton, MPE Report 279, 103

[68] Ferland, G. J., & Netzer, H. 1983, ApJ, 264, 105

[69] Ferrarese, L., & Ford, H. C. 1999, ApJ, 515, 583

[70] Ferrarese, L., & Merritt, D. 2000, ApJ, 539, L9

[71] Ferrarese, L., Pogge, R. W., Peterson, B. M., Merritt, D., Wandel, A., & Joseph, C. L. 2001, ApJ, 555, L79

[72] Ferruit, P., Wilson, A. S., Falcke, H. et al., 1999, MNRAS, 309, 1

[73] Filippenko, A. V. & Sargent, W. L. W, 1985, ApJS, 57, 503

[74] Forster, K., Green, P. J., Aldcroft, T. L. et al., 2001, ApJS, 134, 35

[75] Fukazawa, Y., Iyomoto, N., Kubota, A., Matsumoto, Y., & Makishima, K. 2001, PASJ, 53, 595

[76] Fukugita, M., Hogan, C. J., Peebles, P. J. E., 1998, ApJ, 503, 518

[77] Gabriel, C. 2002, PHT Interactive Analysis User Manual (ESA), http://www.iso.vilspa.esa.es/users/handbook

[78] Galavis, M. E., Mendoza, C., Zeippen, C. J., 1997, A&AS, 123, 159

[79] Gallagher, S. C., Brandt, W. N., Chartas, G., Garmire, G. P., & Sambruna, R. M., 2002, ApJ, 569, 655

[80] Galliano, E., Alloin, D., Pantin, E., Lagage, P.O., & Marco, O., 2005, A&A, 438, 803

[81] Gallo, L. C., Boller, Th., Brandt, W. N., et al., 2004, A&A, 417, 29

[82] Gebhardt, K., et al. 2000a, ApJ, 539, L13

[83] Gebhardt, K., et al. 2000b, ApJ, 543, L5

[84] Gebhardt, K., et al. 2003, ApJ, 583, 92

[85] Genzel, R., Lutz, D., Sturm, E., Egami, E., et al., 1998, ApJ, 498, 579

[86] Genzel, R., Weitzel, L., Tacconi-Garman, L. E., et al., 1995, ApJ, 444, 129

[87] Georgantopoulos, I. Panessa, F., Akylas, A., et al., 2002, A&A, 386, 60

[88] Georgantopoulos, I., Georgakakis, A., & Koulouridis, E., 2005, MNRAS, 360, 782

[89] Giveon, U., Sternberg, A., Lutz, D., Feuchtgruber, H., & Pauldrach, A. W. A. 2002, ApJ, 566, 880

[90] Gliozzi, M., Sambruna, R. M., & Brandt, W. N. 2003, A&A, 408, 949

[91] Griffin, D. C. & Badnell, N. R., 2000, JPhB, 33, 4389

[92] Goncalves, A. C., Veron-Cetty, M.-P.; & Veron, P., 1999, A&AS, 135, 437G

[93] Gonzalez-Martin, O., & Masegosa, J. et al., 2006, A&A, 460, 45

[94] Griffiths, R. E., Homeier, N., Gallagher, J., & HST/WFPC2 Investigation Definition Teamn, 1997, AAS, 191, 7607

[95] Grupe, D., & Mathur, S. 2004, ApJ, 606, L41

[96] Grupe, D., Leighly, K. M., Burwitz, V., Predehl, P., & Mathur, S. 2004, AJ, 128, 1524

[97] Guainazzi, M., Matt, G., Brandt, W. N., et al., 2000, A&A, 356, 46

[98] Guainazzi, M., Oosterbroek, T., Antonelli, L. A., & Matt, G. 2000, A&A, 364, L80

[99] Guainazzi, M., Matt, G., & Perola, G. C., 2005, A&A, 444, 119

[100] Guilbert, P. W. & Rees, M. J., 1988, MNRAS, 233, 475

[101] Haas, M., Chini, R., Meisenheimer, K., et al. 1999, in The Universe as Seen by ISO, ed. P. Cox & M. F. Kessler (ESA SP-427; Noordwijk: ESA), 887

[102] Haas, M., Siebenmorgen, R., Schulz, B., Krugel, E., & Chini, R., 2005, A&A, 442, 39

[103] Haehnelt, M. G., Natarajan, P., & Rees, M. J. 1998, MNRAS, 300, 817

[104] Haehnelt, M. G., & Kauffman, G. 2000, MNRAS, 318, L35

[105] Hao, C. N., Xia, X. Y., Mao, S., Wu, H., & Deng, Z. G. 2005, ApJ, 625, 78

[106] Hao, L., Spoon, H. W. W., Sloan, G. C., et al. 2005, ApJ, 625, 75

[107] Halpern, J. P. & Steiner, J. E., 1983, ApJ, 269, 37

[108] Heckman, T. M., 1980, A&A, 87, 152

[109] Heckman, T. M., Kauffmann, G., Brinchmann, J., Charlot, S., Tremonti, C., & White, S. D. M. 2004, ApJ, 613, 109

[110] Hernquist, L., & Mihos, J. C. 1995, ApJ, 448, 41

[111] Higdon, S. J. U., Devost, D., Higdon, J. L., et al., 2004, PASP, 116, 975

[112] Ho, L. C., Filippenko A. V., & Sargent, W. L. W. 1995, ApJS, 98, 477

[113] Ho, L. C., 1996, ASPC, 103, 103

[114] Ho, L. C., Filippenko A. V., & Sargent, W. L. W. 1997a, ApJS, 112, 315

[115] Ho, L. C., Filippenko, A. V., Sargent, W. L. W., & Peng, C. Y. 1997b, ApJS, 112, 391

[116] Ho, L. C. 1999, Adv. Space Res., 23, 813

[117] Ho, L. C. 1999, ApJ, 516, 672

[118] Ho, L. C., et al. 2001, ApJ, 549, L51 (H01)

[119] Ho, L. C., Filippenko, A. V., & Sargent, W. L. W. 2003, ApJ, 583, 159

[120] Hogg, D. W., et al. 2002, AJ, 124, 646

[121] Hönig, S. F., Bekcert, T., Ohnaka, K. & Weigelt, G., 2006, A&A, 452, 459

[122] Houck, J. R., Roellig, T. L., Van Cleve, J. et al., 2004, ApJS, 154, 18

[123] Huang, S., Gu, Q. S., Su, H., Hawarden, T. G., Liao, X. H., & Wu, G. X. 1996, A&A, 313, 13

[124] Hummer, D. G., Berrington, K. A., Eissner, W. et al., 1993, A&A, 279, 298

[125] Humphrey, P. J. & Buote, D. A., 2006, ApJ, 639, 136

[126] Hunt, L. K., & Malkan, M. A. 1999, ApJ, 516, 660

[127] Imanishi, M. & Terashima, Y., 2004, AJ, 127, 758

[128] Isaak, K. G., Priddey, R. S., McMahon, R. G., et al. 2002, MNRAS, 329, 149

[129] Ishigaki, T., Yoshida, M., Aoki, K., et al., 2000, PASJ, 52, 185

[130] Isobe, T., & Feigelson, E. D. 1992, ApJS, 79, 197

[131] Israel, F. P, 1998, A&ARv, 8, 237

[132] Iyomoto, N., Makishima, K., Fukazawa, Y., Tashiro, M. & Ishisaki, Y., 1997, PASJ, 49, 425

[133] Jackson & Browne, 1990, Nature, 343, 43

[134] Johansson, L. & Bergvall, N., 1988, A&A, 192, 81

[135] Joy, M. & Harvey, P. M., 1987, ApJ, 315, 480

[136] Kant, I., 1755, *Unveral Natural History and the Theory of Heavens*

[137] Kaspi, S., Smith, P. S., Netzer, H., Maoz, D., Jannuzi, B. T., & Giveon, U. 2000, ApJ, 533, 631

[138] Keel, W. C., 1983, ApJ, 269, 466

[139] Keel, W. C. 1993, Rev. Mex. AA, 27, 77

[140] Kendall, M., & Stuart, A. 1976, The Advanced Theory of Statistics, Vol. 2 (New York: Macmillan)

[141] Kennicutt, R. C., Jr, 1978, PhDT, 6

[142] Kennicutt, R. C., Jr. 1998, ApJ, 498, 541

[143] Kewley, L. J., Heisler, C. A., Dopita, M. A., & Lumsden, S., 2001, ApJS, 132, 37

[144] Kewley, L. J., Geller, M. J., Jansen, R. A., & Dopita, M. A. 2002, AJ, 124, 3135

[145] Khachikian, E. Y. & Weedman, D. W., 1974, ApJ, 192, 581

[146] King, A. 2003, ApJ, 596, L27

[147] Knapen, J. H., Beckman, J. E., Shlosman, I, Peletier, R. F., Heller, C. H., & de Jong, R. S. 1995, ApJ, 443, L73

[148] Kollatschny, W. & Kowatsch, P., 1998, A&A, 336, 21

[149] Komossa, S. & Schulz, H., 1998, A&A, 339, 345

[150] Koratkar, A., Deustua, S. E., & Heckman, T. 1995, ApJ, 440, 132

[151] Kormendy, J., & Richstone, D. 1995, ARA&A, 33, 581

[152] Kuraszkiewicz, J. K., Green, P. J., Forster, K., et al., 2002, ApJS, 143, 257.

[153] Kuraszkiewicz, J. K., et al. 2003, ApJ, 590, 128

[154] Kuraszkiewicz, J. K., Green, P. J., Crenshaw, D. M., et al., 2004, ApJS, 150, 165

[155] Laine, S., van der Marel, R. P., & Rossa, J.; et al., 2003, AJ,126, 2717

[156] Laureijs, R. J., Klaas, U., Richards, P. J., Schulz, B., & Abraham, P. 2003, ISO Handbook, Volume IV: PHTThe Imaging Photo-Polarimeter (ESA SP-1262; Noordwijk: ESA), http://www.iso.vilspa.esa.es/users/handbook

[157] Lehnert, M. D., & Heckman, T. M. 1996, ApJ, 472, 546

[158] Lewis, K. T., Eracleous, M., & Sambruna, R. M. 2003, ApJ, 593, 115

[159] Lahuis, F., Wieprecht, E., Bauer, O. H., et al. 1998, adass, 7, 224

[160] Lindblad, P. O., Hjelm, M., Hoegbom, J., et al., 1996, A&AS, 120, 403

[161] Lindblad, P. 1999, A&ARv, 9, 22

[162] Lipari, S., Mediavilla, E., Diaz, R. J., et al., 2004, MNRAS, 348, 369

[163] Lasota, J.P., Abramowicz, M. A., Chen, X., Krolik, J., Narayan, R., Yi, I., 1996, ApJ, 462, 142

[164] Luhman, M. L., Satyapal, S., Fischer, J., Wolfire, M. G., Sturm, E et al., 2003, ApJ, 594, 758

[165] Lutz, D.; Maiolino, R.; Moorwood, A. F. M.; Netzer, H.; Wagner, S. J, et al., 2002, A&A, 396, 439

[166] Lutz, D., Spoon, H. W. W., Rigopoulou, D., Moorwood, A. F. M., & Genzel, R. 1998, ApJ, 505, L103

[167] Lutz, D., Veilleux, S. & Genzel, R. 1999, ApJ, 517L, 13L

[168] Lutz, D.; Genzel, R., Sternberg, A., et al., 1996, A&A, 315, 137

[169] Maiolino, R., Marconi, A., Salvati, M. et al., 2001a, A&A, 365, 37

[170] Maiolino, R., Marconi, A., & Oliva, E., 2001b, A&A, 365, 37

[171] Majewski, S. R., Hereld, M., Koo, D.C. Illingworth, G. D., & Heckman, T. M., 1993, ApJ, 402, 125.

[172] Marchesini, D., Celotti, A., & Ferrarese, L. 2004, MNRAS, 351, 733

[173] Marconi, A.; Oliva, E.; van der Werf, P. P.; et al., 2000, A&A, 357, 24

[174] Marconi, A., & Hunt, L. K. 2003, ApJ, 589, L21

[175] Martini, P. 2004, preprint (astro-ph/0404426)

[176] Mason, R. E., Geballe, T. R., Packham, C., et al., 2006, ApJ, 640, 612

[177] Mathews, W. G. & Ferland, G. J. 1987, ApJ, 323, 456

[178] Mazzarella, J. M., Gaume, R. A., Aller, H. D., & Hughes, P. A., 1988, ApJ, 333, 168

[179] Mazzarella, J. M., Bothun, G. D., & Boroson, T. A., 1991, AJ, 101, 2034

[180] Mazzarella, J. M., Voit, G. M., Soifer, B. T., et al., 1994, AJ, 107, 1274

[181] Mazzei, P., & de Zotti, G. 1994, ApJ, 426, 97

[182] McClintock, J. E., & Remillard, R. A. 2003, preprint (astroph/0306213)

[183] McLure, R. J., & Dunlop, J. S. 2001, MNRAS, 327, 199

[184] McLure, R. J., & Dunlop, J. S. 2002, MNRAS, 331, 795

[185] McMahon, R. G., Priddey, R. S., Omont, A., Snellen, I., & Withington, S. 1999, MNRAS, 309, L1

[186] Meixner, M., Puchalsky, R., Blitz, L., Wright, M. & Heckman, T., 1990, ApJ, 354, 158

[187] Mendoza, C., & Zeippen, C. J., 1982, MNRAS, 199, 1025

[188] Merloni, A., Heinz, S., & Di Matteo, T. 2003, MNRAS, 345, 1057

[189] Meurer, G. R., Heckman, T. M., Lehnert, M. D., Leitherer, C., & Lowenthal, J. 1997, AJ, 114, 54

[190] Misiriotis, A., Xilouris, E. M., Papamastorakis, J., 2006, A&A, 459, 113

[191] Mooney, T. J., & Solomon, P. M. 1988, ApJ, 334, L51

[192] Morrison, R., & McCammon, D. 1983, ApJ, 270, 119

[193] Mulchaey, J. S., & Regan, M. W. 1997, ApJ, 482, L135

[194] Murayama, T. & Taniguchi, Y., 1998, ApJ, 497, 9

[195] Mushotzky, R. F., Fabian, A. C., Iwasawa, K., et al., 1995, MNRAS, 272, 9

[196] Nagao, T., Taniguchi, Y, & Murayama, T. 2000, AJ, 119, 2605

[197] Nagao, T., Murayama, T , & Taniguchi, Y, 2001a, ApJ, 549, 155

[198] Nagao, T., Murayama, T , & Taniguchi, Y, 2001b, PASJ, 53, 629

[199] Nagao, T., Murayama, T., Shioya, Y, & Taniguchi, Y, 2003, 125, 1729

[200] Nagar, N. M., Falcke, H., Wilson, A. S., & Ho, L. C. 2000, ApJ, 542, 186

[201] Nagar, N. M., Wilson, A. S., Falcke, H. 2001, ApJ, 559L, 87

[202] Nagar, N. M., Falcke, H., Wilson, A. S., & Ulvestad, J. S. 2002, A&A, 392, 53

[203] Nagar, N. M., Falcke, H., & Wilson, A. S. 2004, in Proc. 7th Symp. of the European VLBI Network on New Developments in VLBI Science and Technology, ed. R. Bachiller et al. (Madrid: Obs. Astron. Nacional), 51

[] agar, N. M., Falcke, H., & Wilson, A. S., 2005, A&A, 435, 521

[204] Narayan, R., & Yi, I. 1995, ApJ, 444, 231

[205] Narayan, R., Mahadevan, R., & Quataert, E. 1998, in Theory of Black Hole Accretion Disks, ed. M. A. Abramowicz, G. Bjornsson, & J. E. Pringle (Cambridge: Cambridge Univ. Press), 148

[206] Narayan, R., Quataert, E., Igumenshchev, I. V., & Abramowicz, M. A. 2002, ApJ, 577, 295

[207] Oliva, E.; Salvati, M.; Moorwood, A. F. M.; & Marconi, A., 1994, A&A, 288, 457

[208] Oliva, E., Pasquali, A., & Reconditi, M., 1996, A&A, 305, L21

[209] Onken, C. A., & Peterson, B. M. 2002, ApJ, 572, 746

[210] Osterbrock, D. E., & Pogge, R. W. 1985, ApJ, 297, 166

[211] Pastoriza, M. & Gerola, H., 1970, ApL, 6, 155

[212] Paturel, G., et al. 1997, A&AS, 124, 109

[213] Peeters, E., Spoon, H. W. W., & Tielens, A. G. G. M., 2004, ApJ, 613, 986

[214] Penfold, J. E., 1979, MNRAS, 186, 297

[215] Peterson, B. M. 1997, An Introduction to Active Galactic Nuclei (Cambridge: Cambridge Univ. Press)

[216] Peterson, B. M., et al. 2000, ApJ, 542, 161

[217] Peterson, B. M., et al. 2004, ApJ, 613, 682

[218] Phillips, M. M., Edmunds, M. G., Pagel, B. E. J, & Turtle, A. J., 1983, MNRAS, 203, 759

[219] Priddey, R. S., Isaak, K. G., McMahon, R. G., Robson, E. I., & Pearson, C. P. 2003, MNRAS, 344, L74

[220] Prieto, M. A., & Viegas, S., 2000, RMxAC, 9, 324

[221] Protassov, R., van Dyk, D. A., Connors, A., Kashyap, V. L., & Siemiginowska, A. 2002, ApJ, 571, 545

[222] Ptak, A., Yaqoob, T, Mushotzky, R., Serlemitsos, P., & Griffiths, R. 1998, ApJ, 501, L37

[223] Quataert, E. 2003, Astron. Nachr., 324, 435

[224] Quataert, E., & Narayan, R. 1999, ApJ, 520, 298

[225] Quillen, A. C., Bland-Hawthorn, J., Brookes, M. H. et al. 2006, ApJ, 641, 29

[226] Radomski, J. T., Pina, R. K., Packham, C., et al., 2003, ApJ, 587, 117

[227] Rees, M. J. 1982, in IAU Symp. 97, Extragalactic Radio Sources, ed. D. S. Heeschen & C. M. Wade (Dordrecht: Kluwer), 211

[228] Rees, M. J. 1984, ARA&A, 22, 471

[229] Rigopoulou, D., Spoon, H. W. W., Genzel, R., et al., 1999, AJ, 118, 2625

[230] Risaliti, G., Bianchi, S., Matt, G., et al., 2005, ApJ, 630, 129

[231] Roberts, T.P., Schurch, N. J., & Warwick, R. S., MNRAS, 2001, 324, 737

[232] Roche, P. F.; Aitken, Smith, & Ward, 1991, MNRAS, 248, 606

[233] Rots, A. H, 1978, AJ, 83, 219

[234] Rowan-Robinson, M., & Crawford, J. 1989, MNRAS, 238, 523

[235] Rowan-Robinson, M. 2000, MNRAS, 316, 885

[236] Rownd, B. K., & Young, J. S. 1999, AJ, 118, 670

[237] Rubin, R. H., Colgan, S. W. J., Daane, A. R. & Dufour, R. J. 2002, AAS, 34, 1252

[238] Rubin, R. H., 2004, IAUS, 217, 190

[239] Sadler, E. M., Slee, O. B., Reynolds, J. E., & Roy, A. L. 1995, MNRAS, 276, 1373

[240] Sanders,D.B., Soifer,B.T., Elias,J.H., et al., 1988, ApJ., 325, 74.

[241] Sanders, D. B., Phinney, E. S., Neugebauer, G., Soifer, B. T., & Matthews, K. 1989, ApJ, 347, 29

[242] Sanders, D. B., & Mirabel, I. F. 1996, ARA&A, 34, 749

[243] Satyapal, S., Sambruna, R. M., & Dudik, R. P. 2004, A&A, 414, 825

[244] Satyapal, S. Dudik, R. P., O'Halloran, B. & Gliozzi, M, 2005, ApJ, 633, 86

[245] Sauvage, M., & Thuan, T. X. 1994, ApJ, 429, 153

[246] Schmitt, H. R. & Kinney, A. L., 1996, ApJ, 463, 498

[247] Schmitt, H. R., 1998, ApJ, 506, 647

[248] Schmitt, H. R. 2001, AAS Meeting, 198, 36.01

[249] Schmitt, H. R., Donley, J. L, Antonucci, R. R., et al., 2003, ApJ, 597, 768

[250] Schreier, E. J., Capetti, A., Macchetto, F., Sparks, W. B., & Ford, H. J., 1996, ApJ, 459, 535

[251] Schulz, H., Komossa, S., Schmitz, C., & Mücke, A., 1999, A&A, 346, 764

[252] Schwarz, M. P. 1984, MNRAS, 209, 93

[253] Scoville, N. Z., et al. 2000, AJ, 119, 991

[254] Shakura, N. I., & Sunyaev, R. A. 1973, A&A, 24, 337

[255] Shemmer, O., Netzer, H., Maiolino, R., Oliva, E., Croom, S., Corbett, E., & di Fabrizio, L. 2004, ApJ, 614, 547

[256] Shlosman, I., Frank, J., & Begelman, M. C. 1989, Nature, 338, 45

[257] Shlosman, I., Frank, J., & Begelman, M. C. 1990, Nature, 345, 679

[258] Shuder & Osterbrock, 1981, ApJ, 250, 55.

[259] Siebenmorgen, R., Freudling, W., Krgel, E., & Haas, M. 2004, A&A, 421, 129

[260] Silk, J., & Rees, M. 1998, A&A, 331, L1

[261] Smith, D. A. & Wilson, A. S., 2001, ApJ 557, 180

[262] Sparke, L., 1996, ApJ, 473, 810

[263] Spinoglio, L, Malkan, M. A., Smith, Howard, A., Gonzalez-Alfonso, E., & Fischer, J., 2005, ApJ, 623, 123

[264] Spinrad, H., Marr, J., Aguilar, L., & Djorgovski, S. 1985, PASP, 97, 932

[265] Spoon, H. W. W., Keane, J. V., Tielens, A. G. G. M., Lutz, D., Moorwood, A. F. M., & Laurent, O. 2002, A&A, 385, 1022

[266] Stasinska, G., 1984, A&A, 55, 15

[267] Stauffer, J. R. 1982, ApJS, 50, 517

[268] Storchi-Bergmann, T.; Mulchaey, J. S.; & Wilson, A. S. 1992, ApJ, 395, 73

[269] Sturm, E., Bauer, O. H., Brauer, J., et al., 1998, adass, 7, 161

[270] Sturm, E., Lutz, D, Verma, A, et al., 2002, A&A, 393, 821

[271] Sturm, E., Schweitzer, M., Lutz, D., et al., 2005, ApJ, 629, 21

[272] Sturm, E., Rupke, D., Contursi, A. et al. 2006, ApJ, 653, 13

[273] Surace, J. A., & Sanders, D. B. 1999, ApJ, 512, 162

[274] Tacconi, L. J., Genzel, R., Lutz, D, et al, 2002, ApJ, 580, 73

[275] Tadhunter, C. N., Morganti, R., di Serego-Alighieri, S., Fosbury, R. A. E., & Danziger, I. J. 1993, MNRAS, 263, 999

[276] Tayal, S. S., & Gupta, G. P., 1999, ApJ, 526, 544

[277] Teng, Stacy H., Wilson, A. S., Veilleux, S., Young, A. J., Sanders, D. B. & Nagar, N. M., 2005, ApJ, 633, 664

[278] Terashima, Y., Kunieda, H. & Misaki, K., 1999, PASJ, 51, 277

[279] Terashima, Y., Ho, L. C., & Ptak, A. F. 2000, ApJ, 539, 161

[280] Terashima, Y, Iyomoto, N., Ho L. C., & Ptak, A. F., 2002, ApJ, 139, 1

[281] Terashima, A. Y., & Wilson, A. S. 2003, ApJ, 583, 145

[282] Terashima, Y. 2004, Prog. Theor. Phys. Suppl., 155, 431

[283] Terlevich, R., & Melnick, J. 1985, MNRAS, 213, 841

[284] Terlevich, R., Tenorio-Tagle, G, Rozyczka, M., Franco, J., & Melnick, J. 1995, MNRAS, 272, 198

[285] Thompson, K. L., 1992, ApJ, 395, 403

[286] Toomre, A., & Toomre, J. 1972, ApJ, 178, 623

[287] Tran, H.D., Cohen, M. H., & Villar-Martin, M., 2000, AJ, 120, 562

[288] Tremaine, S., et al. 2002, ApJ, 574, 740

[289] Ulvestad, J. S., & Wilson, A. S., 1984, 285, 439

[290] Ulvestad, J. S., & Wilson, A. S. 1989, ApJ, 343, 659

[291] Usui, T., Saito, M., & Tomita, A. 1998, AJ, 116, 2166

[292] van Bemmel, I. M., & Dullemond, C. P. 2003, A&A, 404, 1

[293] Van Hoof, P. A. M., Beintema, D. A., Verner D. A. & Ferland, G. J., 2000, A&A, 354, 41

[294] Veilleux, S. & Osterbrock, D. E., 1987, ApJS, 63, 295

[295] Veilleux, S., Kim, D. C., Sanders, D. B., Mazzarella, J. M., & Soifer, B. T. 1995, ApJS, 98, 171

[296] Veilleux, S., Sanders, D. B., & Kim, D. C., 1999, ApJ, 522, 139

[297] Verma, A., Lutz, D., Sturm, E., et al., 2003, A&A, 403, 829

[298] Veron-Cetty, M. P. & Veron, P., 1986, A&AS, 66, 335

[299] Veron-Cetty, M. P. & Veron, P., 2003, A&A, 412, 399

[300] Vignati, P., et al. 1999, A&A, 349, L57

[301] Vila, M. B., Pedlar, A., Davies, R. D., Hummel, E., & Axon, D. J. 1990, MNRAS, 242, 379

[302] Wada, K. 2004, in Coevolution of Black Holes and Galaxies, ed. L. C. Ho (Cambridge: Cambridge Univ. Press), 187

[303] Wandel, A., & Boller, Th. 1998, A&A, 331, 884

[304] Wang, J., Heckman, T. M., Weaver, K. A., & Armus, L. 1997, ApJ, 474, 659

[305] Weedman, D. W., Hao, L., Higdon, S. J. U., et al. 2005, ApJ, 605, 578

[306] Weingartner, J. C., & Murray, N., 2002, ApJ, 580, 88

[307] Weiprecht, E., Lahuis, F., Bauer, O. H., et al., 1998, adass, 7, 279

[308] Weisskopf, M. C., 1999, BAAS, 31.1514

[309] White, N. E., Nagase, F., & Parmar, A. N. 1995, in X-Ray Binaries, ed. W. H. G. Lewin, J. van Paradijs, & E. P. J. van den Heuvel (Cambridge: Cambridge Univ. Press), 1

[310] Wilkes, B. J., Hooper, E. J., McLeod, K. K., et al. 1999, in The Universe as Seen by ISO, ed. P. Cox & M. F. Kessler (ESA SP-427; Noordwijk: ESA), 845

[311] Wilson, A. S., Baldwin, J. A., Sun, S., & Wright, A. E., 1986, ApJ, 310, 121

[312] Woo, J.H., & Urry, C. M., 2002, ApJ, 579, 530

[313] Worrall, D. M., Birkinshaw, M., & Hardcastle, M. J. 2003, MNRAS, 343, L73

[314] Wyithe, J. S. B., & Loeb, A. 2003, ApJ, 595, 614

[315] Xia, X. Y., Xue, S. J., Mao, S., Boller, Th., Deng, Z. G., & Wu, H., 2002, ApJ, 564, 196

[316] Young, J. S., Allen, L., Kenney, J. D. P., Lesser, A., & Rownd, B. 1996, AJ, 112, 1903

[317] Yuan, F., Markoff, S., Falcke, H., & Biermann, P. L. 2002, A&A, 391, 139

[318] Zhang, X., Wright, M., & Alexander, P., 1993, ApJ, 418, 100

[319] Zhao, H., Haehnelt, M. G., & Rees, M. 2002, NewA, 7, 385

Curriculum Vitae

Rachel Dudik spent her formative years, along with five siblings, on a small family farm in central Pennsylvania. She attended Penns Valley High School where she developed wide ranging interests, including fine art, language, literature, science, and mathematics. She spent most of her spare time painting, sketching, running or completing farm chores.

After graduating high school, Rachel attended St. Johns College, in Annapolis, Maryland, where she participated in the Great Books of Western Civilization curriculum, an all-required course of study, based on reading (including Greek), study and discussion of the books which form the foundations of Western traditions in philosophy, humanities and sciences. At St. Johns College, she developed the analytical, writing and communication skills critical to the research she pursued in her graduate studies. In her sophomore year she was nominated for the Sophomore Thesis Essay Prize. She graduated, in 2002, with a Bachelor of Arts with majors in philosophy and history of mathematics and science along with minors in classical and comparative literature.

In the summer of 2002, Dr. Shobita Satyapal of George Mason University awarded Rachel a research internship. Soon after, she matriculated at GMU as a full-time graduate student in physics and astronomy, and assumed the roles of graduate research assistant, awarded by Dr. Satyapal, and teaching assistant (one year), granted by the GMU Department of Physics and Astronomy. Ms. Dudik's research centers on multi-wavelength X-ray and Mid-IR studies of nuclear regions of galaxies in an attempt to link galaxies with actively accreting black holes with inactive galaxies such as the Milky Way. In 2004, Sigma Xi, professional fraternity, awarded Rachel a Grant-In-Aid of Research for studies of Low Ionization, Nuclear Emission-line Regions. George Mason University bestowed on Rachel the degree of Masters in Applied and Engineering Physics in May, 2005.

In the subsequent years required for completing her doctorate, Rachel used observations from the NASA Great Observatories Program, *Chandra* and *Spitzer* to further her investigation of Low Ionization, Nuclear Emission-line Regions and their connection to other galaxies. This research direction became the central focus of her dissertation. Rachel has presented the results of her research at national scientific conferences, and she has authored or coauthored seven refereed papers which have appeared in international journals, such as *Astronomy & Astrophysics* and *The Astrophysical Journal*. In July 2006, she received a NASA Graduate Student Research Fellowship, which supported her during the final phases of her graduate education and dissertation preparation.